

TOWARDS PHOTOINDUCED CHARGE
ACCUMULATION
IN PURELY MOLECULAR d^6 METAL COMPLEXES
WITH OLIGO-TRIARYLAMINE DONORS

Inauguraldissertation

zur Erlangung der Würde eines Doktors der Philosophie

vorgelegt der
Philosophisch-Naturwissenschaftlichen Fakultät
der Universität Basel



von

Annabell G. Bonn

aus Miltenberg, Bayern

Basel 2015

Originaldokument gespeichert auf dem Dokumentenserver der Universität Basel

edoc.unibas.ch

Genehmigt von der Philosophisch-Naturwissenschaftlichen Fakultät
auf Antrag von

Fakultätsverantwortlicher/Dissertationsleiter: Prof. Dr. Oliver S. Wenger
Korreferentin: Prof. Dr. Catherine E. Housecroft

Basel, den 24.03.2015

Prof. Dr. Jörg Schibler

Scientists will eventually stop flailing around with solar power and focus their efforts on harnessing the only truly unlimited source of energy on the planet: STUPIDITY.

Scott Adams

Für meine Eltern
und Ella

ACKNOWLEDGEMENT

I thank **Prof. Dr. Oliver S. Wenger** for accepting me in his group and thus giving me the chance to work on such an interesting topic, I've developed a rather intense love-hate relationship with. I do thank him very much for his ever open door, the discussions, and his constant support. I couldn't have wished for a better *Doktorvater*.

I thank **Prof. Dr. Catherine E. Housecroft** for kindly agreeing to be my 2nd examiner.

Sincere thanks is given to **Prof. Dr. Thomas Pfohl** for chairing my examination.

I am very grateful to **Sylvie Mittelheisser** for measuring the EA, to **Dr. Heinz Nadig** for measuring all the ESI-HRMS spectra, and to **Dr. Markus Neuburger** for measuring and solving the OTA crystal structure.

Very special thanks go to the 'unsung heroes': The whole **Werkstatt-Team** for making the move to Basel and the every-day lab life as smooth as possible. **Brigitte Howald** and **Beatrice Erismann** for their help in all organizational matters. Special thanks goes to **Markus Hauri** for always being available and ever so helpful.

The whole Häussinger group, particularly **Heiko, Kaspar, and Thomas** I thank for the occasional help with my NMR's and more importantly for their readiness to participate in inter-group mingling and the coffee breaks.

My thanks also goes to **Angelo Lanzilotto** for the introduction to the Quantaaurus-Tau/-QY and, most importantly, for the key.

Concerning the start up with \LaTeX , I thank **Johannes Becker** for not having me start completely from scratch.

For the help in the synthesis of two reference molecules, I do thank my very last intern **Benedikt Ganter**.

I want to thank all past and present members of the **AK Wenger** so much:

For the warm welcome in Göttingen, the joint efforts in moving to Switzerland, and the great time in Basel.

Particularly,

Martin for discussing (photo-)chemistry with me and answering all the questions, even the JACS paper couldn't help me with.

Ann-Christin for the pep-talks and our conversations about everything, but 'Gott und die Welt'.

Julia for sharing a sink and bearing with me especially in the final stage of my presence in the lab.

Laura, Hauke, and **Andrea** I thank very much for introducing me to a sport I, against all odds, really do enjoy a lot – Look, it's a muscle!

Last but not least, I thank my fellow in misery **Luisa** for sharing the burden with me and restoring my faith in blondes.

A very special thanks goes to the "**harte Kern**" of the AK Wenger for being reliable companions on many an Apéro. I think you know who you are!

Furthermore, I want to thank all the people I was fortunate enough to meet here in Basel, making the decision to move the right one.

My aunt **Jane** and uncle **Horst**, I thank a lot for the provision of spatial, technical, sweet, and liquid support during the last four years.

There are a handful of people who deserve special honors for helping me to stay on track these past years:

Roland, I thank you very much for the years together and your encouragement and support during those last months.

The most important people I couldn't have done it without are my **Ma, Pa,** and my sister **Vi**. You have supported every decision I have made so far, especially moving to Basel, and will most likely still do so in the future. I do not have words that can express my deepest gratitude for your lifelong support and faith in me and my abilities.

HYPOTHESES

Section III.1

Photoinduced hole accumulation on OTA in a $\text{Re}_2\text{-OTA}$ triad. Increased chance of absorption of a second photon due to the presence of two rhenium photosensitizers.

Section III.2

Twofold charge separation resulting in $\text{AQ}^{2-}\text{-Re-OTA}^{2+}$ after consecutive absorption of two photons. Increase of the first charge-separated state lifetime due to prolongation of the D-A distance and addition of BRØNSTED acids (PCET).

Section III.4

Substitution of rhenium by ruthenium in AQ-Ru-OTA allowing for significantly higher excitation densities. Addition of metal ions (LEWIS acids) as substitutes for stronger BRØNSTED acids to circumvent premature oxidation of OTA and promote the second charge separation step.

Section III.6

Detection of an extremely long-living photoproduct in the time-resolved experiments in presence of Sc^{3+} . Photo-accumulation of the second scandium ion-stabilized, charge-separated state $\text{AQ}^{2-}\text{-Ru-OTA}^{2+}$ on UV-Vis timescale.

Section III.7

Combination of two AQ acceptors and two ruthenium photosensitizers with one OTA donor in a pentad. Allowing for the accumulation of two holes on OTA entirely without the help of additives.

Section IV

Employment of the strong electron donor OTA in push-pull systems in combination with boron mesityl acceptors leads to superior CT and solvatochromic behavior.

ABSTRACT

One major problem humanity faces these days is the use of fossil fuels and even more pressing, the consequences of their combustion. Therefore, multiple research groups of various scientific backgrounds have made it their business to find a way to produce energy from sunlight and water. In order to successfully produce these so-called solar fuels, one has to go beyond charge transfer on a single-electron level. Most fuel-forming reactions, such as H_2 production or CO_2 reduction, require multiple redox equivalents.

The main focus of this thesis was on the creation of a simple, purely molecular (nanoparticle-free) donor–photosensitizer–acceptor (D–P–A) assembly capable of twofold photoinduced charge accumulation without the use of sacrificial agents. Anthraquinone (AQ) was chosen as the two-electron acceptor, on which charge built-up can be mitigated by proton-coupled or metal ion-coupled electron transfer. Oligotriarylamine (OTA) displays excellent ability to donate two electrons. In combination with d^6 transition metal complexes, AQ and OTA present themselves as viable building blocks for D–P–A compounds for the study of photodriven charge accumulation. Initial photophysical investigation of rhenium containing triads gave charge separation on a single-electron level. In an AQ–Re–OTA triad, the charge-separated state lifetime could be significantly increased in presence of a strong BRØNSTED acid due to PCET. A long lifetime of the first charge-separated state is an important prerequisite for a second, charge-accumulating step to occur.

Advancing the systems by incorporation of ruthenium polypyridyl photosensitizers allowed for higher excitation densities. AQ–Ru–OTA exhibited a lifetime in the microsecond range for the first charge-separated state already without acids. In presence of Sc^{3+} , the lifetime was even increased beyond the detection limit of a nanosecond transient absorption setup. In the AQ–Ru–OTA triad, a ruthenium–OTA dyad, and in an AQ–Ru–OTA–Ru–AQ pentad, spectral evidence for OTA^{2+} was detected in presence of non-sacrificial additives, such as tetracyanobenzene or diphenylthiourea.

Furthermore, push-pull systems comprised of OTA and a boron mesityl acceptor were studied with regard to their emission behavior and the suitability of OTA for use in charge transfer emitters. This led to guidelines for the design of new charge transfer fluorophores.

CONTENTS

I	GENERAL INTRODUCTION	1
II	BACKGROUND AND MOTIVATION	5
II.1	Natural Photosynthesis and Water Oxidation	5
II.2	Fuel Production	8
II.3	About The Excited State – Population, Fate, and Photochemistry	11
II.3.1	Population and Fate	11
II.3.2	Photoinduced Electron Transfer	13
II.3.3	Energy Transfer	17
II.4	Accumulative Electron Transfer	18
II.5	Artificial Photosynthesis	20
II.6	Chosen Molecular Moieties	25
II.6.1	Metal Photosensitizers	25
II.6.2	Anthraquinone Acceptor	27
II.6.3	Oligo-triarylamine Donor	27
III	TOWARDS PHOTOINDUCED CHARGE ACCUMULATION IN D^6 METAL COMPLEXES	29
III.1	Triads with Two Rhenium Photosensitizers	30
III.1.1	Synthesis of the OTA Donor	30
III.1.2	Synthesis of Precursors and the Reference Molecules	31
III.1.3	Synthesis of the Studied Triads	33
III.1.4	Characterization by IR and Optical Absorption Spectroscopy	34
III.1.5	Determination of the Redox Potentials and Establishment of the En- ergy Level Diagrams	36
III.1.6	Steady State Luminescence Spectroscopy	39
III.1.7	Possibility of Triplet-Triplet Energy Transfer	40
III.1.8	Time-Resolved Luminescence Spectroscopy	41

III.1.9	Identification of the Photoproducts	42
III.1.10	Oxidative Flash-Quench Experiments	46
III.1.11	Influence of the Excitation Density on the Photochemistry	47
III.2	Electron Transfer in an AQ-Re-OTA Triad	51
III.2.1	Synthesis of AQ-Re-OTA	51
III.2.2	Spectroscopical Characterization of the Triad	54
III.2.3	Electrochemical Study of AQ-Re-OTA and Establishment of the Energy-Level Diagram	55
III.2.4	Influence of Acids on the OTA Donor	57
III.2.5	Influence of Hydrogen-Bond Strength on the Photoproducts	58
III.2.6	Kinetics of the Photogenerated Products	60
III.2.7	Dependence of the Transient Spectral Absorption on the Excitation Power	61
III.3	Summary and Conclusions on Photoinduced Electron Transfer in Rhenium-OTA-Complexes	62
III.4	Photoinduced Electron Transfer in an AQ-Ru-OTA Triad	64
III.4.1	Synthesis of the AQ-Ru-OTA Triad and a Reference Dyad	64
III.4.2	Optical Spectroscopic and Electrochemical Characterization	67
III.4.3	Kinetic Emission Behavior	70
III.4.4	Chemical Oxidation of OTA	70
III.4.5	Time-Resolved Absorption Studies on the Ru-OTA Dyad	71
III.4.6	Time-Resolved Study of AQ-Ru-OTA in Pure MeCN	74
III.4.7	Time-Resolved Study of AQ-Ru-OTA in Presence of LEWIS Acids	75
III.4.8	Time-Resolved Studies on AQ-Ru-OTA in presence of $\text{Sc}(\text{hmpa})_3^{3+}$	83
III.4.9	Time-Resolved Studies in Presence of <i>N,N</i> -Diphenylthiourea	84
III.4.10	Summary on Electron Transfer in AQ-Ru-OTA	87
III.5	Ferrioxalate Actinometry	90
III.6	Continuous Irradiation Experiments on Ru-OTA and AQ-Ru-OTA	93
III.6.1	Reference Experiments	94
III.6.2	Irradiation of Aerated Samples in Presence of Sc^{3+}	96
III.6.3	Irradiation of Aerated Samples in Absence of Sc^{3+}	100
III.6.4	Dark Reactions of Aerated Samples in Presence and Absence of Sc^{3+} ..	101
III.6.5	Irradiation of De-Oxygenated Samples in Presence of Sc^{3+}	102
III.6.6	Irradiation of De-Oxygenated Samples in Absence of Sc^{3+}	104

III.6.7	Dark Reactions of De-Oxygenated Samples in Presence and Absence of Sc^{3+}	105
III.6.8	Possibility of Photo-Degradation	106
III.7	Towards Accumulative Electron Transfer in an AQ–Ru–OTA–Ru–AQ Pentad	108
III.7.1	Synthetic Pathway to AQ–Ru–OTA–Ru–AQ	108
III.7.2	Electrochemical Characterization	110
III.7.3	Optical Spectroscopic Characterization	111
III.7.4	Photophysical Behavior in Different Solvents	112
III.7.5	Time-Resolved Experiments in Different Solvents	113
III.7.6	Photophysical Behavior in Presence of Thiourea	119
III.7.7	Summary and Conclusion on Electron Transfer in AQ–Ru–OTA–Ru–AQ	122
IV	SOLVENT DEPENDENT EMISSION OF OTA–B(MES) ₂ MOLECULES ...	125
IV.1	Synthesis of Studied Molecules	126
IV.2	Solvent-Dependent Charge Transfer Behavior	128
IV.2.1	Electrochemical Characterization	128
IV.2.2	Absorption and Emission Behavior in Hexane	130
IV.2.3	Solvatochromism	132
IV.2.4	Difference between Ground and Excited State Dipole Moments	134
IV.2.5	Luminescence Lifetimes and Quantum Yields	137
IV.3	Summary	138
V	GENERAL SUMMARY	141
VI	EXPERIMENTAL PART	143
VI.1	Analytical Methods	143
VI.2	Syntheses of the OTA donor	146
VI.3	Syntheses of General Building Blocks	147
VI.4	Syntheses of ligands and metal complexes with rhenium	151
VI.5	Syntheses of ligands and metal complexes with ruthenium	159
VI.6	Syntheses of the D–bridge–A molecules	171
VII	BIBLIOGRAPHY	181

A	ABBREVIATIONS AND SYMBOLS	V
B	LIST OF FIGURES	IX
C	LIST OF TABLES	XIX
D	CURRICULUM VITAE	XXI

I. GENERAL INTRODUCTION

With world's population growing, estimated to reach 9.6 billion by 2050,¹ humanity needs to find a way to secure Earth as a living environment for as long as possible. The number of inhabitants is going to increase significantly and the energy consumption per head and thus the absolute energy demand has already increased measurably. With the rapid technological progress and the power this continues to require, mankind's energy needs will most likely increase at a much steeper rate than population itself. According to estimates, the world's energy consumption rate will have increased to 40.8 TW by 2050. For comparison, in 2001 it was 13.5 TW.²

So far, fossil fuels like coal, crude oil, and gas have been the means of choice to meet the energy needs. In 2013, 85% of our energy requirements have been covered by fossil fuels. Thus, they have enabled new inventions and further advancement. Though abundant at times, only limited reserves are left and most of them are classified as 'not recoverable'. However, our immediate problem does not lie in the lack of fossil fuels but in the consequences of their combustion. Having burned them for years, we continuously polluted Earth with greenhouse gases (GHG) such as CO₂ or the even more harmful, synthetic hydrofluorocarbons (HFCs). The latter are mostly industrially released, which is again driven by fossil fuel combustion. Therefore, we promoted the depletion of the stratospheric ozone layer and global warming.

Fossil fuels are essentially biomass generated via natural photosynthesis millions of years ago. Their combustion is simply reverse photosynthesis, setting free again the pollutants Nature so elegantly recycled. We tend to call the biomass we burn today, and which covers about 11% of our energy needs, renewable energy.³ This denotation is certainly not quite accurate, if there are no plans afoot to e.g. reforest the woods we lumber. The truly renewable energy source we should focus on is solar energy. In the beginning of the 20th century, scientists realized that light, if converted properly, can serve us as an infinite energy source.⁴ With 100000 TW per annum, one hour of sunlight could cover the energy needs of mankind for one year.

Another abundant material on earth is water. Direct dissociation of H₂O into hydrogen and oxygen by simple irradiation with sunlight, however, is not possible. The

lack of overlap between the absorption spectrum of H₂O and the emission spectrum of sunlight prevents this.⁵ If we manage to find a way for using sunlight to split water into hydrogen and oxygen, we will be close to solving our energy problems. Both resources are present in abundance, hydrogen gas is considered the most environmentally friendly fuel, and oxygen would be the only side-product.

Since the emergence of the field of photochemistry, interdisciplinary research teams have devoted themselves to understanding the working principles of natural photosynthesis. With that, Nature has provided a blue-print for successful solar energy conversion and fuel production. It is certainly not desirable to build a faithful replica of PSII to cover our energy needs. For once, it will most likely be synthetically very demanding, if not unfeasible at all. Furthermore, natural photosynthesis in plants and bacteria does not exhibit a high quantum yield for energy conversion. It was designed by Nature as a repetitiously successful process with a high turn-over number. As a result, the beauty of energy harvesting, conversion and storage in the photosynthetic centers does not lie in their efficiency. Around 80% of the initially absorbed light energy is discarded again, unused, because it simply cannot be processed by the photosynthetic organism. Natural photosynthesis was developed for the sake of survival, not for efficient, excessive energy production the organism has no need for.^{6,7} Nowadays, we have a very firm grasp on the underlying mechanisms of the photosynthetic process. We know that charge separation, creating a high energy state, plays a pivotal role. More accurately, the separation of multiple redox equivalents is crucial for the production of high-energy substances, i.e. solar fuels.

So far, we have made use of sunlight in various types of manufactured solar cells.³ They provide the necessary electricity for driving electrochemical water splitting, producing oxygen and hydrogen. The latter can then directly be used as fuel or converted into other high-energy compounds, e.g. carbohydrates. Another possibility for hydrogen production is the use of photosynthetic organisms such as cyanobacteria or green algae.⁸ Unfortunately, though indeed producing solar fuel, the above mentioned ways do so in an indirect fashion. Losses are inevitable. The bio organisms, for example, will use a certain amount of the solar energy to survive. Therefore, designing a single system that combines the sites for direct light harvesting, solar energy conversion by charge separation, and fuel generation is preferable. By successfully mimicking the essential steps in natural photosynthetic centers, we might one day achieve fully renewable fuel production from sunlight and water. Figure I.1 depicts the schematic structure of such a proposed system.

An important prerequisite for the conversion of H₂O and also CO₂ to usable fuels is the accumulation of multiple redox equivalents. For this, a profound knowledge

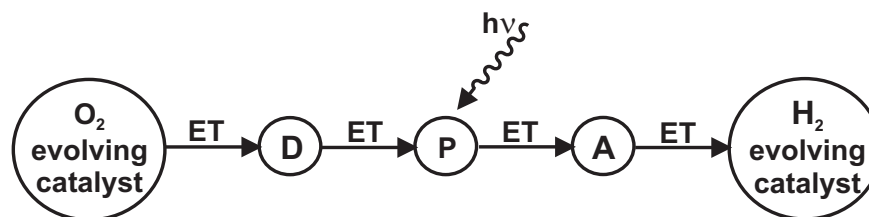


Figure I.1 Schematic structure of a system combining light-harvesting, charge separation, and fuel production. D = donor, P = photosensitizer, A = acceptor, ET = electron transfer.

of the factors governing successful charge accumulation is essential for the creation of a working example of the system in Figure I.1. Reported systems so far, have achieved only either water oxidation or fuel production and they are usually in need of high-energy sacrificial (“dead-end”) reactants. However, the ultimate artificial photosynthetic system has not yet been realized.

The main aim of this thesis was on achieving charge accumulation in purely molecular, nanoparticle-free D–P–A assemblies. They were designed to combine the half-reactions of hole and electron accumulation on two specific sites within one single molecular system. The focus hereby was on the realization of a self-sufficient central building block D–P–A as depicted in Figure I.1, which would not rely on sacrificial agents anymore.

For this, purely molecular (nanoparticle-free) systems theoretically capable of twofold charge accumulation via successive photoinduced electron transfer were designed, synthesized, and investigated physicochemically. Rhenium or ruthenium polypyridyl complexes were employed as photosensitizers. Anthraquinone (AQ), able to accept up to two electrons, was used as the acceptor in adaption of the quinone acceptors present in natural photosynthesis. The role of the electron donor was in all cases adopted by an oligo-triarylamine (OTA). This very strong donor can sequentially release up to three electrons. The manufactured systems were usually comprised of these three main molecular moieties covalently linked and combined in various combinations. By always improving the complex setup it was worked towards achieving twofold charge accumulation on the donor and/or acceptor site without the help of sacrificial reagents.

The following chapter will first give an introduction into natural photosynthesis and the oxygen evolving catalyst. A profound understanding of the systems we are trying to mimic in order to generate solar fuels is essential. Subsequently, the basic principles of photochemistry are introduced, as well as the problems associated with the accumulation of multiple redox equivalents. This will be followed by an overview

of reported charge accumulating systems in literature and the molecular units chosen in this thesis.

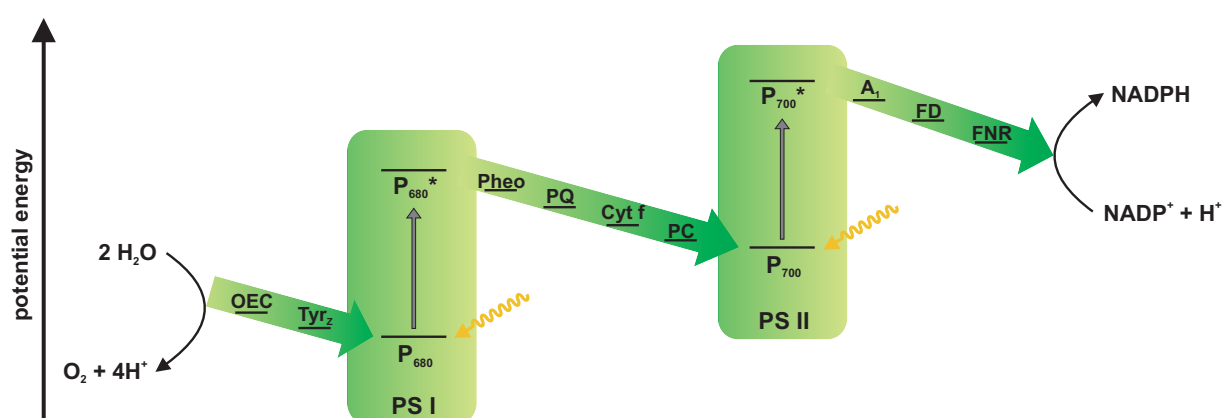
In a small side-project unrelated to artificial photosynthesis, the oligo-triarylamine donor was employed in a series of organic D–A dyads. These push-pull systems were investigated with respect to their solvent-dependent charge transfer properties. A lot of research is still focusing on the creation of very powerful, versatile emitters, and efficient blue and pure white light emitting compounds for use in OLEDs still attract a lot of scientific attention.^{9,10}

II. BACKGROUND AND MOTIVATION

II.1 Natural Photosynthesis and Water Oxidation

Over millions of years, Nature has established and perfected a means to capture sunlight and store the solar energy by converting CO_2 and H_2O to carbohydrates and other high-energy substances – the photosynthetic process. This endeavor requires the fine-tuning of several complex processes: light-harvesting by antenna chromophores, charge separation by several consecutive electron transfer steps, regeneration of the reaction center by oxidation of water, and CO_2 conversion to high-energy compounds, such as sugars.

The photosynthetic process is usually separated into two individual steps, the light reaction and the dark reaction. In the latter, CO_2 is captured and the solar energy acquired in the light reaction is ultimately stored in form of high-energy carbohydrates which then serve as ‘fuel’ for the organism. The focus of the following section, however, will be on the light-dependent reactions taking place in photosystems I and II (PSI and PSII) located in the thylakoid membranes of the chloroplasts. This is also where the oxidation of H_2O occurs. To mimic this reaction is the primary objective of many research groups.



Scheme II.1 Simplified Z-scheme of the light-dependent reactions in PSI and PSII.

Scheme II.1 depicts the charge-transfer chain as followed in the photosynthetic process. This simplified representation is referred to as a so-called Z-scheme.¹¹ The first

step of the photosynthetic process is the capture of solar energy by specially designed antenna chromophores. These transfer the excitation energy to P_{680} , a chlorophyll dimer located in the reaction center of PSII, within 1 ps. The photoexcited P_{680}^* then reduces a nearby pheophytin (Pheo), the primary electron acceptor. As a result a primary charge-separated state, $P_{680}^+Pheo^-$, is formed. This initial charge-separating step exhibits a thermodynamic efficiency of 70%.¹² The electron is then shuttled along an electron transfer chain with two protein bound quinone acceptors Q_A and Q_B (not shown in Scheme II.1), located in the plastoquinone pool (PQ). Upon two successive excitation and charge-separation steps the twofold reduced Q_BH_2 leaves PSII via the PQ on the other side of the protein. The reducing equivalents are then transported further along another electron transfer chain over cytochrome f (Cyt f), plastocyanin (PC), phylloquinone (A_1), and a ferredoxin unit (FD) among others. With the excitation of P_{700} enough energy is accumulated to fixate CO_2 at a ferredoxin-NADP reductase (FNR) where $NADP^+$ and $2H^+$ are reduced to produce NADPH, the natural form of H_2 storage. CO_2 can then be transformed into high-energy substrates by means of NADPH.

To ensure efficient use of the harvested solar energy, the rapid spatial separation of both, electrons and holes is crucial. Within 200 ps the electron is separated from the excited P_{680}^* by 26 Å to form $P_{680}^+Q^-$. This fast initial electron transfer enables a stable charge-separated state with a lifetime of hundreds of microseconds.⁶ The oxidized chlorophyll P_{680}^+ , as a strong oxidant ($E_{ox} = +1.2$ V vs. NHE),¹³ is regenerated by electron transfer from a tyrosine unit (Tyr_Z).

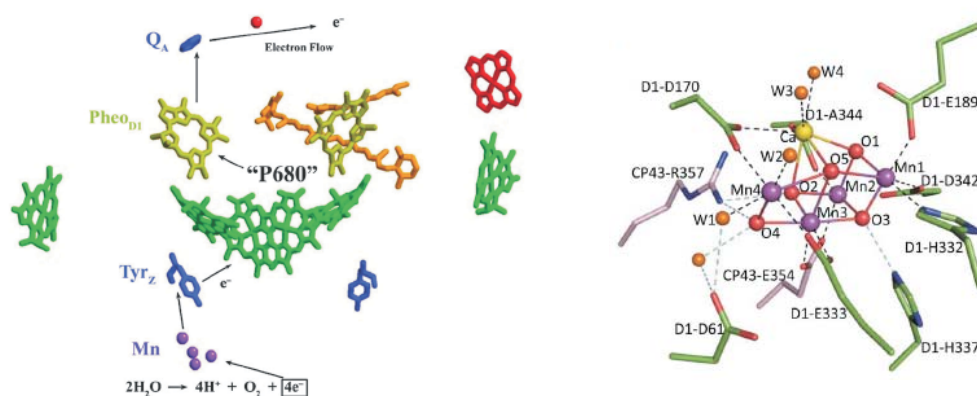
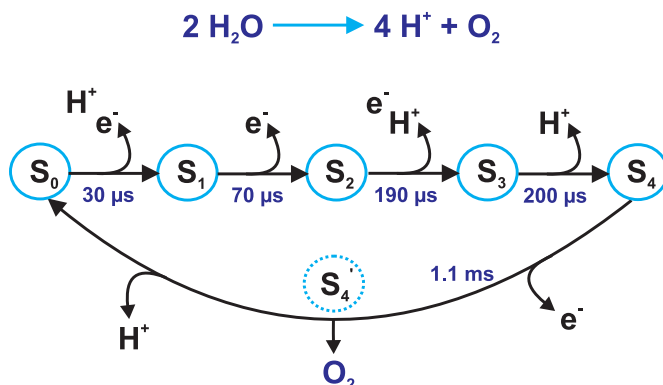


Figure II.1 Left: Reaction center of PSII. The surrounding protein structure was omitted for clarity. Electron transfer pathways are indicated by arrows.¹⁴ Right: Crystal structure of the OEC with its ligand environment.¹⁵ Reproduced with permission from^{14,15} © Royal Society of Chemistry and Nature Publishing Group.

This electron is originally released by oxidation of the so-called oxygen evolving complex (OEC), a pentanuclear CaMn_4 -cluster located in the heart of PSII. In the last years, a lot of attention was given to the elucidation of the structure of OEC. Only quite recently Umena *et al.* were able to obtain a crystal structure of the very complicated oxygen-evolving PSII with a resolution as high as 1.9 \AA .^{15–17} Figure II.1 displays the reaction center of PSII with the corresponding electron transfer pathways (left part). The right side depicts the OEC with its ligand environment. Comprised of one calcium atom and four oxygen-bridged manganese atoms, the OEC is also surrounded by a protein matrix separating it from the thylakoid lumen. (Figure II.1) Due to the surrounding amino acids the OEC is well insulated, allowing for a slow, stepwise oxidation. Another advantage of this insulation is the prevention of premature proton loss or uptake. As a result, the OEC is not converted into its reduced resting state prior to the release of O_2 by complete oxidation of H_2O .^{13,18}



Scheme II.2 Extended S-state cycle according to DAU and HAUMANN, depicting sequential proton and electron removal from the CaMn_4 -cluster. The times correspond to the half-lives of the S-transitions.¹⁸

The general mechanism of H_2O oxidation, taking place on the OEC as suggested by KOK in 1970 proved correct. Since then, several groups attempted to elucidate the exact underlying mechanism. KOK's initial catalytic cycle did not involve protons or reactions with H_2O in any of the four steps. It only stated the stepwise accumulation of four oxidation equivalents on the OEC, as indicated by the different numbers of the S-states. Eventually, this would lead to the oxidation of H_2O . Recent studies were able to shed light on a possible reaction mechanism involving H_2O molecules bound in the vicinity of the CaMn_4 -cluster. HAUMANN *et al.* have experimentally studied pigments of PSII by time-resolved EPR, UV-Vis and XAS spectroscopy and summarized their results in the extended S-cycle as depicted in Scheme II.2.¹⁸ The given times correspond to the half-lives of the S-transitions. A full cycle requires the sequential absorption of four photons. Due to dark-adaptation, S_1 is the predominant, long-term dark-stable

state. Therefore, the starting point was found to be an $S_1 \rightarrow S_2$ transition. Upon the first photon uptake, oxidation of one manganese atom is induced. Deprotonation, however, was not observed. A second photon uptake, promoting an $S_2 \rightarrow S_3$ transition leads to the formation of $\text{Tyr}_Z^{\bullet+}$ with concomitant manganese oxidation and proton release. The absorption of a third photon starts a series of transitions, $S_3 \rightarrow S_4 \rightarrow S_4' \rightarrow S_0$, which ultimately result in O_2 formation by H_2O oxidation. The $S_3 \rightarrow S_4$ transition is believed to involve proton release. Whereas the subsequent electron transfer from manganese to Tyr_Z takes place in the $S_4 \rightarrow S_4'$ transition. In the next step, H_2O is oxidized, O_2 released, and manganese oxidized one last time. After proton release the OEC reaches S_0 . With a final $S_0 \rightarrow S_1$ transition the cycle is closed. No charge accumulation occurs in this last step, since the electron transfer is supposed to be accompanied by deprotonation.¹⁹

In addition to the extended S-cycle in Scheme II.2, DAU and HAUMANN have proposed a cycle of alternating proton and electron release which would entail more intermediates still in need of characterization.¹⁸ Despite the well-resolved crystal structures of the OEC, the exact mechanics of water splitting is still partly speculative. The concomitant release of four protons and electrons to prevent the built-up of charge, however, is certain.

II.2 Fuel Production

Nowadays, humanity aims to store solar energy in form of chemical bonds, producing so-called solar fuels. As shown by natural photosynthesis, these reactions entail multiple charge-separating steps. Water oxidation, reduction of CO_2 , and hydrogen production each require more than one electron to be transferred in order to make and break chemical bonds.

Hydrogen Production

The storage of energy in form of hydrogen gas is a very clean and environmentally friendly way, since its only oxidation product is H_2O . Hydrogen could also be used directly as a fuel to drive machinery or be converted into electricity by means of fuel cells. Regarding the number of charges in need of accumulation, the production of H_2 is one of the easier reactions to master. As shown in Equation II.1, only two electrons have to be accumulated which then react with two protons to form H_2 .

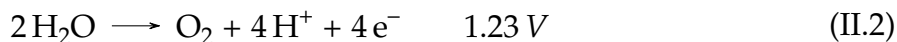


As a result, a lot of research has focused on visible light-driven hydrogen generation.

One approach is sunlight-induced reforming of biofuels such as glucose, ethanol or methanol. For that, we make use of Nature by applying natural systems that already successfully produce hydrogen. These species are e.g. natural hydrogenase enzymes.^{8,20} The earliest purely man-made approach to homogeneous hydrogen production were molecular three-component systems. They were comprised of a metal photosensitizer, sacrificial reagents to re-reduce the photosensitizer, and an electron relay station. As the actual hydrogen producing site mostly colloidal platinum was employed. In recent years the concept was developed further, linking the light-harvesting photosensitizer and the photocatalyst covalently. In 1983 LEHN and co-workers reported a combination of $\text{Ru}(\text{bpy})_3^{2+}$ and a cobalt catalyst, which produced hydrogen in presence of a sacrificial electron donor. This system was among the first to directly reduce the photocatalyst by the photosensitizer.²⁰⁻²²

Water Oxidation

The idea of using earth-abundant materials for future fuel production, inevitably leads to H_2O as a potent basic raw material. Directly observable from the chemical equation for the splitting of H_2O (Equation II.2) is that in addition to the generation of O_2 , protons and electrons are released. The latter can be recombined to yield H_2 .



The above reaction has a reported standard potential of 1.23 V vs. NHE. In reality, driving this reaction requires a higher potential, the so-called overpotential. It is needed to overcome activation barriers that are present for the electrolysis of pure water. As a result, to ensure efficient water splitting a minimum potential of $\approx 2\text{ V}$ is necessary.²³ In Nature, PSII absorbs photons with a wavelength of 680 nm to drive the photosynthetic process and thus, water splitting in the OEC. One such photon carries 1.83 eV of energy. Therefore, also visible light should enable photocatalytic water splitting, despite the need for an overpotential. Nevertheless, water oxidation catalysts, as for example the OEC in PSII, are used to minimize the overpotential in order to facilitate the process.

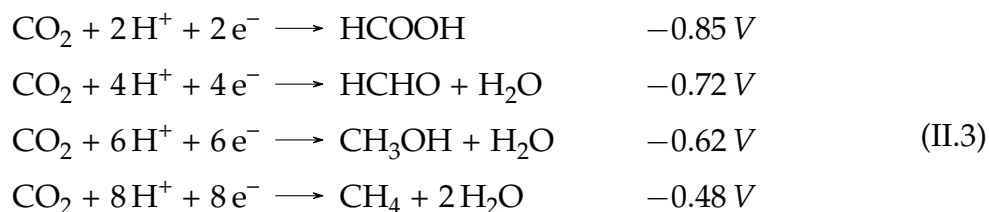
In 1972, FUJISHIMA and HONDA were the first to demonstrate heterogeneous photocatalytic water splitting in a photoelectrochemical cell by irradiation of TiO_2 with UV light. Oxygen evolution occurred at the TiO_2 photoanode, whereas hydrogen was detected at a platinum counter electrode.²⁴

In contrast to heterogeneous photocatalysis as performed by FUJISHIMA, the advantage of molecular systems is the easy customization of their structural and electronic

properties. Furthermore, their well-defined structure facilitates the study of underlying mechanisms. MEYER and co-workers were the first to report a molecular water oxidation catalyst, a dinuclear ruthenium polypyridyl complex ("blue dimer", *cis,cis*-[Ru(bpy)₂(H₂O)]₂(μ-O)⁴⁺) in the 1980s.²⁵ Following this pioneer work, multiple binuclear and mononuclear molecular water oxidation catalysts, mostly ruthenium polypyridyl complexes, have been reported in recent years. Yet, molecular complexes for water oxidation in homogeneous systems are still quite rare, compared to the heterogenous approach.^{23,26-29}

CO₂ Reduction

Even more challenging than water oxidation, from a kinetic and thermodynamic viewpoint, is the photoelectrochemical reduction of CO₂ to carbon monoxide or hydrocarbons as shown in Equations II.3. Preparation of hydrocarbons, e.g. formic acid, methanol or sugars is preferable. They are high-energy compounds that can be of direct use again. Whereas CO gas has to be further transformed, mostly industrially, into useful chemicals such as acetic acid, formic acid, or methanol. In all reactions listed below more than one reducing equivalent has to be accumulated. The potentials are given in V vs SCE at pH7.³⁰



Homogeneous photocatalysis for CO₂ reduction usually makes use of a light absorbing molecule and a transition metal catalyst, both promoting proton-coupled transfer of multiple electrons. Single electron reduction of CO₂ to form CO₂^{•-} requires a reduction potential of ≈ -2.14 V vs. SCE. Additionally, an overpotential of up to 0.6 V has to be considered.³⁰ Therefore, the concomitant transfer of both electrons and protons is preferred. The latter help avoid charge built-up. One advantage of transition metal complexes is the tunability of their photophysical properties simply by ligand modification. One example of photoinduced CO₂ reduction systems are cobalt or nickel tetraaza-macrocyclic complexes with [Ru(bpy)₃]²⁺ as photosensitizer. In another approach, ruthenium polypyridyl sensitizers were covalently linked to Re(bpy)(CO)₃X catalysts.³⁰⁻³²

In order to successfully perform the above listed reactions driven by light, a deeper

understanding of the mechanics, challenges, and problems associated with the accumulation of multiple redox equivalents is crucial.

II.3 About The Excited State – Population, Fate, and Photochemistry

The following section will give an introduction in the basics of photophysics and photochemistry to the extent necessary to understand the topics and results of this thesis. It will mainly focus on the underlying concepts of electronic absorption of light and the possible deactivation pathways of the excited state. Deactivation can hereby occur via radiative or non-radiative pathways, electron or energy transfer.

II.3.1 Population and Fate

In classical electrodynamics light is defined as high-frequency electromagnetic waves bearing a variety of different energies. However, to understand the concept of absorption and emission of light by matter, this approach is insufficient. Excitation of a transition metal photosensitizer P to form P* is initiated by the elevation of an electron from a low-lying energy state to a state higher in energy. Hereby, the minimum energy needed equals the difference between the energy levels of the ground state and excited state. The energetic position of the states is dependent on the nature of the complex. As a result, the energy needed can be quantified. Quantum mechanics, therefore, more accurately describes the transition of an electron as the absorption of a so-called photon with a defined energy content. From the absorption spectra of metal complexes one can deduce the probability of the different transitions. Spin-allowed transitions, such as ligand-centered $\pi \rightarrow \pi^*$ or $^1\text{MLCT}$ (metal-to-ligand charge transfer) transitions produce absorption bands of rather high intensity. On the other hand, spin-forbidden transitions ($^3\text{MLCT}$, d-d transition) produce very weak bands and are more difficult to detect in absorption spectroscopy.³³

The JABLONSKI diagram (Figure II.2) displays the different possible transitions upon absorption of a photon in a metal complex. All non-radiative pathways are shown by black, wiggly arrows.

In the ruthenium and rhenium transition metal complexes used in this thesis, excitation occurs from a singlet ground state (S_0) to a thermally excited singlet state (S_n). Faster than any photochemical or photophysical process, S_n relaxes to the vibrational ground state of the lowest-lying singlet excited state via radiationless deactivation (internal conversion IC, $> 10^{11} \text{ s}^{-1}$). Despite the excitation to a spin-allowed singlet

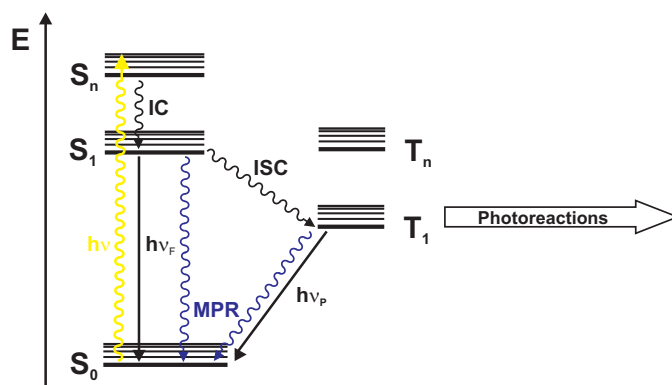


Figure II.2 Simplified JABLONSKI diagram.

state, the actual luminescent, lowest-energy excited state in transition metal complexes is usually a triplet state T₁. This state is accessible via intersystem crossing (ISC, $10^6 - 10^{11} \text{ s}^{-1}$) from the S₁ state. The transition between states of different spins is enabled by the strong spin-orbit coupling present in the transition metal complexes. In addition to undergoing IC, ISC, or multi phonon relaxation (MPR), the system can return to its ground state by releasing the excess energy as a photon. If the emission of light originates from S₁ the radiative process is called fluorescence ($h\nu_F$). Whereas the spin-forbidden transition from T₁ to the singlet ground state is referred to as phosphorescence ($h\nu_P$). It usually occurs at a much longer timescale than fluorescence exceeding the duration of excitation. The radiative deactivation processes are indicated by the solid arrows in Figure II.2.^{34,35}

Once the photoluminescent state T₁ of the metal complex is populated via the above discussed pathways it can be deactivated by various processes. Already mentioned were radiative deactivation by luminescence ($h\nu_F$, $h\nu_P$) and radiationless deactivation by heat dissipation (IC, ISC). For the calculation of the excited state lifetime all possible radiative and non-radiative processes have to be considered. Each one of them is assigned a rate constant (k_i) and the inverse of their sum gives the lifetime τ (Equation II.4 left).

$$\tau = \frac{1}{\sum_i k_i} \quad \phi = \frac{n_{h\nu}(\text{emitted})}{n_{h\nu}(\text{absorbed})} \quad (\text{II.4})$$

In addition to the lifetime of the excited state, its luminescence quantum yield ϕ is of interest. It can be calculated by dividing the amount of emitted photons by the number of absorbed photons (Equation II.4 right).

In case of sufficiently long lifetimes of P*, it can partake in photochemical reactions forming new products, or it can be quenched by energy or electron transfer to or from nearby molecules (Equations II.5).³⁶



If an electron donor is in close proximity to the excited photosensitizer, it can transfer an electron to P^* quenching it reductively. In presence of an electron acceptor this process is called oxidative quenching. Furthermore, energy transfer between P^* and a suitable quencher Q is possible.

II.3.2 Photoinduced Electron Transfer

The simplest setup capable of undergoing electron transfer requires a donor D and an acceptor A . In the work presented in this thesis D and A are covalently linked via bridging units and in some cases the role of A is played by a photosensitizer. In the following, electron transfer theory according to MARCUS and HUSH will be introduced to the extent necessary for the understanding of this thesis.³⁷

The original, classical theory about electron transfer as pioneered by R. A. MARCUS addresses outer-sphere, self-exchange reactions. MARCUS communicated his theory in numerous papers in extraordinary mathematical detail.^{38–44} Later, N. S. HUSH extended the theory, taking inner-sphere reactions into account.⁴⁵ In outer-sphere reactions, a term adapted from coordination chemistry, no chemical bonds are formed or broken, however, due to the transfer of electrons and the accompanying redistribution of charge, bond lengths and angles can change. Furthermore, the surrounding solvent shell, as well as the involved redox sites have to adapt to the changed charge distribution. Thus, the need for reorganization results in an increase of the activation barrier, which in turn decreases the reaction rate.

Figure II.3 depicts the potential wells for an exergonic electron transfer reaction, as defined by MARCUS-HUSH theory. For non-adiabatic electron transfer reactions, i.e. weak electronic coupling (H_{AB}) between D and A , the reactant and product states retain their individuality (cyan parabola). In this case, the electron has to hop from the reactant state ($D-A$) to the product state (D^+-A^-), overcoming the free energy of activation (E_A). The energy of the activation barrier can be derived from the intercept of the two cyan parabolas.

The horizontal axis represents the reaction coordinate and the vertical axis the free energy for electron transfer G_{ET}^0 . In MARCUS-HUSH theory, the reaction coordinate is a

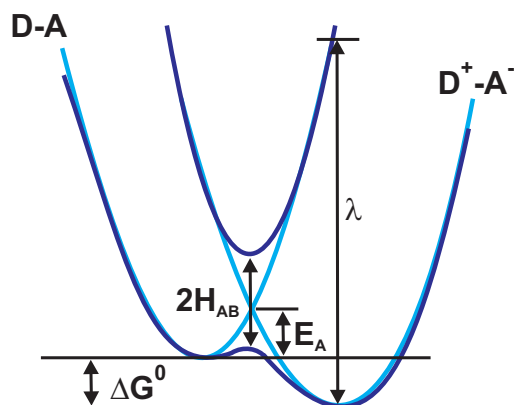


Figure II.3 Potential energy wells for exergonic electron transfer in D-A including inner and outer sphere reorganization.

combined representation of changes in the outer-sphere (solvent shell reorganization) and inner-sphere (bond lengths and angles adjustment). The systems investigated in this thesis usually undergo non-adiabatic electron transfer, due to the relatively weak electronic coupling between the donor and acceptor units.

For adiabatic electron transfer processes H_{AB} is strong, resulting in a splitting of the energy wells at their intercept. The maximum splitting is $2H_{AB}$. In this particular case, the charge transfer system remains on the lower potential energy surface when passing from D-A to D^+A^- (blue parabola).

For non-adiabatic electron transfer reactions the following semi-classical equation can be applied to calculate the rate constant.

$$k_{ET} = \sqrt{\frac{4\pi^3}{h^2\lambda k_B T}} H_{AB}^2 \cdot \exp\left[-\frac{(\Delta G^0 + \lambda)^2}{4\lambda k_B T}\right] \quad (\text{II.6})$$

Equation II.6 shows that the electron transfer rate is mainly dependent on three parameters: 1) the reorganization energy λ ; 2) the reaction free energy, or driving force ΔG^0 ; and 3) the electronic coupling, H_{AB} , between donor and acceptor. Further parameters needed to calculate the reaction rate are the BOLTZMANN constant k_B and the temperature T .

Reorganization Energy

In order for electron transfer to occur, the reactants have to obtain nuclear configurations similar to the products. The necessary change in configuration is achieved by vibrational reorganization. When estimating the systems reorganization energy λ , contributions of both the inner and outer sphere have to be considered. For the inner sphere (Equation II.7) this means the adjustment of bond lengths and angles upon

charge transfer. Following a changed charge distribution in the D–A system, D and A have to adapt to the new situation. In Equation II.7, k_i are the normal mode vibrational force constants and Δq_i corresponds to the changes in the nuclear configuration of the normal vibrational modes.

$$\lambda_{in} = \frac{1}{2} \sum (k_i \Delta q_i^2) \quad (\text{II.7})$$

$$\lambda_{out} = \frac{\Delta e^2}{4\pi\epsilon_0} \left(\frac{1}{\epsilon_{op}} - \frac{1}{\epsilon_s} \right) \left(\frac{1}{2r_D} + \frac{1}{2r_A} - \frac{1}{d_{DA}} \right) \quad (\text{II.8})$$

In addition to changes in the inner-sphere of D–A, a transfer of charge always entails changes in the solvent shell as well. Directly observable from Equation II.8 is the dependence of the outer reorganization energy on the D–A distance d_{DA} and the radii of D and A (r_D , r_A), respectively. For an easy estimation of the radii, D and A are regarded as hard spheres. The bigger these spheres, the smaller is the interaction between the solvent molecule and the charge on D or A, resulting in a small λ_{out} . Furthermore, the amount of transferred charge Δe has to be considered. Most importantly, the value of the outer reorganization energy is dependent on the static (ϵ_s) and optical (ϵ_{op}) dielectric constants of the surrounding solvent. The effect of solvent reorientation is especially prominent when charge transfer reactions occur in polar solvents. In the initial state D–A, usually a charge-neutral state, the electric field is weaker than in the charge-separated product state. Therefore, solvents with a strong electric dipole moment show a higher affinity to the product state. As a result, the contribution of λ_{out} to the total reorganization energy is quite small in apolar solvents.

Driving Force

When passing from the relaxed ground state of D–A to its charge separated D^+A^- state, a certain amount of change in the free energy is observed. This change in energy is called the driving force of the electron transfer process, ΔG^0 . The transfer of charge from the reactant to the product energy well requires the system to overcome the activation barrier E_A . For the calculation of this activation energy barrier, Equation II.9 can be applied. Semi-classical treatment of electron transfer processes has shown that E_A mainly arises from the necessary reorganization of the inner and outer sphere due to the changed charge distribution in the reactant and product states. Therefore, λ is also part of Equation II.9.

$$E_A = \frac{(\Delta G^0 + \lambda)^2}{4\lambda} \quad (\text{II.9})$$

The electron transfer rate constant, k_{ET} , reaches a maximum when $-\Delta G^0 = \lambda$. At this saddle point of the parabola in the lower part of Figure II.4, the system has reached its optimal electron transfer rate and no activation energy barrier is present. An increase of the reaction rate with increasing driving force ($-\Delta G^0$) is a well expected and accepted phenomenon.

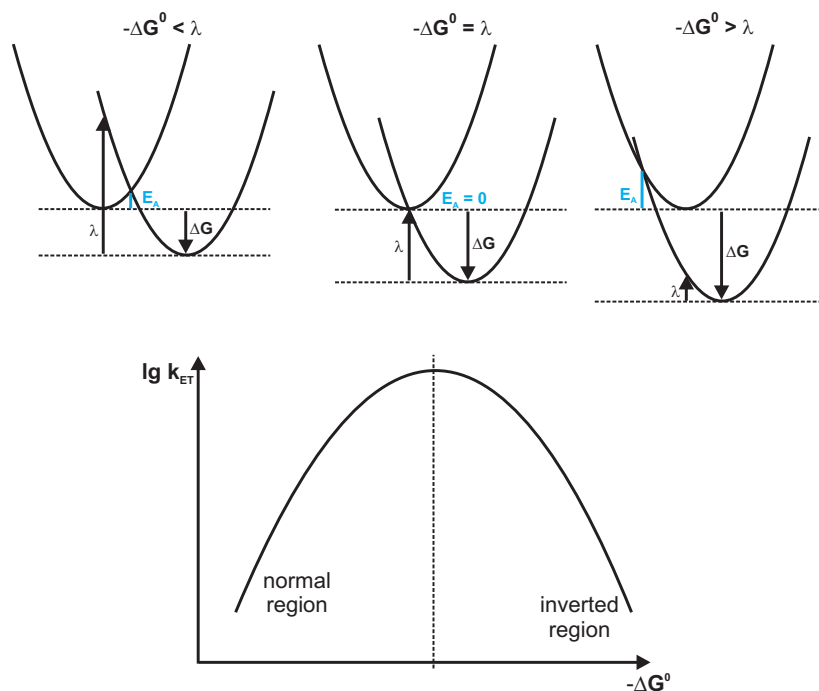


Figure II.4 Depiction of the normal and inverted region as proposed by MARCUS.

However, given the quadratic contribution of ΔG^0 , Equation II.9 implies a decrease in the electron transfer rate with a further increase in exergonicity. This counter-intuitive behavior starts when $-\Delta G^0 > \lambda$, as can be seen in the depiction of the different MARCUS regions in Figure II.4. Once the saddle point is overcome, the system operates in the MARCUS-inverted region. The phenomenon of the inverted region stems from the fact that in a system of very high exergonicity, a lot of energy is released upon charge transfer. This much energy cannot be discharged by the system fast enough, which might lead to the proposed decrease in the reaction rate. Roughly 20 years after MARCUS first postulated his theory, MILLER and CLOSS have found experimental proof of the inverted region.^{46,47} They studied intramolecular electron transfer rates in a series of covalently linked D and A molecules. A rigid spacer allowed them to keep D and A at a fixed distance and variation of the driving force was achieved by altering D and A, respectively.

A rough estimation of the driving force can be achieved by using the approximation $\Delta G^0 \approx e(E_{\text{ox}} - E_{\text{red}}) - E_{00}$. Where E is the electronic ground state potential of the donor and acceptor, respectively, and e is the elementary charge. For photoinduced electron

transfer processes the excitation energy E_{00} of the photosensitizer has to be considered as well, because it contributes to its redox properties.

Electronic Coupling

In addition to the factors introduced above, the reaction rate is also dependent on the probability of the electron transfer, once the system has reached the crossing point from one parabola to the other. This probability is a function of the electronic coupling between donor and acceptor, H_{AB} , more accurately, the overlap between the donor and acceptor orbitals. Evidently, the orbital overlap is maximal for systems with D and A separated only by their VAN-DER-WAALS distance; then, $H_{AB} = H_0$. In systems with very strong electronic coupling, differentiation between the reactant and product states is no longer possible (blue parabolas in Figure II.3) and the charge might no longer be assigned to one specific point in the system. It is delocalized as for example in the CREUTZ-TAUBE ion.⁴⁸

$$H_{AB} = H_0 \cdot \exp\left(-\frac{\beta}{2}r_{DA}\right) \quad (\text{II.10})$$

r_{DA} in the above Equation II.10 is the donor-acceptor distance. With increasing distance between D and A, the orbital overlap decreases exponentially. For weakly coupled systems (cyan parabolas in Figure II.3) the probability of electron transfer is dependent on the value of E_A . Is the excitation energy too low for photoinduced electron transfer to occur, the system will remain in its initial state.

β is the attenuation factor for electron tunneling. It is a system-specific parameter, also dependent on the matrix D and A are embedded in. In vacuo, e.g. the probability for electron tunneling is very low.⁴⁹ In D–A systems linked via covalently attached bridging units, two different mechanistic pathways for long-range electron transfer are possible. If the bridge itself is redox-active the electron or hole can be transferred sequentially via a hopping mechanism. In doing so, intermediates with a temporarily oxidized or reduced bridge are formed. Another possibility is direct tunneling of the charge from the reactant state to the product state. Electron tunneling is usually observed in systems with a high activation barrier.

II.3.3 Energy Transfer

Another possibility for deactivation of the excited state besides electron transfer is non-radiative energy transfer from an excited photosensitizer P^* to a so-called quencher Q (energy acceptor). For successful electron transfer and thus, prevention of this unwanted side-reaction, the triplet energies of the molecular building blocks

of the studied complexes have to be adjusted carefully. In energy transfer theory two different mechanisms can be distinguished. An important prerequisite for both mechanisms is a lower-lying energy state of Q, compared to P*. Only then can energy be transferred. Usually the probability for energy transfer can be deduced from the spectral overlap between the energy donor emission and energy acceptor absorption. The higher the spectral overlap, the more likely is energy transfer from one molecular entity to the other.

In 1947 T. FÖRSTER developed his theory of non-radiative fluorescence resonance energy transfer (FRET).⁵⁰ FRET is mostly dependent on electronic dipole interactions between the energy donor and acceptor. Its probability decreases with the sixth power of the P*-Q distance. As a result, FRET is the predominant form of energy transfer in systems with P*-Q distances up to 100 Å.

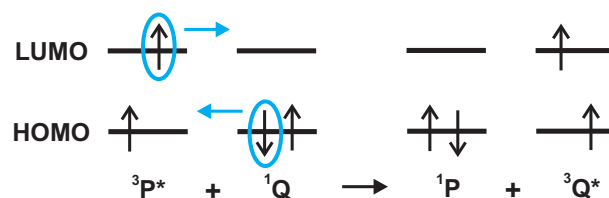


Figure II.5 Schematic diagram for electron-exchange triplet energy transfer according to DEXTER.

D. L. DEXTER formulated his theory of energy transfer on terms of an electron exchange between P* and Q.⁵¹ Therefore, sufficient overlap of the orbitals of P* and Q is necessary. Due to this fact, unlike FRET, the electron-exchange energy transfer is more strongly distance-dependent. It usually occurs in systems where P and Q are located within 10 Å of each other, and thus is also termed short-distance energy transfer mechanism. Figure II.5 depicts the mechanism for DEXTER energy transfer between an excited P* in its triplet state and the quencher Q in its singlet state in a schematic fashion. This is the most likely energy transfer mechanism to occur in the complexes studied in this thesis. Its probability is dependent on the excitation energies of the present molecular units and will be discussed in the respective sections. The denomination “photosensitizer” for P* can also be explained with the aid of Figure II.5. Electron exchange between $^3P^*$ and 1Q leads to the excitation of 1Q to its lowest triplet state. This process is called “sensitization”.

II.4 Accumulative Electron Transfer

In a system designed to achieve multiple, consecutive charge separation, new undesired deactivation processes have to be considered that can not occur in molecules de-

signed for single charge separation. Figure II.6 illustrates the different energy states and electron transfer steps involved in twofold charge separation in an exemplary D–P–A assembly.^{37,52} The left half depicts the familiar electron transfer pathways resulting in the formation of the first charge-separated state D^+PA^- (CSS1) after the absorption of one photon (solid, blue arrows). Once CSS1 is formed, its main deactivation occurs via charge recombination (black, dashed arrow), resulting in the DPA triad in its ground state. To obtain a charge separated state in which two electrons and two holes are accumulated on the acceptor and the donor, respectively, the photosensitizer in D^+PA^- has to be excited again. An important prerequisite hereby is a sufficiently long lifetime of CSS1 to allow for a second excitation. Given successful consecutive absorption of two photons, ideal formation of the desired second charge separated state $D^{2+}PA^{2-}$ (CSS2; solid, cyan arrows) would follow a similar pathway as the formation of CSS1. However, after absorption of a second photon the excited CSS1 $D^+P^*A^-$ can follow deactivation pathways that are not relevant in DP^*A . In principle, four major problems are likely to complicate successful accumulative electron transfer.

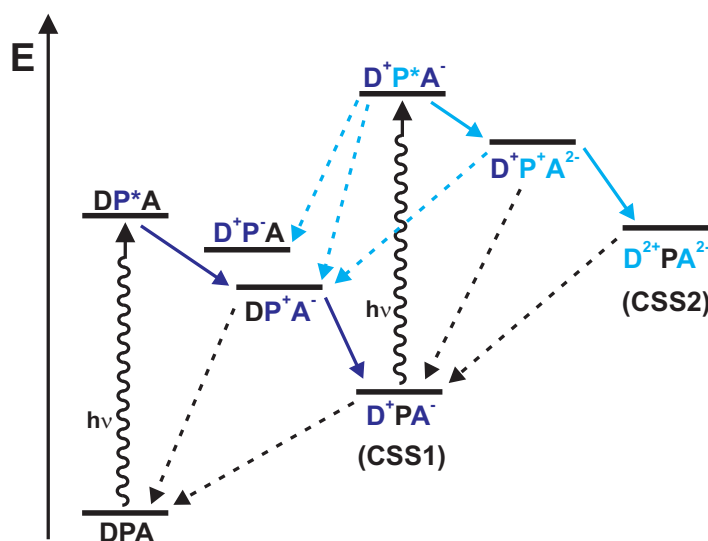


Figure II.6 Schematic depiction of possible reaction pathways leading to the accumulation of charge in a DPA triad. Undesired reaction pathways are depicted with dashed arrows.

First, the accumulation of charge, may it be holes or electrons, on one specific reaction site does entail electrostatic problems. It is known that the second oxidation or reduction of one molecular entity is more difficult than the first and requires a higher amount of energy. In a photosensitized assembly, the redox potential of the electron transfer-inducing moiety P^* does not change. Therefore, multiple oxidation/reduction of the respective donor/acceptor has to occur in a very narrow po-

tential range. Only then can P^* drive a second charge separation. In principle, the built-up of charge could be compensated, e.g. by coupling it with proton transfer, as seen in PSII and the OEC (Section II.1).

A second problem is that the excited photosensitizer P^* is both a strong oxidant, as well as reductant. In the $D^+P^*A^-$ state it is surrounded by a reduced, electron-rich acceptor and an oxidized, electron-deficient donor. Thus, P^* might be quenched by reverse electron transfer from A^- or to D^+ , as indicated by the dashed, cyan arrows forming D^+P^-A or DP^+A^- . Differentiation between the above mentioned reverse electron transfer and back electron transfer is necessary. The latter term is commonly used for direct charge recombination yielding the system in its ground state.

Third, the spatial proximity of P^* to D^+ and A^- might also entail undesired quenching of the photosensitizer by energy transfer. The singly reduced acceptors or oxidized donors are mostly radicals or paramagnetic metal centers in their doublet states. Triplet-doublet energy transfer might be less likely in $D^+P^*A^-$ than reverse electron transfer. However, it was observed in other systems and has to be taken into consideration for giving a full evaluation of possible deactivation mechanisms.⁵³ Thus, careful matching of the energies both in DPA, as well as in D^+PA^- is crucial.

Lastly, the intermediate charge-accumulated states, as e.g. $D^+P^+A^{2-}$ cannot only undergo reverse electron transfer, resulting in CSS1 (dashed, black arrow). An additional deactivation pathway would be direct recombination of electrons and holes. The twofold reduced acceptor A^{2-} can, in principle, transfer an electron to D^+ , transforming the DPA assembly to an intermediate state of the CSS1 formation. As a result thereof, controlling the electronic coupling between the molecular moieties is of even greater importance than for standard photoinduced electron transfer.

II.5 Artificial Photosynthesis

When it comes to artificially creating a system capable of multiple charge separation and the subsequent use of these separated redox equivalents, Nature has provided a working blue-print. It reveals several basic requirements needed for reverse-engineering artificial systems that are as follows. The harvesting of as much sunlight as possible requires suitable chromophores or antennas that display strong absorption in a large part of the solar spectrum. Upon light absorption the energy has to be transferred loss-free to a reaction center which promotes fast charge separation. In order to prevent undesired back-reactions and thus, recombination of the separated charges, spatial separation of the charge accumulation sites is essential. Ideally, the different sites of charge accumulation are redox active and therefore, can

transfer multiple redox equivalents to catalysts for H₂ and O₂ evolution, respectively. In addition to the prevention of unwanted back-reactions, the spatial separation of the hydrogen- and oxygen-producing sites does not allow for O₂ and H₂ to partake in undesired reactions before they can be removed from the system. Lastly, the built-up of charge bears an electrostatic problem. Thus, Nature has coupled the separation of multiple redox equivalents with proton transfer to maintain electric neutrality.⁵⁴

Up until now several research groups have synthesized molecular systems capable of charge accumulation and a few reviews concerning this topic exist in literature.^{55–57} Excitation usually occurred by visible light irradiation or with the help of lasers. For most of the systems the use of sacrificial electron donors or acceptors was necessary in order to re-reduce/-oxidize the photosensitizer. However, some of the systems were even reported to produce hydrogen. Hereafter, selected charge accumulating systems will be introduced.

Electron-Accumulating Systems

The first electron-accumulating system that did not even rely on a sacrificial electron donor, was presented in 1992 by WASIELEWSKI and co-workers.⁵⁸ They reported a D–A–D compound comprised of two free-base porphyrin donors (P) and one central perylene bis(dicarboxyimide) acceptor (PBDCI) (Figure II.7).

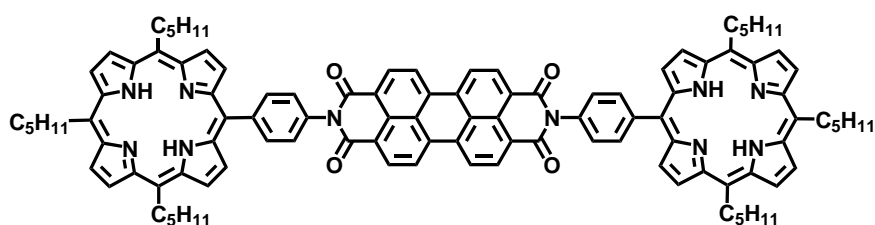


Figure II.7 P–PBDCI–P

Excitation of the porphyrins with a low-energy picosecond laser pulse induced the formation of singly charge-separated HP⁺–PBDCI[–]–PH in pyridine solution. Upon increasing the laser excitation power from one photon per pulse per molecule to 20, the doubly reduced PDBCI unit could be observed after two successive electron transfers. Even the 20-fold increase in the photon-count led to only 20% HP⁺–PBDCI^{2–}–PH⁺ formation, though quantitative conversion at such high powers was expected. However, charge recombination seemed to occur in the inverted region, since the doubly charge-separated state exhibited a longer lifetime (5 ns) than HP⁺–PBDCI[–]–PH (5 ps). Six years later, IMAHORI has communicated a similar charge accumulation system

with two peripheral zincporphyrin (ZnP) donors and a central tetracyanoanthraquinodimethane (TCAQ) acceptor. Double-pulse excitation beginning with a 532 nm laser pulse, followed by a 233 ps-delayed laser pulse at 555 nm resulted in spectral changes evidential for twofold reduced TCAQ. The obtained second charge-separated state $\text{ZnP}^+-\text{TCAQ}^{2-}-\text{ZnP}^+$ decayed in only 1.2 ns.⁵⁹

Other early examples for electron accumulation were reported by BREWER *et al.* They synthesized molecular heteropolymetallic complexes that showed electron accumulation at the central complex. In a first Ru–Ir–Ru triad (Figure II.8 left), a central iridium complex was attached to two ruthenium complexes via two 2,3-bis(2-pyridyl)benzoquinoline (dpb) bridging ligands. Visible light irradiation of the triad in MeCN solution lead to twofold reduction of the central iridium complex after absorption of two photons in presence of dimethylaniline as sacrificial electron donor. More accurately, the accumulated electrons are located one on each of the two dpb ligands. Though accumulated at the central iridium complex, the reduction equivalents stay spatially somewhat separated.⁶⁰

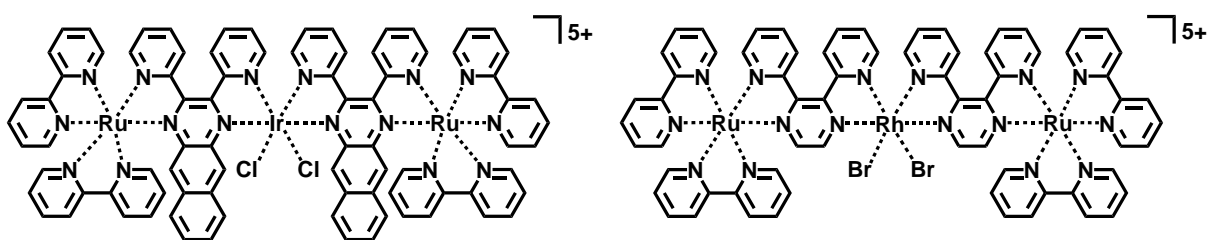


Figure II.8 Trinuclear Ru–Ir–Ru (left) and Ru–Rh–Ru (right) complexes.

BREWER *et al.* also presented structurally similar Ru–Rh–Ru triads (Figure II.8 right) capable of photoinduced electron accumulation on the central rhodium metal complex. The different metal complexes are connected via 2,3-bis(2-pyridyl)pyrazine (dpp) bridging ligands. In presence of dimethylaniline, excitation at 470 nm of a chloro-substituted analog of Ru–Rh–Ru in an acidic MeCN/H₂O mixture showed hydrogen production by water oxidation.^{61–65}

KONDURI *et al.* have synthesized two bridged ruthenium dimers, one of which is able to perform photoinduced accumulation of four electrons and four protons on the central bridging unit. Both complexes are comprised of two ruthenium phenanthroline photosensitizers, linked either by a tetraazatetrapyridopentacene (tatpp) or a tetraazatetrapyridoquinone (tatpq) bridge (Figure II.9).

Irradiation of a de-oxygenated MeCN solution of the quinone complex with a tungsten light bulb ($\lambda > 360$ nm) resulted in the sequential reduction and protonation of the bridging unit. The generation of the quadruply reduced and protonated form was finished within minutes and proved to be fully reversible upon exposure to

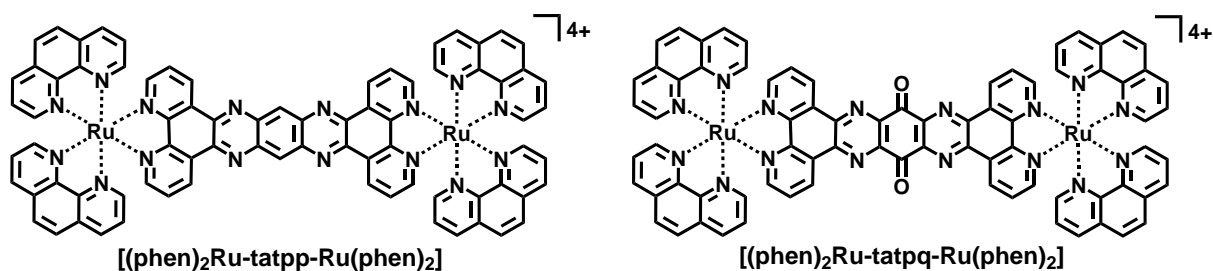


Figure II.9 Ruthenium Photocatalysts

air.⁶⁶ A more extensive study of the pyridopentacene containing complex revealed photochemical generation of the doubly reduced and protonated species.⁶⁷ An excess of NEt_3 as a sacrificial electron donor was needed in every case.

In contrast to the systems presented above, Fox *et al.* have reported a purely organic dendritic system comprised of 16 naphthyl groups arranged around one methylviologen unit. Excitation of the compound at 266 nm with strong ($> 6 \text{ mJ}$) laser pulses lead to the absorption of about 12 photons by the naphthyl groups, which resulted in twofold reduced methylviologen. Though this system exploits the antenna effect nicely and therefore has no need for an additional sacrificial electron donor, the high excitation density and the very short excitation wavelength limits its usefulness for solar energy conversion.⁶⁸

Due to the intrinsic difficulties accompanying electron accumulation in purely molecular systems, the focus of current research turned towards the design of hybrid systems. Quite recent examples are phthalocyanine-sensitized single wall carbon nanotubes (SWCNs)^{69,70} or polyoxometalate (POM)-photosensitizer hybrids.^{71,72} Continuous visible light irradiation of the latter usually leads to the accumulation of two electrons on the POM moieties that are well suited as charge reservoirs. The POM-containing compounds also exhibited hydrogen production at their headspace, albeit always in presence of sacrificial electron donors such as triethanol- or triethylamine.

Hole-Accumulating Systems

Molecular systems capable of hole accumulation on one specific site are quite rare in literature. The ones that can be found are combinations of ruthenium polypyridyl photosensitizers and dinuclear manganese clusters, like the ones prepared by ÅKERMARK *et al.* In presence of $[\text{Co}(\text{NH}_3)_5\text{Cl}]^{2+}$ as the sacrificial electron acceptor, accumulation of three holes was observed at the dinuclear Mn-cluster.^{73,74} Another reported system, comprised of three ruthenium polypyridyl sensitizers bound to a

$[\text{Mn}(\text{bpy})_3]^{2+}$ moiety, can accommodate up to four holes after reorganization to a μ -oxido-bridged manganese dimer.^{75,76} Despite their hole accumulation abilities, both systems are stuck in their highly oxidized form due to the lack of oxygen evolution, which prevents them from returning to their initial state.

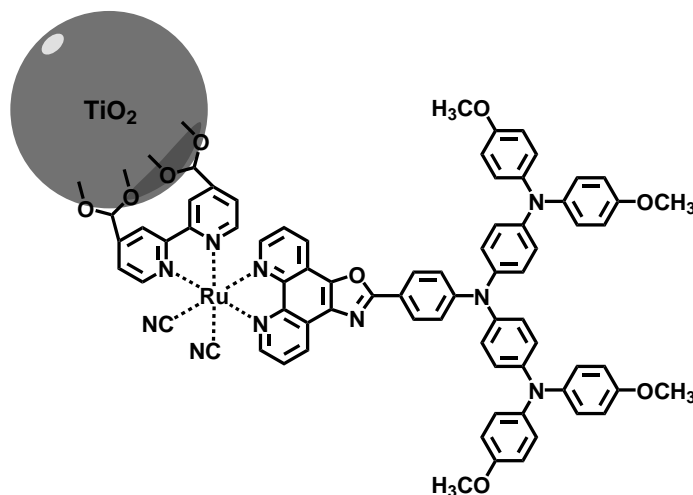


Figure II.10 TiO_2 -Ru-OTA

In 2010 KARLSSON *et al.* have presented an oligo-triarylamine (OTA)-Ru-sensitized TiO_2 nanoparticle system (Figure II.10). To the extent of the author's knowledge, it is so far the only example for twofold electron and hole accumulation at two specific sites in the same compound. Furthermore, twofold charge separation was observed entirely without the help of sacrificial agents. After double pulse excitation of the ruthenium photosensitizer, the two electrons donated by the OTA are injected into the nanoparticles. The same result was observed in high-energy single pulse experiments. Though, not a purely molecular system, employment of TiO_2 nanoparticles as electron acceptors lead to very fast charge separation and significantly slowed down back electron transfer.^{52,77}

For the determination of the exact whereabouts of both holes and electrons in a system, a molecular, homogeneous approach would be preferable. Furthermore, a more directed electron transfer pathway may be obtained in a linear D-P-A assembly that could then ideally be incorporated directly in an artificial photosynthetic setting as depicted in Figure I.1. An entirely molecular system would allow for a facilitated understanding of the underlying charge transfer, charge accumulation, and fuel generation mechanisms. All reported systems so far have achieved only half reactions where either water oxidation or fuel production is replaced by sacrificial ("dead-end") reactants. However, the ultimate artificial photosynthetic system has not been realized yet.

II.6 Chosen Molecular Moieties

II.6.1 Metal Photosensitizers

Transition metal complexes, most notably $[\text{Ru}(\text{bpy})_3]^{2+}$ or $[\text{Re}(\text{bpy})(\text{CO})_3(\text{py})]^+$, have been extensively studied and applied as photosensitizers.^{36,78–81} This can mostly be attributed to their superior chemical and photostability, and their redox properties both in the ground and excited state. Furthermore, their excited states are easily accessible by irradiation, the luminescent states are populated quantitatively and have long lifetimes. By switching from the rhenium photosensitizer to the ruthenium analog, irradiation with visible light is possible which becomes evident from the ground state absorption spectra in Figure II.11.

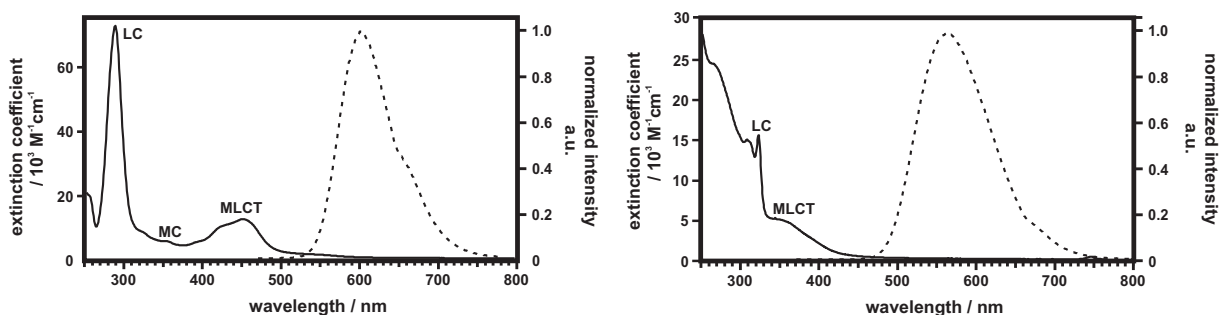


Figure II.11 Absorption (solid trace) and emission (dashed trace) spectra of $[\text{Ru}(\text{bpy})_3](\text{PF}_6)_2$ on the left and $[\text{Re}(\text{bpy})(\text{CO})_3(\text{py})](\text{OTf})$ on the right in MeCN at RT.

$[\text{Ru}(\text{bpy})_3]^{2+}$ with Ru^{2+} as a d^6 transition metal, exhibits D_3 , slightly distorted octahedral symmetry. The absorption spectrum of $[\text{Ru}(\text{bpy})_3](\text{PF}_6)_2$ in MeCN at RT (Figure II.11 left) shows a very prominent band at 290 nm which is assigned to a ligand-centered $\pi \rightarrow \pi^*$ transition. The rather weak absorption band at 350 nm results from a metal-centered transition (MC). The $[\text{Ru}(\text{bpy})_3]^{2+}$ $^1\text{MLCT}$ band can be seen at 452 nm. The shoulder at 422 nm stems from the slightly distorted geometry of the metal center.^{36,82}

The rhenium metal center in $[\text{Re}(\text{bpy})(\text{CO})_3(\text{py})]^+$ also exhibits approximately octahedral coordination symmetry. The absorption spectrum of this complex shows bands of the same general origin as the ruthenium polypyridyl spectrum. The high-energy bands from 250 nm to the sharp band at 320 nm are assigned to $\pi \rightarrow \pi^*$ transitions centered on the bpy ligand. The $^1\text{MLCT}$ band for the $d\pi(\text{Re}) \rightarrow \pi^*(\text{bpy})$ transition is located at higher energies compared to $[\text{Ru}(\text{bpy})_3]^{2+}$. It is partially overlapped by the ligand-centered transitions, but clearly visible from 330 nm to longer wavelengths and tailing into the visible region.⁸⁰

After excitation at 450 nm for the ruthenium complex and 350 nm for the rhenium sensitizer, both metal complexes show intense, broad, structureless emission spectra at RT in MeCN. The emission maximum for $[\text{Ru}(\text{bpy})_3]^{2+}$ in MeCN is located at 603 nm, whereas the maximum rhenium emission is further into the blue at 553 nm in the same solvent.

Light-induced excited state formation and electrochemical characteristics of the metal complexes in their ground and excited states can be summarized in a LATIMER diagram (Figure II.12). Excitation of the metal photosensitizers usually occurs into their $^1\text{MLCT}$ state and ISC to the actual luminescent $^3\text{MLCT}$ state occurs quantitatively. The excited state lifetime is $0.8 \mu\text{s}$ for $[\text{Ru}(\text{bpy})_3]^{2+}$ in de-oxygenated MeCN solution with an emission quantum yield of 0.06.⁸³ The emissive state of $[\text{Re}(\text{bpy})(\text{CO})_3(\text{py})]^+$ has a lifetime of $0.6 \mu\text{s}$ in de-oxygenated DCM and $\phi_{em} = 0.16$.⁸⁴

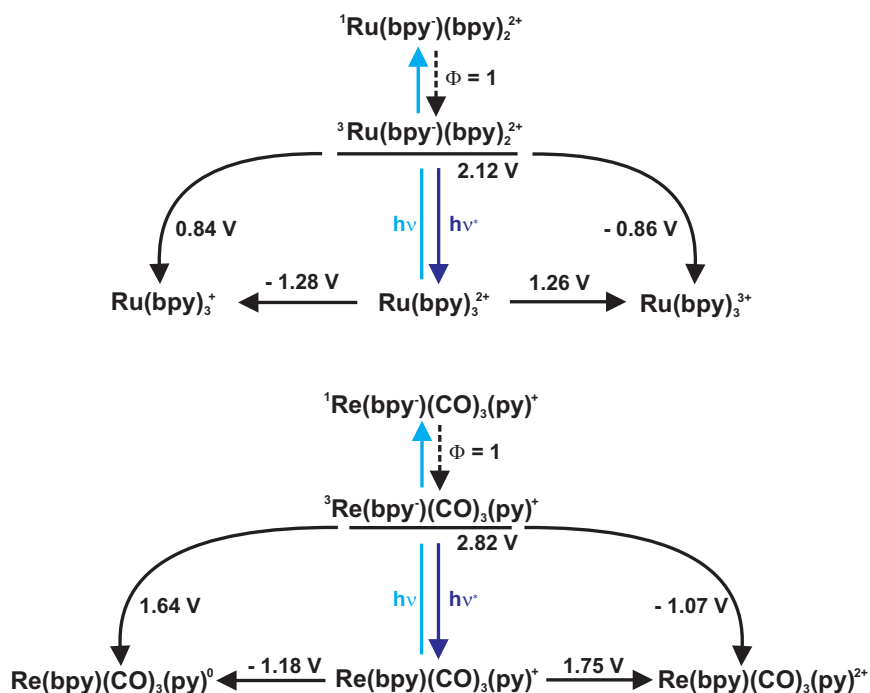


Figure II.12 Latimer diagrams for the metal photosensitizers.

After excitation into the $^1\text{MLCT}$ band, the excited metal polypyridyl complexes are both stronger reductants, as well as oxidants than in their ground states. This can be explained by their higher energy content, compared to the ground state. The connection between ground state redox potentials and the zero-zero excitation energy (E_{00}) is visualized in the LATIMER diagram. Redox potentials are given in V vs. NHE in H_2O for $[\text{Ru}(\text{bpy})_3]^{2+}$ and in V vs. SSCE in MeCN for $[\text{Re}(\text{bpy})(\text{CO})_3(\text{py})]^+$.^{54,84} An estimation of the excited state redox potentials is possible with the help of the following Equations II.11. Here, the ground state potentials and the zero-zero excitation energy have to be taken into account.⁸⁵

$$\begin{aligned} E(M^+ / M^*) &= E(M^+ / M) - E_{00} \\ E(M^* / M^-) &= E(M / M^-) + E_{00} \end{aligned} \quad (\text{II.11})$$

II.6.2 Anthraquinone Acceptor

Nature has successfully used quinones as the final electron acceptors in PSII. Following this example, quinone derivatives, such as anthraquinone, have already been employed as electron acceptors in photoinduced charge transfer studies.⁸⁶⁻⁸⁹

Anthraquinone is able to accommodate two electrons and its electron accepting behavior has been studied extensively.⁹⁰⁻⁹³ Electrochemical studies have shown two reversible one-electron reduction waves for the first ($-1.20\text{ V vs. Fc}^{+/0}$) and second reduction ($-1.8\text{ V vs. Fc}^{+/0}$) in DMF. The second reduction occurs at a potential that is too low to be reached by the reduced/oxidized rhenium or ruthenium photosensitizer. However, addition of BRØNSTED or LEWIS acids or strongly hydrogen bond-donating solvents (HFIP) leads to merging of the two separate reductions, forming a new two-electron reduction wave at a more positive potential. Protonation of AQ^- is usually followed by instant disproportionation of AQH to twofold reduced and protonated AQH_2 and AQ, because AQH is more readily reduced than AQ. Together with the positive shift of the second reduction potential, the reversibility of the two-electron reduction wave around $-1.20\text{ V vs. Fc}^{+/0}$ is crucial for achievement of twofold charge separation in the rhenium and ruthenium containing triads reported below.

II.6.3 Oligo-triarylamine Donor

Oligo-triarylamine (OTA) was chosen as the electron donor, due to its formidable electron donating abilities. It can release two electrons within a very narrow potential range of about 0.3 V. Since it displays very low potentials of about -0.05 and $0.25\text{ V vs. Fc}^{+/0}$ for the first two oxidations, it is a much stronger electron donor than its ordinary triarylamine analog. The first oxidation of OTA occurs at the central N atom, the most electron-rich position in the donor, and the charge of the resulting radical cation can be stabilized due to the extended ring system.⁹⁴ Due to its superior electron-donating properties, OTA has already been employed successfully in donor-metal photosensitizer-acceptor assemblies as well as in organic hole transport materials.^{52,95,96}

III. TOWARDS PHOTOINDUCED CHARGE ACCUMULATION IN d^6 METAL COMPLEXES

Electron transfer plays a pivotal role in many biological and physiological processes and the elucidation of its mechanism and dependency on various parameters, as well as the creation of artificial electron transfer systems has received a lot of attention in the last decades. More recently the focus of electron transfer studies turned towards the accumulation of charges. With solar fuel generation in mind, more than one, even multiple redox equivalents are required for successful H_2 production or CO_2 reduction. Several purely molecular systems capable of either hole or electron accumulation with the help of sacrificial agents have been reported. However, none so far that can accumulate both holes and electrons at two specific sites in a completely molecular setup.

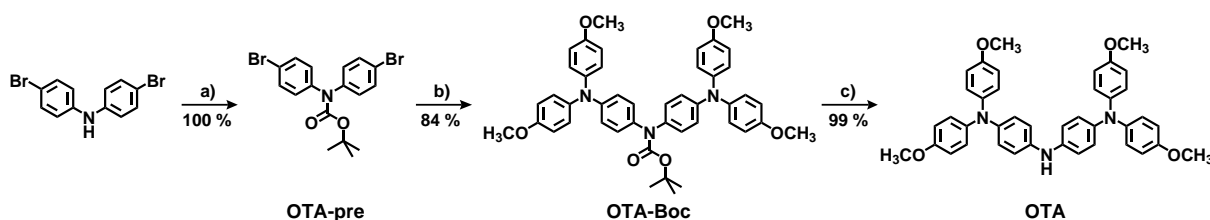
Therefore, the primary objective of the research in this thesis was to bridge this gap and to synthesize model systems, built as simple as possible, to study possible photo-accumulation of redox equivalents on specific sites within the same purely molecular (nanoparticle-free) compound. A major advantage of such systems will be their independence of the high-energy sacrificial agents and thus, their self-sufficiency. In principle, the initial target molecule, comprised of an OTA donor and two rhenium photosensitizers should allow us to accumulate two holes on OTA with each of the rhenium complexes being reduced once. In Section III.2, a slightly more extended, yet every bit as simple a system (AQ-Re-OTA) will be studied for the same goal. The first part of this chapter will focus on the investigation of the rhenium complexes, what difficulties we encountered, what we learned, and what changes we made in order to achieve our goal of accumulating redox equivalents. The second part will give an overview of the results gained from an AQ-Ru-OTA triad (III.4) and the corresponding pentad AQ-Ru-OTA-Ru-AQ (III.7) and how they differ from the ones obtained from the rhenium triads. In all following sections synthesis, spectroscopic measurements and efforts on our side to achieve photo-accumulative electron transfer will be discussed in detail.

III.1 Triads with Two Rhenium Photosensitizers

The triads studied in this section are each comprised of two rhenium chromophores covalently linked to either an oligo-triarylamine (OTA) or a triarylamine (TAA) donor. The latter triad, in which hole accumulation is impossible, was used as a reference complex.

III.1.1 Synthesis of the OTA Donor

The oligo-triarylamine (OTA) which was used as an electron donor throughout this thesis was synthesized by adapting literature protocols.^{95,97} The reaction sequence for its preparation is shown in Scheme III.1. Of this three step synthesis, the first step was performed exactly as HIRAO *et al.* described. Commercial bis(4-bromophenyl)amine, DMAP and Boc₂O were refluxed in THF which yielded the Boc-protected amine (OTA-pre) quantitatively after the workup procedure. This step was necessary to prevent unwanted side reactions in the subsequent BUCHWALD-HARTWIG coupling with dianisylamine in order to obtain the Boc-protected OTA (OTA-Boc). The synthetic procedure of HIRAO *et al.* was changed insofar that Pd(dba)₂ and (HP^tBu₃)BF₄ were used as catalysts. In this way, the reaction time could be reduced from 5 d to 19 h and OTA-Boc was obtained in a superior yield of 84%. Deprotection occurred in an acetone solution with an excess of TFA at RT as described by BOZIC-WEBER *et al.* and gave the desired OTA in 99% yield. The donor was obtained as a beige solid with an overall yield of 83%. In order to obtain a well resolved ¹H NMR spectrum of OTA and thus enabling a clear assignment of signals, the addition of a drop of TFA to the NMR sample was necessary. This resulted in the solution turning green, most likely due to oxidation of some of the amine.⁹⁸ However, OTA could be recovered by evaporation of the solvent and filtration of the NMR sample over basic alumina with EtOAc as eluent.



Scheme III.1 Synthesis of the OTA donor: **a)** Boc₂O, DMAP, toluene, reflux, 3 h; **b)** dianisylamine, NaO^tBu, Pd(dba)₂, (HP^tBu₃)BF₄, toluene, reflux, 19 h; **c)** TFA, acetone, RT, over night.

In addition to the characterization by ^1H NMR spectroscopy a crystal structure (Figure III.1) of the donor was obtained thanks to single crystal formation by slow evaporation of a saturated acetone solution. The structure was deposited at the Cambridge Crystallographic Data Centre (CCDC) under the reference number 1011917. Directly observable from the crystal structure is the propeller-like array of the aryl rings around the nitrogen atoms. This is observed for many arylamines and contributes greatly to their stability when oxidized, and their rather low basicity.^{99,100}

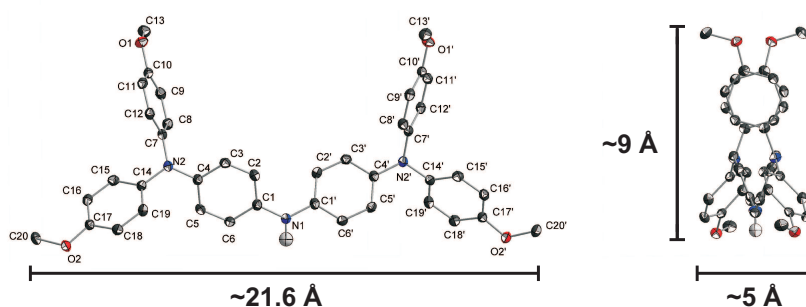


Figure III.1 Molecular structure of the OTA donor. ADPs: 50% thermal ellipsoid probability. Carbon atoms: black; hydrogen atom: grey; nitrogen atoms: blue; oxygen atoms: red. (Symmetry operation used to generate equivalent atoms: $0.5-x, 0.5-y$.)

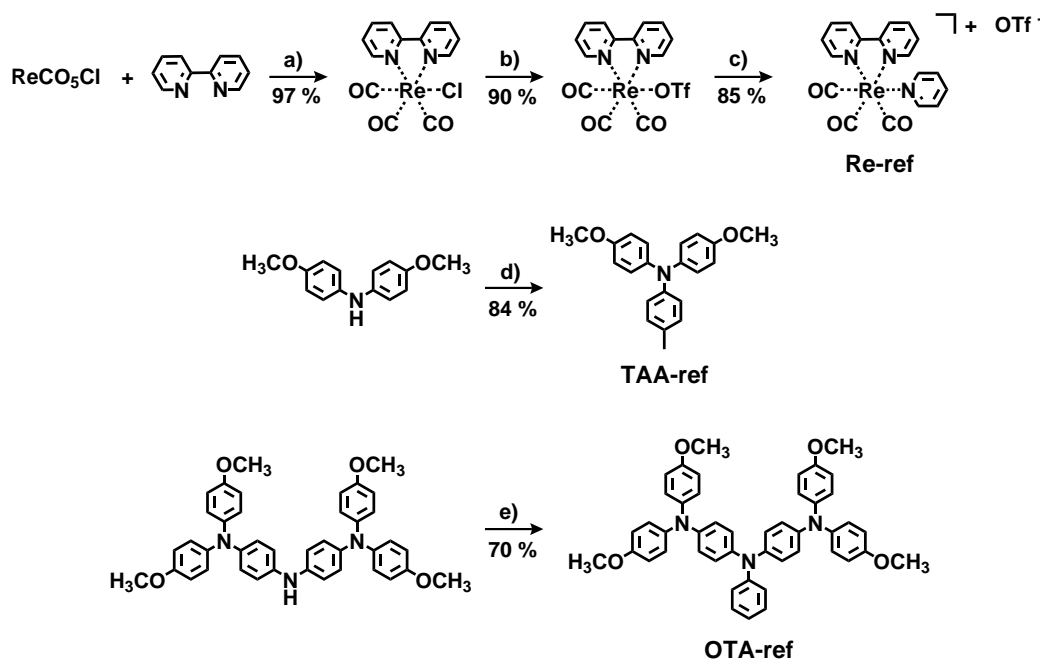
OTA crystallizes in the orthorhombic space group Pccn. The distance between C20 and C20' is 21.6 Å and the through-space distance measured from C13 to the hydrogen atom as indicated in the side view of the donor in Figure III.1 is ≈ 9 Å. Considering the depth of 5 Å, OTA shows ellipsoid geometry.

III.1.2 Synthesis of Precursors and the Reference Molecules

To aid the complete understanding of the data obtained from the target complexes, reference compounds comprised of the individual molecular building blocks of $\text{Re}_2\text{-TAA}$ and $\text{Re}_2\text{-OTA}$ were synthesized.

The known Re-ref complex, $[\text{Re}(\text{bpy})(\text{CO})_3(\text{py})]^+$, could be obtained in three synthetic steps as shown in the upper third of Scheme III.2 with an overall yield of 74%. The procedures followed hereby were adapted from literature.^{80,101,102} $\text{Re}(\text{CO})_5\text{Cl}$ and 2,2'-bipyridine (bpy) were stirred in refluxing toluene for 1 h and after cooling the reaction mixture in the fridge the yellow product was filtered and washed with Et_2O . Substitution of the chloro-ligand in the $[\text{Re}(\text{bpy})(\text{CO})_3\text{Cl}]$ precursor by the weakly coordinating triflate ligand was performed to facilitate the following complexations with the amino-decorated ligands. For the exchange, $[\text{Re}(\text{bpy})(\text{CO})_3\text{Cl}]$ was suspended in DCM and trifluoromethanesulfonic acid was added very slowly. Precipitation of the

product from the clear mixture was induced by drop wise addition of Et_2O . Finally, the $[\text{Re}(\text{bpy})(\text{CO})_3(\text{OTf})]$ precursor was refluxed in MeOH, possibly forming the intermediate complex $[\text{Re}(\text{bpy})(\text{CO})_3(\text{MeOH})]\text{OTf}$ which then reacts with an excess of pyridine to give Re-ref.



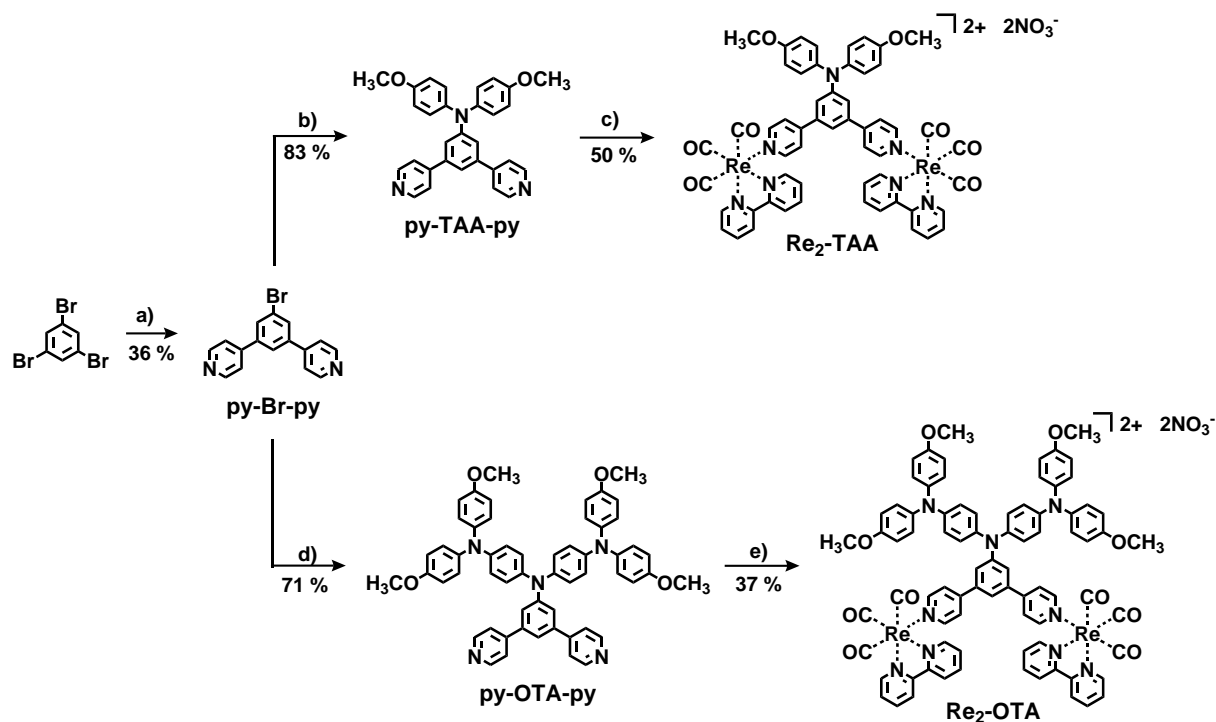
Scheme III.2 Synthesis of the reference compounds: **a)** toluene, reflux, 1 h; **b)** trifluoromethanesulfonic acid, DCM, RT, 1 h; **c)** pyridine, MeOH, 85 °C, 24 h; **d)** bromotoluene, NaO^tBu , $\text{Pd}(\text{dba})_2$, $(\text{HP}^t\text{Bu}_3)\text{BF}_4$, toluene, reflux, 23 h; **e)** bromobenzene, KO^tBu , $\text{Pd}(\text{dba})_2$, $(\text{HP}^t\text{Bu}_3)\text{BF}_4$, toluene, reflux, over night.

The secondary amines TAA and OTA were reacted with *p*-bromotoluene and bromobenzene, respectively, in BUCHWALD–HARTWIG-type couplings to yield the tertiary arylamines. The Pd-catalyzed N-C coupling of dianisylamine with bromotoluene yielded the desired TAA-ref in 84% yield. The initially beige oil crystallized within a few weeks. For the Pd-catalyzed synthesis of OTA-ref a procedure of HIRAO *et al.* was adapted.⁹⁴ During the work-up and purification steps absence of acidic substances proved to be crucial. Recrystallization from MeOH, washing and thorough drying afforded pure OTA-ref as a beige solid in 70% yield.

The resulting TAA-ref and OTA-ref were used to help predict the optical spectroscopic and electrochemical behavior of the amines in the complexes. Furthermore, OTA-ref was needed to determine the triplet energy of OTA due to the lack of literature values.

III.1.3 Synthesis of the Studied Triads

Scheme III.3 outlines the synthetic pathway pursued to obtain the desired $\text{Re}_2\text{-OTA}$ complex and the corresponding complex $\text{Re}_2\text{-TAA}$ which was used as a reference.



Scheme III.3 Synthesis of the studied complexes $\text{Re}_2\text{-OTA}$ and $\text{Re}_2\text{-TAA}$: **a)** pyridine-4-boronic acid hydrate, Na_2CO_3 , $\text{Pd}(\text{PPh}_3)_4$, THF/ H_2O , reflux, 24 h; **b)** dianisylamine, NaO^tBu , $\text{Pd}(\text{dba})_2$, $(\text{HP}^t\text{Bu}_3)\text{BF}_4$, toluene, 100 °C, 22.5 h; **c)** $[\text{Re}(\text{bpy})(\text{CO})_3\text{OTf}]$, MeOH, 85 °C, over night; **d)** OTA, NaO^tBu , $\text{Pd}(\text{dba})_2$, $(\text{HP}^t\text{Bu}_3)\text{BF}_4$, toluene, reflux, 19 h; **e)** $[\text{Re}(\text{bpy})(\text{CO})_3\text{OTf}]$, MeOH/ CHCl_3 , reflux, 1.5 d.

The first step towards the complexes consisted of the synthesis of a central molecule (py-Br-py) used for both, the $\text{Re}_2\text{-TAA}$ and $\text{Re}_2\text{-OTA}$ complex. It is comprised of a benzene ring bearing two pyridines as coordination sites for the rhenium precursor ($[\text{Re}(\text{bpy})(\text{CO})_3\text{OTf}]$) and a bromine substituent which allowed for the coupling of the respective amine. 1,3,5-tribromobenzene was reacted with 3 eq of 4-pyridine boronic acid in presence of Na_2CO_3 as base and catalytic amounts of $\text{Pd}(\text{PPh}_3)_4$ in a biphasic solvent mixture of THF and H_2O , as is common for SUZUKI-type couplings. The use of 3 eq of the pyridine reactant seemed to be crucial for the conversion of 1,3,5-tribromobenzene to the desired compound in an acceptable yield. Still, py-Br-py could only be isolated with a yield as low as 36%. Purification of the product was achieved by column chromatography on silica with DCM + 1% NEt_3 as eluent. The ^1H NMR spectrum in CDCl_3 showed three signals (s, 5.66 ppm; q, 3.64 ppm; t,

1.48 ppm) in addition to the product signals. Those signals are most likely due to a decomposition product of NEt_3 in the weakly acidic DCM. This was concluded, because the signals were absent after column chromatography in DCM with MeOH. However, only insufficient purity could be achieved with the latter eluent mixture. The decomposition product was always present throughout the next synthetic steps, but could be successfully removed in the purification steps of the complexes. Due to a lack of participation in the following synthetic steps and its possible removal during complex preparation and purification the decomposition product was tolerated. Coupling of OTA with py-Br-py was performed under the same conditions used for the synthesis of OTA-Boc as shown above and produced py-OTA-py in 71% yield. The combination of $\text{Pd}(\text{dba})_2$ and $(\text{HP}^t\text{Bu}_3)\text{BF}_4$ as catalysts with either NaO^tBu or KO^tBu as base in toluene consistently provided the best yields in the performed N-C couplings and was therefore used as the standard reaction condition. Complexation of the py-OTA-py ligand with $[\text{Re}(\text{bpy})(\text{CO})_3\text{OTf}]$ in a MeOH/ CHCl_3 solvent mixture produced Re_2 -OTA, as well as the singly complexed by-product. The desired product was isolated by column chromatography on silica by first eluting unreacted ligand with pure acetone, then the complex was eluted with acetone/ H_2O /sat. KNO_3 200:9:1 (v:v:v). After evaporation of the acetone the complex was extracted from the aqueous phase with DCM, dried and further recrystallized from hexane. This gave Re_2 -OTA as the nitrate salt in form of an orange solid with an overall yield of 9%.

Because the synthesis of the reference complex Re_2 -TAA was performed in analogy to Re_2 -OTA it will not be discussed in detail. The upper half of Scheme III.3 shows the reaction sequence following which Re_2 -TAA was synthesized in three steps starting from the commercially available 1,3,5-tribromobenzene. The complex was obtained as a nitrate salt with an overall yield of 15%.

III.1.4 Characterization by IR and Optical Absorption Spectroscopy

For spectroscopic characterization, IR spectra and UV-Vis absorption spectra of all the complexes were measured. The IR spectra were directly obtained from the solids, whereas the absorption spectra were measured on 10^{-5} M solutions of the complexes in MeCN.

The IR spectra (Figure III.2) show two prominent bands corresponding to vibrations of the CO-ligands on the rhenium photosensitizers. The band at 2030 cm^{-1} is assigned to the totally symmetric in-phase vibration and the one at 1900 cm^{-1} to the out-of-phase totally symmetric vibration superimposed by the asymmetric stretching of the equatorial CO-ligands.¹⁰³ The fingerprint regions, especially of Re_2 -TAA and Re_2 -OTA, show identical bands, because both complexes are comprised of the same functional

groups (N-heterocycles, methoxy groups, and tertiary arylamines).

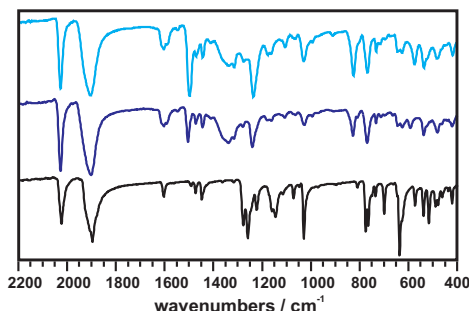


Figure III.2 IR spectra of the investigated complexes Re-ref (black), Re_2 -TAA (blue), and Re_2 -OTA (cyan).

In Figure III.3 the optical absorption spectra of the investigated complexes are depicted. The spectrum of the Re-ref complex is as expected and coincides with that reported in the literature.⁸⁰ The high-energy bands at 260-320 nm are assigned to ligand-centered $\pi \rightarrow \pi^*$ transitions and the ones at 340-390 nm to a $d\pi(\text{Re}) \rightarrow \pi^*(\text{bpy})$ ($^1\text{MLCT}$) transition. For the investigated complexes Re_2 -OTA and Re_2 -TAA the same assignment is applicable. However, the $^1\text{MLCT}$ band at 350 nm is less clearly observable in the TAA complex and completely superimposed by OTA absorption in Re_2 -OTA. UV-Vis spectra recorded on TAA-ref and the OTA-ref show absorption of the amines at 355 nm with extinction coefficients of $1700 \text{ M}^{-1}\text{cm}^{-1}$ and $24000 \text{ M}^{-1}\text{cm}^{-1}$, respectively. As a result, compared to Re-ref with $\epsilon = 4700 \text{ M}^{-1}\text{cm}^{-1}$, Re_2 -TAA and Re_2 -OTA exhibit very large extinction coefficients at 355 nm ($\epsilon = 16300 \text{ M}^{-1}\text{cm}^{-1}$ and $\epsilon = 36000 \text{ M}^{-1}\text{cm}^{-1}$), not unusual for systems with an extended π -conjugation.

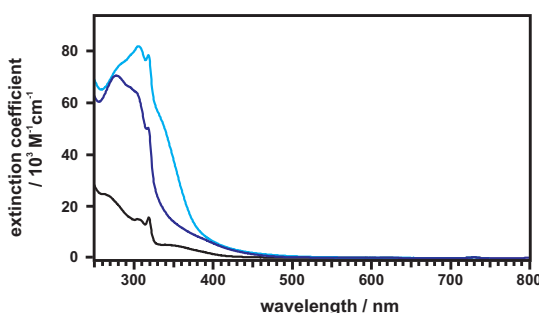


Figure III.3 UV-Vis absorption spectra of the investigated complexes Re-ref (black), Re_2 -TAA (blue), and Re_2 -OTA (cyan).

Considering the information gathered from the absorption data it is to be expected that, by exciting at 355 nm with a Nd:YAG laser, the amines will also be excited to a significant extent. However, instant relaxation of their excited state (π^*) and energy transfer to the excited state ($^3\text{MLCT}$) of the photosensitizer will result in the systems

in their expected photoexcited state. Therefore, this circumstance should have little effect on the formation of possible photoproducts.

III.1.5 Determination of the Redox Potentials and Establishment of the Energy Level Diagrams

The redox potentials of the individual molecular moieties in the complexes were determined by means of cyclic voltammetry. All cyclic voltammograms (Figure III.4) were recorded in de-oxygenated MeCN solutions at complex concentrations of about 1 mM and are referenced versus the ferrocenium/ferrocene redox couple $\text{Fc}^{+/0}$. 0.1 M TBAF_6 was used as supporting electrolyte, and for all measurements the potential scanning rate was 0.1 V/s.

$[\text{Re}(\text{bpy})(\text{CO})_3(\text{py})]^+$ was also measured as an unsubstituted reference complex, in order to evaluate changes in the redox potentials due to attachment of the amine moieties. Measuring reduction and oxidation in two separate sweeps proved to provide higher quality results for $\text{Re}_2\text{-TAA}$ and Re-ref .

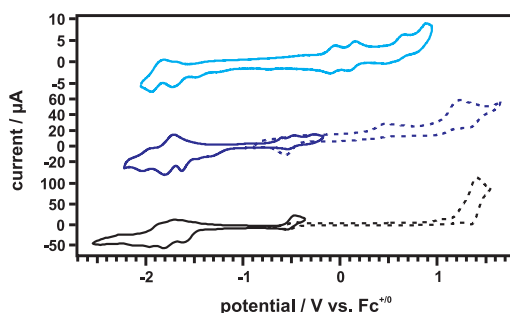


Figure III.4 Cyclic voltammograms of $\text{Re}_2\text{-OTA}$ (cyan), $\text{Re}_2\text{-TAA}$ (blue), and Re-ref (black) in de-oxygenated MeCN solutions referenced to $\text{Fc}^{+/0}$.

The direct use of decamethylferrocene (Me_{10}Fc) as an internal standard for the measurement of $\text{Re}_2\text{-OTA}$ produced data which was not evaluable due to interactions with the complex. More precisely, the redox chemistry of Me_{10}Fc became irreversible with the appearance of new waves not belonging to the complex itself and the oxidation waves for OTA increased with every redox cycle and seemed to merge, thus prohibiting a clear determination of the proper values. To assure calibration of the potentials the following procedure was applied. First, only the supporting electrolyte dissolved in MeCN was measured to establish a baseline, then $\text{Re}_2\text{-OTA}$ was added, and the cyclic voltammograms were recorded. After that, Me_{10}Fc was added and the sample was measured with the same settings again. In the data evaluation, the wave corresponding to Me_{10}Fc was shifted to reference the voltammogram to the potential of the $\text{Fc}^{+/0}$ couple. The voltammograms without the internal standard were shifted

by the exact same value. Table III.1 summarizes the redox potentials as extracted from the cyclic voltammograms in Figure III.4.

Table III.1 Redox potentials in MeCN. All values are given in V vs. $\text{Fc}^{+/0}$.

complex	$\text{Re}^{2+/+}$ / V	$\text{bpy}^{0/-}$ / V	amine $^{+/0}$ / V	amine $^{2+/+}$ / V	amine $^{3+/2+}$ / V
Re-ref	1.37	-1.77			
Re_2 -TAA	1.23	-1.77	0.46		
Re_2 -OTA	0.88	-1.88	-0.07	0.25	0.65

The literature potentials for Re-ref given in V vs. SCE in MeCN were converted to V vs. $\text{Fc}^{+/0}$ according to PAVLISHCHUK *et al.*¹⁰⁴ The reduction with $E_{\text{red}} = -1.77$ V is ligand-centered, whereas the oxidation is metal-centered ($E_{\text{ox}} = 1.37$ V).⁸⁰ The measured values are in good agreement with literature. Re_2 -TAA shows one quasi-reversible oxidation at 0.46 V for the oxidation of TAA to TAA^+ . Re_2 -OTA on the other hand, shows three oxidation waves at -0.07 V, 0.25 V, and 0.65 V with the first two reversible. These values coincide well with literature ones obtained from molecules comprised of oligo-triarylamine moieties.^{77,96} The very low oxidation potentials at around 0 V indicate that, in principle, OTA can easily be oxidized by the excited rhenium photosensitizer. Therefore, OTA is a suitable electron donor and, in the present complex Re_2 -OTA, can readily accumulate two holes transferring one electron to either one of the rhenium complexes.

Interestingly, the CV data shows that the rhenium oxidation potential is shifted to less positive values starting at 1.37 V for the unsubstituted Re-ref complex, to 1.23 V for the TAA substituted complex and down to 0.88 V for Re_2 -OTA. This behavior is due to the increasing electron-donating ability of the attached amines. The electron donating resonance effect (+M effect) of the methoxy group, if attached in *para*-position, surpasses its electron withdrawing effect (-I effect). 4-[bis(4-methoxyphenyl)amino]phenyls in general possess a high π -donor strength, a measure for their ability to act as intramolecular electron donors towards conjugated π -systems.¹⁰⁵ Hence, the attached amines push negative charge towards the rhenium metal center facilitating its oxidation. This effect, already influencing the oxidation potential of rhenium in Re_2 -TAA, will most certainly be stronger in Re_2 -OTA. Due to the more extended arylamine system with three nitrogen atoms each bearing a lone pair and the four attached methoxy groups, OTA is even more electron-rich than TAA. The ancillary bpy-ligands are connected to the rhenium center via coordinative bonds and are not covalently linked to the amines. Furthermore, the distance between bpy and amine is larger which also contributes to their reduction potential not being influenced in such a way. As a result,

all complexes show similar values for the bpy-centered reduction around -1.8 V.

Establishment of the Energy Level Diagrams

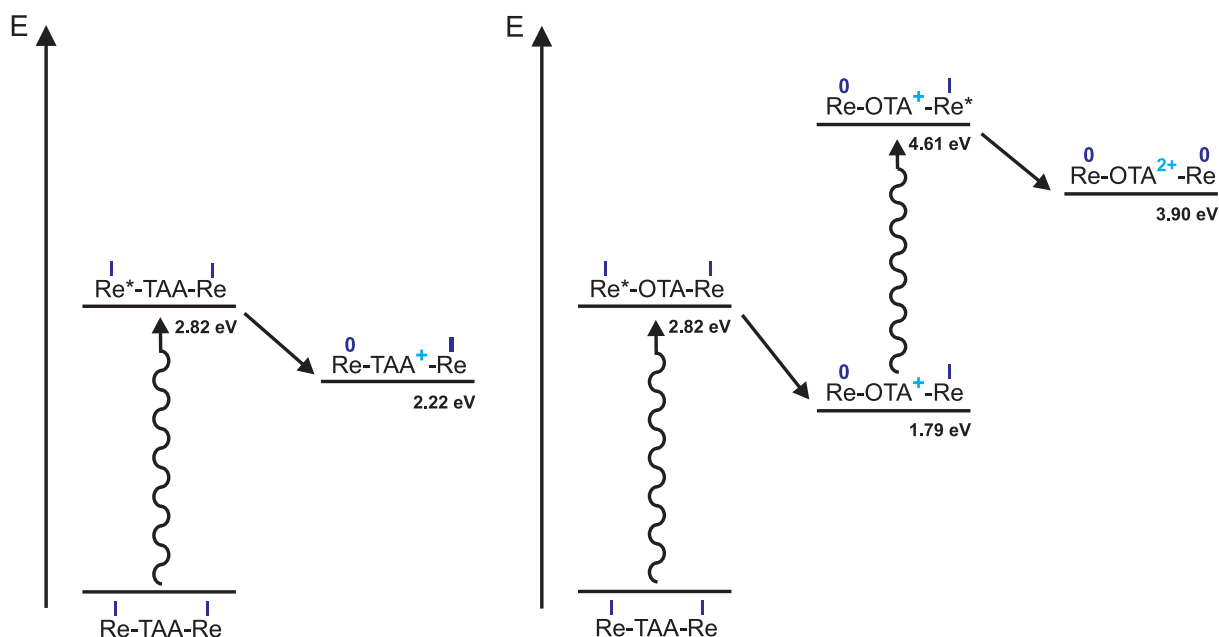
The values for the energies of the different redox states were estimated using the following Equation (III.1).¹⁰⁶ Errors of this estimation typically lie in the range of 0.1 eV.

$$\Delta G_{ET}^0 = e(E_{ox} - E_{red}) - E_{00} - \frac{e^2}{4\pi \cdot \epsilon_0 \cdot \epsilon_s \cdot R_{DA}} \quad (\text{III.1})$$

with

- E_{ox} oxidation potential
- E_{red} reduction potential
- E_{00} ³MLCT energy
- e elementary charge
- ϵ_0 vacuum permittivity
- ϵ_s dielectric constant of MeCN (35.94)
- R_{DA} donor-acceptor distance ($\approx 12 \text{ \AA}$).

The D–A distance of 12 \AA was estimated from the distance between the ancillary bpy ligand on the rhenium photosensitizer over the central benzene ring to the first nitrogen atom on the amine donor. The resulting energy level diagrams for both, $\text{Re}_2\text{-TAA}$ and $\text{Re}_2\text{-OTA}$ are depicted in Scheme III.4.



Scheme III.4 Energy level diagrams for $\text{Re}_2\text{-TAA}$ (left) and $\text{Re}_2\text{-OTA}$ (right).

As can be seen, the electron transfer step from TAA to the rhenium photosensitizer

in $\text{Re}_2\text{-TAA}$ is exergonic by 0.60 eV and therefore very likely to occur, at least from a purely thermodynamic point of view. For $\text{Re}_2\text{-OTA}$, the transfer of the first electron from OTA to rhenium is exergonic by 1.03 eV. Likewise, the second electron transfer to form OTA^{2+} and a second reduced rhenium sensitizer is exergonic by 0.71 eV, but only after absorption of a second photon. The thermodynamic data therefore suggests formation of the second charge-separated state in $\text{Re}_2\text{-OTA}$ is indeed possible. This is mainly due to the very low first two oxidation potentials of OTA. Nevertheless, formation of OTA^{2+} does still require a two-photon process which is not only dependent on thermodynamics.

III.1.6 Steady State Luminescence Spectroscopy

The luminescence spectra of the investigated complexes show a broad emission band as displayed in Figure III.5. Rhenium polypyridyl complexes are known to give unstructured emission bands especially at RT which are attributed to forbidden electronic transitions from the $^3\text{MLCT}$ excited state to the ground state.^{80,107,108}

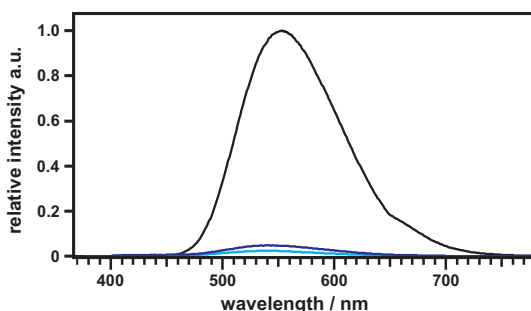


Figure III.5 Luminescence spectra of the investigated complexes ($\text{Re}_2\text{-TAA}$ in blue and $\text{Re}_2\text{-OTA}$ in cyan) measured on de-oxygenated 10^{-5} M MeCN solutions after excitation at 355 nm. All spectra were corrected for differences in extinction at 355 nm and normalized to the emission of Re-ref (black).

Re-ref shows an emission maximum at 553 nm, whereas the maxima of the TAA and the OTA complex are blue-shifted by 12 nm. $\text{Re}_2\text{-TAA}$ and $\text{Re}_2\text{-OTA}$ show significant quenching of the rhenium luminescence. For $\text{Re}_2\text{-TAA}$ it is quenched by 95% and for $\text{Re}_2\text{-OTA}$ by 97.5% which is consistent with relatively strong electronic coupling between rhenium and the amines, due to their spatial proximity. This strong $^3\text{MLCT}$ quenching is indicative of photochemistry in the investigated complexes. However, apart from the desired electron transfer from the amines to the rhenium chromophores, energy transfer might be an unwanted non-radiative deactivation pathway. The possibility of this will be discussed in the following subsection.

III.1.7 Possibility of Triplet-Triplet Energy Transfer

In order to assess the efficiency of energy transfer from the excited rhenium photosensitizers to the amines which may prevent charge separation by fast deactivation of the excited $^3\text{MLCT}$ state, one must know the energies of the lowest-lying triplet states of the involved molecular entities.

On account of lacking information on the triplet state energy of OTA it was experimentally determined by recording the luminescence spectrum of OTA-ref in a frozen glass (MeTHF, 10^{-5} M) at 77 K (Figure III.6 b). The triplet energy of Re-ref was measured accordingly, albeit in a EtOH/MeOH 4:1 glass matrix (Figure III.6 a). E_T (in eV) then corresponds to the luminescence origin at this temperature.

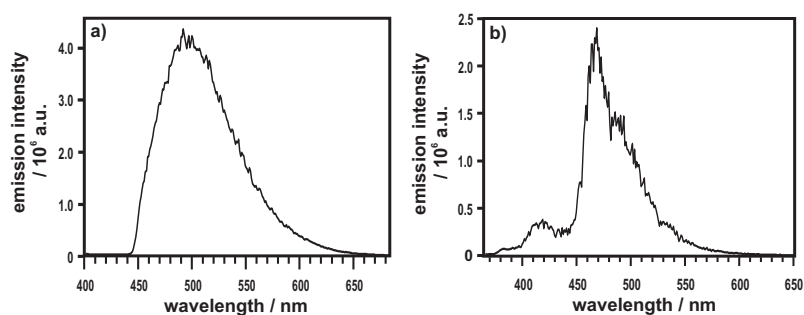


Figure III.6 Steady-state luminescence spectra at of Re-ref (a), in an EtOH/MeOH 4:1) and OTA-ref (b), in MeTHF) at 77 K.

Excitation occurred at the respective absorption maxima, i.e. 340 nm for OTA-ref and 355 nm for Re-ref. The E_T values obtained, summarized in Table III.2, are 3.32 eV for OTA and 2.82 eV for Re-ref. The latter is comparable to the value that can be extracted from the emission spectrum at 77 K shown by SACKSTEDER *et al.*⁸⁰ Furthermore, a value of 3.04 eV for the lowest triplet excited state of TAA can be found in literature.¹⁰⁹

Table III.2 Luminescence origin and triplet energies.

	origin / nm	E_T / eV
Re-ref	440	2.82
OTA-ref	373	3.32

On the basis of the above determined values, it becomes clear that triplet energy transfer from the excited rhenium chromophore to TAA is endergonic by 0.22 eV and to OTA even by 0.5 eV. Consequently, quenching of the excited state most likely occurs by electron transfer and not energy transfer. Direct evidence for the importance of electron transfer will be provided in III.1.9.

III.1.8 Time-Resolved Luminescence Spectroscopy

To gain further insight into the photochemical processes occurring in the Re_2 -OTA and Re_2 -TAA triads, time-resolved emission measurements were performed to determine at what rate luminescence was quenched. In de-oxygenated 10^{-5} M MeCN solutions of the triads immediate quenching of the luminescence after laser excitation (pulse duration ≈ 10 ns) was observed. This corroborates the results from the steady-state measurements. Exponential fitting of the decay gives a luminescence lifetime of 239 ns for Re-ref. The rhenium triads show a biexponential decay indicating the existence of two different luminescent species. The data for Re_2 -TAA suggests one species whose luminescence decays with $\tau = 21$ ns representing the main product with a contribution of 76% and another product ($\tau = 332$ ns) contributing only to 24%. In the case of Re_2 -OTA, the values present themselves as follows: short-lived luminescent species with $\tau = 27$ ns (64%) and long-lived luminescent species with $\tau = 423$ ns (36%).

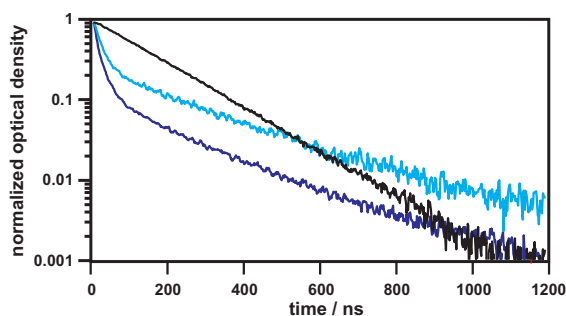


Figure III.7 Luminescence decays of Re-ref (black), Re_2 -TAA (blue), and Re_2 -OTA (cyan) in de-oxygenated MeCN solutions (10^{-5} M) after excitation at 335 nm.

These findings might be caused by the presence of two rhenium complexes in these triads. By excitation with a laser pulse at 335 nm both rhenium chromophores in one complex could be excited simultaneously. Following the luminescence quenching of one by electron transfer from the amine to the metal center, the other chromophore might still be emissive. The longer lifetimes in the triads need not match the luminescence lifetime of the free Re-ref exactly, due to a changed electronic and possibly even structural environment following the charge separation. An interpretation such as this seems much more valid for Re_2 -TAA, because here the amine can only be oxidized once and hence quench solely one excited metal center. Re_2 -OTA, however, was designed to quench both rhenium photosensitizers by two successive oxidations of OTA. In the present measurement the photon flux density might have been too low to accomplish the required two-photon process, leading to a mixture of two

different photoproducts. Quadratic excitation power dependency is a well known characteristic of two-photon processes.^{110,111} An alternative interpretation would be that the biexponential luminescence decays in the rhenium triads are attributable to minor, yet highly luminescent impurities.

Equation III.2 was applied to the luminescence lifetimes of the short-living species of $\text{Re}_2\text{-TAA}$ and $\text{Re}_2\text{-OTA}$ in order to obtain the quenching constants for both complexes in MeCN solution.

$$k_Q = \tau_{obs}^{-1} - \tau_{ref}^{-1} \quad (\text{III.2})$$

k_Q is the quenching constant calculated from the luminescence lifetimes of $\text{Re}_2\text{-TAA}$ and $\text{Re}_2\text{-OTA}$, respectively (τ_{obs}^{-1}), and the luminescence lifetime of the unsubstituted reference complex $[\text{Re}(\text{bpy})(\text{CO})_3(\text{py})]^+$ (τ_{ref}^{-1}).

For $\text{Re}_2\text{-TAA}$ a k_Q -value of $4.34 \cdot 10^7 \text{ s}^{-1}$ was calculated, as compared to $k_Q = 3.29 \cdot 10^7 \text{ s}^{-1}$ for $\text{Re}_2\text{-OTA}$.

III.1.9 Identification of the Photoproducts

With both, quenching of the steady state rhenium emission and shortening of the excited-state lifetime being observed, it seems certain that photochemistry in form of electron transfer is indeed occurring in the Re_2 -triads. The occurrence of energy transfer as a possible deactivation pathway of the excited state was found to be unlikely by estimating the triplet energies of the different molecular moieties (Subsection III.1.7).

Based on the above mentioned data for $\text{Re}_2\text{-TAA}$, upon excitation of a de-oxygenated MeCN solution electron transfer from the TAA moiety to one rhenium photosensitizer is expected. In order to get an idea of what to expect for TAA^+ in transient absorption spectra, chemical oxidation studies have been made by titrating an MeCN solution of the complex with $\text{Cu}(\text{ClO}_4)_2$. Figure III.8 shows the UV-Vis-absorption data of the titration leading to $\text{Re}_2\text{-TAA}^+$ (top), as well as the transient absorption spectrum after excitation at 355 nm (bottom).

The transient spectrum of $\text{Re}_2\text{-TAA}$, recorded in a 200 ns time window directly after the excitation pulse shows two bands at 771 nm and 363 nm attributable to the formation of the TAA radical cation. These are typical features observed for oxidized TAA.^{112,113} Reductive flash-quench experiments of rhenium polypyridyl complexes with amine quenchers, such as DPA or TEOA, indicate that the positive absorption

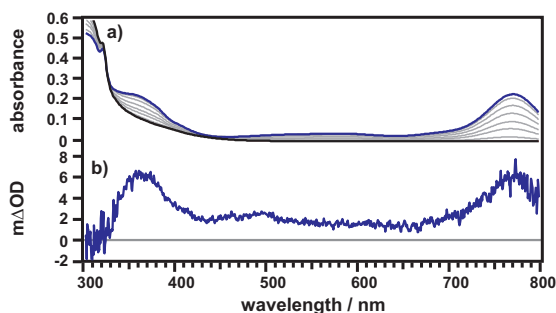


Figure III.8 Top: UV-Vis absorption spectrum of a 10^{-5} M MeCN solution of $\text{Re}_2\text{-TAA}$ (black) and its stepwise oxidation to $\text{Re}_2\text{-TAA}^+$ (blue) upon addition of increasing amounts of $\text{Cu}(\text{ClO}_4)_2$; bottom: transient absorption spectrum after 355 nm excitation of a 35 μM de-oxygenated MeCN solution of $\text{Re}_2\text{-TAA}$.

around 450-500 nm is due to the reduced rhenium photosensitizer.¹¹⁴ A bleach at 320 nm is also expected for the reduced rhenium complex.^{108,115} However, this is not observed here, presumably because of the rather high optical density of the complex solution in this spectral range.

Given the direct evidence for the formation of a charge-separated state with a hole on the TAA and a negative charge on the rhenium photosensitizer, or more exactly on the ancillary bipyridine ligand, we expect both radical species to decay with the same time constant. The decay of the photoproduct to its ground state as detected at different wavelengths is displayed in Figure III.9, and it can be seen that this expectation is indeed met. The charge-separated photoproduct $(\text{Re}^+)(\text{Re}^0)\text{-TAA}^+$ is generated within the 10 ns duration of the laser pulse and decays within 39 ns. Though not a very long-living species, this short lifetime could be expected for rather closely connected donor and acceptor moieties, as is the case in the present molecule.

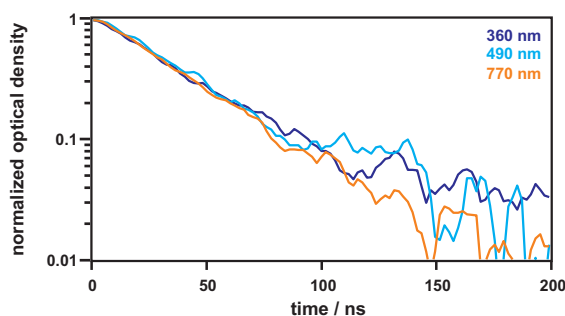


Figure III.9 Decay of transient absorption signals at 360 nm (blue), 490 nm (cyan) and 770 nm (orange).

In contrast to $\text{Re}_2\text{-TAA}$, twofold charge separation to yield $(\text{Re}^0)_2\text{-OTA}^{2+}$ with two holes on the OTA donor and one electron at each of the two rhenium acceptors could be anticipated. To test the possibility of achieving the necessary two-photon

absorption an ordinary pump-probe technique was applied. The laser pulse duration was ≈ 10 ns. From the experiments on $\text{Re}_2\text{-TAA}$ it is known that the photoproduct is formed within the 10 ns laser pulse since no rising signal could be detected. With OTA having such low oxidation potentials that it can be oxidized twice until the potential to oxidize TAA to TAA^+ is reached, we hoped to gain access to the twofold charge-separated state of $\text{Re}_2\text{-OTA}$.

The lifetime of the first charge-separated state, $(\text{Re}^+)(\text{Re}^0)\text{-OTA}^+$, is estimated to be in the same order of magnitude as for $\text{Re}_2\text{-TAA}$ which is long enough to excite one molecule two times within the duration of the laser pulse.

In order to understand the changes in the absorption of $\text{Re}_2\text{-OTA}$ upon undergoing photoinduced electron transfer, it was chemically oxidized by titration with $\text{Cu}(\text{ClO}_4)_2$. Figure III.10a depicts the data collected by stepwise chemical oxidation and excitation with a 10 ns laser pulse at 355 nm (Figure III.10b). On the basis of the data obtained hereby it becomes clear that OTA^+ exhibits positive absorption throughout the whole spectral range from 400 to 800 nm with local maxima at 427 nm and 765 nm and a very broad absorption band in the NIR region with a maximum at around 1350 nm. When $\text{Re}_2\text{-OTA}^+$ is further oxidized to $\text{Re}_2\text{-OTA}^{2+}$, the absorption at 427 nm decreases to approximately one third of the initial OTA^+ absorption with a concomitant increase between 500 and 650 nm resulting in a new absorption maximum at 600 nm. Furthermore, the absorption at 765 nm is also still increasing, albeit only slightly. However, the most distinctive difference between $\text{Re}_2\text{-OTA}^+$ and its twofold oxidized form can be seen in the NIR region. There, a new and very prominent band at 1138 nm arises which can undoubtedly be assigned to $\text{Re}_2\text{-OTA}^{2+}$.

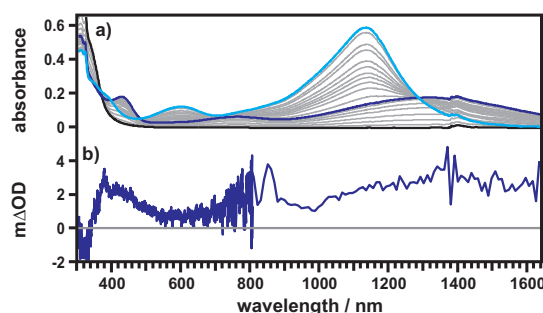


Figure III.10 Top: stepwise chemical oxidation of a 10^{-5} M MeCN solution of $\text{Re}_2\text{-OTA}$ (black) to $\text{Re}_2\text{-OTA}^+$ (blue) and $\text{Re}_2\text{-OTA}^{2+}$ (cyan); bottom: transient absorption spectrum of a de-oxygenated 10^{-5} M MeCN solution of $\text{Re}_2\text{-OTA}$ directly after 355 nm excitation in a 50 ns time window.

A definite distinction between the two oxidation states of OTA in the spectral range from 400 to 800 nm may prove difficult due to their similar absorbance in that area.

Therefore, in addition to the transient absorption data acquired by a PMT between 300 and 800 nm, the laser setup was equipped with an NIR detector to cover the spectral region up to 1700 nm. The actual absorption spectrum from 800 to 1700 nm was obtained by mapping the area, which means measuring kinetic absorption every 10 nm and subsequently slicing the collected data in equal sections, using an available feature of the software (P900).

Directly observable from the transient data is the very low optical density and a rather low signal to noise ratio, yet all relevant information could still be extracted. Variation of the sample concentration did not result in any improvement of the signal. Considering the transient data, the most likely photoproduct is the singly oxidized $(\text{Re}^+)(\text{Re}^0)\text{-OTA}^+$ with absorption maxima at 405, 780, and 1360 nm. From the spectrum between 400 and 800 nm alone, it is difficult to make a clear statement about the nature of the photoproduct due to the above discussed points. However, the lack of the prominent band at 1140 nm strongly suggests that little or no $(\text{Re}^0)_2\text{-OTA}^{2+}$ was generated in the experiment at hand. Though thermodynamically favored ($\Delta G^0_{\text{ET}} = -0.71$ eV), formation of the second charge-separated state $(\text{Re}^0)_2\text{-OTA}^{2+}$ would require the successful absorption of a second photon which seemed not to happen in the present case. Furthermore, additional deactivation pathways are open for $(\text{Re}^0)_2\text{-OTA}^{2+}$ that are not available to $(\text{Re}^+)(\text{Re}^0)\text{-OTA}^+$. This will decrease the lifetime of $(\text{Re}^0)_2\text{-OTA}^{2+}$ significantly. Thus, the observation that $(\text{Re}^+)(\text{Re}^0)\text{-OTA}^+$ is the predominant species generated in the above experiment is not a big surprise.

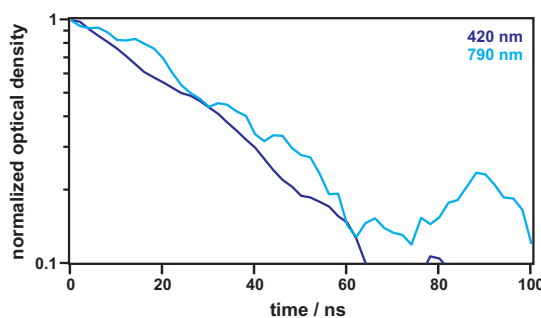


Figure III.11 Transient absorption decays of the photoproduct of $\text{Re}_2\text{-OTA}$ at 420 nm and 790 nm.

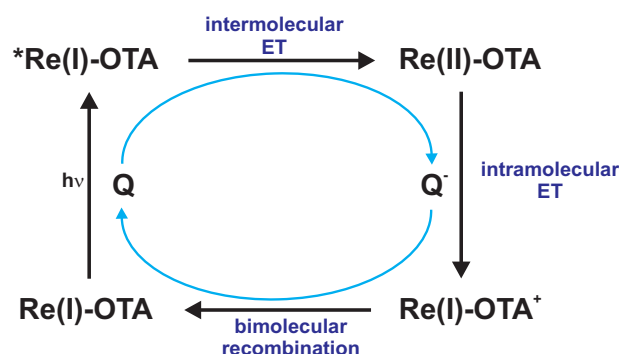
The lifetime of 36 ns extracted from the decays from Figure III.11 resemble those obtained in the reference complex $\text{Re}_2\text{-TAA}$. Unfortunately, due to the low signal strength and the relatively poor sensitivity of the NIR detector it was not possible to measure a decent transient absorption decay in the infrared region.

On account of the short lifetime of $(\text{Re}^+)(\text{Re}^0)\text{-OTA}^+$, our attention turned towards the use of the flash-quench technique. This approach should significantly increase the charge-separated state lifetime, since the electron will be transported further away

from the OTA radical cation and recombination will then be a diffusion controlled step.

III.1.10 Oxidative Flash-Quench Experiments

The basic principle of the flash-quench experiment is depicted in Scheme III.5 with an exemplary complex Re–OTA.



Scheme III.5 Principle of flash-quench experiments.

Once in its excited form, the rhenium photosensitizer ($^*\text{Re(I)}$), as a strong reductant, is able to reduce an appropriate quencher (Q). Thus, intermolecular electron transfer forms the reduced quencher Q^- and oxidized Re(II) . This is followed by rapid intramolecular electron transfer from the OTA donor to Re(II) . The recombination process resulting in the molecules in their ground-states, Re(I)-OTA and Q , is now diffusion controlled. This will prolong the lifetime of the charge-separated species significantly, typically up to several microseconds. By this approach, we hoped to increase the probability of exciting $(\text{Re}^+)(\text{Re}^0)\text{-OTA}^+$ a second time with our nanosecond setup.

A suitable quencher needed to fulfill two major criteria: First, its reduction by the excited rhenium photosensitizer had to be thermodynamically possible. Second, its reduced form should not display any absorption beyond 350 nm to prevent superposition with bands of oxidized OTA and absorption of laser light. Based on these requirements, 1,2,4,5-tetracyanobenzene (TCNB) was chosen as the quencher for the following flash-quench experiment. Its reduction potential of $E_{\text{red}} = -1.04 \text{ V vs. Fc}^{+/0}$ allows for $^*\text{Re(I)}$ ($E_{\text{ox}} = -1.94 \text{ V vs. Fc}^{+/0}$) to reduce it, and $\text{TCNB}^{\cdot-}$ shows only weak absorption in the spectral range we are interested in. Furthermore, it proved to be very stable in de-oxygenated solution.¹¹⁶

The left part of Figure III.12 shows the transient absorption spectrum of a de-oxygenated 10^{-5} M MeCN solution of $\text{Re}_2\text{-OTA}$ with an excess of TCNB (0.2 M). The spectrum was recorded directly after the excitation pulse in a 200 ns time window.

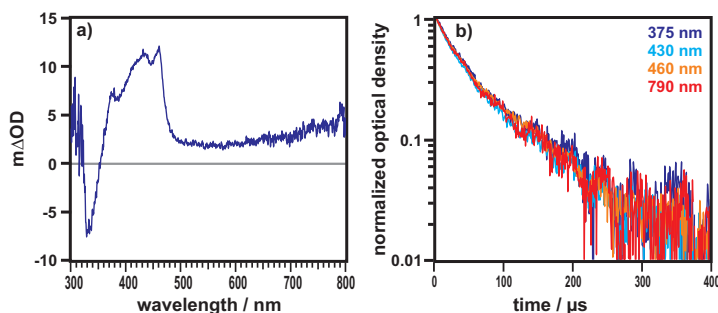


Figure III.12 a) Transient absorption spectrum after 355 nm excitation of a de-oxygenated 10^{-5} M MeCN solution of $\text{Re}_2\text{-OTA}$ with an excess of TCNB; b) Corresponding decays at different wavelengths.

Directly observable is the similarity of the flash-quenched transient absorption spectrum and the one obtained after excitation of the pure complex solution, with bands at 430 nm and 790 nm being again attributed to the singly oxidized $\text{Re}_2\text{-OTA}$. The two new bands at 375 nm and 460 nm belong to the reduced TCNB, as was demonstrated by PROTTI *et al.* who generated $\text{TCNB}^{\bullet-}$ quantitatively by addition of an excess of NEt_3 to a de-oxygenated MeCN solution of TCNB.¹¹⁶ Investigations in the NIR region were impeded by the same reasons already mentioned above, especially the poor sensitivity of the detector. The signals from Figure III.12a) decay on a 400 μs timescale (Figure III.12b)). Alas, despite the prolonged lifetime of $\text{Re}_2\text{-OTA}^+$, even the flash-quench method could not produce any sign of the twofold charge-separated species.

Thus, the multitude of deactivation processes open to $\text{Re}_2\text{-OTA}^{2+}$ could not be influenced to ensure its higher population. In addition, prolongation of the lifetime of $\text{Re}_2\text{-OTA}^+$ also did not result in the desired photoproduct. Consequently, our focus turned towards studying the influence of variations in the excitation power output.

III.1.11 Influence of the Excitation Density on the Photochemistry

Generating OTA^{2+} requires the absorption of two photons upon excitation which is intrinsically more difficult to achieve and also less trivial than simple separation of one electron from one hole. Studies on photon-upconversion have shown that the dependence of two-photon absorption on the excitation density is often of quadratic nature.^{110,111}

By variation of the excitation power, a change in the transient absorption spectrum was anticipated which might indicate the formation of OTA^{2+} on top of a stronger signal caused by OTA^+ . It is known from the chemical oxidation of $\text{Re}_2\text{-OTA}$, as well as from earlier studies on oligotriarylaminines that OTA^{2+} shows increased absorption at

600 nm compared to OTA^+ .^{52,77,96} Figure III.13 shows the transient absorption spectra of $\text{Re}_2\text{-OTA}$ in MeCN solution recorded at high (3.8 mJ, cyan trace) and low (1.1 mJ, blue trace) excitation power as well as the difference spectrum (black trace). To obtain the difference spectrum, the low-energy spectrum was multiplied by a factor of 3.45, the quotient of 3.8/1.1 mJ and then subtracted from the cyan spectrum recorded at an excitation power of 3.8 mJ. A laser density of 1.1 mJ proved to be the lower limit. Decreasing the excitation intensity further impaired the already weak transient signal and the signal-to-noise ratio.

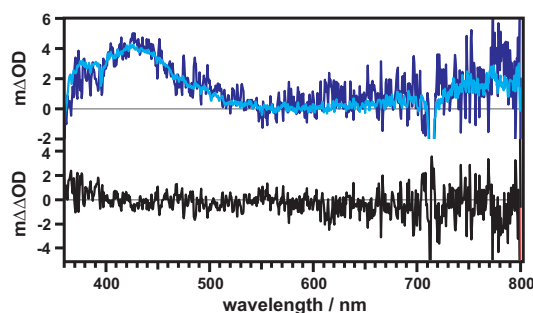


Figure III.13 Intensity-dependent transient absorption spectra of a de-oxygenated 10^{-5}M MeCN solution of $\text{Re}_2\text{-OTA}$. Cyan: 3.8 mJ, blue: 1.1 mJ, and the difference spectrum in black.

Despite the increase in the excitation density to 3.8 mJ, no increased absorption around 600 nm could be detected as was expected for the formation of OTA^{2+} . Though, measurements at different laser powers did not reveal any spectral changes indicative of OTA^{2+} , power-dependent kinetic absorption spectra at 420 nm were recorded to corroborate these results. On the basis of the lack of spectral evidence for OTA^{2+} , a linear dependence of the signal intensity on the laser excitation power P is expected. This expectation is met as can be directly observed from the graph in Figure III.14a).

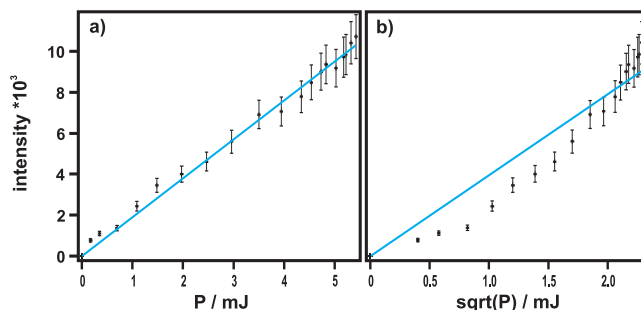


Figure III.14 Dependence of the signal intensity on the laser power. Left: linear dependency due to formation of $(\text{Re}^+)(\text{Re}^0)\text{-OTA}^+$ in a single-photon process. Right: non-linear behavior of intensity vs. \sqrt{P} because no two-photon process takes place.

By the provision of TCNB as an electron acceptor we hoped to promote the second charge separation as discussed in Subsection III.1.10. Recombination now being a diffusion controlled step, should increase the possibility of forming $\text{Re}_2\text{-OTA}^{2+}$ with a detectable concentration and lifetime. However, despite the increased lifetime of $\text{Re}_2\text{-OTA}^+$ in presence of the quencher, still no spectral evidence for OTA^{2+} was observed (Figure III.15) at 3.1 mJ. Even higher laser powers result in the decomposition of the sample by photodissociation of CO ligands of the photosensitizer.¹¹⁷

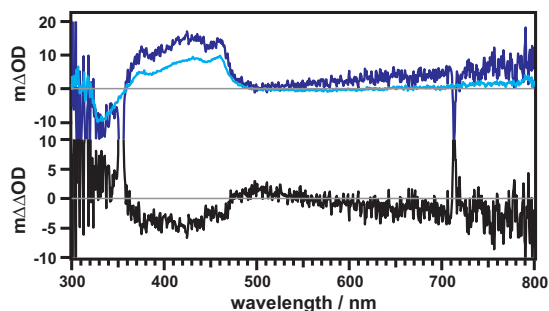


Figure III.15 Intensity-dependent transient absorption spectra obtained from the same solutions as in III.1.10. Cyan trace: 3.1 mJ, blue trace: 1.0 mJ, black: difference spectrum obtained by subtracting the blue trace from the cyan trace.

Even laser intensity dependent measurements could not reveal twofold oxidized oligotriarylamine in the present $\text{Re}_2\text{-OTA}$ triad. As discussed earlier, if generated at all, $(\text{Re}^0)_2\text{-OTA}^{2+}$ will most likely have a very short lifetime due to the manifold of possible deactivation pathways of this high-energy photoproduct. It might in fact be possible that the lifetime of the twofold charge-separated state is less than 10 ns, which is the pulse duration of the laser, making it impossible to detect $(\text{Re}^0)_2\text{-OTA}^{2+}$ with our laser setup. In an attempt to increase the lifetimes of the charge-separated states by elongating the D-A distance, a triad comprised of an anthraquinone (AQ) acceptor, a rhenium photosensitizer, and the OTA donor was synthesized.

Another process that may be responsible for the lack of the second charge-separated state is undesired energy transfer between the rhenium photosensitizer in its excited $^3\text{MLCT}$ state and the present oxidized amines in the first charge-separated state. Due to the low-energy absorptions of TAA^+ and OTA^+ this undesired deactivation process might indeed occur. In order to assess its possibility, luminescence lifetime measurements were performed on de-oxygenated MeCN solutions of $\text{Re}_2\text{-TAA}^+$ and $\text{Re}_2\text{-OTA}^+$ (Figure III.16).

If energy transfer from the excited rhenium sensitizer to the oxidized amines occurs, the emission lifetimes are expected to be shorter than for the triads before amine oxidation. Measurements of the non-oxidized species gave luminescence lifetimes of

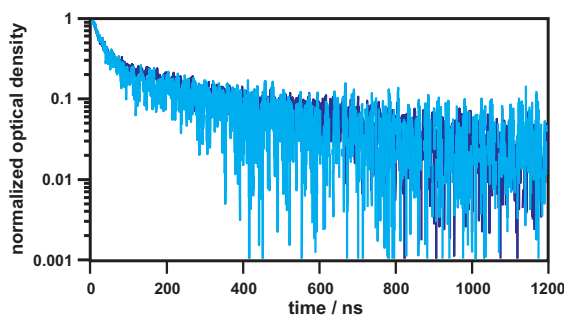


Figure III.16 Emission decays of $\text{Re}_2\text{-TAA}^+$ (blue) and $\text{Re}_2\text{-OTA}^+$ (cyan) after excitation of a de-oxygenated MeCN solution at 355 nm.

21 ns for $\text{Re}_2\text{-TAA}$ and 27 ns for $\text{Re}_2\text{-OTA}$ (III.1.8). In the reference experiment on the oxidized species the emission lifetimes are 25 ns for $\text{Re}_2\text{-TAA}^+$ and 27 ns for $\text{Re}_2\text{-OTA}^+$. Within the accuracy of the measurement and the fit of the decays the $^3\text{MLCT}$ lifetimes of the non-oxidized species, compared to the data obtained from $\text{Re}_2\text{-TAA}$ and $\text{Re}_2\text{-OTA}$ before amine oxidation are the same. It is therefore concluded that energy transfer between the excited photosensitizer and the oxidized amines is rather inefficient.

However, another possibility for unwanted deactivation is reverse electron transfer from the oxidized amines to the excited photosensitizer after absorption of a second photon. As discussed in II.4 this undesired electron transfer reaction can also contribute to not achieving the twofold charge-separated state.

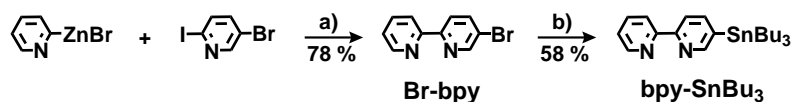
III.2 Electron Transfer in an AQ–Re–OTA Triad

Based on the insights gained from the studies on Re₂–OTA and known photochemistry and kinetics of donor-photosensitizer-acceptor molecules, a structurally simple triad comprised of an anthraquinone acceptor (AQ), a rhenium photosensitizer, and the OTA donor was synthesized. The design of the triad was aimed at accumulating two holes on the OTA and the transferred electrons on the AQ acceptor. It is already known from Nature that quinones are two-electron acceptors. Charge accumulation in this triad does require the twofold excitation of the one rhenium photosensitizer. In the following section efforts on our side for achieving this twofold charge separation will be discussed.

III.2.1 Synthesis of AQ–Re–OTA

For the synthesis of AQ–Re–OTA some general building blocks, such as 2,2'-bipyridine derivatives and a xylene bridging unit, were needed.

The different bipyridine derivatives used for ligand synthesis are 5-bromo-2,2'-bipyridine (Br-bpy) and 5-(tributylstannyl)-2,2'-bipyridine (py-SnBu₃). The reaction pathway for their synthesis is depicted in Scheme III.6.



Scheme III.6 Synthesis of the bpy building blocks: **a)** Pd(PPh₃)₄, THF, RT, 24 h; **b)** *n*BuLi, tributyltin chloride, Et₂O, RT, over night.

All of these molecules are known in literature and were synthesized accordingly or with slight modifications in the purification steps. Therefore, their synthesis will not be discussed in detail here.^{118–120}

In the AQ–Re–OTA triad, the distance between donor/acceptor and the pyridine/bipyridine coordination sites was elongated by inserting a xylene bridging unit. Being a frequently used spacer in earlier works, its synthesis (Scheme III.7) mostly followed literature procedures. For the first step, the instructions of FREYS *et al.*¹¹⁹ were accurately followed, and for the introduction of the boronic acid, a procedure of So *et al.* was adapted.¹²¹

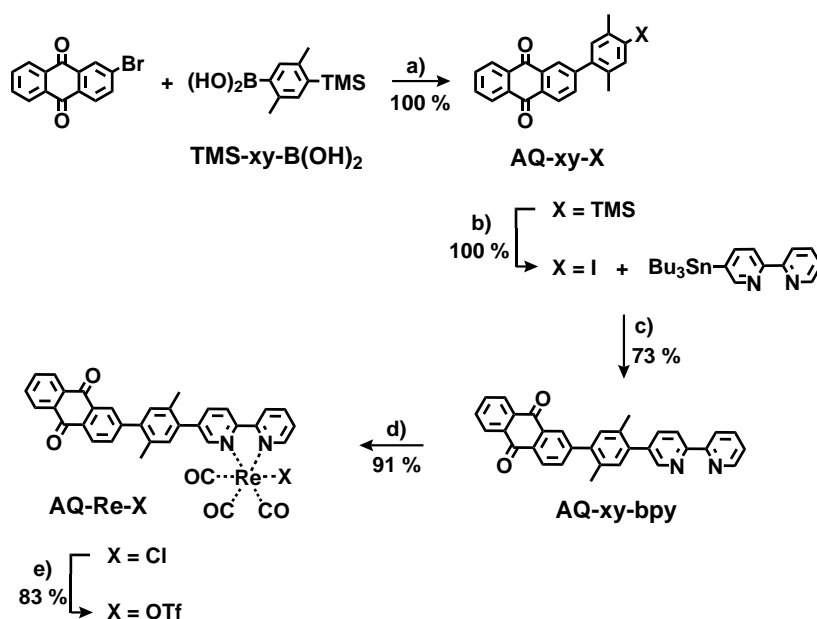
In this way, the xylene bridging unit could be obtained in an overall yield of 70%.

Synthesis of the AQ–Re–OTA triad begun with preparation of an AQ–Re precursor (Scheme III.8) which was later reacted with a py–xy–OTA ligand to yield the final



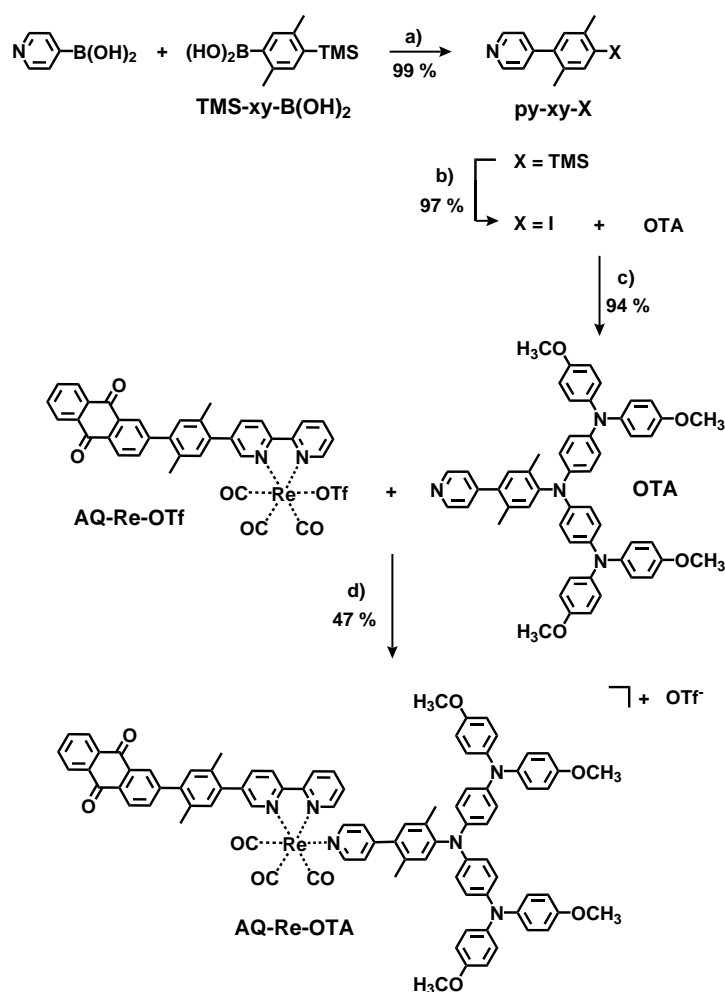
Scheme III.7 Synthesis of the xylene spacer: **a)** $n\text{BuLi}$, trimethylsilyl chloride, THF, RT, over night; **b)** $n\text{BuLi}$, trimethyl borate, THF, RT, over night, 6 M HCl.

AQ-Re-OTA complex. For obtaining the required AQ-xy-bpy ligand, a previously published procedure of our own group was followed.⁸⁸



Scheme III.8 Synthesis of the AQ-Re-OTf precursor: **a)** Na_2CO_3 , $\text{Pd}(\text{PPh}_3)_4$, toluene/EtOH/ H_2O , reflux, 1.5 d; **b)** ICl, DCM/MeCN, 0 °C/RT, over night; **c)** $\text{Pd}(\text{PPh}_3)_4$, *m*-xylene, 150 °C, 70 h; **d)** $\text{Re}(\text{CO})_5\text{Cl}$, toluene, reflux, over night; **e)** trifluoromethanesulfonic acid, DCM, RT, 2 h, Et_2O .

SUZUKI coupling of 2-bromo-9,10-anthraquinone to TMS-xy-B(OH)_2 , as well as subsequent deprotection of the TMS group with ICl was achieved in essentially quantitative yields for each reaction. Preparation of the final ligand via STILLE coupling of AQ-xy-I with bpy-SnBu_3 in hot *m*-xylene required a rather long reaction time of about 70 h, and purification by column chromatography proved challenging. Nevertheless, the desired product could be obtained in sufficient purity and an acceptable yield after recrystallization from pentane. The overall yield was 73%. Complexation of AQ-xy-bpy with $\text{Re}(\text{CO})_5\text{Cl}$ in refluxing toluene and subsequent exchange of the chloro ligand with triflate gave the AQ-Re-OTf precursor. This was then used in a complexation reaction with py-xy-OTA to yield AQ-Re-OTA. The strategy for preparation of py-xy-OTA as well as the final synthetic step to yield AQ-Re-OTA are depicted in Scheme III.9.



Scheme III.9 Reaction pathway to AQ-Re-OTA: **a)** Na₂CO₃, Pd(PPh₃)₄, toluene/EtOH/H₂O, reflux, 1.5 d; **b)** ICl, DCM/MeCN, 0 °C/RT, over night; **c)** KO^tBu, Pd(dba)₂, (HP^tBu₃)BF₄, toluene, 100 °C, 2.5 d; **d)** MeOH/CHCl₃, reflux, 43 h.

For the synthesis of the py-xy-OTA ligand the first two steps were performed in analogy to AQ-xy-I. SUZUKI coupling of 4-bromopyridine hydrochloride with TMS-xy-B(OH)₂ followed by TMS to iodine exchange by means of ICl gave py-xy-I. In a subsequent Pd-catalyzed BUCHWALD-HARTWIG coupling with OTA the final ligand was obtained in an overall yield of 90%. AQ-Re-OTA was then synthesized by complexation of the AQ-Re-OTf precursor and py-xy-OTA. After column chromatographic purification and recrystallization from Et₂O the desired complex was received as the triflate salt. Prior to performing electrochemical and spectroscopic measurements the complex was fully characterized by ¹H NMR, HRMS, and elemental analysis.

III.2.2 Spectroscopical Characterization of the Triad

The FT-IR spectra of AQ-Re-OTA (blue trace) and Re-ref (black trace) are both displayed in Figure III.17 for direct comparison. As already observed for the rhenium triads in Subsection III.1 the most prominent features around 2000 cm^{-1} are attributed to totally symmetric and asymmetric stretching vibrations of the three carbonyl ligands.¹⁰³ The additional band at 1670 cm^{-1} , as a typical frequency for quinone vibrations, is most likely due to a stretching of the anthraquinone-related carbonyls. Furthermore, it is neither visible in the infrared spectrum of Re-ref nor in the ones of Re₂-OTA or Re₂-TAA.

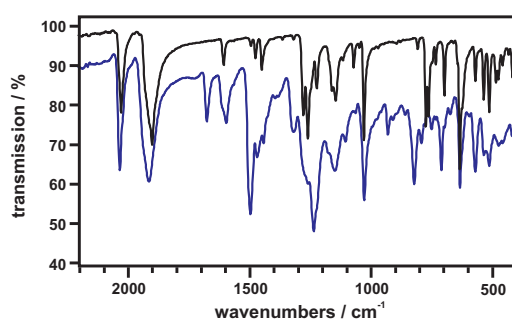


Figure III.17 Near infrared spectra of Re-ref (black) and the new triad AQ-Re-OTA (blue).

The fingerprint region of AQ-Re-OTA between 400 and 1400 cm^{-1} shows great resemblance to Re₂-OTA and Re₂-TAA since it contains the same functional groups such as N-heterocycles, methoxy groups, and arylamines. An increase in absorbance is also observed in the optical absorption spectrum of a 10^{-5} M MeCN solution of AQ-Re-OTA. Compared to Re-ref and Re₂-OTA, it exhibits distinctly stronger absorption, possibly due to its more extended π -system. At 355 nm the extinction coefficient of $49500\text{ M}^{-1}\text{ cm}^{-1}$ is relatively large.

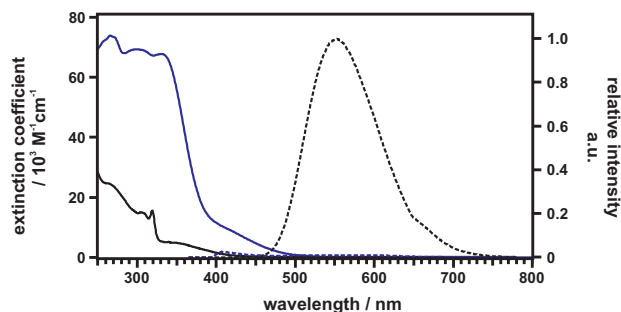


Figure III.18 Optical absorption (left) and steady-state emission spectrum (right) of 10^{-5} M MeCN solutions of AQ-Re-OTA (blue) and Re-ref (black). The emission spectra were recorded after excitation of the de-oxygenated complexes at 355 nm .

The left part of Figure III.18 shows that the absorption of AQ-Re-OTA increases rapidly below 400 nm. The $^1\text{MLCT}$ transition around 360 nm is not discernible anymore, but a shoulder at 425 nm probably attributable to intramolecular charge-transfer between the attached electron-donating substituents and the carbonyls on AQ is visible.¹²² The band structure between 250 and 330 nm seen here is a superposition of $\pi - \pi^*$ -transitions of the rhenium photosensitizer, OTA, and the newly introduced AQ acceptor.^{80,86,122}

As in $\text{Re}_2\text{-OTA}$, the MLCT emission is completely quenched in AQ-Re-OTA. Based on the results obtained from $\text{Re}_2\text{-OTA}$ it is therefore likely that photoinduced electron transfer is taking place in AQ-Re-OTA. With a triplet energy of 2.72 eV for AQ,¹²³ energy transfer from the excited rhenium ($E_T = 2.82$ eV) to anthraquinone would be exergonic by 0.1 eV, however, we reasoned that the very exergonic and therefore presumably very fast oxidation of OTA will be the dominating process and allow for the desired photoproducts to be built. Conclusive evidence for photoinduced ET will be presented below.

III.2.3 Electrochemical Study of AQ-Re-OTA and Establishment of the Energy-Level Diagram

Concerning the electrochemical properties of AQ-Re-OTA a similar behavior as for $\text{Re}_2\text{-OTA}$ was expected. Figure III.19 shows the recorded cyclic voltammograms of a 1 mM solution of the triad in MeCN. 0.1 M TBAPF_6 was again used as the supporting electrolyte and Me_{10}Fc as internal standard, and Re-ref (black trace) is also shown to facilitate comparison of redox potentials. In this case, as for $\text{Re}_2\text{-TAA}$ and Re-ref, separate recording of oxidation and reduction provided superior results.

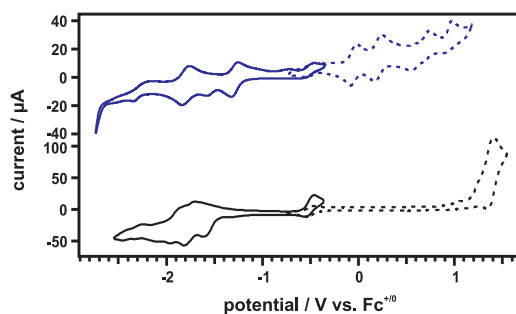
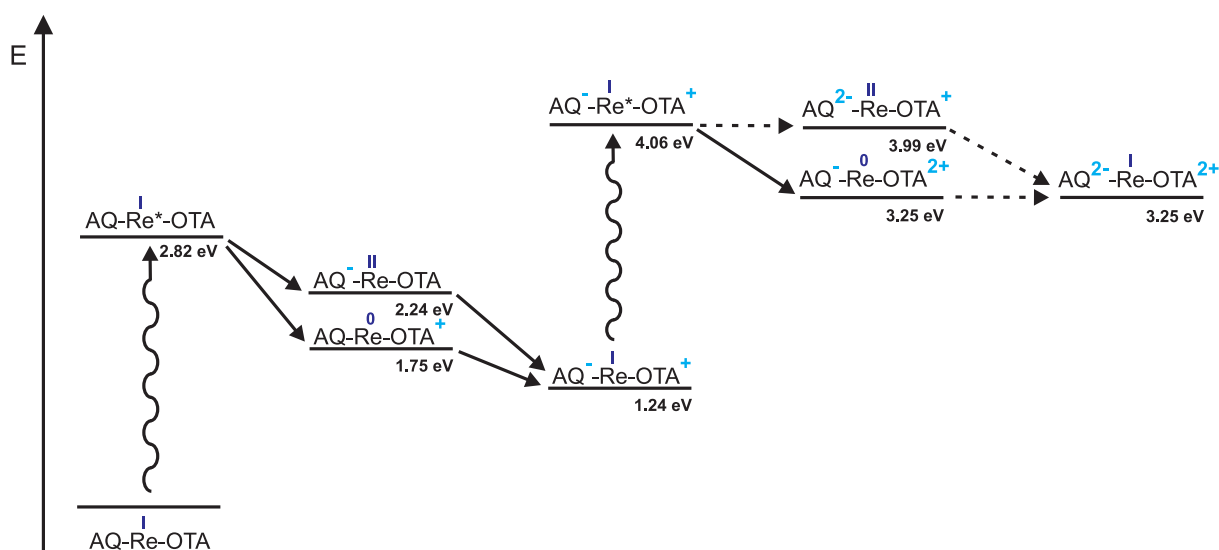


Figure III.19 Cyclic voltammogram of AQ-Re-OTA (blue) as a 1 mM solution in MeCN. The waves at -0.5 V correspond to the internal reference Me_{10}Fc . Re-ref (black) is depicted for direct comparison.

The values of 0.95 V for the rhenium oxidation and -1.8 V for the bpy reduction closely resemble those obtained in the $\text{Re}_2\text{-OTA}$ triad. Here, the metal center is oxi-

dized easier than in the Re-ref complex for the same reason as discussed in Subsection III.1.5, namely the covalent attachment of the very electron rich OTA donor. Oxidation of the OTA donor occurs at equally low potentials, -0.05 V for the first and 0.21 V for the second oxidation, as was found in $\text{Re}_2\text{-OTA}$ and other systems containing oligotriarylamines.^{77,96} With the attachment of the anthraquinone acceptor, two new reduction waves have to be considered. At -1.29 V vs. $\text{Fc}^{+/0}$ AQ is reduced to $\text{AQ}\cdot^-$ and the second reduction to AQ^{2-} around -1.8 V overlaps with the bpy reduction. The additional wave at -1.58 V is assumed to be due to an electrochemical decomposition product.



Scheme III.10 Energy-level diagram for the theoretical formation of $\text{AQ}^{2-}\text{-Re-OTA}^{2+}$.

The energy-level diagram depicted in Scheme III.10 clearly shows that the thermodynamical driving force for the generation of the first charge-separated state $\text{AQ}^{-}\text{-Re-OTA}^{+}$ is -1.58 eV. Considering only the ground state redox potentials extracted from the cyclic voltammogram, formation of $\text{AQ}^{2-}\text{-Re-OTA}^{2+}$ after two-photon absorption is exergonic by 0.81 eV. However, the excited rhenium photosensitizer ($^*E_{\text{ox}} = -1.87$ V vs. $\text{Fc}^{+/0}$) as well as its reduced species can not reduce AQ ($E_{2,\text{Red}} = -1.8$ V) a second time.

Former studies on the electrochemical behavior of quinones have shown that upon addition of acids or strongly hydrogen bond-donating solvents the two one-electron reduction waves for the first and second reduction of the quinone merge forming a new two-electron reduction wave at more positive potentials.^{90,93,124} This circumstance is in fact crucial for the formation of the second charge-separated state in $\text{AQ-}\text{Re-OTA}$ due to the above mentioned reasons. Addition of acid will shift the potential of the second AQ reduction to less negative values probably around -1.2 V, allowing for the rhenium photosensitizer to reduce it a second time. The expected photoproduct

hereby is then $AQH_2-Re-OTA^{2+}$.

III.2.4 Influence of Acids on the OTA Donor

Prior to transient experiments on the triad, OTA-ref was titrated with chloroacetic acid and triflic acid ($pK_a = 0.7$ in MeCN).^{125,126} Although the addition of acid is necessary to protonate AQ and enable twofold charge separation, protonation of the OTA donor is not desirable. Triarylamines in general exhibit low basicity due to their propeller-like shape. From the crystal structure in Figure III.1 it is known that OTA exhibits a similar propeller-like structure. Therefore, protonation by chloroacetic acid is not expected.

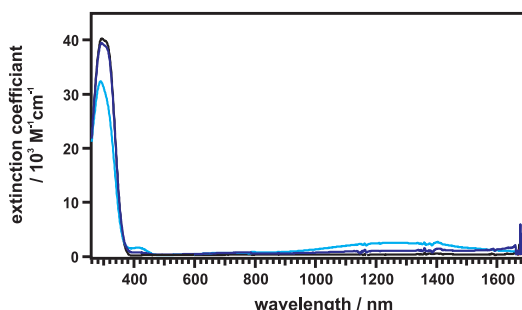


Figure III.20 UV/Vis absorption spectra of 10^{-5} M MeCN solutions of pure OTA-ref (black), after addition of an excess of chloroacetic acid (blue), and triflic acid (cyan).

However, titration of OTA-ref with the very strong acid triflic acid was performed to clarify if the oligotriarylamine could be protonated at all. Figure III.20 shows the UV-Vis spectroscopical signatures of pure OTA-ref (black), with an excess of chloroacetic acid (blue), and triflic acid (cyan), respectively. Observable from the graphs is that chloroacetic acid, later used in the transient experiments, has negligible effects on the absorption spectrum of OTA-ref. For triflic acid, on the other hand, absorption bands at 420 and 1280 nm appear. These bands, though still very weak compared to the initial OTA-ref signature, closely resemble the spectral signatures obtained by chemical oxidation of the OTA donor in AQ-Re-OTA with $Cu(ClO_4)_2$ as depicted in Figure III.21.

Chemical formation of $AQ-Re-OTA^+$ by means of $Cu(ClO_4)_2$ does not influence spectral features of the AQ acceptor so that the absorption spectrum is more or less identical to the one obtained by oxidation of Re_2-OTA . Local maxima at 426, 733, and 1300 nm are attributed to OTA^+ , whereas new absorptions arise at 590 and 1127 nm with a concomitant disappearance of the band at 426 nm when the amine is further oxidized to OTA^{2+} .

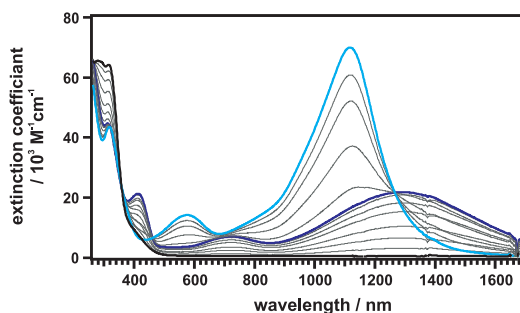


Figure III.21 Stepwise chemical oxidation of a 10^{-5} M MeCN solution of AQ-Re-OTA with $\text{Cu}(\text{ClO}_4)_2$. Blue trace = OTA^+ , cyan trace = OTA^{2+} .

Considering the non-redox active triflic acid used here, it is surprising to find features of oxidized OTA upon acid addition.¹²⁷ KANTNER *et al.*, however, found the apparent oxidation of triphenylmethane by triflic acid was rather due to elimination of one benzene followed by hydride transfer from an unreacted triphenylmethane. Therefore, making it a disproportionation not an oxidation.¹²⁸ Despite the lack of a transferable hydrogen atom in OTA-ref, the donor molecule is very electron-rich. It might undergo similar mechanisms as described above resulting in the seemingly oxidized species observable in the spectrum. However, chloroacetic acid, not triflic acid, was the strongest acid used as a proton source in the following transient experiments. This less strong acid induced no spectral changes in the preliminary test. Hence, protonation of the OTA donor by chloroacetic acid seems unlikely in MeCN.

III.2.5 Influence of Hydrogen-Bond Strength on the Photoproducts

As discussed above, reduced AQ needs to be protonated for the second charge separation to occur. Experiments were therefore conducted with de-oxygenated MeCN solutions of the pure complex, with addition of benzoic acid ($\text{pK}_a = 21.5$ in MeCN),¹²⁹ and addition of chloroacetic acid ($\text{pK}_a = 18.8$ in MeCN)¹³⁰ to explore the influence of acids of different strengths on the nature of the generated photoproducts. In principle, already benzoic acid should be able to protonate AQ^- rendering stronger acids unnecessary.⁹³

Kinetic emission measurements on the de-oxygenated MeCN solutions of AQ-Re-OTA with and without acids (Figure III.22) showed complete quenching of the initial rhenium emission, as was already seen in the steady state emission experiment. The lifetimes extracted from single exponential fits were shorter than 10 ns which is the instrumental limit. For the spectra showed in Figure III.23 excitation occurred with a 10 ns laser pulse at 355 nm and detection in a 200 ns time window (100 ns with benzoic

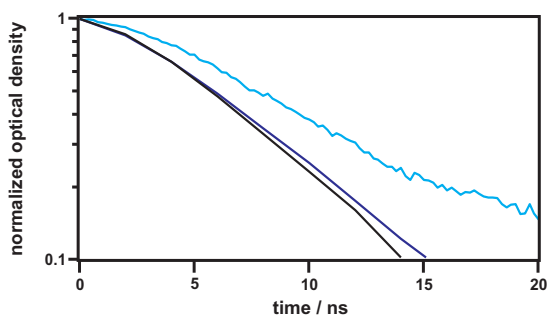


Figure III.22 Luminescence decays of 10^{-5} M MeCN solutions of pure AQ-Re-OTA (black), with 0.2 M benzoic acid (blue), and 0.2 M chloroacetic acid (cyan).

acid) directly after the pulse. For the triad in pure MeCN absorption bands at 427, 564, and 1290 nm, as well as a bleach at 330 nm can be observed. The bleach and the 564 nm absorption can be attributed to $AQ^{\cdot-}$, whereas the band at 427 nm and especially the very broad band in the NIR peaking at 1290 nm are assigned to singly oxidized OTA.^{90,93,96,113} These results are indeed expected for $AQ^{\cdot-}$ -Re-OTA⁺ in pure MeCN since the absence of a proton source or a Lewis acid should not allow for the twofold charge separation to occur.

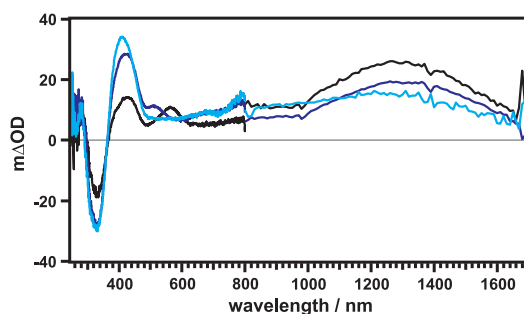


Figure III.23 Transient absorption spectra of de-oxygenated MeCN solutions of pure AQ-Re-OTA (black), with 0.2 M benzoic acid (blue), and 0.2 M chloroacetic acid (cyan) after 355 nm excitation.

In the case of added benzoic acid the bleach at 330 nm still persists. WIGHTMAN *et al.* showed that benzoic acid was able to protonate $AQ^{\cdot-}$ in DMF solution yielding the hydroquinone form of AQ (AQH_2) which exhibited spectral features at 384 and 420 nm. The same was observed by BABAEI *et al.*^{90,93} Twofold oxidation of OTA would lead to the disappearance of the band at 427 nm with a rise of absorption at 590 nm which was not observed in the blue spectrum. The band at 423 nm could have been considered a sign of hydroquinone formation and corresponding twofold oxidized OTA, was it not for the lack of the very prominent band at 1127 nm attributed to OTA^{2+} . Furthermore, the transient spectrum shows a band at 512 nm which can be assigned to AQH, the semiquinone form of AQ. In summary, it can be stated that the most likely photoproduct in presence of benzoic acid is the singly charge-separated

state stabilized by hydrogen-bonding via the acid. The transient absorption spectrum of AQ-Re-OTA with an excess of chloroacetic acid (cyan trace in Figure III.23) shows slight differences to the two previously discussed ones except for the still present bleach at 330 nm. A band at 409 nm is clearly visible which is blue-shifted by 14 nm compared to the data with benzoic acid, and there is no additional band around 500 nm anymore, yet it might be shifted further into the blue and be hidden under the band at 409 nm. Though twofold reduced and protonated AQ (AQH₂) does not exhibit spectral features beyond 420 nm, formation of twofold oxidized OTA can not be assumed due to the lack of the band at 1127 nm. It is therefore concluded that the main photoproduct in presence of chloroacetic acid is the first charge-separated state consisting of OTA⁺ and singly reduced and protonated AQ.

III.2.6 Kinetics of the Photogenerated Products

The transient spectra show three different photoproducts depending on the acid strength. The simple charge-separated state AQ⁻-Re-OTA⁺ in pure MeCN, the hydrogen-bonded AQ⁻-Re-OTA⁺ in presence of benzoic acid, and AQH-Re-OTA⁺ with an excess of chloroacetic acid. Therefore, differences in the lifetimes are expected. Earlier studies on hydrogen-bonding effects of different acids and hydrogen-bond donating solvents have shown that upon their addition, the lifetimes of the charge separated-states with quinone acceptors can increase significantly.^{88,131}

In Figure III.24 the decays of the transient absorption signals of AQ-Re-OTA in pure MeCN are depicted in the left graph. Fitting of the decays gives an average lifetime of 205 ns for the generated photoproduct AQ⁻-Re-OTA⁺. Upon addition of chloroacetic acid the lifetime of the charge-separated state (AQH-Re-OTA⁺) is indeed prolonged as can be seen on the rightmost side of Figure III.24 and single exponential fitting gives $\tau = 3.7 \mu\text{s}$.

The data obtained from AQ-Re-OTA in de-oxygenated MeCN with 0.2 M benzoic acid (Figure III.24 b), on the other hand, clearly shows biexponential decays with $\tau = 101 \text{ ns}$ and $\tau = 2.3 \mu\text{s}$. This presence of two different species, as indicated by the biexponential decays, corroborates the interpretation of the transient absorption spectrum. In presence of benzoic acid, AQ⁻-Re-OTA⁺ and its hydrogen-bonded equivalent seem to be in equilibrium. Since the lifetimes resemble that of AQ-Re-OTA in pure MeCN (205 vs 101 ns) and that observed in presence of 0.2 M chloroacetic acid (3.7 vs 2.3 μs), simultaneous appearance of photoproducts with AQ⁻ and hydrogen-bonded AQ⁻ is suggested. Considering the pK_a values for benzoic acid and chloroacetic acid, the latter is the stronger acid and therefore able to fully protonate AQ, generating only the

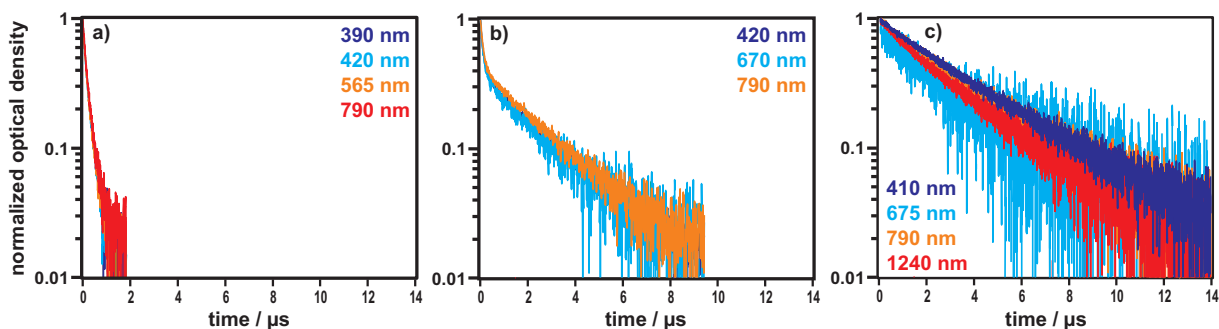


Figure III.24 Transient absorption decays of photoproducts generated after excitation with a 10 ns laser pulse at 355 nm of a de-oxygenated MeCN solution of AQ-Re-OTA (a), with 0.2 M benzoic acid (b), and 0.2 M chloroacetic acid (c).

more stable semiquinone form.

III.2.7 Dependence of the Transient Spectral Absorption on the Excitation Power

Formation of the twofold charge-separated state $AQH_2\text{-Re-OTA}^{2+}$ is again a two-photon process and therefore expected to be quadratically dependent on the laser excitation density. To test this hypothesis on AQ-Re-OTA, transient spectra of a de-oxygenated MeCN solution with 0.2 M chloroacetic acid were recorded at high (3.4 mJ) and low (1.1 mJ) excitation powers. In Figure III.25 the obtained spectra after excitation at 355 nm with 3.4 mJ (cyan) and 1.1 mJ (blue) per pulse are depicted. The difference spectrum (black) was obtained by multiplication of the cyan spectrum with a factor of 3.09 (3.4 mJ/1.1 mJ) and subtraction from the blue spectrum.

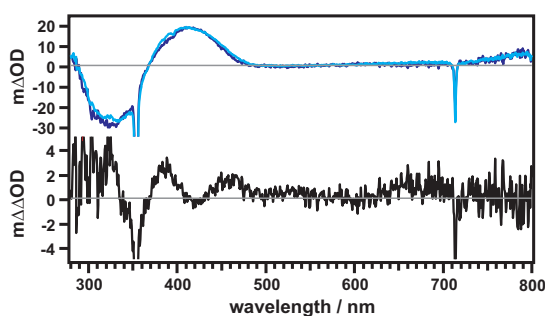


Figure III.25 Transient absorption spectra of a 10^{-5} M MeCN solution of AQ-Re-OTA with 0.2 M chloroacetic acid at 3.4 mJ (cyan trace) and 1.1 mJ (blue trace) laser power. The blue spectrum was multiplied by a factor of 3.09 and subtracted from the cyan spectrum to give the difference spectrum in black.

Generation of $AQH_2\text{-Re-OTA}^{2+}$ should lead to a rise of absorption around 600 nm

as was earlier established by chemical oxidation of the complex with $\text{Cu}(\text{ClO}_4)_2$. In addition, it should show positive absorption at 400 nm, indicative of formation of the hydroquinone form of AQ (AQH_2). Alas, no change was observed in the transient spectrum after increase of the excitation power.

III.3 Summary and Conclusions on Photoinduced Electron Transfer in Rhenium-OTA-Complexes

The preceding two sections gave an insight in our efforts on creating a wholly molecular, nanoparticle-free donor-acceptor system with rhenium polypyridyl complexes as the photosensitizers. Two new triads, Re_2 -OTA and AQ-Re-OTA were synthesized, characterized, and studied in terms of their ability to undergo twofold charge separation. The main advantage of Re_2 -OTA is the presence of two rhenium photosensitizers. This should allow for the simultaneous absorption of two photons within one single laser pulse, provided the excitation laser power is high enough. In AQ-Re-OTA, though having only one photosensitizer, it is possible to separate the charges over a longer distance. This should increase the lifetime of the first charge-separated state and the possibility of a second excitation before charge recombination occurs. It is known from earlier studies that the formation of the first charge-separated state in a similar AQ-Ru-TAA triad occurs within ≈ 200 ps.¹³² Since OTA has proven to be an even better electron donor, formation of $\text{AQ}^-\text{Re-OTA}^+$ is expected to lie in the same time range or it could be even faster. It was therefore concluded that twofold charge separation should be possible with relatively long (10 ns) and sufficiently strong (>3 mJ) pulses.

Kinetic absorption experiments on Re_2 -OTA and AQ-Re-OTA indeed showed instant formation of the photoproducts within the duration of the laser pulse (10 ns). In contrast to AQ-Re-OTA with a lifetime of 205 ns for the singly charge-separated state, $\text{Re}_2\text{-OTA}^+$ decays to its ground state in 36 ns. A conjectural value for the close proximity of the OTA donor and rhenium acceptors. Furthermore, AQ-Re-OTA undergoes PCET in presence of acids which increased the lifetime of the generated AQH-Re-OTA^+ to 3.7 μs . In addition, transient absorption spectra of pure Re_2 -OTA and AQ-Re-OTA with chloroacetic acid were recorded at different laser excitation powers since the formation of the twofold charge-separated state, being a two-photon process, should exhibit quadratic dependence on the excitation intensity. Alas, even at the highest possible laser power there were no spectral features observable that could be unambiguously attributed to formation of AQH_2 or OTA^{2+} . Higher powers than ≈ 4 mJ led to decomposition of the sample solutions, especially in presence of acids.

A major challenge of creating a molecular system capable of twofold charge separation is to minimize the multitude of possible unwanted deactivation pathways that are open to the second charge-separated state enabling its fast decay. In the investigated complexes the lifetime of the second charge-separated state, compared to the first, might be very short and its population very small, if it is generated at all. These circumstances make its detection difficult.

The major problem from a spectroscopic point of view was probably the choice of rhenium polypyridyl complexes as photosensitizers. Though synthetically more easily accessible than their ruthenium analogs, because ligand synthesis could be split in a pyridine and a bipyridine-part, they are prone to carbonyl ligand-loss. Furthermore, the short excitation wavelength (355 nm) required to excite the photosensitizers will also result, at least partly, in the excitation of AQ and OTA which both show significant absorption at this wavelength. In addition, once OTA^+ is generated as a photoproduct, a second pulse will excite the oxidized OTA since it also exhibits absorption around 355 nm. These circumstances might interfere with the formation of the second charge-separated state.

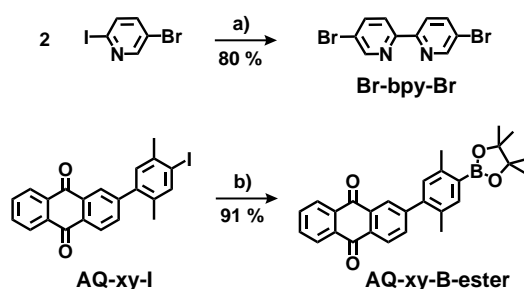
Lastly, the most sobering insight we gained from the experiments on the rhenium triads was that with around 4 mJ the excitation density was simply not high enough to initiate twofold charge separation. A 355 nm laser pulse of 4 mJ provides $7 \cdot 10^{15}$ photons and only one third of the molecules of a 10 μM solution in the cuvette can be excited by the pulse, i.e. $6 \cdot 10^{15}$ molecules. As a result, a 4 mJ laser pulse provides roughly one photon per molecule which hampers the possibility of generating a twofold charge-separated state in our rhenium complexes.

III.4 Photoinduced Electron Transfer in an AQ–Ru–OTA Triad

The following section will focus on our efforts to achieve accumulative electron transfer in an AQ–Ru–OTA triad. Being the ruthenium analog of the rhenium triad discussed in III.2 we hope to eradicate some flaws encountered in the rhenium complex. First, the ruthenium MLCT band should not be superimposed by absorptions from OTA and AQ, allowing for the exclusive excitation of the ruthenium sensitizer. Second, the laser setup for excitation at 532 nm should allow us to measure with higher intensities gaining a higher photon flux, hopefully resulting in two-photon absorption. In addition to the laser experiments, continuous irradiation experiments were performed monitoring the charge separation behavior over a longer time period.

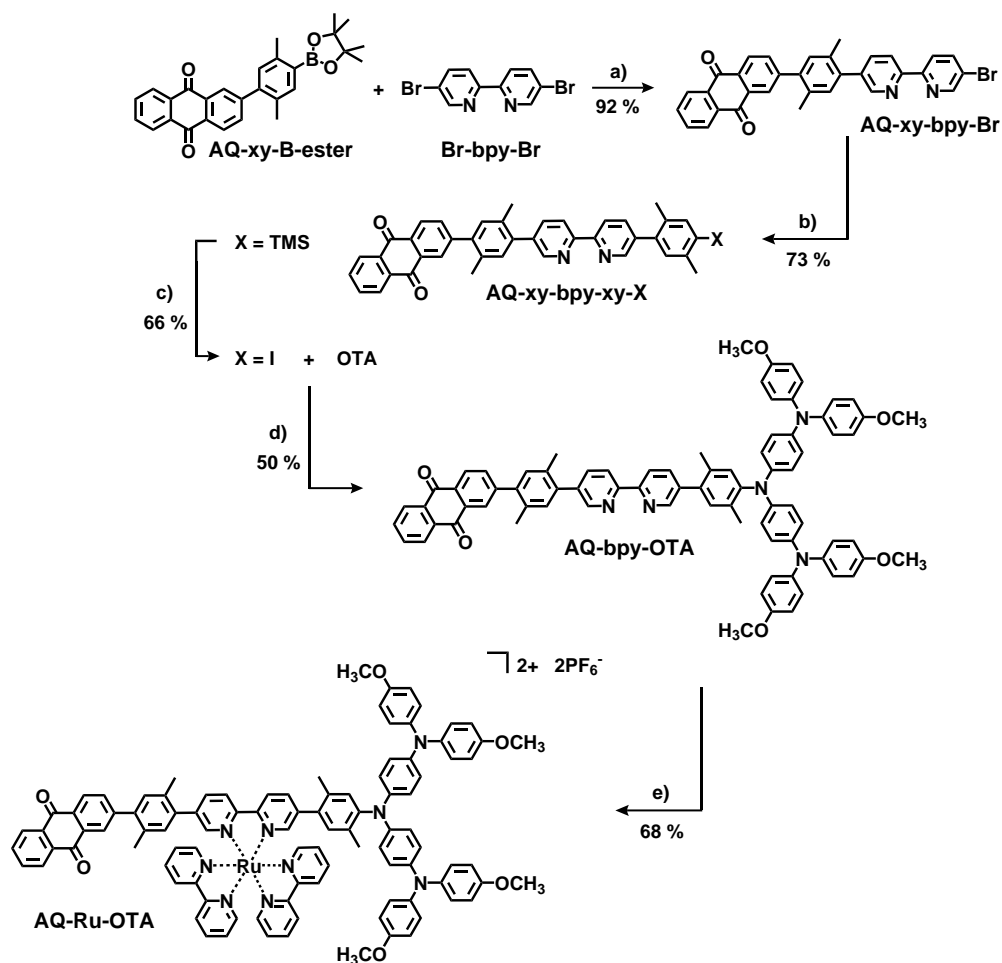
III.4.1 Synthesis of the AQ–Ru–OTA Triad and a Reference Dyad

In order to prepare the triad yet another bpy derivative, Br–bpy–Br, was synthesized as depicted in Scheme III.11 by adopting a previously published protocol.¹²⁰ Br–bpy–Br was hereby obtained via *Stille*-coupling in 80% yield as a beige solid. The AQ acceptor was attached to Br–bpy–Br via a xylene bridging unit. For that, AQ–xy–I was reacted in a *SUZUKI*-coupling with bis-pinacolato diboron to yield AQ–xy–B-ester.



Scheme III.11 Synthesis of Br–bpy–Br (top): **a)** hexa-*n*-butylditin, Pd(PPh₃)₄, *m*-xylene, 180 °C, 3 d; Synthesis of AQ–xy–B-ester (bottom): **b)** bis-pinacolato diboron, KOAc, PdCl₂(PPh₃)₂, DMF, 100 °C, 24 h.

As depicted in Scheme III.12, AQ–xy–B-ester was then coupled Pd-catalyzed to Br–bpy–Br. The resulting product AQ–xy–bpy–Br precipitated from the hot reaction mixture due to its very low solubility and was directly filtered and washed with MeOH. After column chromatography on silica with an eluent mixture of DCM and 1% NEt₃, pure AQ–xy–bpy–Br was obtained as a yellow solid in 92% yield.



Scheme III.12 Synthesis of the AQ-Ru-OTA triad: **a)** Na_2CO_3 , $\text{Pd}(\text{PPh}_3)_4$, THF/ H_2O , reflux, over night; **b)** TMS-xy-B(OH)₂, Na_2CO_3 , $\text{Pd}(\text{PPh}_3)_4$, toluene/EtOH/ H_2O , reflux, 2 d; **c)** ICl, DCM/MeCN, 0 °C/RT, over night; **d)** NaO^tBu , $\text{Pd}(\text{dba})_2$, $(\text{HP}^t\text{Bu}_3)\text{BF}_4$, toluene, reflux, 27 h; **e)** $\text{Ru}(\text{bpy})_2\text{Cl}_2$, $\text{CHCl}_3/\text{EtOH}$, reflux, 2 d.

To elongate the D-A distance further, another xylene bridge was introduced via Pd-catalyzed Suzuki-coupling of TMS-xy-B(OH)₂ to AQ-xy-bpy-Br. Subsequent TMS exchange by I gave AQ-xy-bpy-xy-I in 66% yield as a yellow solid. This was then coupled to OTA to give the ligand AQ-bpy-OTA as a brown solid in 50% yield after column chromatographical purification and recrystallization from hexane. Synthesis of the final complex AQ-Ru-OTA was achieved by refluxing the ligand AQ-bpy-OTA and Ru-pre in a de-oxygenated $\text{CHCl}_3/\text{EtOH}$ mixture for 2 d. The complex was then purified by column chromatography with an eluent mixture of acetone/ H_2O /sat. KNO_3 solution (90:10:1). After concentration of the product fraction, the final complex was precipitated as the PF_6^- salt by dropwise addition of a saturated KPF_6 -solution. Filtration, washing with water, and drying yielded the complex as a dark brown solid in 68%. The overall yield for the AQ-Ru-OTA

complex as described here was 15%.

The ruthenium precursor $\text{Ru}(\text{bpy})_2\text{Cl}_2$ (Ru-pre) needed for the preparation of the desired complex AQ-Ru-OTA was synthesized by refluxing $\text{RuCl}_3 \cdot 3\text{H}_2\text{O}$ with 2 eq. 2,2'-bipyridine, and lithium chloride under nitrogen atmosphere. The resulting product was precipitated from the cool reaction mixture by dropwise addition of acetone. Filtration and excessive washing with acetone, H_2O , and Et_2O gave Ru-pre as a dark violet solid.

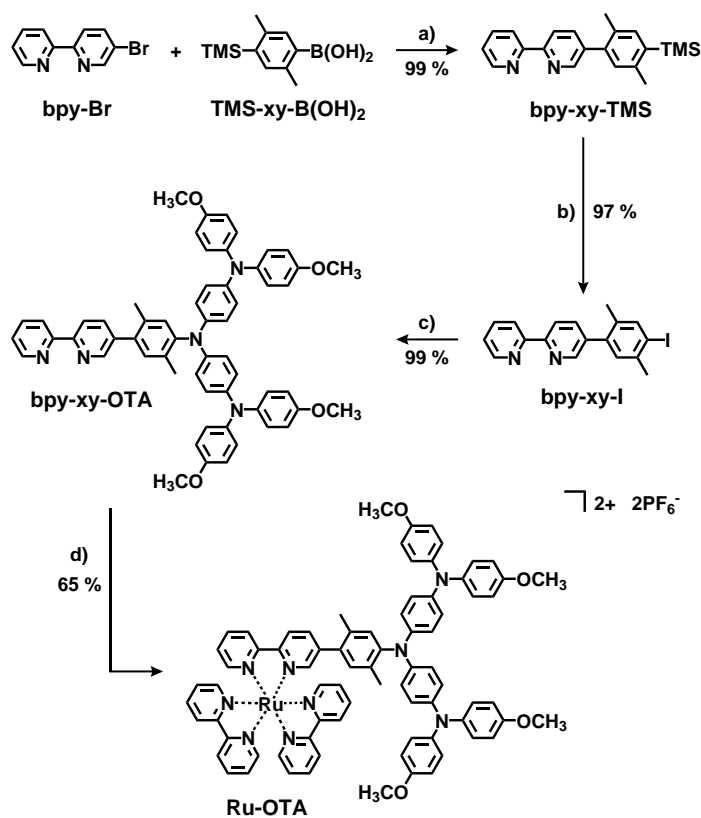


Figure III.26 Synthetic route for preparation of Ru-OTA: **a)** Na_2CO_3 , $\text{Pd}(\text{PPh}_3)_4$, $\text{H}_2\text{O}/\text{EtOH}/\text{toluene}$, 90°C , over night; **b)** ICl , DCM , $0^\circ\text{C}/\text{RT}$, over night; **c)** NaO^tBu , $\text{Pd}(\text{dba})_2$, $(\text{HP}^t\text{Bu}_3)\text{BF}_4$, toluene, 110°C , 24 h; **e)** $\text{Ru}(\text{bpy})_2\text{Cl}_2$, $\text{CHCl}_3/\text{EtOH}$, reflux, 21 h.

In order to evaluate the influence and relevance of the AQ acceptor in continuous irradiation experiments a reference complex was synthesized. In this Ru-OTA dyad the AQ unit was simply omitted. Figure III.26 depicts the synthetic route followed for its preparation. Starting point hereby was Br-bpy which was reacted in a Pd-catalyzed Suzuki-coupling with TMS-xy-B(OH)₂ to give bpy-xy-TMS in essentially quantitative yield. Deprotection of bpy-xy-TMS by addition of ICl gave bpy-xy-I which was then coupled to OTA. This gave the final ligand bpy-xy-OTA as a brown solid in 99% yield. Complexation of bpy-xy-OTA with Ru-pre gave the reference

dyad Ru–OTA with an overall yield of 62% following the route outlined above. As another reference complex $[\text{Ru}(\text{bpy})_3](\text{PF}_6)_2$ was used. This is a standard reference which had been prepared in our group in sufficient amounts and was used in this work as received. It will further be denoted Ru–ref.

III.4.2 Optical Spectroscopic and Electrochemical Characterization

Absorption spectra of Ru–ref, Ru–OTA and AQ–Ru–OTA (Figure III.27) show an intense band assigned to a ligand-centered $\pi \rightarrow \pi^*$ transition at 287 nm as well as a broad band around 450 nm for the $^1\text{MLCT}$ ($d\pi(\text{Ru}) \rightarrow \pi^*(\text{bpy})$) transition.³⁶ The intense shoulder at 340 nm in Ru–OTA (cyan trace in Figure III.27) is attributed to an OTA absorption band since it is not present in Ru–ref. The AQ–Ru–OTA triad shows an additional plateau at 320 nm which is not visible in the dyad and can thus be interpreted to be an absorption of the AQ acceptor.^{36,86,122}

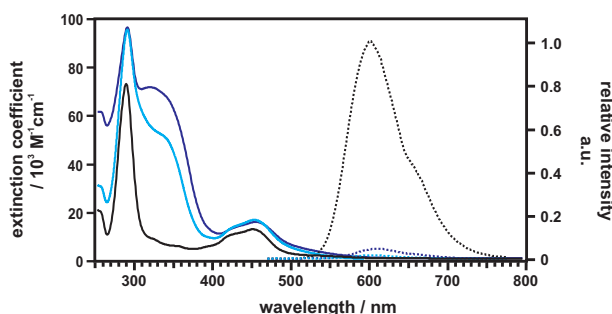


Figure III.27 UV-Vis absorption (solid line) and steady state emission spectra (dashed line) of the triad (blue), dyad (cyan), and Ru–ref (black). 10^{-5}M MeCN solutions were used for the absorption measurements. Steady state emission was measured of de-oxygenated MeCN solutions, the spectra were corrected for differences in the absorption at 450 nm, and normalized to the Ru–ref emission.

As can be observed on the right side of Figure III.27 the excited state emission of the ruthenium photosensitizer in the triad is quenched by 96%. In the dyad the original luminescence is quenched by 98%. This strong quenching of the photosensitizer MLCT luminescence is indicating a non-radiative deactivation process. In the triad it is most likely electron transfer from the OTA donor to the AQ acceptor via the ruthenium sensitizer. In the dyad the electron will be transferred from OTA to the ruthenium photosensitizer which acts as the electron acceptor in this case. Furthermore, the emission maximum is red-shifted from 603 nm in Ru–ref to 612 nm in the triad. In the dyad on the other hand, the emission maximum is again at 603 nm.

In order to evaluate the thermodynamic possibility for electron transfer, the redox

potentials of the synthesized complexes were determined via cyclic voltammetry. Figure III.28 depicts the voltammograms of Ru-ref (top, black), Ru-OTA (middle, blue), and AQ-Ru-OTA (bottom, cyan) measured in Ar-purged MeCN solutions. The scan rate was 0.1 V/s and 0.1 M TBAF₆ was used as supporting electrolyte. The waves marked by asterisks correspond to the added internal reference. Fc^{+ / 0} was used for Ru-ref, whereas AQ-Ru-OTA was measured in presence of Me₁₀Fc. The sharp peak at -2 V in the cyan trace might be due to unwanted reaction at the electrode, however it does not interfere with the assignment of the redox potentials in the triad.

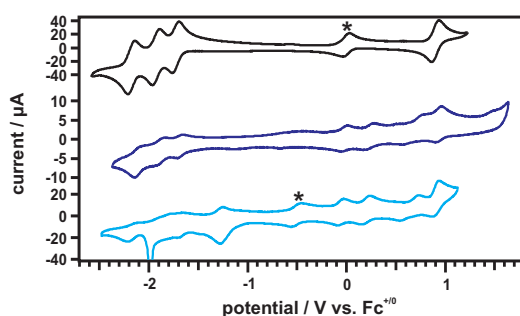


Figure III.28 Cyclic voltammograms of Ru-ref (black), Ru-OTA (blue) and AQ-Ru-OTA (cyan) in MeCN. The waves marked by asterisks correspond to the internal references Fc^{+ / 0} for Ru-ref and Me₁₀Fc for the triad.

The redox potentials were extracted from the data in Figure III.28 and summarized in Table III.3. Directly observable is the conformity of the potentials for the ruthenium oxidation and bpy reductions in Ru-ref, Ru-OTA, and AQ-Ru-OTA. In the case of the studied ruthenium complexes, the photosensitizer-based oxidation potentials are not influenced by the attached electron rich amine. In contrast to AQ-Re-OTA, where the donor and acceptor ligands are two separate units, here the amine donor is part of a rigid ligand, also containing the AQ acceptor. The study of a very similar complex previously synthesized in our group, AQ-Ru-TAA, also showed a lack of shift for the ruthenium redox potentials.¹¹³

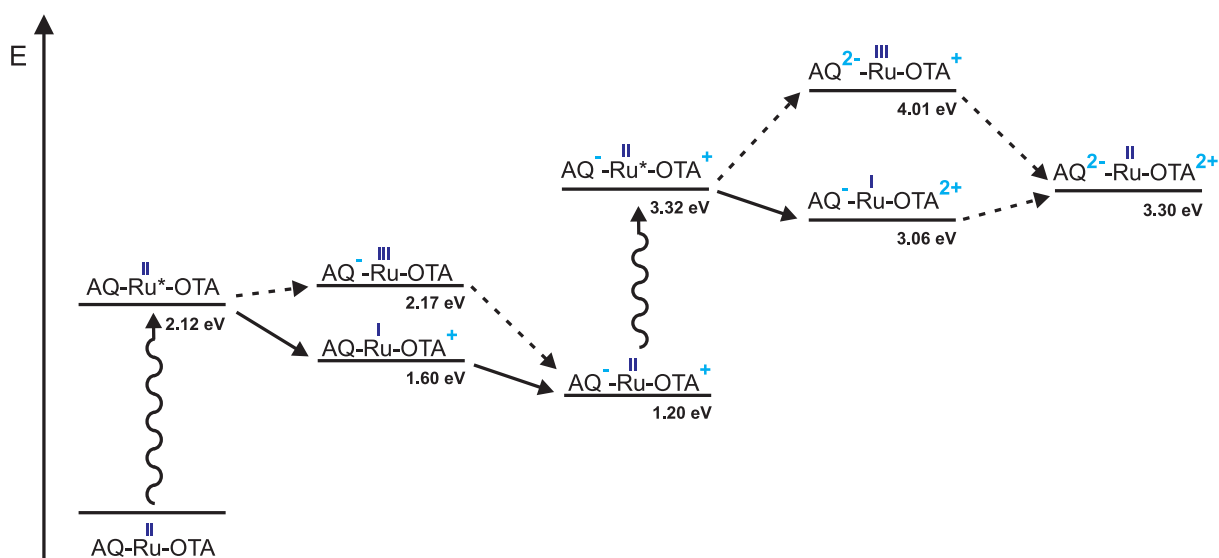
The oxidation potentials for the stepwise oxidation of OTA to OTA³⁺ are in good agreement with the literature values found for OTA-containing organic molecules or transition metal complexes.^{77,96} Considering the first two reversible oxidations for OTA at -0.06 V and 0.20 V, these very low potentials should facilitate the generation of the second charge-separated state of AQ-Ru-OTA. Reduction of AQ occurs at -1.26 V vs. Fc^{+ / 0} in good agreement with literature, which gives the first reduction of AQ at -1.20 V vs. Fc^{+ / 0} in DMF.⁹⁰ The second reduction to form AQ²⁻ usually takes place at a potential of -1.9 V. This, however, can not be observed in AQ-Ru-OTA, possibly due to superposition with the bpy reductions.

With the help of the cyclic voltammetry data, an energy level diagram (Figure III.29)

Table III.3 Redox potentials in Ar-purged MeCN solutions. All values are given in V vs. $\text{Fc}^{+/0}$.

redox couple	Ru-ref / V	Ru-OTA / V	AQ-Ru-OTA / V
$\text{Ru}^{3+/2+}$	0.90	0.94	0.91
$\text{bpy}^{0/-}$	-1.72	-1.68	-1.66
$\text{bpy}^{0/-}$	-1.92	-1.88	-1.92
$\text{bpy}^{0/-}$	-2.17	-2.11	-2.16
$\text{OTA}^{+/0}$		-0.02	-0.06
$\text{OTA}^{2+/+}$		0.24	0.20
$\text{OTA}^{3+/2+}$		0.68	0.64
$\text{AQ}^{0/-}$			-1.26

depicting all possible electron transfer steps for the formation of the desired photo-product $\text{AQ}^{2-}\text{-Ru-OTA}^{2+}$ can be constructed.


Figure III.29 Energy level diagram for AQ-Ru-OTA.

Formation of the first charge separated state $\text{AQ}^-\text{-Ru-OTA}^+$ is exergonic by 0.92 eV. As for $\text{AQ}^{2-}\text{-Ru-OTA}^{2+}$, ΔG_{ET} for the second charge separation after absorption of a second photon is close to zero. The reduced ruthenium photosensitizer ($E_{\text{red}} = -1.66$ V) will not be able to reduce AQ ($E_{\text{red}} = -1.9$ V) a second time. Therefore, the addition of BRØNSTED or LEWIS acids is necessary. In their presence, the second reduction potential will be shifted to less negative values, thus, in principle enabling a second charge transfer.^{90,93}

III.4.3 Kinetic Emission Behavior

Studies on the kinetic behavior of the dyad and triad were performed on de-oxygenated MeCN solutions. As a reference, Ru-ref was investigated as well. In absence of oxygen, Ru-ref has an emission lifetime of 834 ns in solution.

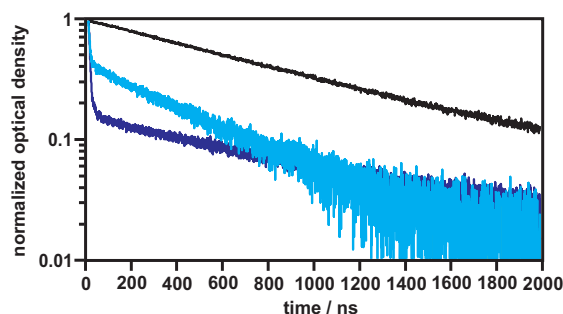


Figure III.30 Normalized emission decays of Ru-ref (black), Ru-OTA (blue), and AQ-Ru-OTA (cyan). The decays were recorded on 10^{-5} M de-oxygenated MeCN solutions.

In agreement with the steady state emission behavior, the lifetime of the ruthenium luminescence is completely quenched ($\tau < 10$ ns). The double exponential decay in Ru-OTA can be explained by highly luminescent trace impurities of $[\text{Ru}(\text{bpy})_3](\text{PF}_6)_2$ (Ru-ref); the lifetime of the longer-living species ($\tau = 899$ ns) is very similar to the one of free Ru-ref. Also AQ-Ru-OTA gives a double exponential luminescence decay, indicating the presence of two luminescent species. However, the longer luminescent species with $\tau = 495$ ns is probably not free $[\text{Ru}(\text{bpy})_3](\text{PF}_6)_2$, but another highly luminescent impurity not observable in the product characterization.

Conclusive evidence for electron transfer in the studied ruthenium complexes will be given below.

III.4.4 Chemical Oxidation of OTA

In order to facilitate assignment of the bands corresponding to oxidized species of OTA in the following transient laser experiments, chemical oxidation of OTA was performed. AQ-Ru-OTA, as a 10^{-5} M solution in MeCN, was oxidized with incremental amounts of $\text{Cu}(\text{ClO}_4)_2$. Successive oxidation gave the blue spectrum in Figure III.31 for OTA^+ after the addition of 1 eq Cu^{2+} and the cyan spectrum for OTA^{2+} after 2 eq. The spectra were recorded as difference spectra. Thereby, directly subtracting the ground state absorption features of the complex and allowing for direct comparison with the transient absorption spectra. Furthermore, the spectra show two isosbestic points at 478 and 1285 nm. At those wavelengths, OTA^+ and OTA^{2+} show identical

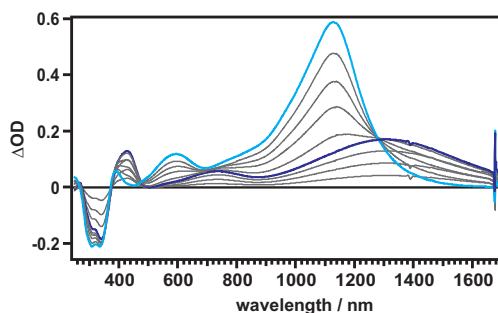


Figure III.31 Difference spectra for the chemical oxidation of OTA to OTA^+ (blue) and OTA^{2+} (cyan) obtained by addition of incremental amounts of $\text{Cu}(\text{ClO}_4)_2$.

absorbances which will later help with the normalization of the transient absorption spectra.

III.4.5 Time-Resolved Absorption Studies on the Ru–OTA Dyad

Pure MeCN Solution

Before the investigation of the AQ–Ru–OTA triad, the photoinduced electron transfer behavior of the reference dyad was studied. In Ru–OTA, photoinduced accumulation of two holes on the OTA donor moiety should not occur in pure MeCN solution. OTA would be able to carry two holes upon successive oxidation. The photosensitizer, however, cannot accommodate two electrons. In Figure III.32 the expected transient absorption spectrum of the dyad in a 10^{-5}M solution in de-oxygenated MeCN is depicted. The sharp spike at 532 nm is due to scattered light from the laser beam.

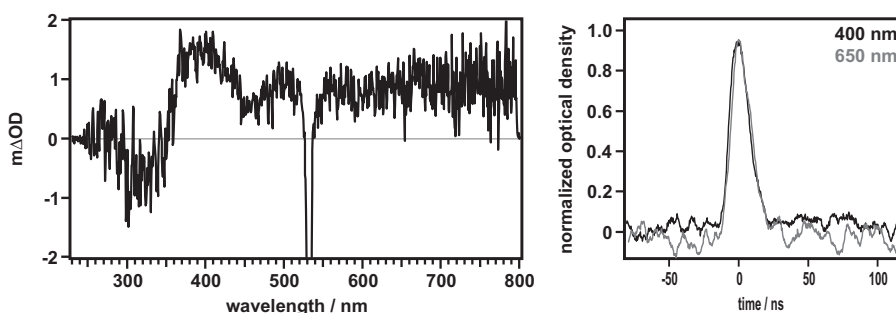


Figure III.32 Transient absorption spectrum (left) and corresponding transient absorption kinetics (right) of the Ru–OTA dyad in a de-oxygenated 10^{-5}M MeCN solution.

The band at 400 nm indicates the presence of OTA^+ . Together with the plateau-like signature starting at 600 nm on to lower energies, also observed for $(\text{Re}^+)(\text{Re}^0)\text{-OTA}^+$, this points towards $\text{Ru}^+\text{-OTA}^+$ as the main photoproduct. Due to the rather low signal-to-noise ratio, measurement in the NIR region was not possible. Kinetic ab-

sorption measurements at 400 nm and 650 nm showed that Ru^+-OTA^+ has a lifetime of only 10 ns, which is the detection limit of the nanosecond setup. Due to the close proximity of the OTA electron donor and the ruthenium photosensitizer, acting as the electron acceptor, this very short lifetime of the first charge-separated state is not surprising.

Flash Quenching with TCNB and Intensity Dependence

In order to achieve a longer living charge-separated state and possibly hole accumulation in the dyad a suitable electron acceptor needs to be present. The ruthenium polypyridyl photosensitizer cannot accept two electrons and the sole charge accumulating site in this system is OTA. One important prerequisite for successful hole accumulation in this system is a long enough lifetime of Ru^+-OTA^+ to allow for the absorption of a second photon within the 10 ns laser pulse. In an intermolecular electron transfer experiment between TCNB and the dyad, the back electron transfer would be diffusion controlled. Therefore, provision of an additional electron acceptor, such as TCNB, should lead to the necessary prolongation of the first separated state lifetime. The basic principle of an oxidative flash quenching experiment was already introduced in Section III.1.10 and will not be discussed here again. TCNB was mainly chosen as a quencher, due to the lack of strong absorption of its reduced species in the spectral region beyond 460 nm. This allows for unperturbed investigation of the expected bands for twofold oxidized OTA at 600 nm and especially in the NIR region. The traces depicted on the left of Figure III.33 correspond to the transient absorption spectra of $\text{Ru}-\text{OTA}$ in presence of an excess of TCNB. Excitation occurred at 532 nm with a nanosecond pump-probe setup. Hereby, the blue spectrum was recorded at a low excitation power of 10 mJ, whereas the cyan one was recorded at a laser power of 75 mJ. Both spectra show similar absorption features.

The rather strong absorption from 378 to 459 nm is indicative of $\text{TCNB}^{\bullet-}$ formation.¹¹⁶ Furthermore, the transient spectrum reveals a broad band stretching over the whole NIR region with a local maximum at 1300 nm. This feature can be attributed to singly oxidized OTA, usually also exhibiting a band at 430 nm which is superimposed by the $\text{TCNB}^{\bullet-}$ band in the present case. Between 500 and 800 nm a more or less steady rise of the absorption is observed. However, no clear bands can be distinguished. In general, no distinct differences between the low- and high-power transient spectrum are observable, apart from the difference in intensity. As a result, the most likely photoproduct in the present flash-quench experiment is $\text{Ru}-\text{OTA}^+$. On the right side of Figure III.33 the decays of the absorption signals at 378, 459, and 795 nm are depicted. The first two correspond to signals of reduced TCNB and the one at 795 nm

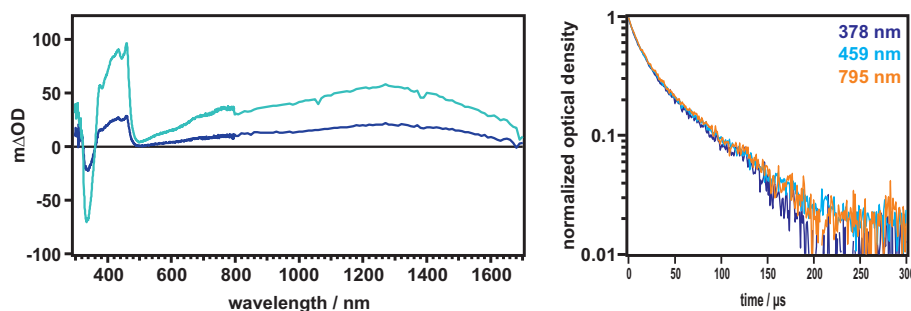


Figure III.33 Left: Power-dependent transient absorption spectra of Ru-OTA in presence of an excess of TCNB after excitation at 532 nm. Blue: 10 mJ; cyan: 75 mJ. Right: Decays of the transient absorption signals at 378 (blue), 459 (cyan), and 795 nm (orange). All spectra were recorded on de-oxygenated MeCN solutions.

is assigned to OTA^+ , as discussed above. As a result, the signals should exhibit the same lifetime. Fitting of the decays gives two different lifetimes, 13 μs and 67 μs . The need for double-exponential fitting can be explained by the presence of trace amounts of free $[\text{Ru}(\text{bpy})_3](\text{PF}_6)_2$ which also undergoes flash-quenching with TCNB. Therefore, the short-living species is assigned to Ru-OTA^+ , whereas the longer-living species is associated with $[\text{Ru}(\text{bpy})_3]^{3+}$ which has a lifetime of 64 μs in flash-quenching experiments with TCNB.

In order to determine, if hole accumulation on the OTA unit can indeed be excluded the difference spectrum between the high and the low-energy spectrum is constructed. Prior to performing the subtraction, the spectra have to be normalized to a point at which they show the same photo-generated species. In the present case, the $\text{TCNB}^{\cdot-}$ band at 459 nm in the visible region of the transient spectrum was used for this purpose. Due to absorption of both OTA^+ and OTA^{2+} over the whole spectral range, the NIR region was normalized to the isosbestic point (1285 nm) between the two differently oxidized amine species. Multiplication of the low-energy spectrum by 7.5 (quotient of 75 mJ and 10 mJ) produced a modified low-energy spectrum with a higher overall optical density than the spectrum at 75 mJ exhibited. This behavior is most likely due to saturation effects at such high energies.

The sharp band at 1064 nm is due to scattered light from the laser beam which comes to effect because of the poor overall signal-to-noise ratio in the difference spectrum. However, three distinct bands at 380, 555, and 1050 nm can be observed in the difference spectrum. Compared to the difference spectra as obtained by chemical oxidation of OTA to OTA^+ (grey trace in Figure III.34) and OTA^{2+} (black trace in Figure III.34), the transient spectrum shows similarities. The orange spectrum does show increased absorption between 500 and 600 nm which might indicate the presence of twofold oxidized OTA. This assumption would be supported by the band peaking at ≈ 1060 -

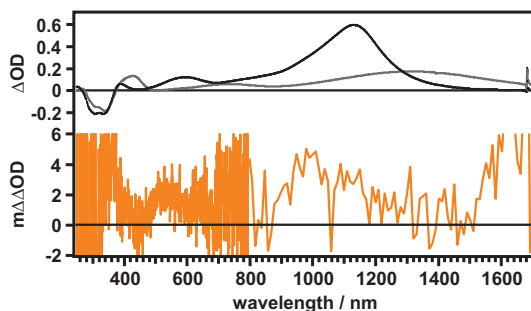


Figure III.34 Top: Difference Spectra of OTA^+ (grey trace) and OTA^{2+} (black trace) obtained by chemical oxidation with $\text{Cu}(\text{ClO}_4)_2$. Bottom: Difference spectrum of the high- and low-energy spectra as shown in Figure III.33 after normalization.

1070 nm in the NIR region, although the expected band maximum for OTA^{2+} is at 1130 nm. Measurements in the NIR region are performed at 10 nm intervals with a set bandwidth of 10 nm to ensure a measurable signal. Additionally, if twofold oxidized OTA were present in the here performed measurement, the transient decays would be expected to be triple exponential. As discussed above, the longest living species (67 μs) is due to flash quenching of $[\text{Ru}(\text{bpy})_3]^{2+}$ with TCNB and the main photoproduct Ru-OTA^+ displays a lifetime of 13 μs .

In flash-quench experiments diffusion always plays a pivotal role and is responsible for the prolongation of the charge-separated state lifetime. Possible formation and back electron transfer reaction of the desired second charge-separated state, Ru-OTA^{2+} is also diffusion controlled in this case and might therefore exhibit a similar lifetime than the first charge-separated state. If Ru-OTA^{2+} is indeed formed in the present flash-quench experiment it will be present to a much smaller amount than the first charge-separated state, due to the multitude of deactivation processes that are open to it. The smaller percentage would explain the poor signal of the difference spectrum, as well as the lack of a third species in the kinetic absorption. However, exclusive assignment to Ru-OTA^{2+} is still questionable and will have to be further investigated by pump-pump-probe experiments.

III.4.6 Time-Resolved Study of AQ–Ru–OTA in Pure MeCN

Regarding the thermodynamics, charge accumulation in AQ–Ru–OTA in pure MeCN solution is deemed rather unlikely (Figure III.29). Especially, considering the large negative potential for the second reduction of AQ. Figure III.35 depicts the data obtained for the time-resolved transient experiments on the triad in pure, de-oxygenated MeCN (10^{-5} M). Excitation occurred at 532 nm and the spectra were obtained at excitation powers of 2.1 (blue) and 58 mJ (cyan). The cyan transient spectrum exhibits a

bleach at 340 nm due to bleaching of ground state absorptions of AQ and OTA observable in the UV-Vis spectrum in Figure III.27. The band at 415 nm can be assigned to singly oxidized OTA, as can be derived from the difference spectra after chemical oxidation of OTA with Cu^{2+} . This observation is supported by the constant rise in optical density from 630 nm on to longer wavelengths. In combination with the broad band stretching over the whole NIR region, also indicative of OTA^+ and the band at 565 nm attributed to $\text{AQ}^{\bullet-}$,¹¹³ the observed photoproduct is $\text{AQ}^{\bullet-}\text{-Ru-OTA}^+$. All transient absorption decays on the right side of Figure III.35 can be fitted single-exponentially, resulting in a lifetime of 2.4 μs for the first charge-separated state.

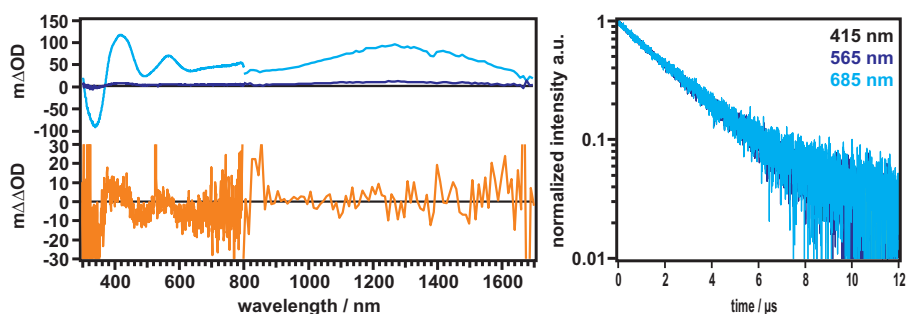


Figure III.35 Left: Transient absorption spectra after excitation of a 10^{-5} M MeCN solution of AQ-Ru-OTA at 532 nm. High and low-energy spectra are shown with cyan (58 mJ) and blue (2.1 mJ) traces. Difference spectrum after normalization at the isosbestic points and subtraction of the blue from the cyan spectrum (orange trace). Right: Transient absorption decays of the signals at 415, 565, and 685 nm.

For the construction of the difference spectrum (orange trace), the high and low-energy spectra were normalized to the band at 565 nm or to the isosbestic point at 1285 nm. Though the lifetime of $\text{AQ}^{\bullet-}\text{-Ru-OTA}^+$ is long enough to allow for a second excitation within the same 10 ns laser pulse, formation of CSS2 is unlikely. In the present system in pure MeCN, AQ cannot be reduced a second time by the reduced or excited ruthenium photosensitizer. As a result, the sole photoproduct is indeed $\text{AQ}^{\bullet-}\text{-Ru-OTA}^+$ as can be derived from the difference spectrum. No spectral indications of OTA^{2+} , such as increased absorption at 600 or 1130 nm are observable.

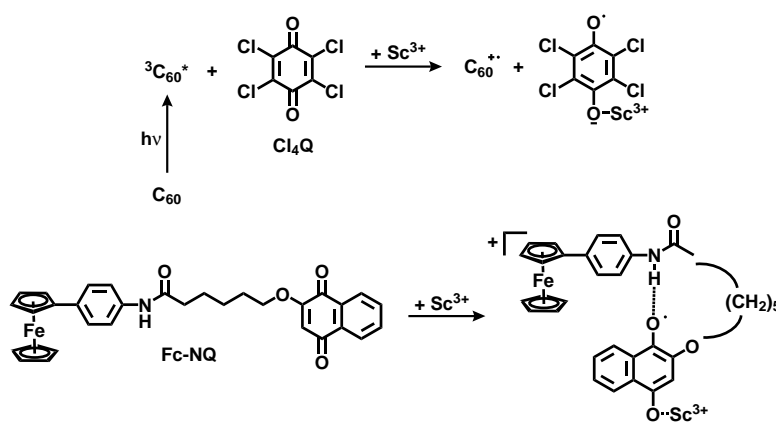
III.4.7 Time-Resolved Study of AQ-Ru-OTA in Presence of LEWIS Acids

In the AQ-Ru-OTA triad, the addition of acids is necessary for shifting the second reduction potential of AQ to more positive potentials. Only then can the excited or reduced ruthenium sensitizer forward another electron to $\text{AQ}^{\bullet-}$. In Section III.2.4 the BRØNSTED acid-induced spectral changes in the OTA absorption was discussed. Despite the expectation, strong acids such as triflic acid seemingly promoted oxi-

dation of the donor. However, only chloroacetic acid was used in the time-resolved experiments investigating AQ-Re-OTA. Though, no premature oxidation of OTA was observed with chloroacetic acid, no twofold charge separation was achieved. By using additives that would bind stronger and more exclusively to AQ, in combination with higher excitation densities, twofold charge separation might be achievable. Instead of BRØNSTED acids, LEWIS acids were chosen as additives. Rare earth metal ions, should bind solely to AQ and not influence OTA.

Metal Ion-Promoted Electron Transfer (MCET)

FUKUZUMI *et al.* have performed extensive studies on the mechanics of the so-called metal ion-coupled electron transfer and its influence on photoinduced electron transfer reactions.^{133–135} With the help of LEWIS acids, electron transfer can be initiated that would otherwise not occur, so-called metal ion-induced electron transfer. Photoinduced electron transfer from C_{60} to *p*-chloranil (Cl_4Q) is endergonic and does not occur in pure benzonitrile. However, in presence of Sc^{3+} the reduction potential of Cl_4Q is less negative which enables the electron transfer reaction (Scheme III.13 top).¹³⁴

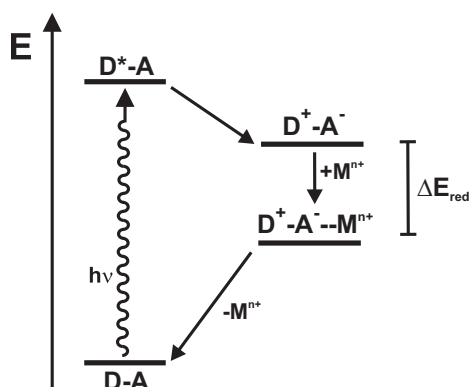


Scheme III.13 Top: Photoinduced MCET in a bimolecular system of C_{60} and Cl_4Q after addition of a LEWIS acid. Bottom: Thermally induced MCET in a Fc-NQ dyad after addition of a strong LEWIS acid.

Not only can photoinduced transfer of an electron be rendered possible by addition of metal ions, they can also induce thermal electron transfer in otherwise inert systems (Scheme III.13 bottom). In a ferrocene-naphthoquinone dyad, Fc-NQ, no thermal electron transfer occurs at RT in MeCN. In presence of $Mg(OTf)_3$, still no charge transfer product could be observed. Only upon addition of Sc^{3+} oxidized ferrocene and reduced NQ was formed. The NQ radical anion was stabilized by complexation with the metal ion.¹³⁶ Consequently, the ability to induce or promote charge transfer is

strongly dependent on the LEWIS acidity of the metal ion. This is very similar to what is observed for BRØNSTED acids.

Similar to PCET, MCET can occur sequentially starting with electron transfer (ET), followed by metal binding (MB) to the reduced acceptor. A concerted mechanism is also possible in which electron transfer and metal binding occur simultaneously.¹³³ Usually, no binding of the metal ion to the neutral acceptor is observed (Scheme III.14).



Scheme III.14 Energy scheme for metal-ion coupled electron transfer after photoexcitation yielding $D^+-A^-M^{n+}$. Metal ion-decoupled back electron transfer produces the dyad in its ground state.

Binding of the metal ion leads to a decrease in driving force for the back electron transfer (ΔE_{red}) due to their strong electrostatic interaction with the reduced acceptor. Setting the dyad back to its ground state requires the removal of the electrophilic metal ion from the reduced acceptor, which is referred to as metal ion-decoupled electron transfer (MDET).¹³⁴

Transient Photoproducts in Presence of Different LEWIS Acids

As discussed above, LEWIS acids of different strengths might influence the nature of the charge-separated state in AQ–Ru–OTA and may even promote formation of the CSS2 without premature oxidation of OTA. For the experiments metal ions of various LEWIS acid strengths were chosen. Their LEWIS acidity can be derived from their charge and ion radius.¹³⁵ The higher the charge and the smaller the metal ion, the stronger a LEWIS acid and the stronger it binds to negative charge. All used metal ions are listed in Table III.4 in descending order of strength, together with their ion radii.

Table III.4 Used metal ions and their radii.¹³⁷

metal ion	Sc ³⁺	Eu ³⁺	Mg ²⁺	Ca ²⁺	Ba ²⁺
radius / Å	0.81	1.07	0.89	1.12	1.42

Figure III.36 displays the transient absorption spectra recorded on de-oxygenated solutions of the triad in MeCN. Complex concentrations were $2.5 \cdot 10^{-5}$ M and of each LEWIS acid an excess of 400 eq was added. Recording of the spectra occurred in a 200 ns time window directly after excitation with a 532 nm laser pulse.

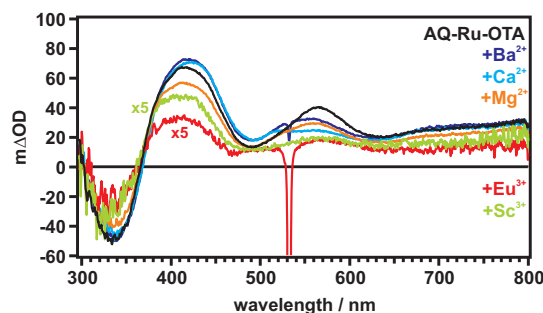


Figure III.36 Transient absorption spectra of de-oxygenated $2.5 \cdot 10^{-5}$ M MeCN solutions of AQ-Ru-OTA with 400 eq of Sc^{3+} , Eu^{3+} , Mg^{2+} , Ca^{2+} , and Ba^{2+} . For better visualization the red and green spectra were multiplied by a factor of 5. The spectrum of the pure triad is shown as reference (black).

All spectra recorded in presence of the metal ions do in principle display the same spectral features, a bleach at 335 nm and bands at 420 nm and around 550 nm, as the triad in pure MeCN. While the bleach at 335 nm can again be attributed to ground state bleaching of OTA and AQ, the presence of the strong band at 420 nm and the lack of increased absorption around 600 nm does indicate the presence of OTA^+ in the photoproduct. Furthermore, the still present band around 550 nm, indicative of AQ^- ,¹¹³ supports the assumption of the first charge-separated as the main photoproduct. The weaker LEWIS acids Mg^{2+} , Ca^{2+} , and Ba^{2+} , induce a slight blue-shift of the AQ^- band over 20 nm, which might be attributable to a very weak coordination of the metal ions to the reduced AQ. Hydrogen bonding between AQ^- and e.g. H_2O , however, induces a more pronounced hypsochromic shift of the band to 500 nm.⁹² The stronger LEWIS acidic ions Sc^{3+} and Eu^{3+} significantly reduced the optical density of the transient spectrum and are multiplied by a factor of 5 for better display and to enable band assignment. Again, a bleach at 330 nm and two bands at 410 and 570 nm are observed. Though, the bands are shifted compared to the spectra with the weaker coordinating metal ions, no spectral indication for twofold oxidized OTA is observable. As a result, the predominant photoproduct in all cases is most likely the first charge-separated state AQ^- -Ru- OTA^+ .

The reason for the missing shift for the band assigned to AQ^- in presence of the strong LEWIS acids is unclear. If already the weaker binding metal ions induce a slight shift, the effect would be expected to be even more severe for the stronger ones, similar to the observations in III.2.5 in presence of different BRØNSTED acids. Another

interesting aspect is the decrease in optical density stemming solely from the LEWIS acidity of the metal ions. Neither the solvent, nor the concentrations were changed in the measurements. If the lifetime of the photoproduct is very short the optical density of the transient signal will be very low because detection with the nanosecond setup will be difficult. On the other hand, an extremely long lifetime of the photoproduct, exceeding the detection limit of the instrument setup will also result in a weak signal. At some point, no more photoproduct can be produced to a sufficient amount in the transient experiment, due to its very slow decay to the ground state. Therefore, not enough triad molecules in the ground state are left before the next excitation pulse.

Kinetic Absorption Behavior in Presence of Different LEWIS Acids

In the following Figure III.37 the decays of the transient absorption signals in the above discussed spectra are depicted. Compared to pure MeCN solution ($2.4\ \mu\text{s}$), AQ^- -Ru-OTA⁺ exhibits a slightly increased lifetime of $3.0\ \mu\text{s}$ in presence of Ba^{2+} (a) or Ca^{2+} (b), when only the signals around 420 and 690 nm are considered. They show a clear single-exponential decay. Thus, the added metal ions do stabilize CSS1 to a certain extent. For the AQ related bands at 560 and 565 nm, however, a clear deviation from the single-exponential character of the decays is observed. Fitting of the decays gives lifetimes of 139 ns for an additional short-living species in presence of Ca^{2+} and 223 ns in the Ba^{2+} containing sample. In the present case no band shift was observed for the AQ-related bands in presence of the LEWIS acids (Figure III.36), as was observed for AQ-Re-OTA in presence of BRØNSTED acids. Coordination of the metal ions might not induce a hypsochromic shift of the AQ^- absorption band. If the band for AQ^- and metal-coordinated AQ^- are superimposed, this might explain the bi-exponential decays only present for the AQ^- -related band around 560 nm.

In presence of Mg^{2+} , also a weaker LEWIS acid, the same deviant behavior is observed for the AQ related band and the lifetime of the charge-separated state is only $2.6\ \mu\text{s}$. Clear bi-exponential character is observed and the fitted lifetimes are 172 and 392 ns, respectively. These, in combination with the very weak transient signal, do not meet the expectations of stabilization of the charge-separated state and might be due to metal ion-promoted sample degradation. However, addition of Sc^{3+} did lead to a significant increase in lifetime as can be seen in Figure III.37 e. After photoexcitation, two species are formed, one of which does not decay within the detection range of the nanosecond setup. Double-exponential fitting gives lifetimes of ≈ 1 and $20\ \mu\text{s}$ for the two species. The real lifetime of the long-living species might indeed be different, due to a high uncertainty in this fit. However, the lifetime of the shorter living species resembles the one of AQ^- -Ru-OTA⁺ in pure MeCN. The longer decay compound

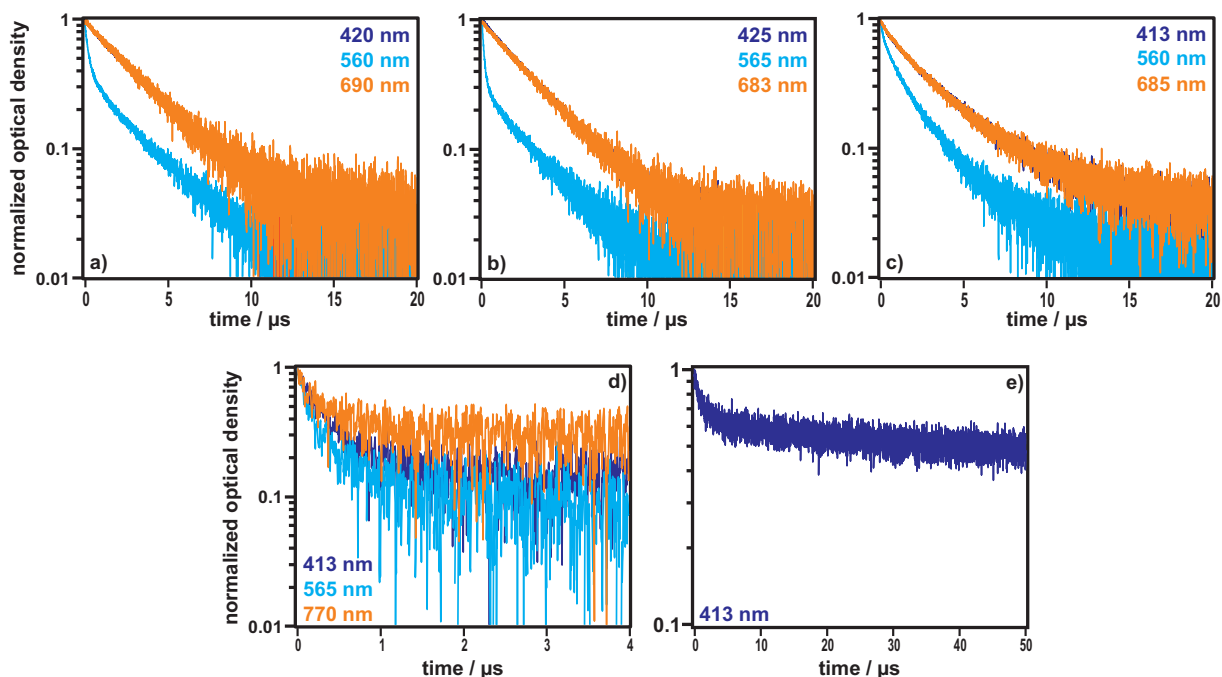


Figure III.37 Decays of the transient photoproduct in presence of various metal ions. a) Ba^{2+} , b) Ca^{2+} , c) Mg^{2+} , d) Eu^{3+} , and e) Sc^{3+} .

might indicate the presence of a charge-separated state which is strongly stabilized by tight binding of Sc^{3+} to the reduced AQ acceptor.

Sc^{3+} Concentration-Dependent Time-Resolved Experiments

Due to the unusually long lifetime of the charge-separated state $\text{AQ}^-\text{-Ru-OTA}$ in presence of an excess of Sc^{3+} the influence of this metal ion on the transient photoproduct was investigated further. Concentration-dependent experiments were performed in de-oxygenated MeCN. On the left of Figure III.38 the emission decays of the triad in presence of varying concentrations of Sc^{3+} are depicted.

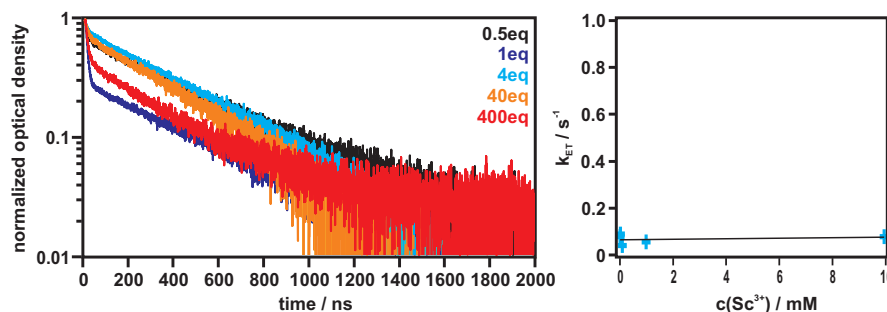


Figure III.38 Emission decays of AQ-Ru-OTA with increasing Sc^{3+} concentrations. Right: Plot of k_{ET} vs $c(\text{Sc}^{3+})$.

The origin of the second, long-lived luminescent species can be attributed to highly

luminescent impurities, as discussed in Figure III.30. Therefore, the short lifetimes were used for determination of the electron transfer rate constants. The latter is plotted vs the Sc^{3+} concentration. Linear fitting gives a basically non-existent slope and the electron transfer rate is therefore not dependent on the Sc^{3+} concentration. This further indicates that metal ion binding occurs after electron transfer, the rate determining step.¹³⁸ Addition of scandium ions is not necessary to initiate electron transfer in AQ–Ru–OTA since charge separation is already observed in pure MeCN. Thus, the fit on the right of Figure III.38 does not intercept at the origin.

The overall spectral shape for the scandium ion concentration-dependent measurements is indicative of AQ^- –Ru– OTA^+ formation as the main photoproduct due to the OTA^+ band at 420 nm and the AQ^- -related band at 565 nm. However, with increasing amounts of Sc^{3+} the optical density decreases in the transient absorption spectra as depicted on the left of Figure III.39.

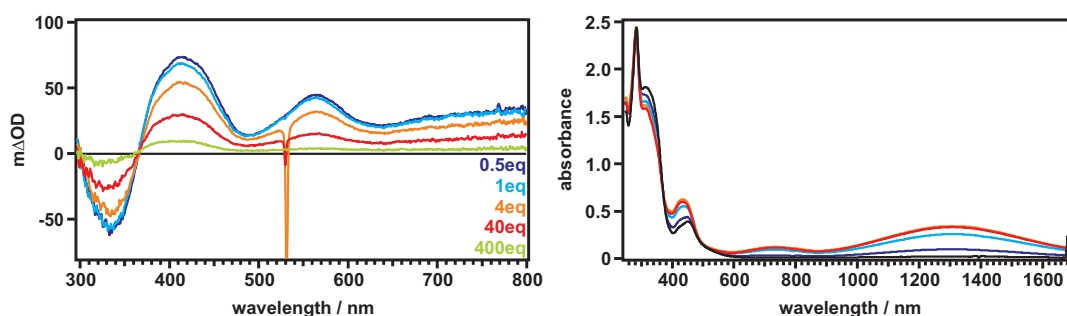


Figure III.39 Left: Transient absorption spectra after excitation of AQ–Ru–OTA at 532 nm in de-oxygenated MeCN with increasing amounts of Sc^{3+} (0.5–400 eq). Right: Ground state absorption spectra of the sample solutions. The color code is the same as on the left and the spectrum in pure MeCN is depicted in black for comparison.

It was further noticed that addition of increasing amounts of Sc^{3+} to the complex solutions seems to initiate premature oxidation, prior to the transient experiments, as depicted on the right side of Figure III.39. In presence of 40 eq $\text{Sc}(\text{OTf})_3$ (red trace) $\approx 77\%$ OTA^+ had already been formed. The percentage was calculated in relation to the amount of OTA^+ formed in the chemical oxidation experiment. The decrease in optical density correlates rather well with the increasing OTA^+ formation. Scandium ions show a very high affinity towards oxygen and facilitate the one-electron reduction of O_2 and the sample solutions are mixed under ambient conditions prior to de-oxygenation. Already at this early stage thermal electron transfer from OTA to O_2 might be induced, which may be responsible for the premature oxidation of OTA .¹³⁶ The possibility of this assumption is further investigated in the continuous experiments discussed in III.6.

Despite the unchanged transient absorption spectra, increasing amounts of Sc^{3+} induced prolongation of the charge-separated state lifetime.

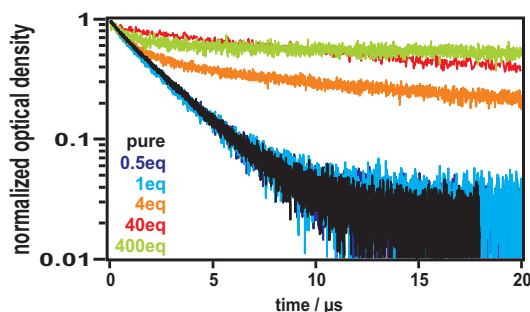


Figure III.40 Kinetic absorption decays of the band at 420 nm (Figure III.39) in presence of various Sc^{3+} concentrations in de-oxygenated MeCN solution.

The transient absorption decays of the band at 420 nm depicted in Figure III.40 clearly show that addition of up to one equivalent of $\text{Sc}(\text{OTf})_3$ does not lead to significant changes in the charge-separated state lifetime. The obtained lifetime of $2.6 \mu\text{s}$ is comparable to the one obtained in pure MeCN ($2.4 \mu\text{s}$). Upon further increase of the scandium ion concentration, the decay character becomes increasingly double-exponential and significantly longer-living species are formed. Their lifetime increases with increasing scandium concentration to $60 \mu\text{s}$ in presence of a 40-fold excess. In presence of a 400-fold excess of Sc^{3+} the decay can not be fitted reliably anymore. However, we can conclude that the lifetime in this particular sample lies well in the microsecond, if not millisecond regime, since its complete decay cannot be detected with the used nanosecond setup.

The presence of this very long-living photoproduct in the de-oxygenated AQ–Ru–OTA solution in presence of a large excess of $\text{Sc}(\text{OTf})_3$ lead us to perform continuous irradiation experiments. With such a long lifetime, photo-accumulation and tracking of the photoproduct on a UV-Vis timescale should be possible. Regarding the premise of premature oxidation of OTA to a certain extent during sample preparation, reducing agents were added. Alas, neither the addition of cobaltocene, nor Na/Hg lead to the desired re-reduction of OTA. The amount of prematurely oxidized OTA is dependent on the scandium concentration and so is the lifetime of the photoproduct. Therefore, finding a balance between the amount of OTA^+ present prior to the experiments and a sufficiently long lifetime of the generated photoproduct was crucial. The exact parameters for the continuous irradiation experiments and their results are discussed in III.5 and III.6.

III.4.8 Time-Resolved Studies on AQ–Ru–OTA in presence of $\text{Sc}(\text{hmpa})_3^{3+}$

For all time-resolved transient experiments above, $\text{Sc}(\text{OTf})_3$ was used as the metal ion source. When the triflate salt is dissolved in MeCN the OTf^- ligands are abstracted and the metal ion exists in its “naked” form as Sc^{3+} . Metal ions display a very high affinity towards oxygen and scandium seemingly induced premature OTA oxidation, especially in this naked form, as discussed above. Since OTA^+ formation in the scandium containing samples proceeded much faster and in higher yield, even the added reductants, cobaltocene or Na/Hg, were not able to counteract and re-reduce OTA^+ . Therefore, the LEWIS acidity of free Sc^{3+} was attempted to be masked by attachment of stronger-binding ligands, such as hexamethylphosphoramide (hmpa). Hmpa as a rather bulky, monodentate ligand limits the coordination number to six for scandium ions and the resulting complex is very stable regarding ligand loss.¹³⁹ Preparation of $\text{Sc}(\text{hmpa})_3^{3+}$ occurred by heating a THF solution of $\text{Sc}(\text{OTf})_3$ and 3 eq hmpa to 50 °C under N_2 atmosphere. $\text{Sc}(\text{hmpa})_3^{3+}$ precipitates from the cooled reaction mixture in form of the triflate salt.

Separate de-oxygenation of the scandium and triad solution and the use of only 20 eq of $\text{Sc}(\text{hmpa})_3^{3+}$ resulted in a decrease of premature OTA^+ formation to 38%. However, complete prevention of premature oxidation was not possible.

In Figure III.41 the transient low- (10 mJ, blue) and high-energy (80 mJ, cyan) spectra are depicted on the left together with the difference spectrum. The latter was obtained after normalization of the high and low energy spectra to the isosbestic points between the OTA^+ and OTA^{2+} species as observed in the chemical oxidation experiment (III.4.4). Due to OTA^+ absorption in the whole spectral range the isosbestic points of OTA^+ and OTA^{2+} seemed to be the most logical choice for normalization.

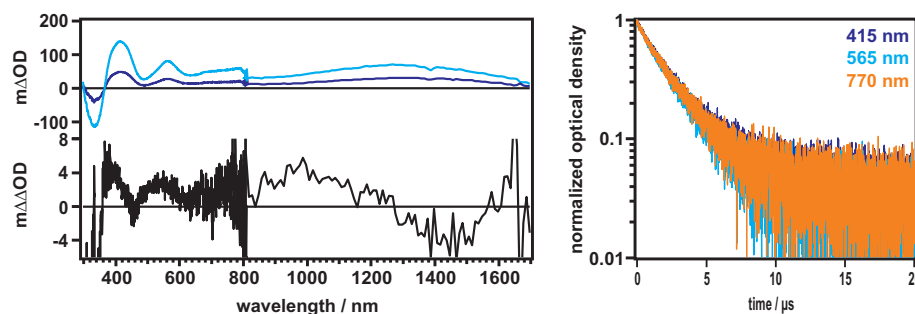


Figure III.41 Left: Transient absorption spectra at high (80 mJ, cyan) and low (10 mJ, blue) pulse energies after excitation of de-oxygenated MeCN solutions at 532 nm. Difference spectrum after normalization at 478 and 1285 nm and subtraction of the low from the high energy spectrum. Right: Kinetic absorption decays of the photoproduct at different wavelengths.

The spectra recorded at high and low energies display the same transient absorption features which indicates the presence of the same photoproduct in both cases. Bands at 415 and 1300 nm indicate once again the formation of OTA^+ . Together with the band at 565 nm assigned to the AQ radical anion, the main photoproduct in presence of $\text{Sc}(\text{hmpa})_3^{3+}$ is most likely $\text{AQ}^- - \text{Ru} - \text{OTA}^+$.

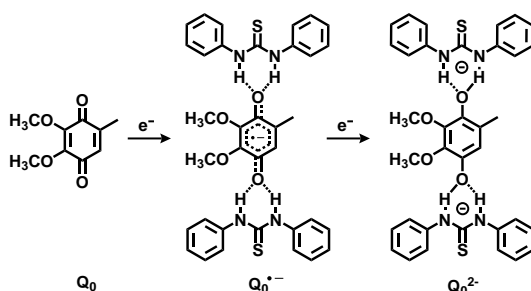
Coordination of the scandium complex to the reduced AQ should result in an increase of the charge-separated state lifetime, as was observed for the use of different metals. Fitting of the decays, however, gave a mean lifetime of 2.1 μs for the photoproduct which is the same as for the triad in pure, de-oxygenated MeCN (2.4 μs), within the accuracy of the measurement and fitting procedure. Even in presence of the weaker LEWIS acids Ba^{2+} and Ca^{2+} the lifetime of $\text{AQ}^- - \text{Ru} - \text{OTA}^+$ was increased to 3.0 μs . It is therefore concluded that the scandium-hmpa complex is not coordinated to the reduced AQ in the photoproduct.

The difference spectrum (black trace in Figure III.41 displays bands at 400, 550, and 1000 nm. Twofold reduced AQ shows absorption at 470 and 622 nm in DMF,⁹⁰ however neither one of the observed bands in the difference spectrum would fit to this assignment. Furthermore, the band for OTA^{2+} is expected at 1130 nm in the NIR region together with increased absorption around 600 nm. Though the observed band at 550 nm might be interpreted in terms of twofold oxidized OTA, the band at 1000 nm shows too large a shift in relation to the expected maximum at 1130 nm.

III.4.9 Time-Resolved Studies in Presence of *N,N*-Diphenylthiourea

In earlier attempts to stabilize the first charge-separated state in order to promote formation of the second one by protons, hydrogen-bonds, or rare earth metal ions (LEWIS acids) the additives seemed to induce premature oxidation of the OTA donor. Therefore, an additive was chosen that should only interact with the AQ acceptor. *N,N*-diphenylthiourea is known to recognize benzoquinones, such as ubiquinone 0 (Q_0) and form a stable complex comprised of two diphenylthiourea molecules and a twofold reduced ubiquinone (Q_0^{2-}) as shown in Scheme III.15.¹⁴⁰ Compared to dialkylthiourea, diphenylthiourea is more acidic and a better hydrogen bond donor. In electrochemical measurements no formation of the twofold reduced ubiquinone was observed in presence of an alkylthiourea derivative. Additionally, the chelating effect proved to be essential for the twofold reduction. Therefore, diphenylthiourea, was added to the triad solution.

Addition of *N,N*-diphenylthiourea should not result in oxidized OTA prior to the laser experiments and it should bind exclusively to reduced AQ, facilitating its second reduction and also stabilizing the final charge-separated state.



Scheme III.15 Stepwise reduction of ubiquinone 0 (Q_0) and coordination with N,N -diphenylthiourea.

Figure III.42 depicts the ground state absorption spectra of the triad in pure MeCN (black trace) and in presence of 1000 eq diphenylthiourea (grey trace). Due to the excess of the thiourea derivative absorption is increasing rapidly below 350 nm.

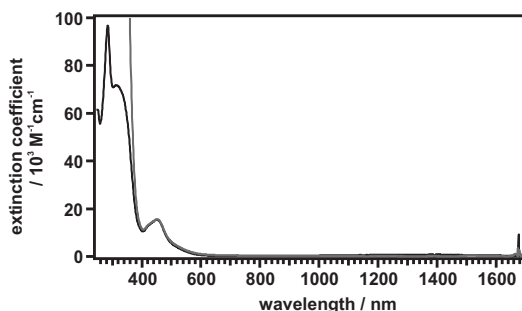


Figure III.42 Ground-state absorption spectra of AQ-Ru-OTA in pure MeCN (black trace) and in presence of 1000 eq of diphenylthiourea (grey trace).

The absorption spectra clearly show no increased absorption around 1300 nm due to premature oxidation of the OTA donor. Therefore, if bands indicate the presence of twofold oxidized OTA in the time-resolved experiments, it can be assumed that its formation is indeed a two-photon process.

In the time-resolved absorption experiments the photoproduct as displayed in Figure III.43 is formed within the pulse duration of the laser (10 ns). Both, the high and low energy spectrum display the similar absorption features in the visible region. The band at 418 nm together with the steady rise of optical density beyond 600 nm are clear signs for OTA^+ (Figure III.31). As counterpart to singly oxidized OTA the singly reduced AQ is expected. The band at 538 nm does not fully coincide with the usual $AQ^{\bullet-}$ band shift of 565 nm or the protonated version, AQH, around 400 nm.^{90,93} For hydrogen-bonded, singly reduced AQ a band at 500 nm is expected.⁹² Nevertheless, the AQ related band is shifted slightly towards shorter wavelengths settling in between the the singly reduced and hydrogen-bonded state. Therefore, the reduced AQ acceptor seems to be only weakly coordinated to diphenylthiourea. In the NIR region

the spectra recorded at high and low energies clearly show differences in their signature. At low energy (12 mJ) the very broad band with a local maximum at 1310 nm is visible which is typical for singly oxidized OTA^+ as determined by chemical oxidation of the donor. The same experiment at a higher excitation density of 66 mJ changes the spectrum and the maximum shows a hypsochromic shift to 1190 nm. OTA^{2+} is known to show an absorption maximum at 1130 nm (Figure III.31). Compared to the band maximum of the transient experiment this gives a deviation of 60 nm. The NIR detector used to record the spectra between 800 and 1700 nm does so in 10 nm intervals. Furthermore, the bandwidth is set to 10 nm to allow for a recordable signal. Due to these necessary settings the NIR detector displays a rather low sensitivity which does lead to a certain insecurity in the assignment of the band maxima. However, a deviation of 60 nm is too large to be explained by the uncertainty of the detector.

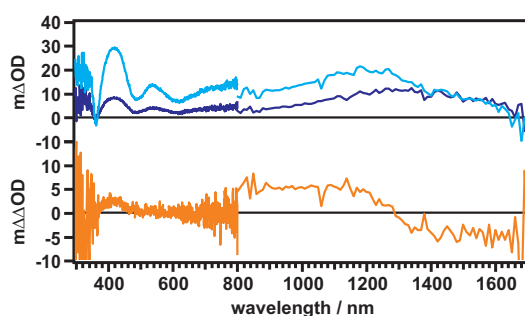


Figure III.43 Transient absorption spectra of AQ-Ru-OTA in presence of 1000 eq diphenylthiourea after excitation at 532 nm. Top: high energy spectrum = cyan (56-66 mJ), low energy spectrum = blue (11-12 mJ). Bottom: Difference spectrum obtained by subtraction of the low from the high energy spectrum after normalization to the isosbestic points at 478 and 1285 nm.

After subtraction of the spectral features of $\text{AQ}^-\text{-Ru-OTA}^+$ only bands assignable to the desired second charge-separated state $\text{AQ}^{2-}\text{-Ru-OTA}^{2+}$ should be present. Therefore, the high and low energy spectra were normalized to the isosbestic points between the OTA^+ and OTA^{2+} species, and the low-energy spectrum was subtracted from the high-energy spectrum. As discussed above, the former represents the first charge-separated state. The bottom part of Figure III.43 displays the difference spectrum created in this manner as an orange trace. It only displays two bands at 420 nm and a rather broad band in the NIR from 800 to 1300 nm. Beyond 1300 nm negative optical density is observed. This might indicate formation of OTA^+ and subsequent further oxidation to OTA^{2+} which results in a decrease of OTA^+ corresponding absorption beyond 1300 nm. If the band in the NIR is considered a sign for OTA^{2+} , another band around 600 nm would be expected. However, the difference spectrum does not show increased absorption in said spectral range. Furthermore, the approximate maximum of the broad band is at 1050 nm which is off by 80 nm compared to

the expected wavelength of 1130 nm. However, some deviation in the band maxima might again be due to the detector settings required for the NIR measurements. From the transient absorption experiments at hand it is therefore concluded that the only photoproduct generated is the singly charge-separated state $AQ^-Ru-OTA^+$.

If $AQ^{2-}Ru-OTA^{2+}$ is indeed formed in the measurement with a high excitation density, it should also be visible in the transient absorption decays. Here, a bi-exponential decay indicating the two different species is expected. Figure III.44 depicts the decays of the bands from the transient absorption experiment.

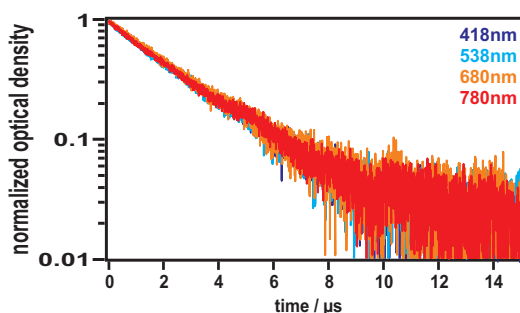


Figure III.44 Absorption decays of the bands at 418, 538, 680, and 780 nm recorded after excitation of the de-oxygenated, diphenylthiourea containing MeCN solution with a 532 nm laser pulse (56 mJ).

All bands show unmistakable single-exponential decay behavior after the excitation with a high-energy laser pulse. The lifetime is given as $2.5 \mu\text{s}$ which is very similar to what was obtained for the triad in pure MeCN solution ($2.4 \mu\text{s}$). From the decay behavior, in conjunction with the transient absorption spectra, especially the constructed difference spectrum it can be concluded that even at high excitation powers the predominant photoproduct is CSS1 $AQ^-Ru-OTA^+$. In addition, the very similar lifetimes of the first charge-separated state with and without an excess of diphenylthiourea indicates only very slight coordination of the thiourea to the reduced AQ acceptor. This was already proposed above due to the shift of the AQ^- related band to 538 nm.

III.4.10 Summary on Electron Transfer in $AQ-Ru-OTA$

In the preceding section electron transfer in a $AQ-Ru-OTA$ triad was studied. Some problems encountered in the analog rhenium triad could be eradicated in $AQ-Ru-OTA$. From the absorption spectrum of the triad in MeCN, the 1MLCT band is now clearly discernible and not superimposed by OTA or AQ absorptions. This allowed for selective excitation of the ruthenium photosensitizer. Furthermore, the excitation wavelength of 532 nm used for ruthenium excitation allowed much higher photon fluxes. The high-energy measurements were performed at laser powers of 50-80 mJ

which translates to roughly 9 to 14 photons per pulse per molecule. From a theoretical viewpoint twofold excitation of the same complex molecule within the same high-energy laser pulse should therefore be possible.

Photoexcitation of a Ru-OTA reference dyad lead to separation of a single charge, and the lifetime of the charge-separated state could be significantly prolonged from 10 ns to 13 μ s in a flash quench experiment with TCNB. Spectral indications at 380, 555, and 1050 nm for twofold oxidized OTA were observed in the difference spectrum after normalization and subtraction of the low- from the high-energy transient spectrum. In the near future, Ru-OTA will be further investigated in flash-quench experiments with TCNB with the help of a pump-pump-probe laser setup. By this, we hope to find more conclusive evidence for the presence of Ru-OTA²⁺.

Photoinduced electron transfer in AQ-Ru-OTA in de-oxygenated MeCN leads to the expected CSS1, AQ⁻-Ru-OTA⁺, with a lifetime of 2.4 μ s. Compared to the rhenium triad in pure, de-oxygenated MeCN this represents a 12-fold increase which is another advantage of this ruthenium complex.

To achieve stabilization of the negative charge on AQ in CSS1 different metal ions were employed. Upon photoexcitation of the ruthenium photosensitizer, metal ion-coupled electron transfer (MCET) was expected. In presence of BRØNSTED acids, premature oxidation of OTA prior to the transient experiments was observed for AQ-Re-OTA. This was not expected to occur when using metal ions. Addition of weaker LEWIS acids such as Ca²⁺, Ba²⁺ or Mg²⁺ did lead to a slight prolongation of the charge-separated lifetime due to their coordination to the singly reduced AQ. By this stabilization of CSS1, the lifetime was increased from 2.4 μ s in pure MeCN, to 3.0 μ s. However, formation of CSS2 was not observed. Presence of the very strong LEWIS acid Sc³⁺ lead to formation of a extremely long-living species that did not show complete decay within the experimental detection limit. Scandium concentration-dependent experiments revealed a decrease in optical density of the transient absorption signal with increasing scandium concentration. Furthermore, a concomitant increase in prematurely formed OTA⁺ was observed. In the case of AQ-Ru-OTA, electron transfer is the rate-determining step for the formation of the photoproduct, not binding of the metal ions to AQ⁻. This is verified by the independence of the electron transfer rate from the scandium concentration.

The oxidation behavior in presence of an excess of Sc³⁺ is further investigated with continuous irradiation experiments in III.6.

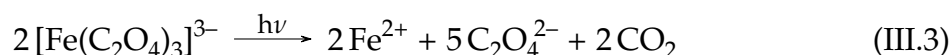
The problem regarding premature OTA⁺ formation due to the added scandium ions could not be solved by attaching the bulkier hmpa ligands to the metal ion. The lifetime of the charge-separated state AQ⁻-Ru-OTA⁺ in presence of Sc(hmpa)₃³⁺ is 2.1 μ s.

This indicates that in its masked form, the scandium ions do not exert any influence on the formed photoproduct.

Only the use of *N,N*-diphenylthiourea did not lead to any spectral changes due to OTA oxidation. The thiourea derivative is known to show exclusive affinity to reduced quinones. In presence of a 1000-fold excess, the lifetime of the predominantly generated photoproduct, $AQ^- - Ru - OTA^+$, is 2.5 μs . Seen in the single-exponential character of the absorption decays, only one species is present. Though no significant increase in lifetime was achieved by addition of diphenylthiourea, at high excitation densities of 66 mJ distinctive differences in the spectral signatures, especially in the NIR region are observed. Therefore, further photophysical investigation of $AQ - Ru - OTA$ in de-oxygenated MeCN in presence of an excess of diphenylthiourea with a pump-pump probe setup might give a more detailed insight. In this case the triad could be excited by temporally delayed laser pulses that might even exhibit different excitation wavelengths. Use of two separate pulses should also allow for a clearer distinction of the one- and two-photon products.

III.5 Ferrioxalate Actinometry

For all continuous irradiation experiments performed on solutions of AQ–Ru–OTA a Fluorolog-322 from Horiba Jobin-Yvon was used. Excitation occurred at 450 nm into the metal-to-ligand charge transfer band of the ruthenium photosensitizer. The entrance slits were opened to the maximum, a bandwidth of 14.7 nm, to allow as much light from the Xe-lamp as possible into the sample solution. In order to determine the exact photon flux and the number of photons available for the excitation of AQ–Ru–OTA, chemical actinometry was performed. A very convenient actinometer for wavelengths up to 450 nm is potassium ferrioxalate. It is characterized by its high quantum yield of photodegradation. Basically 100% of the absorbed photons lead to formation of Fe^{2+} . The quantum yield of the degradation reaction steeply decreases at wavelengths higher than 450 nm. At this wavelength, however, the quantum yield is still 1.0.^{141,142} Therefore, ferrioxalate actinometry exhibits excellent applicability for the determination of the photon flux in a sample.



Upon irradiation of an acidic ferrioxalate solution, Fe^{3+} is reduced to Fe^{2+} and part of the oxalate ligand is oxidized to CO_2 . The simplified chemical equation for photoinduced ferrioxalate degradation is shown in Equation III.3.¹⁴³ The photochemically produced Fe^{2+} subsequently forms an orange-red complex with 1,10-phenanthroline which can be quantified spectroscopically ($\lambda_{\text{max}} = 511 \text{ nm}$).

Table III.5 Sample preparation for the calibration curve.

sample	$(\text{NH}_4)_2\text{Fe}(\text{SO}_4)_2$ / mL	phenanthroline / mL	buffer / mL	H_2SO_4 / mL	H_2O / mL
1	0	1	2.5	5	1.5
2	0.5	1	2.5	4.5	1.5
3	1	1	2.5	4	1.5
4	1.5	1	2.5	3.5	1.5
5	2	1	2.5	3	1.5
6	2.5	1	2.5	2.5	1.5
7	3	1	2.5	2	1.5

Preceding the actual actinometric measurement, a calibration curve needed to be

recorded to determine the extinction coefficient of $[\text{Fe}(\text{phen})_3]^{2+}$ at 511 nm. For this, four solutions had to be prepared. A $4 \cdot 10^{-4}$ M solution of $(\text{NH}_4)_2\text{Fe}(\text{SO}_4)_2$ in 0.05 M H_2SO_4 , a $6.7 \cdot 10^{-3}$ M aqueous 1,10-phenanthroline solution, a 0.6 M acetate buffer, and 0.05 M H_2SO_4 . From these solutions and de-ionized H_2O , six samples with varying Fe^{2+} concentrations were prepared according to Table III.5. Absorption spectra were measured of all samples and the absorbances at 511 nm were plotted vs the Fe^{2+} concentration. The slope of the fit in Figure III.45 gives the molar extinction coefficient of $[\text{Fe}(\text{phen})_3]^{2+}$ at 511 nm to be $11500 \text{ M}^{-1}\text{cm}^{-1}$.

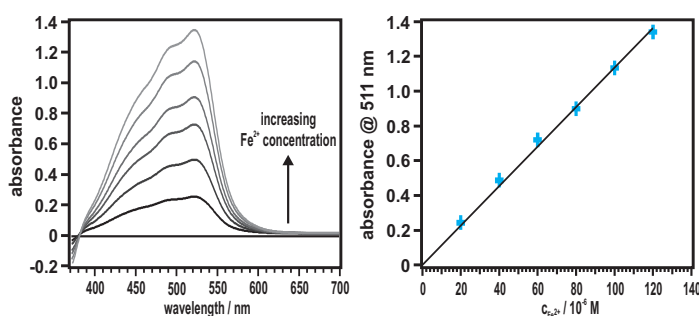


Figure III.45 Left: Absorption spectra of $[\text{Fe}(\text{phen})_3]^{2+}$ with increasing concentrations. Right: Calibration points and fit for the determination of the molar extinction coefficient.

For the determination of the photon flux, a stock solution of 10 mL 1,10-phenanthroline solution ($6.7 \cdot 10^{-3}$ M), 25 mL acetate buffer (0.6 M), 40 mL diluted sulfuric acid (0.05 M), and 15 mL de-ionized H_2O was prepared and 9 glass vials were filled with 9 mL each. The vials were covered with aluminum foil. In the dark, a 0.02 M potassium ferrioxalate solution in 0.05 M H_2SO_4 was prepared. Though, light-induced degradation of the ferrioxalate is key to the photon flux determination by actinometry, premature degradation is unwanted. Therefore, light exclusion during sample preparation is crucial.

As a blank test, 1 mL of the non-irradiated ferrioxalate solution was added to a prepared glass vial and the absorption spectrum was recorded. Due to the lack of Fe^{2+} in the solution, no absorption of $[\text{Fe}(\text{phen})_3]^{2+}$ is expected at 511 nm. Sample preparation for the irradiation measurements occurred as follows. 2 mL ferrioxalate solution were placed in a Quartz cuvette and irradiated for 10 s on the Fluorolog ($\lambda_{exc} = 450$ nm, slits = 14.7 nm). Subsequently, 1 mL was drawn from the cuvette, added to a prepared vial containing 9 mL of the above-mentioned phenanthroline-containing stock solution. After thorough mixing an absorption spectrum of the formed $[\text{Fe}(\text{phen})_3]^{2+}$ was recorded. This procedure was repeated with irradiation times of 20, 30, 40, 50, 60, 90, and 120 s, respectively. The spectra obtained in this manner are depicted on the left in Figure III.46.

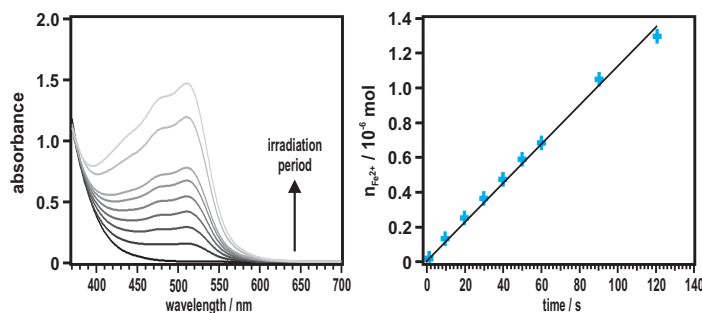


Figure III.46 Left: Absorption spectra recorded after increasing irradiation times. Right: Amount of Fe^{2+} (mol) vs the irradiation period.

With Equation III.4 the amount of Fe^{2+} produced by irradiation can be calculated. V_1 is the irradiated volume, V_2 the 1 mL sample drawn from the cuvette, $A_{511\text{nm}}$ is the absorbance at 511 nm, d the pathlength (1 cm), V_3 is the volume after complexation (10 mL), and ϵ is the molar extinction coefficient ($11500\text{ M}^{-1}\text{cm}^{-1}$).

$$n_{Fe^{2+}} = \frac{V_1 \cdot V_2 \cdot A_{511\text{nm}}}{d \cdot V_3 \cdot \epsilon_{511\text{nm}}} \quad (\text{III.4})$$

By plotting the moles of Fe^{2+} vs the irradiation period the data points show a linear dependency. The photon flux can be derived from the slope of the fit, divided by the quantum yield (1.0). In the performed measurement this lead to a photon flux of $1.12 \cdot 10^{-8} \frac{\text{mol} \cdot h\nu}{\text{s}}$, or $6.74 \cdot 10^{15} \frac{\text{photons}}{\text{s}}$.

This results in a total photon count of 5 photons per molecule per minute for the continuous irradiation measurements on AQ-Ru-OTA with the above given Fluorolog settings and the sample concentrations (10^{-5} M) and volumes (3 mL) used in the experiments described below.

III.6 Continuous Irradiation Experiments on Ru–OTA and AQ–Ru–OTA

As discussed in III.4.7, strong LEWIS acids such as Eu^{3+} or Sc^{3+} lead to the formation of a transient photoproduct with a very long lifetime, exceeding the detection limit of the nanosecond setup. By performing continuous irradiation (CI) experiments with a Xe-lamp as excitation source, we hoped to successively accumulate the long-living photoproduct and to follow its formation with UV-Vis absorption spectroscopy. All experiments on AQ–Ru–OTA were performed in aerated and de-oxygenated MeCN, in absence and presence of 0.02 M $\text{Sc}(\text{OTf})_3$, and under continuous irradiation and dark conditions. As a result, the dependence of the photoproduct on the O_2 content, the Sc^{3+} , and the light source could be evaluated. Furthermore, Ru–OTA was investigated in the same way to assess the influence of the AQ acceptor on the required irradiation times and the spectral differences.

Sample Preparation

Quick sample preparation and direct measurement proved to be crucial for all following experiments. Dry MeCN, stored over molecular sieve, was used as solvent. All aerated samples were prepared just prior to the measurements and used instantly. For the de-oxygenated samples the $\text{Sc}(\text{OTf})_3$, as well as the triad solution were de-oxygenated separately. This was achieved in a Schlenk-cuvette and mixing of both solutions occurred just before the measurement under inert conditions. The final concentrations were 10^{-5} M for AQ–Ru–OTA or Ru–OTA and 0.02 M $\text{Sc}(\text{OTf})_3$. This corresponds to an excess of 2000 eq Sc^{3+} . Despite the fast preparation and separate de-oxygenation of the sample solutions, $\approx 30\%$ OTA^+ had already been formed prior to the start of the actual measurements.

Residual O_2 in De-Oxygenated Samples

The Schlenk-cuvette used for the following measurements has a volume of 47 mL. With the help of the ideal gas equation $p \cdot V = n \cdot R \cdot T$ the moles of gas in the cuvette under ambient conditions can be calculated, which gives an amount of $1.91 \cdot 10^{-3}$ mol; $T = 298.15$ K, $R = 8.314 \frac{\text{J}}{\text{mol} \cdot \text{K}}$, and $p = 100000 \frac{\text{N}}{\text{m}^2}$. Calculation of the residual O_2 content was performed under the assumption that de-oxygenation of the sample solution by three freeze-pump-thaw cycles leads to a complete exchange of the ambient atmosphere with N_2 . The used N_2 (PanGas 5.0) has an O_2 content of ≤ 2 ppm, which means that 0.0002% of the gas in the cuvette is O_2 . This amounts to $3.8 \cdot 10^{-9}$ mol residual O_2 in the de-oxygenated sample solutions and an error of one

order of magnitude is assumed. This value is of interest for later interpretation of some experimental results.

All spectra were recorded as difference spectra, subtracting the initial absorptions of the dyad and triad. If not state otherwise, the excitation wavelength was set to 450 nm. To determine the amounts of OTA^+ and OTA^{2+} generated in the following experiments, the extinction coefficients of the chemical oxidation experiment were used. These are $17300 \text{ M}^{-1}\text{cm}^{-1}$ for OTA^+ at 1310 nm, $59500 \text{ M}^{-1}\text{cm}^{-1}$ for the twofold oxidized OTA at 1130 nm, and each value corresponds to quantitative formation of the respective species. The color of the samples changed from a slight yellow for the non-oxidized species, to greenish-yellow in presence of OTA^+ , and greyish for twofold oxidized OTA.

III.6.1 Reference Experiments

Figure III.47 depicts the obtained difference spectra of Ru-OTA (top) and AQ-Ru-OTA (bottom) after five successive UV-Vis measurements from 1700 to 200 nm. They were recorded immediately one after another. Each measurement takes approximately 3 min which results in a total irradiation time of 15 min. During this time the complexes are slightly irradiated by the light source of the UV-Vis spectrometer. Especially irradiation at 450 nm in the $^1\text{MLCT}$ band of the ruthenium photosensitizer might be problematic. Therefore, the spectral changes due to the UV-Vis measurement were evaluated prior to the actual CI experiments.

Three general insights can be derived from the spectra. As stated above, during the UV-Vis measurements the complexes are irradiated by the light source of the spectrometer and this can lead to photochemistry. The spectra in Figure III.47 indicate the formation of OTA^+ , which represents part of the first expected photoproduct upon irradiation of AQ-Ru-OTA. Furthermore, the amount of formed OTA^+ is higher in the experiments on the triad (Figure III.47 c and d). This is observed best in the spectra recorded on the de-oxygenated solutions, b and d in Figure III.47. On the basis of this, one can conclude that the attached AQ acceptor does influence the generation of the OTA^+ photoproduct upon irradiation. During the same irradiation time, more than twice as much OTA^+ was formed in AQ-Ru-OTA (18%), than in Ru-OTA (7%) in de-oxygenated solutions. The amount of OTA^+ in the de-oxygenated solutions of AQ-Ru-OTA ($5.4 \cdot 10^{-9}$ mol) and Ru-OTA ($2.1 \cdot 10^{-9}$ mol) is similar to the amount of residual O_2 ($3.8 \cdot 10^{-9}$ mol) in the sample solutions. In presence of O_2 (Figure III.47 a and c) the difference in OTA^+ formation between the dyad and triad is smaller. During the same irradiation time as above, 24% OTA^+ is generated in Ru-OTA and

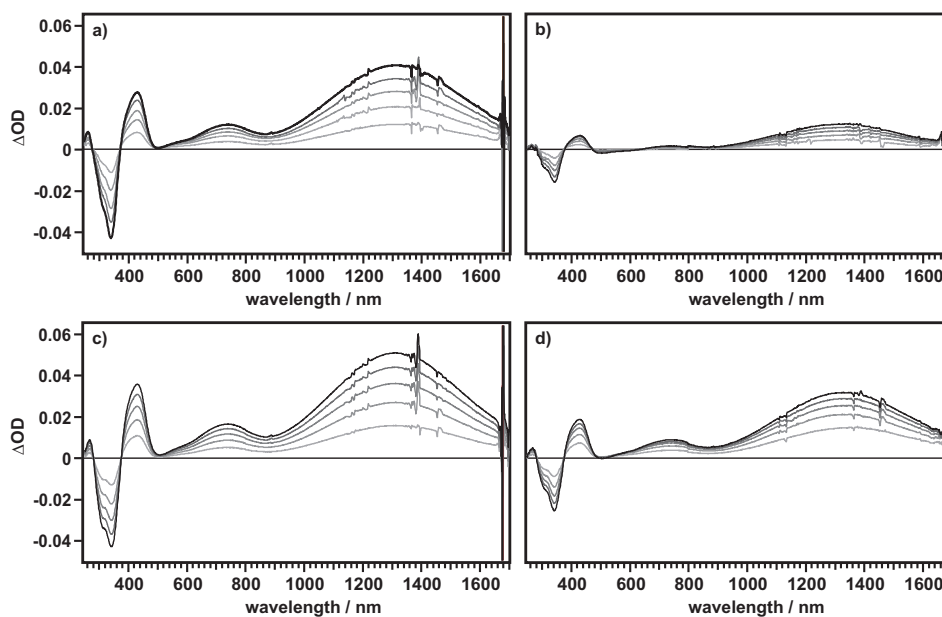


Figure III.47 UV-Vis absorption spectra after five successive measurements. **a)** Ru-OTA + O₂; **b)** Ru-OTA + N₂; **c)** AQ-Ru-OTA + O₂; **d)** AQ-Ru-OTA + N₂. Complex concentrations were 10⁻⁵ M with 0.02 M Sc(OTf)₃.

30% in the triad solution. This indicates that the OTA⁺ formation depends more on the amount of O₂ present in the sample than on the AQ acceptor which leads to the conclusion that O₂ is the terminal electron acceptor.

To verify whether the mere presence of O₂ is responsible for the oxidation of OTA or if OTA⁺ formation is indeed a light-induced reaction, another dark experiment was performed. For this, aerated solutions of Ru-OTA and AQ-Ru-OTA were prepared and a difference spectrum of each was recorded after 15 min in the dark (Figure III.48). The 15 min are the same duration as for the five successive UV-Vis experiments discussed above.

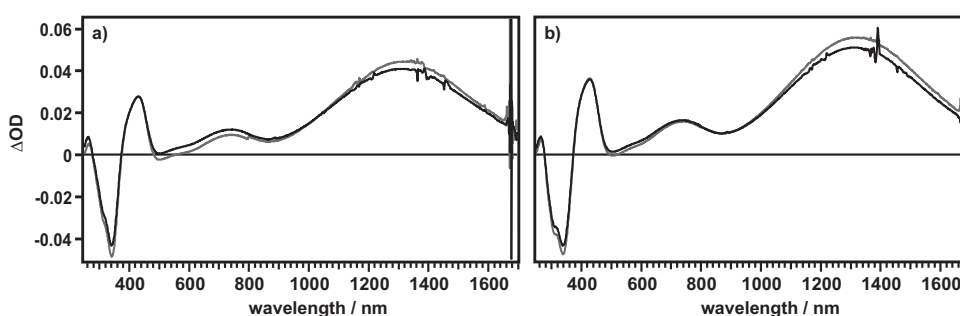


Figure III.48 UV-Vis absorption spectra of aerated MeCN solutions of **a)** Ru-OTA and **b)** AQ-Ru-OTA after 15 min in the dark (grey traces) and five successive measurements (black traces). Complex concentrations were 10⁻⁵ M with 0.02 M Sc(OTf)₃.

The OTA⁺ contents received were 26% for the dyad and 32% for AQ-Ru-OTA. These

closely resemble the amounts of OTA^+ after five successive UV-Vis measurements (black traces) and the deviation of 2% in both cases can be explained by the fact that new sample solutions had to be prepared.

These reference experiments show that not the light source of the UV-Vis spectrometer, but the present amount of O_2 is responsible for the generation of OTA^+ on the time scale of the above experiment. Therefore, storage of the aerated complex solutions with added $\text{Sc}(\text{OTf})_3$ would eventually lead to the complete oxidation of OTA, albeit in a matter of days. Formation of OTA^+ in the triad proceeded 2.6 times faster than in the dyad. Thus, all continuous irradiation experiments were conducted in aerated, as well as de-oxygenated complex solutions.

III.6.2 Irradiation of Aerated Samples in Presence of Sc^{3+}

Figure III.49 depicts the UV-Vis absorption difference spectra after irradiation of Ru-OTA (Figure III.49 a) and AQ-Ru-OTA (Figure III.49 b) with a continuous light source at 450 nm. The spectra are recorded on the aerated solutions. The negative absorbance between 1350 and 1700 nm is due to the presence of OTA^+ already directly after sample preparation.

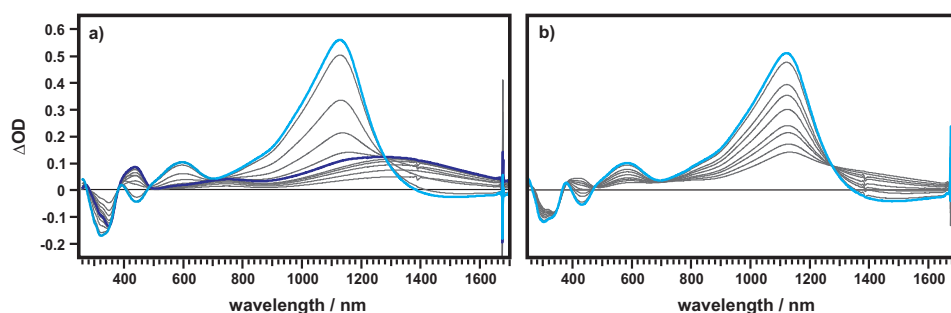


Figure III.49 Changes in absorption upon continuous irradiation of aerated solutions of **a)** Ru-OTA (blue trace: 10 min; cyan trace: 3 h) and **b)** AQ-Ru-OTA (cyan trace: 30 min) in MeCN. $\lambda_{exc} = 450$ nm.

Spectra were recorded after 1, 2, 3, 4, 5, 10, 15, 30, 60, 120, and 180 min for Ru-OTA. Formation of OTA^+ is complete after a little less than 10 min. After exactly 10 min, slight spectral indication of OTA^{2+} is already observable from the small shoulder at 1150 nm in the blue trace. After a total irradiation time of 3 h (cyan trace in Figure III.49 a), no more spectral changes are observed. However, compared to the extinction coefficients from the chemical oxidation experiment (Table III.6) the dyad system has rather reached a steady state, not complete formation of OTA^{2+} , in the irradiation experiment. After 3 h, 70% of OTA^+ is formed. The missing 30% might also be explained by the amount of OTA^+ present prior to the irradiation experiments (see

“Sample Preparation”). Twofold oxidation of OTA was not expected for Ru–OTA, due to lack of an acceptor able to accommodate two electrons. $[\text{Ru}(\text{bpy})_3]^{2+}$ is unlikely to accept two electrons. This again leads to the conclusion that O_2 is the terminal electron acceptor also in the irradiation experiments. Nonetheless, irradiation of the Ru–OTA solution does accelerate the electron transfer reaction from OTA to O_2 significantly. Within 10 min the 3.3-fold amount of OTA^+ is formed in the continuous irradiation experiment as is in the same time in the reference experiment from above.

Table III.6 Extinction coefficients in $\text{M}^{-1}\text{cm}^{-1}$ for OTA^+ and OTA^{2+} species. Percentages are given in parentheses.

	chemical oxidation	Ru–OTA	AQ–Ru–OTA
OTA^+	17300 (100%)	12100 (69%)	–
OTA^{2+}	59500 (100%)	56100 (94%)	51200 (86%)

In case of AQ–Ru–OTA, the spectra were recorded after irradiation times of 1, 2, 3, 4, 6, 8, 10, 15, and 30 min in aerated MeCN (Figure III.49 b). Already after 1 min of irradiation, formation of OTA^+ is finished and a band at 1135 nm indicates the subsequent formation of OTA^{2+} . After a total irradiation time of 30 min the band at 1130 nm for twofold oxidized OTA is present and further irradiation does not result in any more spectral changes. Comparing the extinction coefficient of OTA^{2+} after 30 min to the one obtained in the chemical oxidation experiment (Table III.6), indicates formation of 86% twofold oxidized OTA. This again points towards the system in a steady state. In this respect, the photoinduced formation of OTA^{2+} in the triad proceeds six times faster than in the dyad. Due to the presence of O_2 in both experiments, this acceleration of the OTA oxidation is most likely due to the AQ acceptor in the triad.

Formation of OTA^{2+} in the triad could in principle also yield twofold reduced AQ after two successive electron transfer steps. In order to facilitate the identification of bands due to AQ^{2-} , the OTA^{2+} spectrum obtained through chemical oxidation was subtracted from the final spectrum from Figure III.49 after normalization of the bands at 1130 nm. This was done with the dyad, as well as the triad data and the resulting difference spectra are depicted in Figure III.50. For Sc^{3+} -stabilized twofold reduced AQ a similar band shift as for its strongly hydrogen-bonded or even protonated counterpart is expected. Therefore, a band at 400 nm is expected for twofold reduced AQ in the difference spectrum of the triad.

The traces depicted in the bottom half of Figure III.50 for Ru–OTA (blue) and AQ–Ru–OTA (cyan) do exhibit bands at 400 nm, however, this particular band is

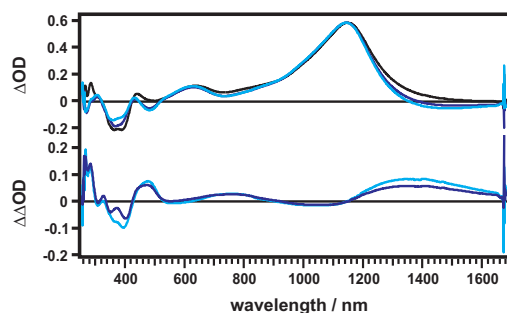
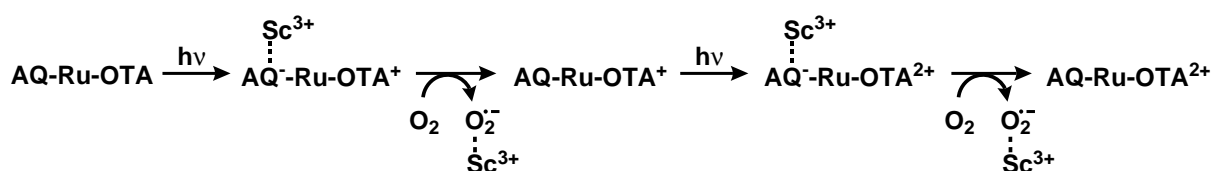


Figure III.50 Top: Normalized spectra of Ru-OTA (blue) and AQ-Ru-OTA (cyan) in aerated MeCN solutions. Chemically generated OTA^{2+} spectrum in black. Bottom: Difference spectra of the dyad (blue) and triad (cyan) after subtraction of the OTA^{2+} spectral signatures.

present in both spectra. Furthermore, the spectra look very similar in general, and no band can be assigned exclusively to AQ in any reduction state.

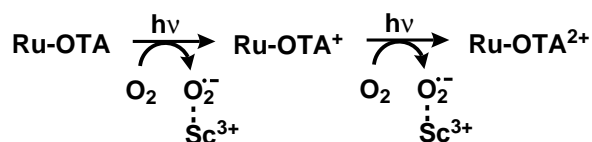
The lack of spectral evidence for reduced AQ is attributable to the present O_2 . The solubility of O_2 in MeCN is $\approx 8.1 \text{ mM}^{144}$ and its one-electron reduction potential is at $-1.25 \text{ V vs. Fc}^{+/0}$ in pure MeCN.¹⁴⁵ Once formed superoxide ($\text{O}_2^{\cdot-}$) anion was previously found to be thermodynamically very stable in MeCN, especially in presence of metal ions such as Sc^{3+} .^{135,138} The mechanism leading to the formation of OTA^{2+} as evident from the spectra above, however without the appearance of reduced AQ related bands, may be interpreted as an AQ-mediated reduction of O_2 (Scheme III.16).



Scheme III.16 Proposed mechanism for stepwise oxidation of OTA in AQ-Ru-OTA in presence of O_2 .

The potentials for the first reduction of AQ ($-1.26 \text{ V vs. Fc}^{+/0}$) and the reduction of O_2 ($-1.25 \text{ V vs. Fc}^{+/0}$) are basically the same. If the potential for the AQ reduction is much more positive than -1.25 V , electron transfer from $\text{AQ}^{\cdot-}$ to O_2 would not occur. On the other hand, a much more negative reduction potential of AQ compared to O_2 would most likely favor direct electron transfer from the reduced photosensitizer to O_2 . In the present case, however, the reduced photosensitizer ($-1.66 \text{ V vs. Fc}^{+/0}$) is able to reduce either AQ or O_2 . Short-term generation of $\text{AQ}^{\cdot-}$ as an electron transfer intermediate is likely, since intramolecular electron transfer from OTA to AQ is very fast and exhibits a driving force of -0.92 eV . Time-resolved studies in pure

MeCN in absence of Sc^{3+} gave a lifetime of $2.4 \mu\text{s}$ for $\text{AQ}^- \text{-Ru-OTA}^+$. During this rather long lifetime, O_2 is able to diffuse towards the reduced AQ acceptor which can then reduce it. In an electrochemical study the bimolecular electron transfer rate from 2-hydroxymethylanthraquinone (2-HM-AQ) to O_2 in MeCN solution was found to be $7 \cdot 10^6 \text{ M}^{-1} \text{ s}^{-1}$.¹⁴⁵ 2-HM-AQ exhibits a potential of -1.33 V for the first reduction which leads to a slightly higher driving force for electron transfer to O_2 than with AQ. Nevertheless, a similar rate constant can be assumed for the electron transfer between the reduced AQ acceptor in the triad and O_2 , especially in presence of the scandium metal ions which strongly bind and therefore stabilize the superoxide anion.^{135,138} The presence of OTA^{2+} in the dyad with no attached two-electron acceptor can be explained by a similar mechanism as above (Scheme III.17).



Scheme III.17 Possible mechanism for the stepwise twofold oxidation of OTA in Ru-OTA upon irradiation.

Though, no AQ-mediated electron transfer can occur in Ru-OTA, the twofold oxidation of OTA is made possible by the acceptance of the electrons by the present O_2 . In presence of $\text{Sc}(\text{hmpa})_3^{3+}$, O_2 was found to exhibit a reduction potential of only -0.2 V vs. $\text{Fc}^{+/0}$ in propionitrile.¹³⁸ The AQ-mediated electron transfer mechanism as discussed above is likely to be the reason for the sixfold slower formation of OTA^{2+} in the dyad. As a result, successful photoinduced hole accumulation on the OTA donor was performed both in AQ-Ru-OTA and Ru-OTA in aerated MeCN. Though, no charge is accumulated on the AQ acceptor, it serves as an electrocatalyst in the system, promoting charge separation.

To determine the influence of the excitation wavelength on the kinetics of the OTA^{2+} formation, dyad solutions in aerated MeCN were irradiated at 430 and 500 nm, respectively. At 430 nm OTA^+ shows a local absorption maximum that superimposes the ruthenium MLCT band, thus, irradiation at 430 nm also excites OTA^+ . This might favor undesired back electron transfer re-reducing OTA^+ . In contrast, no OTA^+ absorption is observed at 500 nm and irradiation at this wavelength should not promote the back reaction. However, excitation of the ruthenium photosensitizer will only occur into the very tail of its $^1\text{MLCT}$ band. As a result, this experiment might also give an insight in the photostability of the generated Ru- OTA^+ species, the influence of OTA^+ excitation on the nature of the photoproduct. The irradiation times were the

same as in Figure III.49.

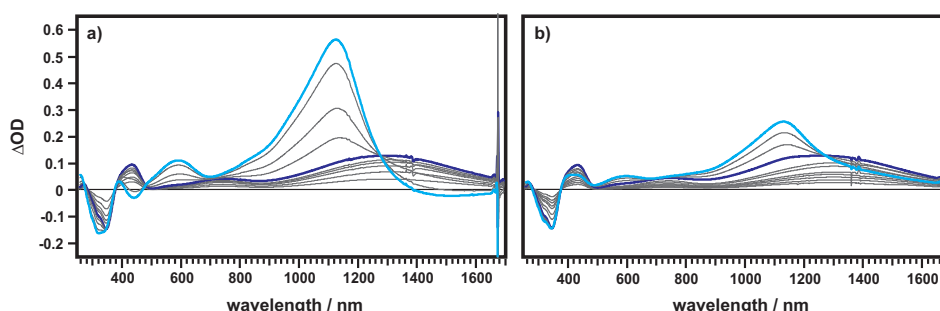


Figure III.51 Continuous irradiation of aerated MeCN solutions of Ru-OTA in presence of an excess of Sc^{3+} . Excitation occurred at a) 430 nm and b) 500 nm.

Directly observable from the spectra in Figure III.51 is the formation of OTA^{2+} in both cases albeit at different rates. Irradiation of Ru-OTA at 430 nm shows complete OTA^+ formation after 10 min (blue trace in Figure III.51 a) and formation of twofold oxidized OTA is finished after 3 h (cyan trace in Figure III.51 a). The obtained spectra are identical to the ones obtained after irradiation at 450 nm and the timescales observed for the OTA^{2+} formation agree well. Irradiation at 500 nm on the other hand shows much slower photoinduced generation of OTA^+ and the twofold oxidized species. This however, is attributed to the fact that the photosensitizer is barely excited at this wavelength.

III.6.3 Irradiation of Aerated Samples in Absence of Sc^{3+}

As shown above present scandium ions lead to a significant positive shift of the O_2 reduction potential from -1.25 V vs. $\text{Fc}^{+/0}$ to -0.2 V. Therefore, oxygen reduction in absence of Sc^{3+} should be somewhat more difficult and strongly influence the electron transfer kinetics in the continuous irradiation experiments.

Figure III.52 depicts the difference absorption spectra after continuous irradiation of aerated samples of Ru-OTA and AQ-Ru-OTA in pure MeCN at 450 nm.

From the graphs in Figure III.52 it is directly observable that no OTA oxidation occurs in the triad or dyad solutions in absence of Sc^{3+} . This leads to the conclusion that not only the presence of O_2 is responsible for the formation of OTA^+ and even OTA^{2+} upon continuous irradiation of the aerated MeCN solutions. Addition of scandium ions is crucial to enable electron transfer from OTA to O_2 , since they significantly reduce the reduction potential of oxygen.

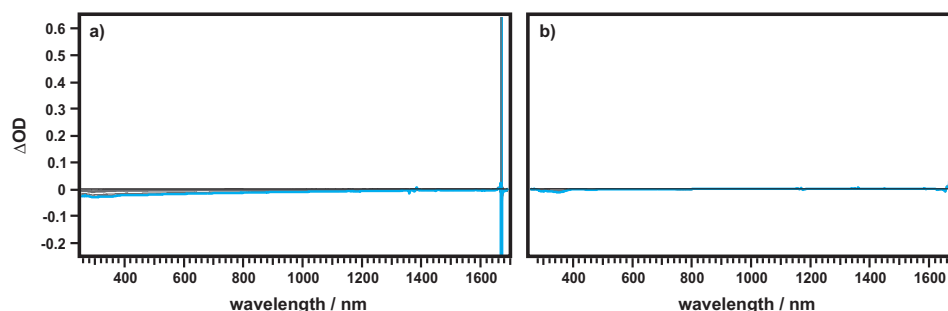


Figure III.52 Continuous irradiation of aerated MeCN solutions of Ru-OTA (a) and AQ-Ru-OTA (b) at 450 nm in absence of Sc^{3+} . Cyan traces: after 3 h.

III.6.4 Dark Reactions of Aerated Samples in Presence and Absence of Sc^{3+}

From the experiments above it is known that electron transfer from OTA to O_2 as the terminal electron acceptor only occurs in presence of scandium ions. In the following the influence of the light source was studied. It was determined whether the electron transfer reaction was only dependent on the presence of O_2 and Sc^{3+} in the sample and also occurs as a dark reaction, or if it is indeed photoinduced.

Figure III.53 depicts the difference spectra recorded on dyad (left) and triad (right) solutions in aerated MeCN in presence (top) and absence (bottom) of Sc^{3+} . All reactions were kept in the dark during the entire duration of the measurements. The total reaction times in presence of Sc^{3+} are the same as for the irradiation experiments (III.6.2); 3 h in case of Ru-OTA, and 30 min for AQ-Ru-OTA.

In presence of 0.02 M scandium ions (Figure III.53 a and b) OTA oxidation is observed in aerated solution even in the dark. After 3 h in the dark, the spectrum recorded on the dyad shows a shoulder at 1140 nm, indicative of OTA^{2+} formation. With respect to the extinction coefficient of $8300 \text{ M}^{-1}\text{cm}^{-1}$ at 1140 nm, 14% OTA^{2+} are formed in the aerated dyad solution after 3 h, even in absence of light. In the aerated AQ-Ru-OTA MeCN solution in presence of scandium ions, OTA^{2+} formation reached a steady state in the irradiation experiment after only 30 min (Figure III.49). In the respective dark experiment (Figure III.53 b) no twofold oxidized OTA was observed after the same reaction time. However, oxidation of 37% of the amine to OTA^+ did occur even in absence of light. Continuing oxidation to OTA^+ and further oxidation to OTA^{2+} in the triad on a longer timescale is likely. Therefore, electron transfer from OTA to O_2 yielding the scandium ion-stabilized superoxide anion is not a photoinduced reaction. Nevertheless, irradiation of the sample solutions does accelerate OTA^{2+} formation.

In accordance with the results from the continuous irradiation experiments of both,

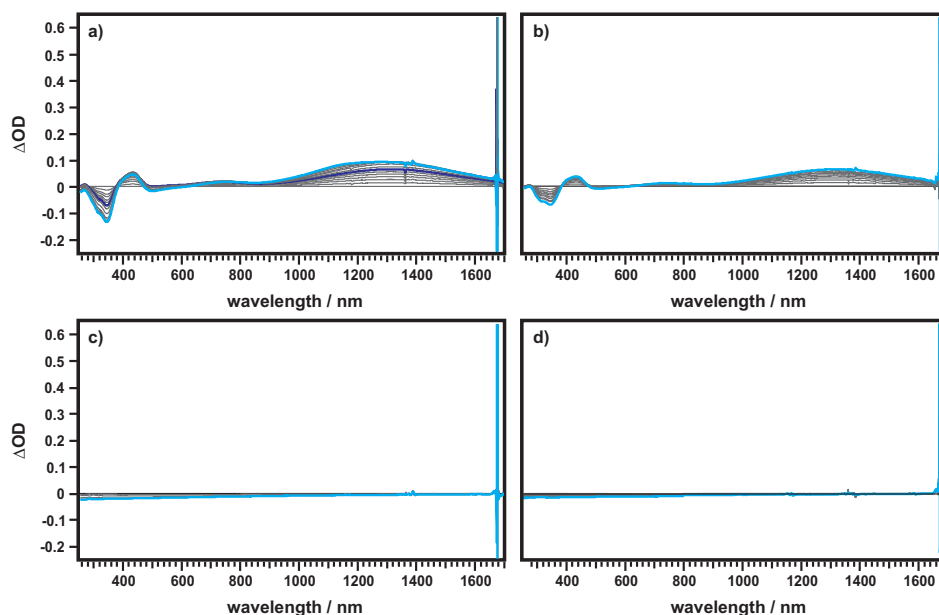


Figure III.53 Difference spectra recorded on aerated MeCN solutions kept in the dark. **a)** Ru-OTA + Sc³⁺ (blue trace = 10 min, cyan trace = 3 h), **b)** AQ-Ru-OTA + Sc³⁺ (cyan trace = 30 min), **c)** Ru-OTA without Sc³⁺ (cyan trace = 3 h), and **d)** AQ-Ru-OTA without Sc³⁺ (cyan trace = 3 h).

aerated dyad and triad solutions (Figure III.52), in absence of Sc³⁺ no OTA oxidation is observed.

Based on the results of the above discussed experiments, it is concluded that O₂, not AQ, is the final electron acceptor in the continuous irradiation experiments. The electron is transferred from OTA to O₂ leading to OTA²⁺ and superoxide anion formation in the samples. The latter is strongly stabilized by coordination of scandium ions. In absence of the scandium ions no amine oxidation is observed. The metal ions are essential for the electron transfer reaction since they significantly facilitate O₂ reduction and stabilize the resulting radical anion. The electron transfer process is not photoinduced, but it can be accelerated by irradiation. Furthermore, an AQ-mediated electron transfer mechanism can be described for the continuous irradiation of AQ-Ru-OTA in aerated MeCN solution in presence of Sc³⁺. This is the reason for the significant acceleration of OTA²⁺ formation in the triad, as compared to the dyad.

III.6.5 Irradiation of De-Oxygenated Samples in Presence of Sc³⁺

Since the generation of twofold oxidized OTA in the aerated samples in presence of 2000 eq Sc³⁺ can be attributed to photo-accelerated electron transfer from OTA to O₂, all measurements were repeated in de-oxygenated solutions. Formation of OTA²⁺ in

de-oxygenated solutions would then point towards accumulative charge separation in the purely molecular AQ–Ru–OTA triad.

Figure III.54 depicts the difference spectra obtained after continuous irradiation of de-oxygenated MeCN solutions of Ru–OTA (a) and AQ–Ru–OTA (b) in presence of Sc^{3+} at 450 nm. Spectra were recorded after irradiation intervals of 1 h.

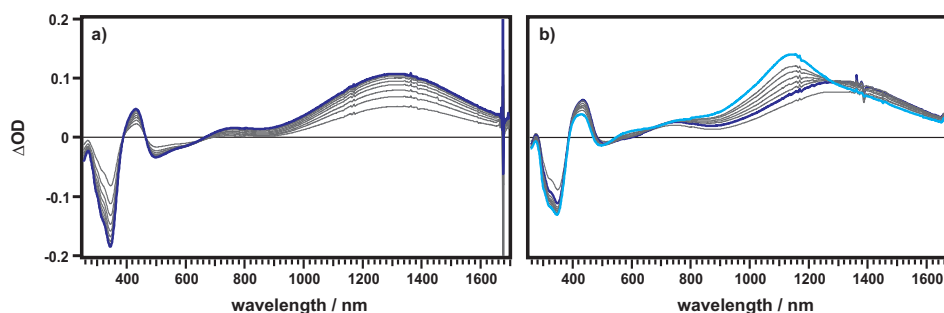


Figure III.54 Difference spectra after continuous irradiation of de-oxygenated MeCN solutions of Ru–OTA (a) and AQ–Ru–OTA (b) in presence of 0.02 M Sc^{3+} at 450 nm. a) blue trace = 9 h. b) blue trace = 2 h, cyan trace = 9 h.

Continuous irradiation of the dyad solution over 9 h shows continuous formation of OTA^+ . After 9 h (blue trace) no more spectral changes are observed. Therefore, in de-oxygenated MeCN solutions no twofold oxidized OTA is formed, as is the expected behavior in the dyad, due to the lack of an acceptor for two electrons. However, roughly $4 \cdot 10^{-9}$ mol ($2.4 \cdot 10^{15}$ molecules) residual O_2 are present during the experiment. With $1.8 \cdot 10^{16}$ Ru–OTA molecules in the sample and considering an error of one order of magnitude for the residual O_2 content in the cuvette, both are present in a 1:1 ratio and formation of OTA^+ in the dyad can be ascribed to the present oxygen. In AQ–Ru–OTA, CI over 2 h leads to the quantitative generation of OTA^+ (blue trace in Figure III.54). Continued irradiation of the sample leads to further oxidation of OTA^+ and formation of the OTA^{2+} related band at 1130 nm. Compared to the data from the chemical oxidation experiment 23% OTA^{2+} is formed in the above experiment. The amount of AQ–Ru–OTA is $3 \cdot 10^{-8}$ mol and calculation gave $4 \cdot 10^{-9}$ mol of O_2 . After single oxidation of all complex molecules, in 23% of them OTA is oxidized a second time. Roughly $4 \cdot 10^{-8}$ mol oxidant are therefore necessary to produce the spectrum in Figure III.54 which is well in range of the calculated amount of residual O_2 . OTA^{2+} formation in absence of O_2 requires the twofold reduction of AQ. The presence of AQ^{2-} should be indicated by an absorption band around 400 nm in the difference spectrum recorded on AQ–Ru–OTA. In the dyad, on the other hand, no such band is expected. Figure III.55 displays the final difference spectrum after an irradiation period of 9 h of the de-oxygenated triad solution (black trace). The black spectrum

can be fitted considering a 23% contribution of the OTA^{2+} (cyan trace) and 47% of the OTA^+ (blue trace) spectrum. In theory, 77% OTA^+ are still present after 9 h, however, the 30% OTA^+ already present prior to the irradiation experiments have to be considered.

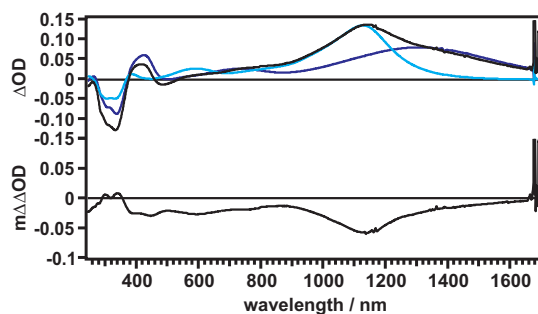


Figure III.55 Top: Difference spectra after 9 h of irradiation (black), of 47% OTA^+ (blue), and 23% OTA^{2+} (cyan). Bottom: Difference spectrum after subtraction of the oxidized OTA contributions.

Though, the band maxima correlate very well in the NIR region, below 800 nm this fitting technique leads to unreliable results. The calculations above show that formation of OTA^+ as well as twofold oxidized OTA can be completely ascribed to the residual O_2 . Therefore, the lack of a spectral signature for twofold reduced AQ in the difference spectrum can be taken as evidence for O_2 being the final electron acceptor, as proposed above.

III.6.6 Irradiation of De-Oxygenated Samples in Absence of Sc^{3+}

In absence of Sc^{3+} no formation of OTA^+ or twofold oxidized OTA is expected. Investigation of the aerated samples showed that OTA oxidation is dependent on the presence of scandium ions in the samples and does not occur without them. Figure III.56 depicts the difference spectra obtained after irradiation of de-oxygenated MeCN solutions of Ru-OTA (Figure III.56 a) and AQ-Ru-OTA (Figure III.56 b) in absence of scandium metal ions.

Irradiation of the dyad solution over 9 h seemed to induce slight degradation of the sample. This finding is not too surprising, considering the irradiation period. Furthermore, bimolecular processes can occur on this timescale that are not that easily tracked. In the case of AQ-Ru-OTA, minimal oxidation of OTA (6%) is observed even in absence of Sc^{3+} which was not expected in the CI experiment. Though photoinduced charge separation in the triad is the goal of the CI studies, the charge-separated state lifetime in pure, de-oxygenated MeCN ($2.4 \mu\text{s}$) was deemed

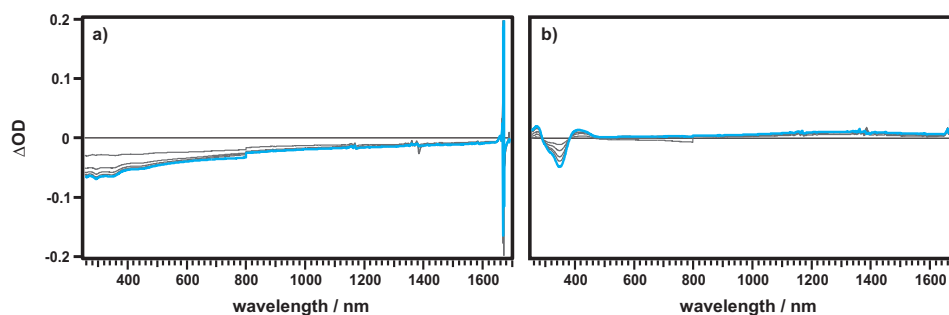


Figure III.56 Difference spectra after continuous irradiation of de-oxygenated MeCN solutions of Ru-OTA (a) and AQ-Ru-OTA (b) in absence of Sc^{3+} at 450 nm.

too short to accumulate enough $\text{AQ}^- \text{-Ru-OTA}^+$ to detect on a UV-Vis timescale. The emission of the light source in the continuous irradiation experiments amounts to 5 photons per molecule per minute. Irradiation of the sample over 1 h then gives a total of 300 photons per molecule.

III.6.7 Dark Reactions of De-Oxygenated Samples in Presence and Absence of Sc^{3+}

In presence of 0.02 M Sc^{3+} AQ-Ru-OTA shows 21% OTA^+ formation after 9 h in de-oxygenated MeCN solution even in the dark. Thus, after 9 h in the dark $6.3 \cdot 10^{-9}$ mol of the triad are oxidized. In the analog dark experiment in the Ru-OTA dyad, 24% ($7.2 \cdot 10^{-9}$ mol) of OTA^+ is formed. Within the accuracy of the calculations, the amounts of OTA^+ formed in the de-oxygenated dyad and triad solutions in presence of Sc^{3+} are the same. Furthermore, the amount of OTA^+ can be explained by the residual O_2 ($3.8 \cdot 10^{-9}$ mol) in the de-oxygenated sample. The amount of residual oxygen in the Schlenk cuvettes is strongly dependent on the velocity of sample preparation and tightness of the cuvette.

The final series of spectra displayed in Figure III.57 clearly shows that OTA is not oxidized in Ru-OTA in absence of Sc^{3+} . Compared to the data obtained from the Sc^{3+} -free de-oxygenated dyad solution that was irradiated over 9 h, decomposition of the sample in the dark is not as severe. In the case of the triad solution extremely slight OTA^+ (4%) formation is observed. The analog experiment performed under irradiation showed formation of 6% OTA^+ after 9 h. Such a small quantity of singly-oxidized OTA even in the dark-experiment might be attributed to the 2.4 μs lifetime of $\text{AQ}^- \text{-Ru-OTA}^+$ in pure, de-oxygenated MeCN and the fact that total light exclusion is not achievable. In contrast to the dark experiments on the aerated solutions, the

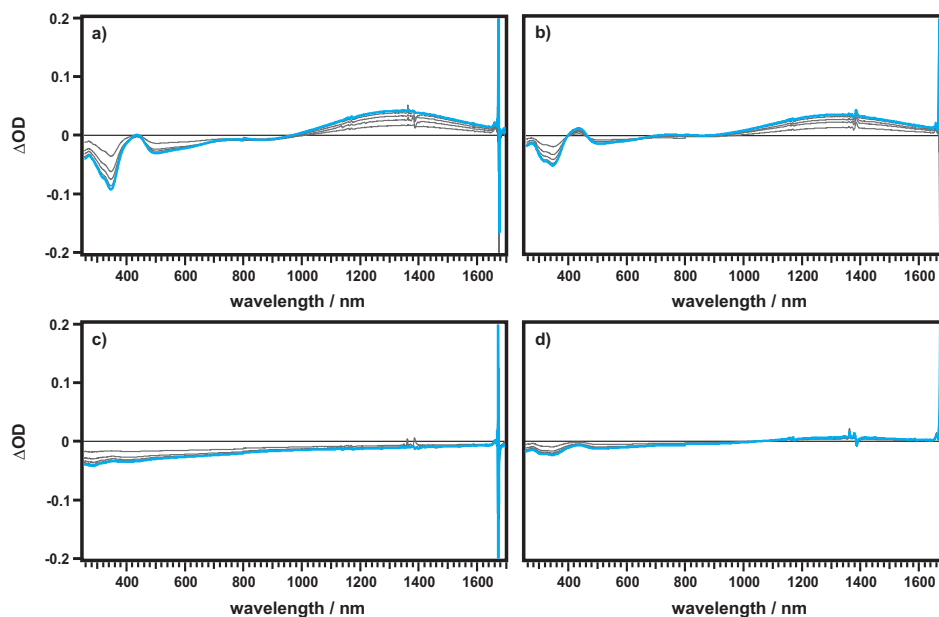


Figure III.57 Difference spectra recorded on de-oxygenated MeCN solutions kept in the dark for the duration of 9 h. **a)** Ru-OTA + Sc^{3+} , **b)** AQ-Ru-OTA + Sc^{3+} , **c)** Ru-OTA without Sc^{3+} , and **d)** AQ-Ru-OTA without Sc^{3+} . The cyan traces correspond to the spectra recorded after 9 h in the dark.

sample compartment cannot be closed with its lid when the Schlenk-cuvette is used for the O_2 -free measurements. Cuvette and sample compartment are only covered by a black cloth that might some light to pass through.

III.6.8 Possibility of Photo-Degradation

On such long timescales of irradiation, photo-degradation cannot be fully excluded. A study on triarylamine radical cations has shown that thermally relatively stable radicals may undergo photoinduced electrocyclization.^{146,147} Visible light irradiation of the radical cations induces formation of the corresponding carbazoles albeit with rather small quantum yields. The probability for setting the triarylamine radical cation back to its uncharged ground state is bigger than electrocyclization. Though the photochemical generation of carbazoles cannot be fully excluded because excitation at 450 nm occurs partly into an OTA^+ absorption band, it is difficult to find conclusive spectral evidence for their presence. Neutral carbazoles usually exhibit ground state absorption below 400 nm, as does neutral OTA.¹⁴⁸ Furthermore, spectral features for oxidized carbazoles are a band around 450 nm and a rather sharp band at 800 nm.^{149,150} Due to the small extinction coefficient of the bands (roughly $450 \text{ M}^{-1} \text{ cm}^{-1}$) their detection in the present CI experiments is difficult.

However, the very similar spectra of AQ-Ru-OTA in pure MeCN and after addition

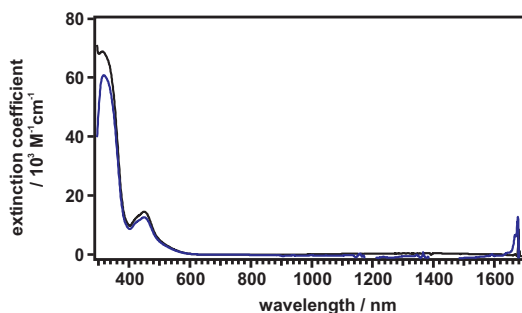


Figure III.58 Absorption spectra of AQ-Ru-OTA in pure MeCN (black trace) and of the de-oxygenated, irradiated solution after addition of NEt_3 .

of the reductant NEt_3 to the irradiated, de-oxygenated sample of AQ-Ru-OTA in MeCN indicate complete re-reduction of OTA in AQ-Ru-OTA (Figure III.58). Addition of NEt_3 induces precipitation of a white solid and the sample color changes back from a greyish tone to yellow. The white precipitate is most likely $\text{Sc}(\text{OH})_6^{3-}$ which is formed in presence of an excess of aqueous alkaline solutions.¹⁵¹ Though, hydroxide formation is not possible in the used pure, dry and de-oxygenated MeCN, the added NEt_3 had not been dried and freshly distilled prior to its use as the reductant. It is therefore possible that the used NEt_3 has imported trace amounts of H_2O which lead to the hydroxide formation with scandium. Nevertheless, also based on the above shown spectra, no clear statement can be made concerning the presence of carbazoles after irradiation.

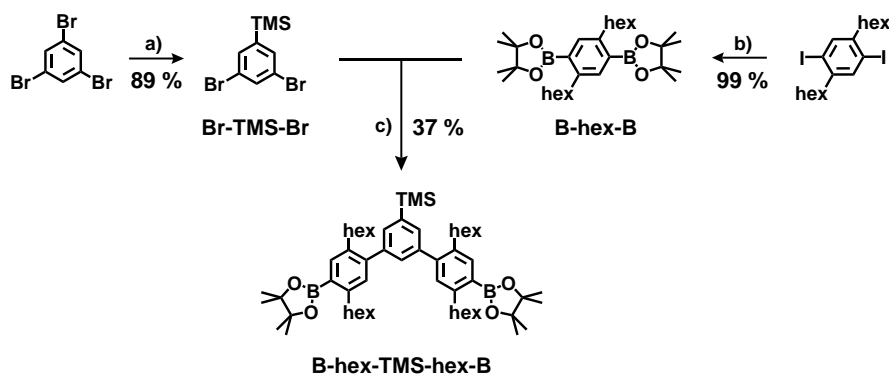
OTA oxidation in Ru-OTA and AQ-Ru-OTA is dependent on the presence of O_2 in the sample. In de-oxygenated solutions, with only trace amounts of O_2 present, formation of OTA^+ is slower than in the aerated samples. Oxidation also only occurs in presence of scandium metal ions and can be further accelerated by visible light irradiation of the sample solutions. As a result, the underlying reason for OTA^{2+} formation in the CI experiments is the interplay between O_2 , light, and the scandium metal ions. No intramolecular charge accumulation takes place in AQ-Ru-OTA. The AQ acceptor merely acts as an electrocatalyst for the electron transport from the OTA to O_2 as the final electron acceptor.

III.7 Towards Accumulative Electron Transfer in an AQ–Ru–OTA–Ru–AQ Pentad

The following section will focus on electron transfer in an AQ–Ru–OTA–Ru–AQ pentad. By attaching an extra ruthenium photosensitizer we hoped to increase the chance of a second excitation of the same molecule. In addition to the two metal sensitizers, a second anthraquinone acceptor was attached. By the provision of two acceptors, the only charge accumulating unit is the OTA donor, therefore hopefully minimizing the electrostatic problems associated with the buildup of charge. Another major advantage of the presence of two AQ acceptors in the pentad is that neither BRØNSTED- nor LEWIS-acids have to be added to enable twofold reduction of AQ by the reduced photosensitizer. As discussed in III.4 and III.2, addition of acids in either form seemed to lead to partial, premature oxidation of OTA.

III.7.1 Synthetic Pathway to AQ–Ru–OTA–Ru–AQ

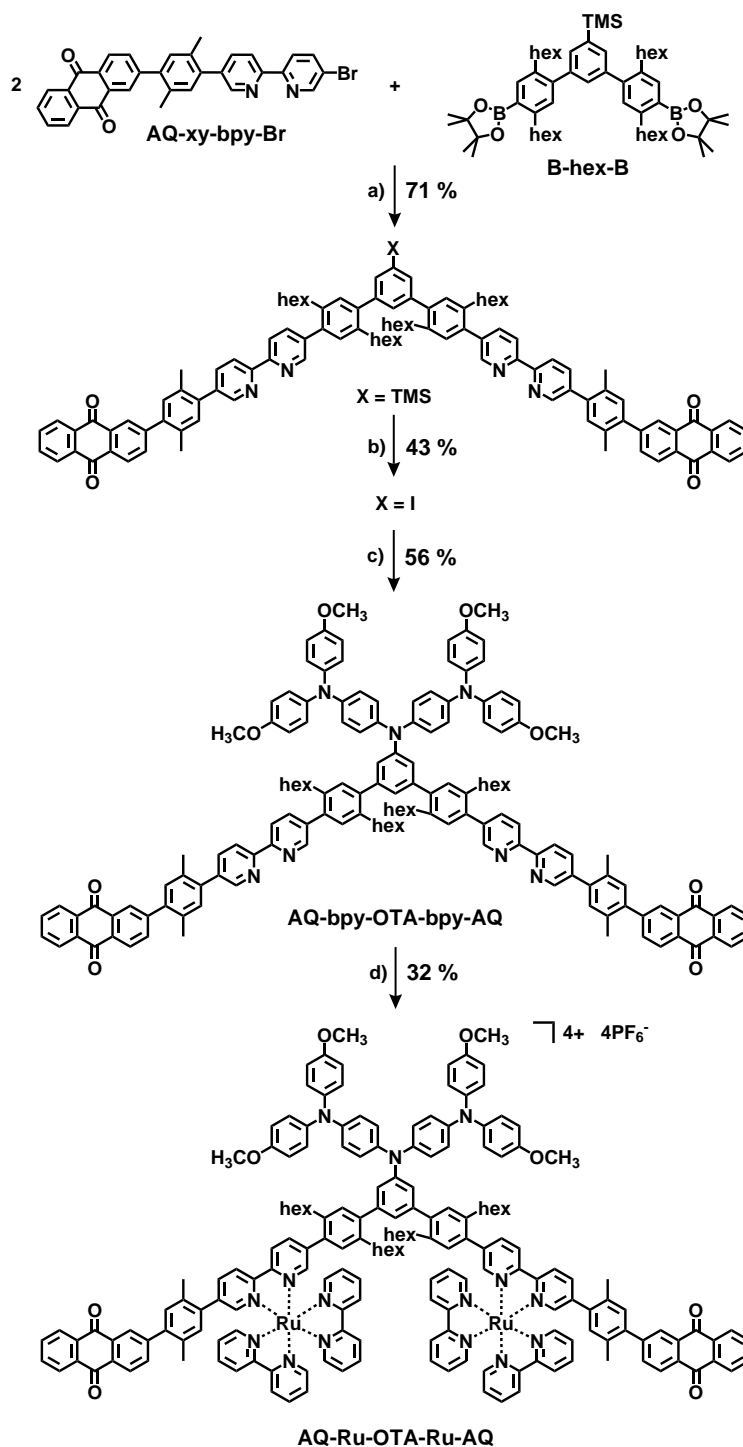
Preparation of the pentad was started with the exchange of one bromine atom on 1,3,5-tribromobenzene by TMS after treatment with 1 eq n BuLi and TMSCl.



Scheme III.18 Synthesis of the core molecule: **a)** n BuLi, TMSCl, Et₂O, -78 °C, 3 h, RT, over night; **b)** bis-pinacolato diboron, KOAc, PdCl₂(PPh₃)₂, DMF, 90 °C, 2 d; **c)** Na₂CO₃, Pd(PPh₃)₄, toluene/EtOH/H₂O, reflux, 3.5 d.

During the preparation of AQ–bpy–OTA as ligand for the Ru-triad solubility problems were observed. Thus, for the more extended organic backbone of the pentad, bearing two bipyridines and AQ, each, a benzyl spacer bearing two hexyl substituents was chosen. By this measure the solubility of the final ligand should be facilitated. The spacer, B–hex–B, was prepared from 1,4-dihexyl-2,5-diiodobenzene via SUZUKI-coupling with bis-pinacolato diboron in DMF in almost quantitative yield.

Br–TMS–Br and B–hex–B were coupled Pd-catalyzed in a toluene/EtOH/H₂O mix-



Scheme III.19 Synthesis of the final ligand: **a)** Na_2CO_3 , $Pd(PPh_3)_4$, toluene/EtOH/ H_2O , $100^\circ C$, 31 h; **b)** ICl , DCM/MeCN, $0^\circ C$ /RT, over night; **c)** OTA, NaO^tBu , $Pd(dba)_2$, $(HP^tBu_3)BF_4$, toluene, reflux, 5 d; **d)** $AgNO_3$, Ru-pre, $CHCl_3$ /EtOH, reflux, 4 d.

ture to give the core compound B-hex-TMS-hex-B as a colorless oil. Regarding this coupling step, a fourfold excess of B-hex-B and a rather long reaction time of 3.5 d provided the best yield of 37%. Furthermore, gravitational column chromatography was necessary in order to fully separate impurities containing boronic ester functionalities (Scheme III.18). The core molecule prepared in this manner was further coupled in a SUZUKI-type reaction to 2 eq of the AQ-xy-bpy-Br sidearm prepared in III.4. This gave AQ-bpy-TMS-bpy-AQ as a yellow solid in 71% yield. Subsequent deprotection of the TMS group by reaction with ICl gave 43% of the desired AQ-bpy-I-bpy-AQ product after column chromatographical purification. Finally, Pd-catalyzed N-C coupling in toluene with the OTA donor gave the ligand AQ-bpy-OTA-bpy-AQ as a brown solid in 56% yield. (Scheme III.19) As a final step, AQ-bpy-OTA-bpy-AQ was reacted with 3 eq of Ru-pre in presence of 6 eq of AgNO_3 to facilitate the complexation. All reactants were suspended in a de-oxygenated $\text{CHCl}_3/\text{EtOH}$ mixture in the dark and heated to reflux for 4 d. The precipitated AgCl was filtered from the cooled reaction mixture and washed with DCM. Repeated column chromatography on SiO_2 with an eluent mixture of acetone/ $\text{H}_2\text{O}/1\%$ aqu. KNO_3 and subsequent precipitation with sat. KPF_6 -solution gave the desired pentad as the PF_6 -salt in 32% yield.

III.7.2 Electrochemical Characterization

In Figure III.59 the cyclic voltammogram of AQ-Ru-OTA-Ru-AQ (bottom) is depicted in comparison to Ru-ref (top). Both voltammograms were recorded in Ar-purged MeCN solutions with different internal standards. In case of Ru-ref, $\text{Fc}^{+/0}$ was added and Me_{10}Fc was used for the pentad. The sweep rate was always 0.1 V/s and 0.1 M TBAF₆ was used as supporting electrolyte.

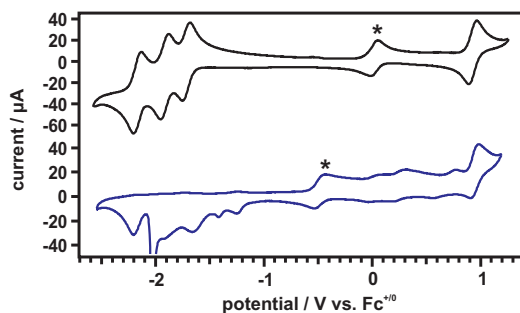


Figure III.59 Cyclic voltammograms of Ru-ref (black trace) and AQ-Ru-OTA-Ru-AQ (blue trace) in Ar-purged MeCN solutions. The internal references $\text{Fc}^{+/0}$ for Ru-ref and Me_{10}Fc for the pentad are marked by asterisks.

The oxidation potential for $\text{Ru}^{3+/2+}$ in Ru-ref is 0.90 V vs. $\text{Fc}^{+/0}$ and the potentials for the three ligand based reductions are -1.72 V, -1.92 V, and -2.17 V vs $\text{Fc}^{+/0}$. These

values agree well with the ones reported in literature.³⁶ All potentials obtained for the pentad are similar to the ones observed in the AQ–Ru–OTA triad. The stepwise oxidation of OTA to OTA^{3+} occurs at -0.01 V, 0.23 V, and 0.65 V vs $\text{Fc}^{+/0}$ and the waves are less pronounced than in AQ–Ru–OTA. A reversible wave for the ruthenium oxidation is observable at 0.91 V. All bpy based reductions at -1.67 V, -1.92 V, and -2.20 V vs $\text{Fc}^{+/0}$ agree well with those of the free ruthenium reference complex. As for the ruthenium triad, no shift in the photosensitizer-based redox potentials is observed in the pentad despite the attachment of the very electron-donating OTA. In the present case the distance between photosensitizer and OTA is too large for the latter to influence the reduction of $\text{Ru}(\text{bpy})_3^{2+}$. The first anthraquinone reduction at -1.25 V vs $\text{Fc}^{+/0}$ is at the same potential as for the triad and coincides well with previously reported values.⁹⁰ When the anthraquinone is reduced a second time to AQ^{2-} (≈ -2 V) the same electrode effect was observed for the pentad as for the triad. The very sharp signal might be attributed to unwanted adsorption and stripping on the electrode which, in turn results in the irreversible reduction potentials. Appearance of the wave at -1.43 V might be due to electrochemical side-reactions and degradation reactions. Due to the more or less identical redox potentials of AQ–Ru–OTA and the pentad, similar thermodynamics are expected. Indeed, the first electron transfer step resulting in the formation of CSS1 ($\text{AQ}^-\text{Ru}^+\text{OTA}^-\text{Ru}^-\text{AQ}^-$) gives a value of -0.88 eV calculated with the formula $\Delta G_{ET}^0 = e(-0.01 \text{ V} - (-1.25 \text{ V})) - E_{00}$. The triplet energy of $[\text{Ru}(\text{bpy})_3]^{2+}$ (E_{00}) is 2.12 eV. ΔG_{ET}^0 for the first electron transfer step in the triad was -0.92 eV. Formation of the second charge separated state $\text{AQ}^-\text{Ru}^+\text{OTA}^{2-}\text{Ru}^-\text{AQ}^-$ is exergonic by 0.6 eV ($\Delta G_{ET}^0 = e((-0.01 \text{ V} + 0.23 \text{ V}) - (-1.25 \text{ V} + (-1.25 \text{ V}))) - E_{00}$) after absorption of a second photon.

III.7.3 Optical Spectroscopic Characterization

UV-Vis spectroscopic investigation of the pentad in MeCN solution gives a very similar spectrum to AQ–Ru–OTA. However, with an overall larger molar extinction, attributable to an even more extended conjugated organic ligand system. The pentad exhibits the typical $^1\text{MLCT}$ band around 450 nm and the very distinct, bipyridine ligand-centered $\pi \rightarrow \pi^*$ transition band at 288 nm.³⁶ The increased absorption between 300 and 400 nm originates from OTA and AQ absorptions, which is also observed in the AQ–Ru–OTA triad.

Compared to the free photosensitizer, the emission maximum of the pentad is red-shifted by 7 nm to 610 nm. The emission intensity is quenched by 93% , indicating non-radiative deactivation of the excited photosensitizer. Regarding the thermodynamic evaluation above, deactivation most likely occurs via electron transfer. Triplet energy

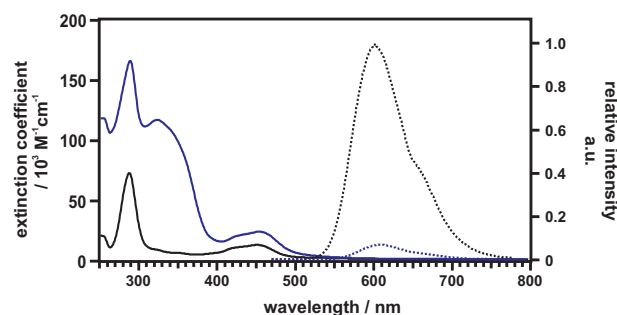


Figure III.60 Absorption (solid trace) and steady-state emission (dashed trace) spectra of AQ–Ru–OTA–Ru–AQ in blue. The spectra of Ru–ref are shown for comparison (black traces). Complexes were measured in de-oxygenated 10^{-5} M MeCN solutions. Emission spectra were corrected for differences in absorption at 450 nm and normalized to the emission of Ru–ref.

transfer between the excited metal center ($E_T = 2.12$ eV) and OTA ($E_T = 3.32$ eV) can be excluded, because this would be a highly exergonic transfer step. The same holds true for energy transfer quenching of the excited photosensitizer by AQ ($E_T = 2.72$ eV).¹²³ Conclusive evidence for electron transfer in the pentad will be given below.

III.7.4 Photophysical Behavior in Different Solvents

In addition to measurements in dry, de-oxygenated MeCN solution, the photoinduced electron transfer behavior of the pentad was investigated in an MeCN/H₂O (v/v 1:1) solvent mixture, as well as in pure HFIP (hexafluoroisopropanol). Though not intrinsically necessary for photoinduced hole accumulation on the OTA donor, hydrogen-bond donors might facilitate it. Already in the MeCN/H₂O solvent mixture AQ⁻ should be stabilized by hydrogen-bond donation from H₂O. In HFIP, a strongly hydrogen bond-donating solvent, the formed hydrogen bonds after photoexcitation should be even stronger.⁸⁸

Usage of hydrogen bond-donating solvents, in contrast to the addition of acids, was expected not to lead to premature oxidation or protonation of OTA. The absorption spectra depicted in Figure III.61 were recorded in MeCN (black), MeCN/H₂O (blue), and HFIP (cyan). No significant differences are observable in the spectra recorded in MeCN and MeCN/H₂O solution. The noise between 1400 and 1500 nm is due to the first-overtone O–H stretching band of H₂O.^{152,153} Contrary to the expectation, dissolution of the pentad in HFIP already leads to changes in the absorption spectrum. A slight hypsochromic shift is observed for the ¹MLCT band of the photosensitizer and a more pronounced two-band character is observed. In addition, the $\pi \rightarrow \pi^*$ band is also blue-shifted from 288 nm to 282 nm. Furthermore, the broad absorption band with a local maximum at 325 nm which is a superposition of absorption bands for

OTA and AQ shows two local maxima at 316 and 350 nm in HFIP. This splitting of the initial band in HFIP might indicate interactions of the solvent with OTA.

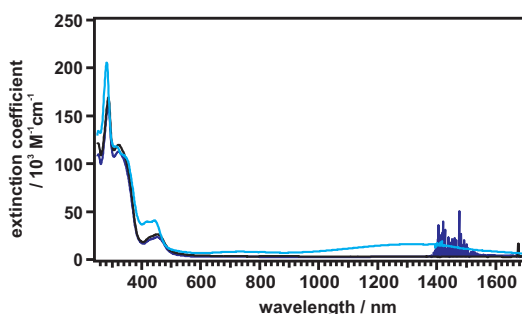


Figure III.61 Absorption spectra recorded on de-oxygenated, 10^{-5} M solutions of AQ–Ru–OTA–Ru–AQ in various solvents. MeCN = black, MeCN/H₂O = blue, and HFIP = cyan.

In addition to the band splits and shifts in the absorption spectrum of AQ–Ru–OTA–Ru–AQ in pure, de-oxygenated HFIP, spectral indications for OTA⁺ are present at 736 and 1310 nm. When compared to the spectra obtained by chemical oxidation to OTA⁺ with Cu(ClO₄)₂, approximately 77% of OTA seem to be oxidized prior to the transient experiments. An extensive study by GUPTA *et al.* has shown the presence of hydrogen bonds between HFIP and quinones in their charge-neutral form.¹³¹ HANKACHE *et al.* have provided clear evidence for hydrogen bond-strengthening between HFIP and AQ^{•-}, once the radical anion was formed after photoexcitation of a Ru–AQ complex. Furthermore, bonding of HFIP to charge-neutral AQ resulted in an increased driving-force for the intramolecular electron transfer from the ruthenium metal sensitizer to AQ.⁸⁸ In this respect, there is most likely hydrogen-bonding between charge-neutral AQ–Ru–OTA–Ru–AQ and the solvent HFIP. As a result, the driving-force for the first charge-separating step might have been increased initiating thermal electron transfer, leading to the partial, premature oxidation of OTA.

III.7.5 Time-Resolved Experiments in Different Solvents

Luminescence Kinetics

The results of the steady-state emission experiment are supported by the kinetic study, showing complete quenching of the photosensitizer luminescence. The emission lifetime of the pentad is slightly increasing from MeCN (≈ 8 ns, $k_Q \approx 10^8$ s⁻¹) and MeCN/H₂O (≈ 10 ns, $k_Q \approx 10^8$ s⁻¹) to HFIP (14 ns, $k_Q = 7.02 \cdot 10^7$ s⁻¹). However, these values are very close to the instrumental detection limit.

In the following, the nature and the lifetimes of the formed photoproducts are investigated and discussed in detail.

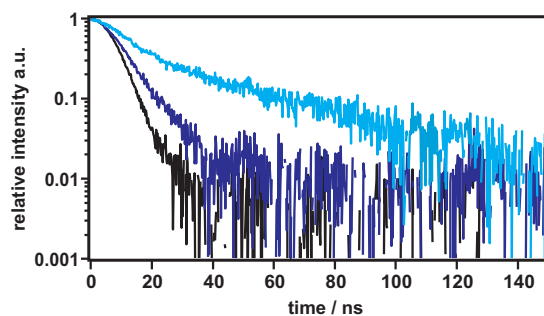


Figure III.62 Emission decays of AQ–Ru–OTA–Ru–AQ in de-oxygenated MeCN (black), MeCN/H₂O (blue), and HFIP (cyan). Excitation occurred at 532 nm and detection at 610 nm.

Identification of the Photoproducts

The transient absorption spectra of the pentad in de-oxygenated solutions of MeCN (black), MeCN/H₂O (blue), and HFIP (cyan) are depicted in the bottom half of Figure III.63. The sharp signal at 1064 nm is due to second order scattering light from the laser beam. All spectra shown were recorded at very high laser powers of 75 mJ. High excitation intensities should promote formation of the second charge-separated state and were therefore chosen for comparison of the transient spectra. More detailed power-dependency studies will be discussed later.

In the visible range from 300 to 800 nm the transient absorption spectra closely resemble those obtained for AQ–Re–OTA (III.2.5) in presence of different acids. The black spectrum recorded in pure MeCN shows local absorption maxima at 410 and 565 nm, as well as a broad band stretching over the NIR region with an approximate maximum at 1320 nm. The features at 410 and 1320 nm correspond to the spectrum of OTA⁺ which is shown as a blue trace in the top half of Figure III.63. The additional band at 565 nm is attributed to the singly reduced AQ. Therefore, the main photoproduct in pure MeCN is AQ–Ru–OTA⁺–Ru–AQ^{•−}.

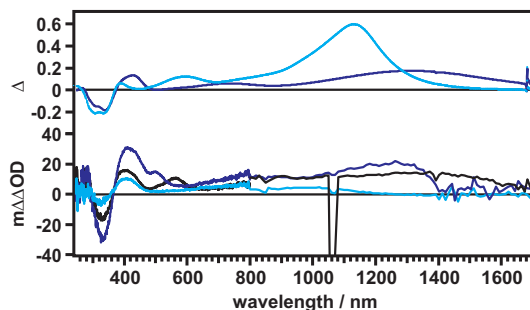


Figure III.63 Top: Spectral characteristics of OTA⁺ (blue) and OTA²⁺ (cyan) after chemical oxidation in MeCN. Bottom: Transient absorption spectra of AQ–Ru–OTA–Ru–AQ in MeCN (black), MeCN/H₂O (blue), and HFIP (cyan). All spectra were measured of 10^{−5}M de-oxygenated solutions.

In the MeCN/H₂O mixture a shift is observed in the visible region for the formed AQ^{•-}. It will most likely be hydrogen-bonded by the present H₂O molecules, resulting in a band-shift from 565 to 500 nm.⁹² Furthermore, formation of the second charge-separated state in the transient experiment would lead to each AQ carrying one electron. In this respect, the intensity of the band corresponding to the reduced AQ is expected to be twice as intense as in the time-resolved experiments on AQ–Ru–OTA. This cannot be derived directly from the above shown spectrum and has to be investigated with power-dependent measurements, discussed later. The band around 400 nm is slightly red-shifted to 415 nm compared to pure MeCN, yet still indicative of OTA⁺. In the NIR region a band with a maximum at 1260 nm is observed. When considered individually and compared to the spectrum in pure MeCN and to the spectral signature of OTA²⁺ it seems to indicate the presence of OTA²⁺ in the photoproduct. However, the maximum is off by 130 nm, when compared to the spectrum obtained after chemical oxidation of OTA by Cu(ClO₄)₂ which shows a maximum at 1130 nm. Though, the general band shapes are similar, the maxima do not fit and the band at 415 nm indicates the presence of the singly oxidized OTA. The dropoff at 1400 nm, leading to the assumption of an OTA²⁺ band can be better explained by the presence of H₂O. The absorption spectrum of the pentad in MeCN/H₂O (blue trace) in Figure III.61 shows noise between 1400 and 1500 nm due to an increased absorption of H₂O in this region. As a result, the NIR band in the transient spectrum is cut off at 1400 nm giving the illusion of a change in the band shape, although it is actually consistent with OTA⁺. The most likely photoproduct in the MeCN/H₂O solvent mixture is the singly charge separated AQ–Ru–OTA⁺–Ru–AQ⁻ with hydrogen bonds between AQ^{•-} and H₂O.

The overall intensity of the transient spectrum obtained from the HFIP solution is lower than in the other solvents. This might be attributable to the fact that oxidized OTA was already present before the photoexcitation experiments in a non-negligible amount. This behavior was also observed for AQ–Ru–OTA in presence of an excess of certain strong LEWIS acids. The obtained spectrum in the visible region closely resembles the one measured of AQ–Re–OTA in presence of chloroacetic acid, which was assigned to AQH–Re–OTA⁺ (Figure III.23). Only one band is observed at 410 nm, and from 490 nm to longer wavelengths no separate bands are recognizable, but the optical density shows a steady rise. Doubly reduced and protonated AQ (AQH₂) is known to show absorption around 400 nm with no further bands at longer wavelengths, which would explain the lack of the band around 500 nm.^{90,93} However, twofold reduced AQ is not expected in the pentad due to the presence of two AQ acceptors. Therefore, the more probable interpretation is the shift of the AQ^{•-} related band further into the

blue, superimposing with the OTA^+ band at 400 nm. Protonation of AQ^- ($\text{pK}_a = 5.3$ in H_2O)⁹⁰ by HFIP ($\text{pK}_a = 9.3$ in H_2O)¹³¹ to form AQH is rather unlikely considering the thermodynamics. However, in the rather acidic HFIP, $\text{AQ}^{\bullet-}$ is very strongly hydrogen-bonded, possibly bordering on protonation. Although the signal in the NIR region is quite weak, a band with a maximum at 1000 nm can be observed. In this case, the dropoff at 1300 nm is not due to solvent absorption since HFIP does not show any absorption in this region. Yet again, the absorption maximum does not correlate with the OTA^{2+} band maximum at 1130 nm obtained in the chemical oxidation measurement. Furthermore, no increased absorption around 600 nm is observed for OTA^{2+} . Consequently, and taking into account the knowledge gained in III.2.5, the photoproduct present in the HFIP solution is most likely $\text{AQ-Ru-OTA}^+-\text{Ru-AQH}$.

Kinetics of the Photoproducts in Different Solvents

Studies on AQ-Re-OTA have shown a remarkable increase in the lifetime of the generated photoproduct $\text{AQ}^--\text{Re-OTA}^+$ depending on the protonation degree. τ was increased from 205 ns for $\text{AQ}^--\text{Re-OTA}^+$ to 3.7 μs for AQH-Re-OTA^+ . Former studies on an AQ-Ru-TAA triad have also shown an increased lifetime of the charge-separated state in presence of HFIP. In pure, de-oxygenated MeCN it was found to be 1.3 μs , which was prolonged to 3.0 μs in pure HFIP. In an equivalent AQ-Os-TAA triad even a 24.5-fold increase in lifetime was observed.¹⁵⁴ In Figure III.64 the decays of the photoproducts of AQ-Ru-OTA-Ru-AQ in the different solvents as discussed above are depicted. Fitting of the decays gives the lifetimes of the singly charge-separated states.

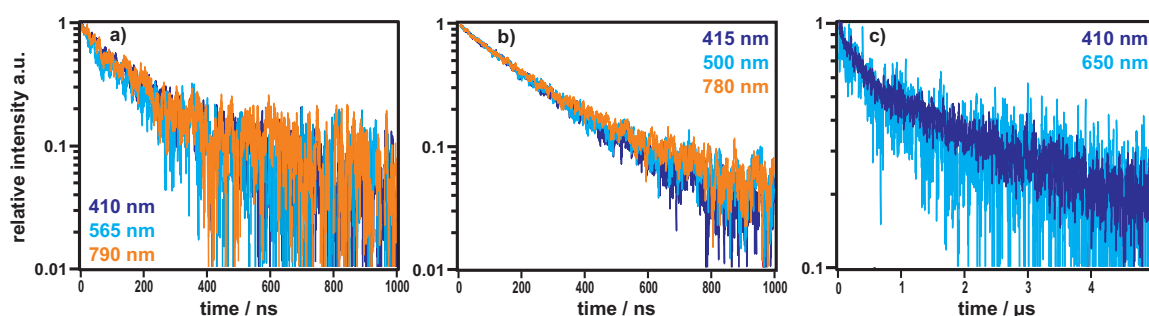


Figure III.64 Transient absorption decays of the photoproducts in MeCN (a), MeCN/ H_2O (b), and HFIP (c).

$\text{AQ-Ru-OTA}^+-\text{Ru-AQ}^-$ in pure, de-oxygenated MeCN has a lifetime of 160 ns. When changing from MeCN to the more hydrogen-donating MeCN/ H_2O mixture, the lifetime is increasing to 220 ns. This increase, though minor, may be attributed to the stabilization of the charge-separated state by hydrogen bonding from the wa-

ter molecules to the reduced AQ. In pure HFIP, a very strong hydrogen-bond donor, the lifetime is further increased. Here, the photoproduct shows a bi-exponential decay with lifetimes of 273 ns and 3.1 μ s. The longer lifetime is very similar to the one obtained for AQ⁻-Ru-TAA⁺ in pure HFIP and might therefore be the real lifetime of the photoproduct in the present experiment.¹⁵⁴ Appearance of two species in the transient absorption experiments, indicated by bi-exponential decays, has been observed before in cases, where OTA was prematurely oxidized (III.4.7 and III.4.7).

Table III.7 GUTMANN acceptor numbers (AN)¹⁵⁵ and dielectric constants (ϵ)¹⁵⁶ of the solvents used. H₂O represents the MeCN/H₂O mixture.

solvent	AN	ϵ	τ / ns
MeCN	18.9	0.460	160
H ₂ O	54.8	1.000	220
HFIP	66.3	1.068	273

The observed trend in the lifetimes correlates well with the expectations due to the polarity and hydrogen bond-donating strengths of the used solvents. As a measure for the hydrogen bond-donating strength, the GUTMANN acceptor number (AN) can be applied.¹⁵⁵ It was presented primarily as a measure for the LEWIS acidity of a solvent. However, in presence of a LEWIS base, such as the reduced AQ, the acceptor number can be interpreted as a measure for the hydrogen bond donor strength of the solvent. The acceptor numbers and dielectric constants of the solvents, as well as the lifetimes of the respective photoproducts are summarized in Table III.7. In case of a 1:1 mixture of MeCN and H₂O, the actual hydrogen bond-donating solvent is H₂O, which is why it is listed in the table. The AN values clearly show an increase in hydrogen bond donor strength when going from pure MeCN to a MeCN/H₂O mixture and to HFIP. HFIP is a very strong hydrogen bond donor due to its fluoro substituents.

Excitation Density-Dependent Transient Absorption Spectroscopy

In the AQ-Ru-OTA-Ru-AQ pentad, formation of the desired second charge-separated state with two holes on the OTA donor and one electron at either one of the AQ acceptors requires two-photon excitation.^{110,111} Therefore, excitation power-dependent measurements were performed. For all solvents, transient absorption spectra were recorded at high (75 mJ), medium (45 mJ), and low (10 mJ) power outputs. For MeCN and HFIP, the difference spectra were constructed from the spectra recorded at high and low power. In the case of MeCN/H₂O, the sharp signal of the laser beam was visible at 45 mJ and it was even more prominent in the measurement with 10 mJ.

Since the rather intense laser signal coincides with the AQ band around 500 nm, the medium energy spectrum was used to construct the difference spectrum. Prior to the subtraction of the low from the high energy spectra, they had to be normalized. For the power-dependent studies on AQ-Re-OTA this was done by multiplying the low energy spectrum with the quotient of high and low power. This however, was not applicable for the measurements on the pentad, presumably due to saturation effects at 75 mJ. Thus, the spectral intensities were matched at 478 and 1285 nm, which represent the isosbestic points between OTA^+ and OTA^{2+} . Singly and doubly oxidized OTA shows absorption in almost all of the spectral range, superimposing also with the spectral signature of reduced AQ. Therefore, using the isosbestic point was deemed the most logical choice to normalize the spectra. Normalization on the AQ signature would seem logical, upon successful two-photon absorption, however, the band was expected to double in intensity.

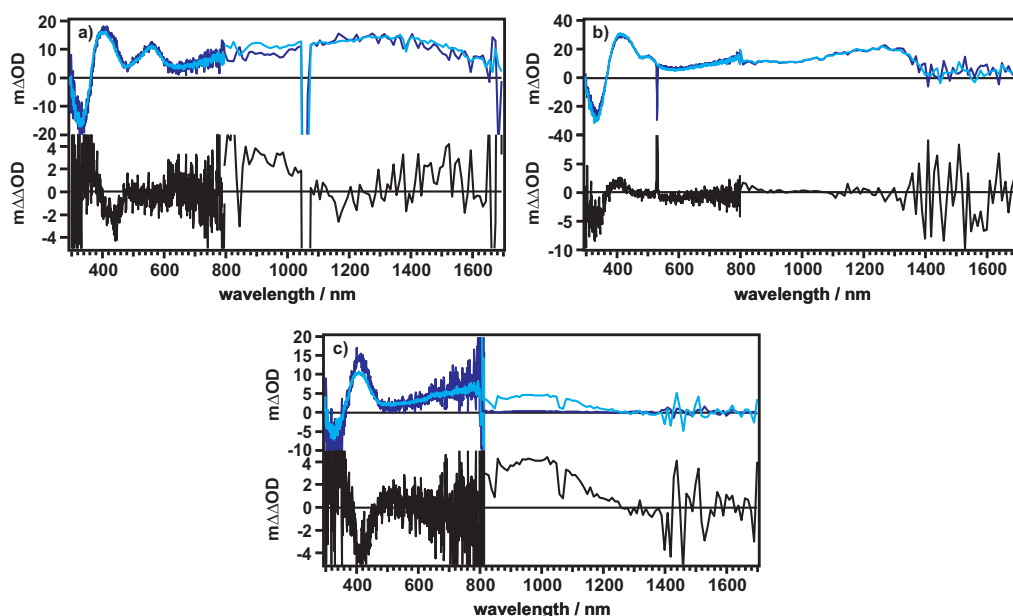


Figure III.65 a) MeCN, b) MeCN/H₂O, and c) HFIP. Top: Intensity-dependent transient absorption spectra (cyan = high energy; blue = low energy). Bottom: Corresponding difference spectra.

The intensity-dependent measurements on the MeCN solution (Figure III.65 a)) did not reveal any spectral indication for OTA^{2+} formation. No increased absorption is observed around 600 nm, or in the NIR region at 1130 nm. The same can be observed for the measurement in MeCN/H₂O. In HFIP, a band at 1000 nm can be observed. However, this maximum deviates too much from the expected absorption at 1130 nm to be explainable by the poor sensitivity of the NIR detector.

In the above experiments performed with our nanosecond pump-probe setup, no

unmistakable indications for the twofold charge-separated state $AQ^- - Ru - OTA^{2+} - Ru - AQ^-$ could be found. The shift of the NIR band to shorter wavelengths in MeCN/H₂O and HFIP may correlate with the formation of OTA^{2+} . However, no increased absorption at 600 nm is observed even at very high excitation powers. Furthermore, 77% of the OTA donor have already been oxidized in HFIP prior to the laser experiments. Therefore, even if OTA^{2+} was observed unmistakably, the underlying mechanism would have been a one-photon process.

III.7.6 Photophysical Behavior in Presence of Thiourea

Analogous experiments to the time-resolved study of $AQ - Ru - OTA$ in presence of an excess of *N,N*-diphenylthiourea were performed on the pentad. In the present case a twofold increased excess was used to see if the increased concentration of diphenylthiourea changes the nature of the generated photoproduct. In Figure III.66 the ground state absorption spectra of the pure pentad (black) and with addition of 2000 eq of diphenylthiourea (grey) are depicted. The large excess of diphenylthiourea leads to the artefact at 340 nm and the noise at smaller wavelengths. All samples were prepared as 10^{-5} M de-oxygenated MeCN solutions. The added 2000 eq represent the upper solubility limit of diphenylthiourea in MeCN.

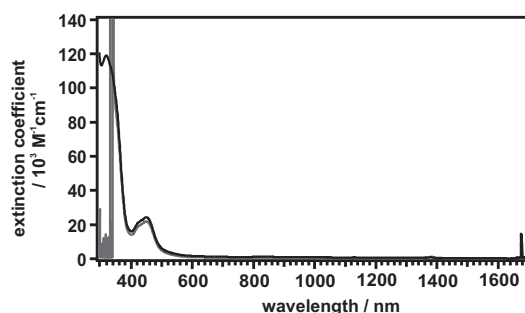


Figure III.66 Ground state absorption spectra of 10^{-5} M MeCN solutions of the pure pentad (black trace) and with 2000 eq diphenylthiourea (grey trace).

It is observable from the graphs that even the addition of a large excess of thiourea does not lead to spectral changes attributable to oxidized OTA. Therefore, eventual spectral signatures for twofold oxidized OTA in the transient experiments can then be credited to a two-photon process.

After the ground state absorption measurements, the same sample solution was investigated with the nanosecond pump-probe setup. The initial photosensitizer luminescence is quenched completely to $\tau = 12$ ns, within the accuracy of the laser setup. In the upper part of Figure III.67 the traces representing the photoproduct after excitation with a 532 nm laser pulse are depicted. Transient spectra of the de-oxygenated

pentad solution were recorded at two different excitation energies. The blue trace corresponds to the photoproduct formed after excitation with a low energy pulse of 10 mJ, which translates to 4 photons per molecule per pulse. For the cyan trace, the pulse energy was 60 mJ which represents a photon count of 26 per molecule per pulse. As a result, generation of the twofold charge-separated state $AQ^- - Ru - OTA^{2+} - Ru - AQ^-$ should theoretically be possible, considering the thermodynamics, as well as the photon flux.

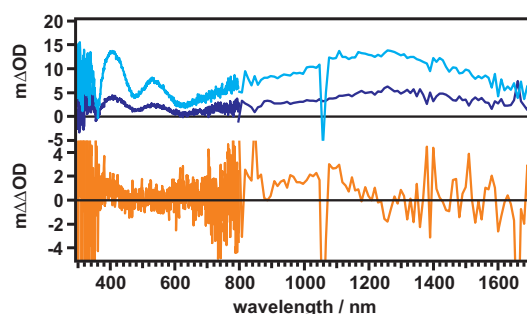


Figure III.67 Top: Transient absorption spectra of AQ-Ru-OTA-Ru-AQ in presence of an excess of diphenylthiourea at low (10 mJ; blue trace) and high energies (60 mJ; cyan trace). Bottom: Difference absorption spectrum by subtraction of the blue from the cyan trace. The spectra were normalized to the isosbestic points (478 nm and 1285 nm) prior to subtraction. All measurements were performed in de-oxygenated MeCN solutions.

In the upper part of Figure III.67 three main bands are observable over the whole spectral range investigated in the transient experiments. The sharp signal at 1060 nm is due to scattering of laser light. The absorption maxima of the two bands located in the visible range of the spectrum do not shift markedly upon the power increase. They are located at 413 and 535 nm. With the information gathered in the previous section III.7.5 and in the chemical oxidation experiment, the bands can be assigned to singly oxidized OTA at 413 nm and slightly hydrogen-bonded, singly reduced AQ at 535 nm. In pure MeCN solution the AQ^- band can be found around 560 nm, whereas the band is blue-shifted to 500 nm upon hydrogen bonding in the MeCN/H₂O mixture. In presence of diphenylthiourea, the band is in between the two extrema, maybe due to weaker hydrogen bonding between AQ^- and the thiourea derivative. In the NIR region, a broad band is observed at low and high excitation energies. The local maximum, however, is slightly blue-shifted from 1300 nm at a low laser power, to 1200 nm at high power. From the chemical oxidation experiments the absorption maximum of OTA^{2+} in the NIR is known to be at 1130 nm once the band is completely developed. Therefore, the band maximum in the NIR does not fully agree with the expected absorption maximum of twofold oxidized OTA. This, however might in part be attributable to the low sensitivity of the NIR detector. As a result, assigning the

high power spectrum to $AQ^- - Ru - OTA^{2+} - Ru - AQ^-$ would be doubtful, especially with the noise in the visible region.

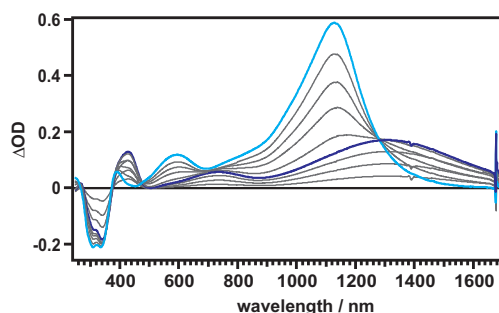


Figure III.68 Stepwise chemical oxidation of $AQ-Ru-OTA-Ru-AQ$ by addition of incremental amounts of $Cu(ClO_4)_2$. Blue trace: OTA^+ ; cyan trace: OTA^{2+} . The arrows mark the isosbestic points used for normalization of the transient absorption spectra.

The supervision of a second, possibly twofold charge-separated state formed at high excitation power should be indicated by a double-exponential decay of the transient absorption signals. Figure III.69 depicts the decays of the absorption signals at 413, 540, and 740 nm in presence of diphenylthiourea.

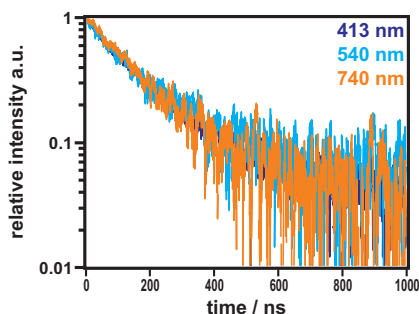


Figure III.69 Kinetic absorption decays of the transient absorption bands at 413, 540, and 740 nm after excitation with a laser pulse of 60 mJ in presence of an excess of diphenylthiourea.

Exponential fitting gives a lifetime of 159 ns for the photoproduct in presence of an excess of thiourea. In pure, de-oxygenated MeCN, $AQ-Ru-OTA^+-Ru-AQ^-$ has a lifetime of 160 ns. With regard to this it can be concluded that the added diphenylthiourea has no lifetime-prolonging effect on the photoproduct. Double-exponential fitting gives lifetimes of 100 ns and 292 ns. These lifetimes are rather similar as is already expected from the shape of the decays. However, it is debatable if a double-exponential fitting of the kinetic absorption data would indeed be logical. To further elucidate the possible presence of trace amounts of a twofold charge-separated state, a difference spectrum of the blue and cyan spectra was constructed (orange spectrum; lower half of Figure III.67). For this, the high- and low-energetic

spectra were normalized at the isosbestic points at 478 nm and 1280 nm, as derived from the chemical oxidation experiment. Again, this approach seemed most reasonable due to oxidized OTA absorption in the whole spectral range, hampering the clear assignment of one neutral point, solely attributable to OTA^+ . An advantage of the difference spectrum is the subtraction of OTA^+ related signatures from the obtained high-energy spectrum, leaving only bands assignable to twofold oxidized OTA and reduced AQ. The orange difference spectrum in Figure III.67 exhibits a rather low signal-to-noise ratio in the visible part of the spectrum. Clear assignment of actual bands is hampered, but slightly increased absorption is observable at 400, 500, and 620 nm. Compared to the difference spectra in the chemical oxidation experiment, the absorptions at 400 and 620 nm might indicate OTA^{2+} formation. In addition, the increased absorption at 500 nm might indicate the presence of hydrogen-bonded AQ^- . The assumption of present OTA^{2+} is supported by the NIR band with a maximum at 1100 nm. Though, the absorption maximum is expected at 1130 nm, the deviation might be attributed to the lower sensitivity of the NIR detector. It is less sensitive than the iCCD camera, used for transient absorption measurements from 300 to 800 nm, and collection of data in the NIR region occurs at intervals of 10 nm with a band width of 10 nm. As a result, twofold charge-separated AQ^- -Ru- OTA^{2+} -Ru- AQ^- might indeed be present in the transient experiment, however, to a very small percentage. Nevertheless, this assumption requires further investigation with faster, maybe more accurate transient techniques, especially in the NIR region.

III.7.7 Summary and Conclusion on Electron Transfer in AQ-Ru-OTA-Ru-AQ

In the preceding section, the synthesis, electro- and photochemical characterization, and photophysical behavior of an AQ-Ru-OTA-Ru-AQ pentad was presented. By the provision of two ruthenium photosensitizers twofold excitation of the same pentad molecule should be facilitated. As for the AQ-Ru-OTA triad, a major advantage of the use of ruthenium polypyridyl sensitizers over their rhenium analogues lies in the excitation wavelength. With the 532 nm pulse used to excite the ruthenium metal center, laser powers up to 80 mJ were achievable.

In contrast to the corresponding triad, the focus in the pentad was solely on hole accumulation on the OTA donor. In principle, each of the AQ acceptors would then carry one electron. This approach should allow us to avoid the addition of strong BRØNSTED or LEWIS acids to facilitate the second reduction of AQ. More importantly, the added acids caused premature oxidation/protonation of OTA in AQ-Ru-OTA,

sometimes to a non-negligible amount. This problem was eliminated by the use of the pentad.

Theoretically and thermodynamically, hole accumulation on OTA should already be possible in pure solvent, such as MeCN. However, to aid the second charge separation by stabilization of the AQ^- intermediate through hydrogen bonds, investigations in an MeCN/H₂O solvent mixture and pure HFIP were performed. In all cases, formation of the photoproducts occurred within the pulse duration of the laser (10 ns) and the main product was found to be singly charge-separated $AQ-Ru-OTA^+-Ru-AQ^-$. In pure MeCN it exhibits a lifetime of 160 ns, whereas the lifetime increased from MeCN/H₂O (220 ns) to HFIP (273 ns/3.1 μ s). This increase in the lifetimes is due to the hydrogen bond-induced stabilization of AQ^- . In HFIP it goes beyond hydrogen-bonding, and the reduced acceptor is protonated to form AQH. Though, the formed photoproduct in HFIP might be optimistically interpreted as the twofold charge-separated state $AQH-Ru-OTA^{2+}-Ru-AQH$, UV-Vis studies showed premature oxidation of OTA. Therefore, formation of OTA^{2+} in the transient experiment would be only a one-photon process. In all cases, an increase of the excitation power did not lead to clear signals indicating the presence of the second charge-separated state.

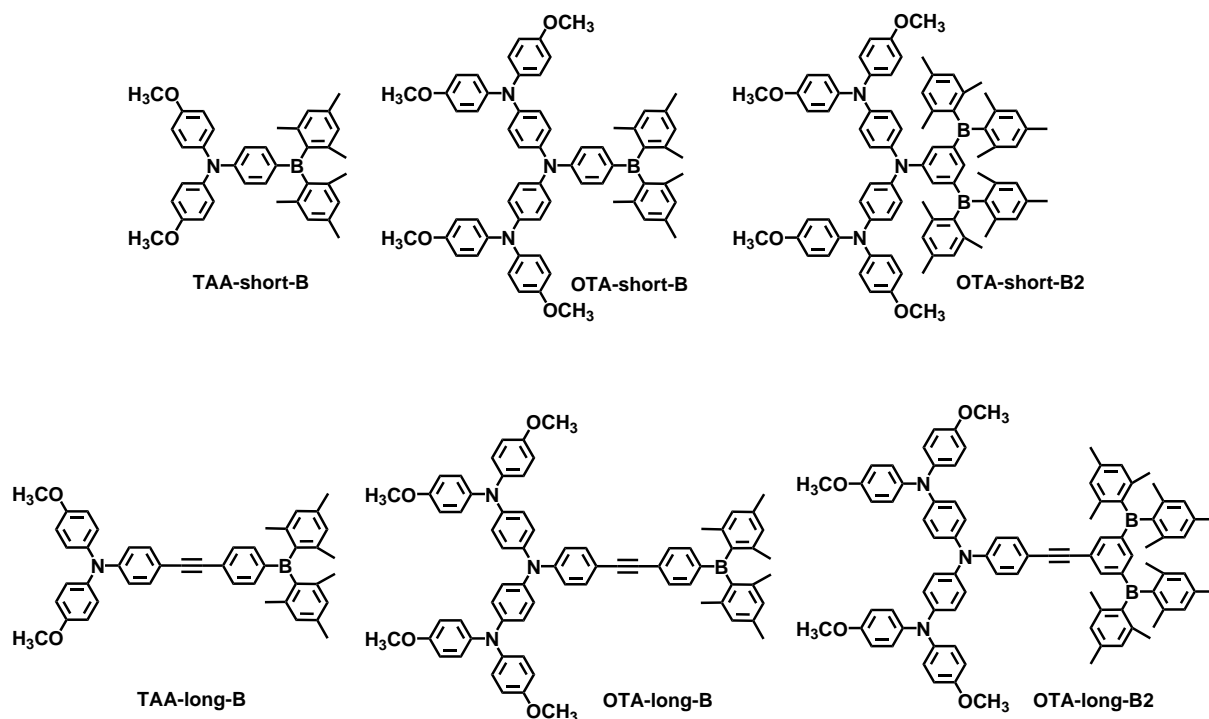
With an excess of N,N-diphenylthiourea, which would selectively coordinate to reduced AQ, no spectral changes indicative of OTA^+ prior to the transient experiments were observed. The lifetime of the observed charge-separated state, most likely being $AQ-Ru-OTA^+-Ru-AQ^-$ was 159 ns. This is an identical value to the one in pure MeCN and addition of diphenylthiourea did not lead to prolongation of the lifetime. Though, no indication for the twofold charge-separated state was found in the transient absorption kinetics, the difference spectrum does indicate formation of twofold oxidized OTA, especially in the NIR region. Clear assignment of the bands in the visible range of the transient spectrum is difficult. Nevertheless, the band at 1100 nm hints at the presence of a small amount of twofold oxidized OTA. Though thermodynamically favored, formation of the second charge-separated state depends on the positive interplay of various parameters, as discussed in section II.4. Even if $AQ^-Ru-OTA^{2+}-Ru-AQ^-$ is formed during the transient measurements, it will most likely be present to a very small percentage, which may complicate its detection.

For the future, investigation of electron transfer reactions in the pentad with different laser setups might provide a more clear proof of hole accumulation on OTA. With a faster technology, e.g. on the femtosecond timescale, it might be possible to track photoproducts whose formation and decay is too fast for our nanosecond setup. Maybe even more promising would be measurements using a pump-pump-probe technique, allowing for the sequential excitation of the sample with two temporally delayed laser

pulses possibly also involving two different excitation wavelengths. Using this technique, the transient spectra after the absorption of one and then two photons can be obtained more accurately than with the increase of the laser power. Furthermore, transient IR-spectroscopy might allow a deeper insight into the exact nature of the AQ acceptor in the charge-separated states. Lastly, a setup for a more precise recording of the NIR region would allow for a clearer assignment of the band to OTA^{2+} .

IV. SOLVENT DEPENDENT EMISSION OF OTA-B(MES)₂ MOLECULES

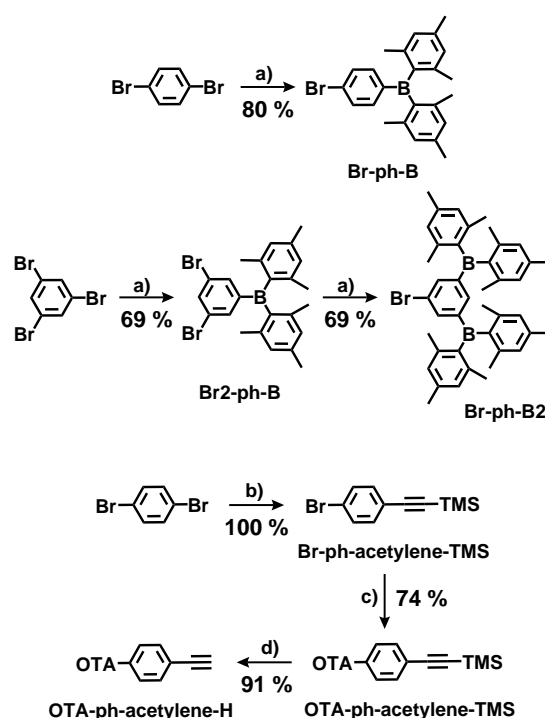
Triarylamine-triarylborane compounds have been studied extensively with regard to their emission properties.¹⁵⁷⁻¹⁶⁰ Organic push-pull systems are employed as dyes in solar cells, non-linear optics, anion sensing, and as emitters in organic light-emitting diodes.^{161,162} Due to this large area of possible applications, fundamental understanding and improvement of existing and creation of new, strong emitters is desirable. The oligo-triarylamine, at hand from the main research focus of this thesis, was further employed in push-pull systems. The main aim was to achieve superior charge transfer (CT) properties due to the remarkable electron donating abilities of OTA. In order to investigate the influence of various parameters on the emission behavior of such D-A compounds, a series of OTA-B(mes)₂ molecules has been synthesized (Scheme IV.1). They vary in the donor and acceptor strength, the distance between D and A, and the position of A relative to D.



Scheme IV.1 Overview of synthesized donor-acceptor molecules.

IV.1 Synthesis of Studied Molecules

The compounds studied in this comparative study are donor–bridge–acceptor molecules comprised of an OTA donor and a boron dimesityl acceptor covalently linked by a conjugated bridging unit. In Scheme IV.2 the reaction pathways for the synthesis of the different acceptor building blocks and the donor–bridge building block are summarized. By coupling of the donor part with the respective acceptor, the final compounds as depicted in Scheme IV.1 were obtained.



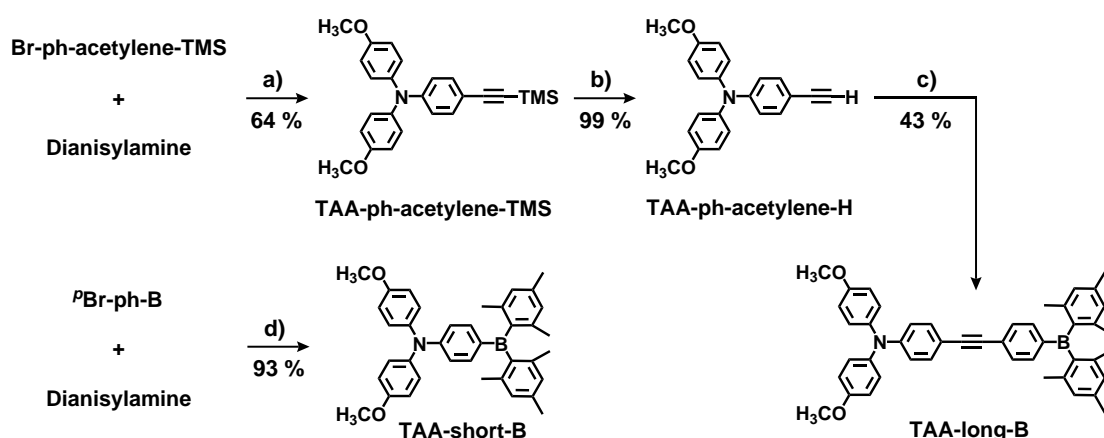
Scheme IV.2 a) *n*BuLi, -78°C , 2-3 h, dimesitylboron fluoride, RT, 1 h to over night; b) trimethylsilyl acetylene, $\text{PdCl}_2(\text{PPh}_3)_2$, CuI, NEt_3 , 100°C , 30 min; c) OTA, NaO^tBu , $\text{Pd}(\text{dba})_2$, $(\text{HP}^t\text{Bu}_3)\text{BF}_4$, toluene, reflux, 20 h; d) TBAF, THF, RT, 1.5 h.

The boron acceptor parts used to synthesize the new D–A compounds were prepared by attaching dimesitylboron units following a bromine-to-lithium exchange on the respective di- or tribromobenzenes. All preparations were performed in a similar manner. To a solution of 1,4-dibromobenzene in Et_2O at -78°C , *n*BuLi was added dropwise and the cold solution was stirred for 3 h. Afterwards, a solution of dimesitylboron fluoride in Et_2O was added in a dropwise fashion, and the reaction mixture was stirred at RT over night. Following the work-up procedure, the product was obtained as a white solid with yields as high as 80%. In case of Br–ph–B2 stepwise attachment of the $\text{B}(\text{mes})_2$ units to 1,3,5-tribromobenzene proved to provide

a far better synthetic route than the one-pot reaction. After the two separate reaction steps the doubly B(mes)₂-substituted product was isolated as a white solid in an overall yield of 48%.

For the synthesis of the D-A molecules in which the donor and acceptor were separated by a longer bridge (OTA-long-B and OTA-long-B2), an acetylene spacer was introduced and coupled to the donor side. The spacer was prepared by SONOGASHIRA coupling of trimethylsilyl acetylene to 1-bromo-4-iodobenzene. OTA was then coupled Pd-catalyzed to Br-ph-acetylene-TMS and the resulting product OTA-ph-acetylene-TMS was deprotected by stirring in a THF solution with TBAF. The donor part obtained in this manner was then coupled to the three different boron acceptors via SONOGASHIRA coupling.

Synthesis of the reference compounds TAA-long-B and TAA-short-B followed the route depicted in Scheme IV.3.



Scheme IV.3 Synthetic route to the references: **a)** NaO^tBu, Pd(dba)₂, (P^tBu₃), toluene, reflux, 30 h; **b)** TBAF, THF, RT, 1 h; **c)** PdCl₂(PPh₃)₂, CuI, NEt₃, 100 °C, 30 h; **d)** NaO^tBu, Pd(dba)₂, (HP^tBu₃)BF₄, toluene, reflux, 2 h.

Of these two references, TAA-long-B was already known, but not yet investigated in terms of its emission behavior.¹⁵⁹ Instead, it was cyclotrimerized to yield a tris-donor-tris-acceptor hexaarylbenzene which was then studied in detail. Preparation of the donor part for TAA-long-B occurred in analogy to OTA-ph-acetylene-TMS. Br-ph-acetylene-TMS was reacted with dianisylamine in a Pd-catalyzed SUZUKI-type reaction to give the intermediate product TAA-ph-acetylene-TMS which was subsequently deprotected by stirring in THF with added TBAF. Final SONOGASHIRA coupling with CuI as co-catalyst in dry and de-oxygenated NEt₃ gave the desired TAA-long-B as a yellow solid in an over yield of 27%. For the preparation of TAA-short-B, Br-py-B was coupled to dianisylamine giving a bright yellow solid in

93% yield.

In Table IV.1 the colors of the individual compounds, as well as the overall yields are summarized. All final compounds were characterized by ¹H NMR and ¹³C NMR, ESI-MS, and elemental analysis.

Table IV.1 Synthesized D–A compounds with overall yields and colors.

compound	color	yield
OTA–long–B	orange	23%
OTA–long–B2	orange	13%
OTA–short–B	bright yellow	62%
OTA–short–B2	orange	37%
TAA–long–B	yellow	22%
TAA–short–B	bright yellow	74%

IV.2 Solvent-Dependent Charge Transfer Behavior

In the following section the six prepared donor–bridge–acceptor fluorophores are investigated with regard to their charge-transfer absorption and emission behavior in solvents of various polarities. The studied compounds are split into two groups (short vs. long) according to their different bridge lengths. In the molecules with the short bridging unit D and A are only separated by one phenyl spacer, whereas in the longer series the bridge consists of a phenyl–acetylene–phenyl unit. Within the two groups, the compounds vary in their donor and acceptor strengths in the order of TAA–bridge–B, OTA–bridge–B, and OTA–bridge–B2. This allows for a direct comparison of absorption, electrochemical, and emission behavior depending on the D–A distance and the strength of D and A.

IV.2.1 Electrochemical Characterization

Figure IV.1 displays the cyclic voltammograms of the studied D–A compounds. All measurements were performed under ambient conditions in dry, Ar-purged THF solutions. The scan rate was 0.1 V/s in all cases and 0.1 M TBAPF₆ was added as supporting electrolyte. The waves marked by asterisks are attributed to electrochemical side reactions as they appear only after one oxidative sweep beyond 0.5 V. All displayed voltammograms were measured on solutions without added Fc^{+ / 0} as the internal reference. In the data evaluation the cyclic voltammograms were shifted ac-

cordingly and are therefore referenced to $\text{Fc}^{+/0}$. Direct addition of ferrocene lead to even more prominent side products than the ones marked by asterisks.

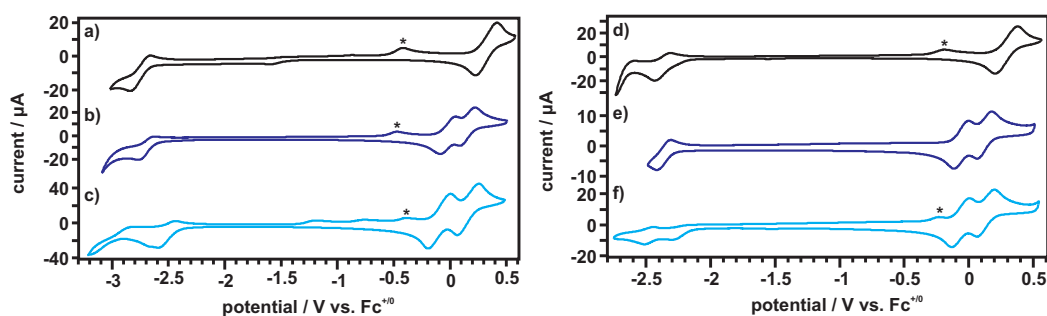


Figure IV.1 Cyclic voltammograms of the six fluorophores in dry, Ar-purged THF in presence of 0.1 M TBAPF₆. Left: **a)** TAA-short-B, **b)** OTA-short-B, and **c)** OTA-short-B2. Right: **d)** TAA-long-B, **e)** OTA-long-B, and **f)** OTA-long-B2. Potential sweep rates are 0.1 V/s.

Oxidation of TAA in TAA-short-B (Figure IV.1 a) occurs at a potential of 0.33 V vs. $\text{Fc}^{+/0}$ which is in line with previously reported values for this triarylamine donor.^{112,113} The first two OTA oxidations in OTA-short-B (Figure IV.1 b) occur at -0.02 V and 0.15 V. Such low oxidation potentials are typical for OTA and were often observed in purely organic, as well as in transition metal complexes containing the oligo-triarylamine donor unit.^{77,96} Usually, OTA exhibits also a third quasi-reversible oxidation wave around 0.6 V vs. $\text{Fc}^{+/0}$ which is not shown in the cyclic voltammograms. In the present study on the emission behavior of the triarylamine-triarylboron compounds only the first oxidation of the amine which occurs at the central N atom is of interest.⁹⁴ It is the electron-richest position in the amine, most readily releasing an electron, and charge transfer is also expected to occur via the shortest pathway between donor and acceptor. Therefore, OTA is a stronger one-electron donor than its TAA analog by ≈ 0.35 eV. Reduction of the boron mesityl acceptor in TAA-short-B, which occurs at -2.75 V, agrees well with values reported earlier.¹⁶³ Substitution of TAA by the stronger electron donor OTA leads to a slight positive shift in the reduction potential of the boron mesityl unit to -2.69 V. In presence of a second acceptor unit in OTA-short-B2 reduction is again shifted positively to -2.52 V vs. $\text{Fc}^{+/0}$. The increase in reduction potential in OTA-short-B2 is due to the presence of two electron withdrawing boron mesityl groups which facilitate reduction of the acceptor. Furthermore, the boron acceptors are located in *meta*-position to the OTA donor in OTA-short-B2, as compared to OTA-short-B. As a result, D and A are electronically more decoupled and transfer of electron density from OTA to the boron acceptor is expected to be weaker.

From the redox potential values one can calculate the free energy for charge transfer

between donor and acceptor, according to $\Delta G_{CT}^0 = e(E_{ox} - E_{red})$. The calculated values, together with the redox potentials extracted from the cyclic voltammograms are summarized in Table IV.2. It is directly observable that the driving force for charge transfer in the short D–A compounds decreases with increasing donor and unchanged acceptor strength, and then further with increasing acceptor strength.

Table IV.2 Redox potentials in THF given in V vs. Fc⁺⁰.

complex	amine ⁺⁰ / V	amine ^{2+/+} / V	borane ^{0/-} / V	ΔG_{CT}^0 / eV
TAA–short–B	0.33		–2.75	3.08
OTA–short–B	–0.02	0.15	–2.69	2.67
OTA–short–B2	–0.09	0.17	–2.52	2.43
TAA–long–B	0.29		–2.37	2.66
OTA–long–B	–0.06	0.12	–2.36	2.30
OTA–long–B2	–0.06	0.16	–2.48	2.42

The electrochemical data obtained for the compounds with the longer D–A distance (Figure IV.1 right) show very similar amine oxidation behavior to their shorter analogs. TAA oxidation occurs at 0.29 V for TAA–long–B and the first two OTA oxidations for OTA–long–B and OTA–long–B2 are at –0.06 V and around 0.14 V vs. Fc⁺⁰. Reduction of the triarylborane units in TAA–long–B and OTA–long–B occurs at a roughly 0.4 V less negative potential than in their analogs with the short phenyl bridge. However, attachment of a second boron mesityl acceptor does not lead to a further increase of the reduction potential of OTA–long–B2. As expected from the redox potentials, no clear ascending or descending trend is observed for the free energy of charge transfer for the longer D–A compounds.

The charge transfer behavior of the studied D–A compounds seems to be less affected by the donor and acceptor strength when D and A are separated over a longer distance.

IV.2.2 Absorption and Emission Behavior in Hexane

For the comparison of absorption and emission behavior of the six compounds, hexane was chosen as solvent. It is the most apolar of all the solvents used and all compounds were readily soluble. Figure IV.2 depicts the absorption (solid traces) and emission spectra (dashed traces) of TAA–short–B (black), OTA–short–B (blue), and OTA–short–B2 (cyan). The absorption spectra of purely organic charge transfer compounds show characteristic charge transfer (CT) bands that can give information about the push-pull system by their location and intensity.¹⁶⁰ For the short D–A sys-

tems the CT bands are assigned to the lowest-energy absorption bands at 383 nm for TAA-short-B and at 410 nm for OTA-short-B. In OTA-short-B2 the CT band is visible only as a shoulder between 400 and 500 nm with an approximate local maximum at 450 nm. All higher-energy absorption bands can be assigned to $\pi \rightarrow \pi^*$ transitions of the amine donors or the triarylboron acceptor. The shift in the CT bands to lower energies correlates well with the calculated ΔG_{CT}^0 values (Table IV.2) and puts in evidence the influence of increased donor and acceptor strengths on the charge transfer behavior. Therefore, the optical absorption data support the interpretation of the electrochemical data that OTA is indeed a better electron donor than TAA. The decrease in molar extinction from TAA-short-B to OTA-short-B and to OTA-short-B2 can be explained by the decrease in electronic coupling between D and A. This becomes particularly important in OTA-short-B2 where OTA and the boron mesityl acceptors are linked in *meta*-position to each other. Electronic coupling is known to be significantly weaker between *meta*-substituents linked via a phenylene bridge than between *para*-substituents.¹⁶⁴

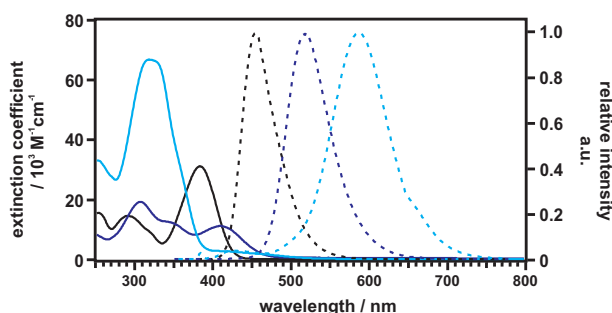


Figure IV.2 Absorption (solid traces) and emission spectra (dashed traces) of TAA-short-B (black, $\lambda_{exc} = 370$ nm), OTA-short-B (blue, $\lambda_{exc} = 330$ nm), and OTA-short-B2 (cyan, $\lambda_{exc} = 345$ nm). All spectra were recorded on 10^{-5} M hexane solutions under ambient conditions and the emission spectra were normalized. λ_{exc} is the respective excitation wavelength.

TAA-short-B, OTA-short-B, and OTA-short-B2 show emission maxima at 454, 518, and 587 nm, respectively, as can be seen in Figure IV.2. These wavelengths correspond to energies of 2.73, 2.39, and 2.11 eV and correlate well with the calculated charge transfer free energies ΔG_{CT}^0 in Table IV.2.

In case of the three compounds with the longer D-A distance, both the CT absorption as well as the emission maxima do not show a steady red shift (Figure IV.3). However, the emission maxima of 443 (2.80 eV) for TAA-long-B, 508 (2.44 eV) for OTA-long-B, and 462 nm (2.68 eV) for OTA-long-B2 do follow the trend predicted by the calculated charge transfer energies in Table IV.2.

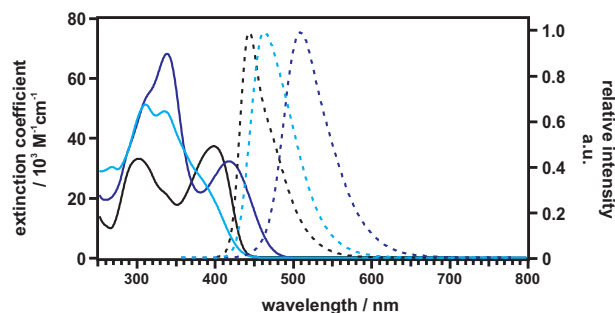


Figure IV.3 Absorption (solid traces) and emission spectra (dashed traces) of TAA-long-B (black, $\lambda_{exc} = 390$ nm), OTA-long-B (blue, $\lambda_{exc} = 345$ nm), and OTA-long-B2 (cyan, $\lambda_{exc} = 345$ nm). All spectra were recorded on 10^{-5} M hexane solutions under ambient conditions and the emission spectra were normalized. λ_{exc} is the respective excitation wavelength.

Similar to the short D-A compounds, the absorption spectra of their longer analogs show $\pi \rightarrow \pi^*$ transitions below 350 nm and the CT bands at lower energies. The exact values of the CT band maxima are 397 nm for TAA-long-B and 417 nm for OTA-long-B. In case of OTA-long-B2, the CT band is only visible as a shoulder at 385 nm. The intensities of the CT bands decrease with increasing donor and acceptor strengths, however, the effect is much less pronounced than in the D-A molecules with the phenyl bridge.

IV.2.3 Solvatochromism

In order to study the dependence of the CT absorption and emission on the solvent polarity, spectra of all six D-A compounds were recorded on 10^{-5} M solutions in five different solvents. The solvent polarity ranges from hexane (as the most apolar), toluene, Et₂O, and THF to DCM as the most polar (Table IV.3). In solvents of higher polarity (e.g. acetone, DMF, and DMSO) the compounds showed very low luminescence quantum yields and unambiguous differentiation between emission originating from the studied compounds and artifacts was difficult. Furthermore, solubility was limited in highly polar solvents such as MeCN and MeOH. Therefore, those solvents were excluded from the studies.

Table IV.3 Solvents and their polarity in terms of REICHHARDT parameters E_T^N .¹⁵⁶

solvent	hexane	toluene	Et ₂ O	THF	DCM	acetone	DMF	MeCN	MeOH
E_T^N	0.009	0.099	0.117	0.207	0.309	0.355	0.404	0.460	0.762

Figure IV.4 depicts the absorption spectra of all compounds in the five selected solvents. The short D-A molecules are depicted in the top half (a-c) and their longer analogs in the bottom part (d-f).

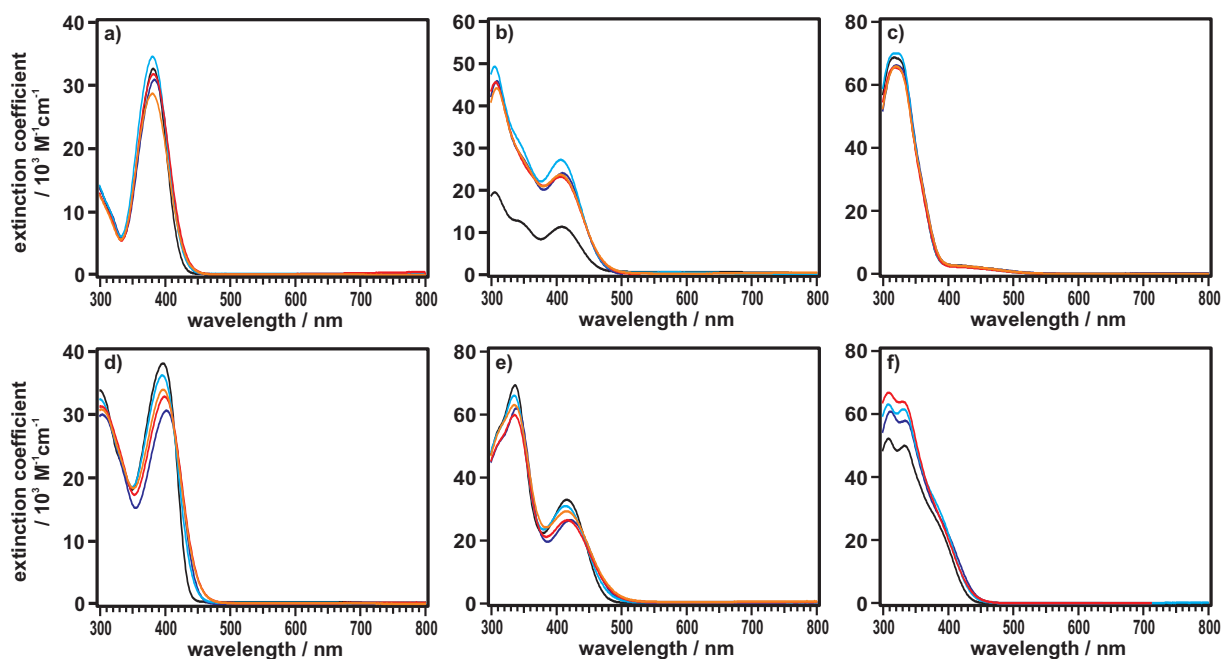


Figure IV.4 Absorption spectra of **a)** TAA-short-B, **b)** OTA-short-B, **c)** OTA-short-B2, **d)** TAA-long-B, **e)** OTA-long-B, and **f)** OTA-long-B2 recorded on 10^{-5} M solutions in hexane (black), toluene (blue), Et₂O (cyan), THF (red), and DCM (orange).

From the spectra it is directly observable that the location of the CT absorption band is not influenced by the different solvents. Strong polarity-dependence or solvatochromism is usually only observed for fluorophores that exhibit a dipole moment themselves.³⁴ In their electronic ground state the investigated compounds are certainly somehow polarized due to their push-pull character, however, the effect is not strong enough to induce spectral shifts in the different solvents.

Once the D-A molecules are excited, charge transfer from the amine moieties to the boron acceptors is induced and the dipole moment is significantly increased in the charge-separated state. As a result, a much stronger solvatochromic effect is expected in the emission spectra (Figure IV.5). All studied compounds show a distinct red-shift of their emission with increasing polarity, as is expected for such push-pull systems.^{34,157,158,165}

The positive solvatochromic shift in TAA-short-B between hexane and DCM amounts to 3050 cm^{-1} whereas in OTA-short-B it is only 2720 cm^{-1} . Overall, the emission maxima for OTA-short-B are shifted further into the red, as was expected due to the lower charge transfer energy. OTA-short-B2 only exhibits significant emission in hexane. The longer analogs also display positive solvatochromism, however, OTA-long-B and OTA-long-B2 do not show significant emission in THF and DCM. Therefore, the shift between hexane and Et₂O is taken as a measure for the solvatochromic shift in

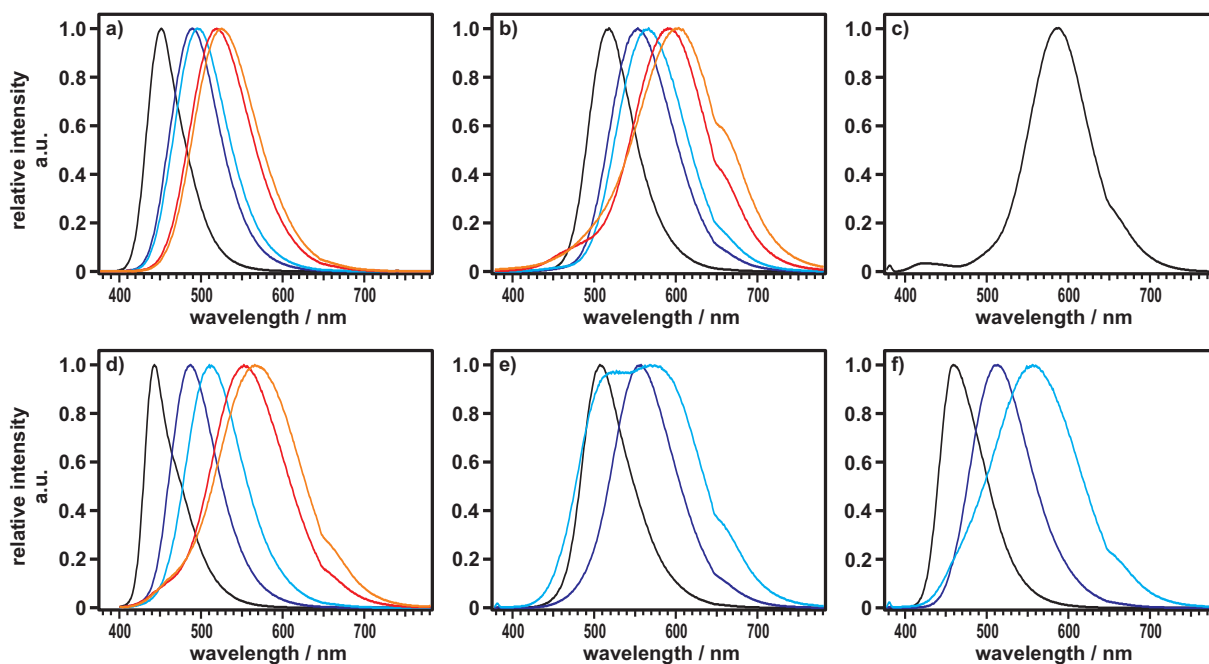


Figure IV.5 Emission spectra of **a)** TAA-short-B, **b)** OTA-short-B, **c)** OTA-short-B2, **d)** TAA-long-B, **e)** OTA-long-B, and **e)** OTA-long-B2 recorded on 10^{-5} M solutions in hexane (black), toluene (blue), Et₂O (cyan), THF (red), and DCM (orange).

those compounds. The magnitudes of the solvatochromic shifts present themselves as follows: 3000 cm^{-1} for TAA-long-B, 2760 cm^{-1} for OTA-long-B, and 3720 cm^{-1} for OTA-long-B2. As a result, the reference compounds TAA-short-B and TAA-long-B show the strongest solvatochromism, with exception of OTA-long-B2.

IV.2.4 Difference between Ground and Excited State Dipole Moments

In 1955 LIPPERT and MATAGA have communicated their theory for solvent-fluorophore interactions. Though it does not consider specific solvent effects (e.g. hydrogen-bonding, acid-base chemistry, CT interactions) it is a valuable method to analyze the solvent-dependent absorption and emission behavior of fluorophores.^{34,166,167}

Equation IV.1 allows for the estimation of the difference between ground- and excited-state dipole moments ($\Delta\mu_{eg}$) on the basis of the experimentally determined STOKES shifts in various solvents.

$$hc \cdot (v_{abs} - v_{em}) = hc \cdot (v_{abs}^{vac} - v_{em}^{vac}) \cdot \frac{2 \cdot (\Delta\mu_{eg})^2}{a_0^3} \cdot \left[\frac{\epsilon - 1}{2\epsilon + 1} - \frac{\eta^2 - 1}{2\eta^2 + 1} \right] \quad (\text{IV.1})$$

In Equation IV.1, $(v_{abs} - v_{em})$ is the STOKES shift that can be extracted from the absorption and emission data from Figure IV.4 and Figure IV.5, h is PLANCK's constant,

and c is the speed of light. Furthermore, ϵ is the dielectric constant, η the refractive index of the solvent, and a_0 is the ONSAGER radius. In LIPPERT-MATAGA theory, the ONSAGER radius is defined as the solvent cavity in which the fluorophore is embedded, and for easier determination of this radius the fluorophores are assumed to be spheres.¹⁶⁸ The solvent polarity is described by the so-called orientation polarizability $\Delta f = (\epsilon - 1)/(2\epsilon + 1) - (\eta^2 - 1)/(2\eta^2 + 1)$. In this term, $(\eta^2 - 1)/(2\eta^2 + 1)$ describes the reorientation of the electrons of the solvent molecules after the change in dipole moment on the CT compound. Electrons adjust basically instantly to the changed environment, hence the term is also called the high-frequency polarizability. $(\epsilon - 1)/(2\epsilon + 1)$ describes the reorganization of the solvent molecules, which occurs on a much slower timescale than electron reorganization and is therefore denoted as low-frequency polarizability.³⁴

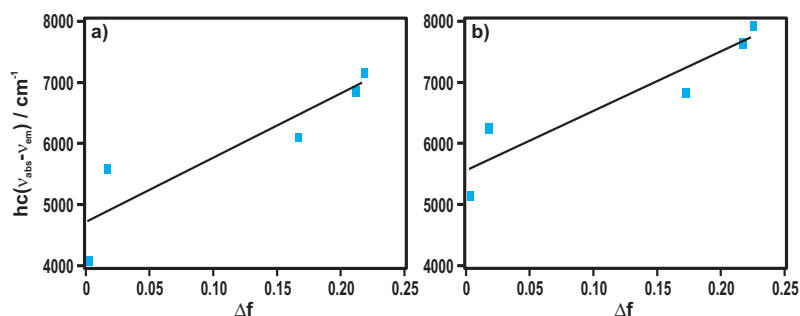


Figure IV.6 LIPPERT-MATAGA plots of the STOKES shift vs. the orientation polarizability Δf . **a)** TAA-short-B, **b)** OTA-short-B.

Figure IV.6 displays the plots of $hc \cdot (v_{abs} - v_{em})$ vs. Δf for TAA-short-B (a) and OTA-short-B (b). Linear regression fits of the data yield values of $10500 \pm 3000 \text{ cm}^{-1}$ (TAA-short-B) and $10000 \pm 2300 \text{ cm}^{-1}$ (OTA-short-B) for the slopes, which are the same within experimental accuracy. Ideally, the difference in ground- and excited-state dipole moments for the investigated compounds can be estimated from the slope which is equal to $\Delta\mu_{eg}^2/a_0^3$. Determination of the ONSAGER radius is always prone to errors and these have an even larger impact on the calculated value for $\Delta\mu_{eg}$ due to its dependence on the third power of a_0 .¹⁶⁹ Furthermore, already the linear regression fits do exhibit a non-negligible error due to the relatively poor linear correlation ($R^2 = 0.81$ for TAA-short-B and $R^2 = 0.86$ for OTA-short-B) between the STOKES shifts and solvent polarity as depicted in Figure IV.6. Another source of error in the LIPPERT-MATAGA equation (IV.1) is the assumption of spherical fluorophores. The structural formula of TAA-short-B and OTA-short-B already imply the deviation from this assumption. Consideration of an elliptical solvent cavity would certainly be better suited for the present compounds.

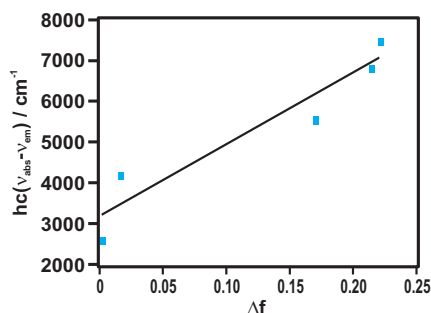


Figure IV.7 LIPPERT-MATAGA plot of the STOKES shift vs. the orientation polarizability Δf for TAA-long-B.

The same general observations as discussed above can be made for TAA-long-B (Figure IV.7). Linear fitting leads to a slope of $18000 \pm 3300 \text{ cm}^{-1}$ which is substantially higher than the ones obtained for TAA-short-B and OTA-short-B. However, the uncertainty of the linear fit is even higher ($R^2 = 0.91$) and the same errors regarding the estimation of the ONSAGER radius have to be considered here. Therefore, also in the longer D-A compound, derivation of an accurate value for $\Delta\mu_{eg}$ from the plots would be questionable. The rather strong deviation of the experimentally obtained values from the ideal, expected linear behavior indicates the presence of more specific interactions between the fluorophores and the solvents.

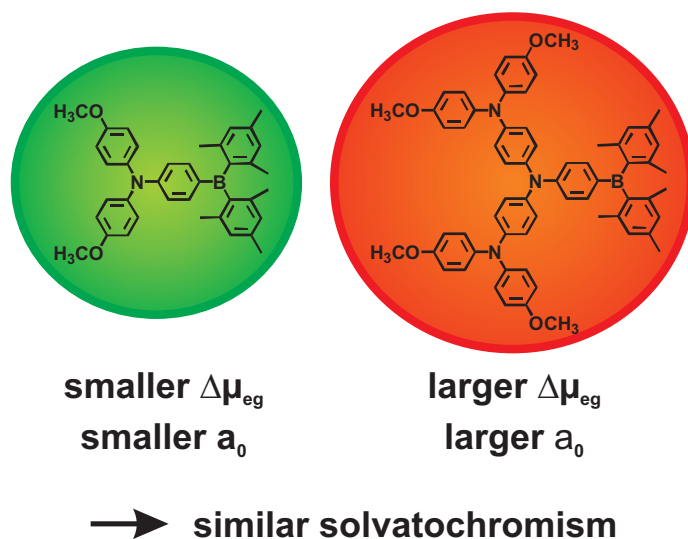


Figure IV.8 Illustration of increased ONSAGER radii in TAA-short-B (left) and OTA-short-B (right).

Nevertheless, a semi-quantitative statement regarding the change in $\Delta\mu_{eg}$ upon an increase in donor strength in a system with a fixed D-A distance might be appropriate. Compared to TAA-short-B, substitution of TAA by OTA may be associated with an increase of the ONSAGER radius by 25% (Figure IV.8). This estimation is based on the increased molecular size of OTA-short-B. Though this increase of the compound

radius is quite small, application of $hc \cdot (v_{abs} - v_{em}) = \Delta\mu_{eg}^2/a_0^3$ with the experimentally determined STOKES shift and the 25% increased a_0 can mask an increase in $\Delta\mu_{eg}$ of up to 40%. OTA-short-B does very likely exhibit a significantly stronger change in its dipole moment after excitation and charge transfer than TAA-short-B, due to the presence of the stronger electron donor OTA. Alas, this effect does not lead to stronger solvatochromism, because the effect of the stronger donor is outbalanced by the increase in a_0 . As a result, to create systems with very strong solvatochromism, the molecular size should be kept as small as possible with increasing donor and acceptor strengths.

IV.2.5 Luminescence Lifetimes and Quantum Yields

The quantum yields and the corresponding luminescence lifetimes of the CT states of the D-A compounds TAA-short-B, OTA-short-B, and TAA-long-B were measured in hexane, toluene, Et₂O, THF, and DCM under ambient conditions. For OTA-long-B and OTA-long-B2, determination of ϕ and τ was only possible in hexane, toluene, and Et₂O, whereas OTA-short-B2 shows significant luminescence in hexane. All measurements were performed on 10⁻⁵ M solutions. Table IV.4 displays the summarized luminescence data.

One general observation that can be made for all investigated compounds is a concomitant decrease in the luminescence quantum yield with decreasing CT energies of the excited states. The so-called energy gap law describes the dependence of the efficiency of non-radiative deactivation processes on the energy gap between the ground state and the luminescent excited state. With decreasing energy gap, non-radiative processes become more and more efficient.⁸⁴ This is in line with the observed decrease in quantum yields for the D-A compounds in different solvents. The lack of correlation between the quantum yields and luminescence lifetimes indicates once more the presence of specific solvent-fluorophore interactions that lead to significant, highly solvent-dependent variations in efficiency for non-radiative and radiative deactivation processes. Interactions between solvent donor molecules and the triarylborane acceptors might open a thermal relaxation pathway to the excited states that becomes even more apparent as the polarity of the solvent increases.

Compared to TAA-short-B, OTA-short-B, TAA-long-B, and even OTA-long-B, the two compounds bearing two boron mesityl acceptors exhibit much poorer luminescence properties. In the present study, the acceptor strength was increased by attachment of two triarylboranes. Due to the design of the D-A compounds this requires the two acceptors to be attached in *meta*-position to the OTA donor. As already stated above, this leads to a significant decrease in electronic coupling between D and A

Table IV.4 Luminescence quantum yields (ϕ) and lifetimes (τ in ns) of the fluorophores in the different solvents. Measured in aerated solvents under ambient conditions.

Compound	hexane		toluene		Et ₂ O		THF		DCM	
	ϕ	τ	ϕ	τ	ϕ	τ	ϕ	τ	ϕ	τ
TAA-short-B	0.59	4.1	0.72	6.0	0.75	7.4	0.63	7.6	0.66	8.6
OTA-short-B	0.49	5.8	0.50	7.8	0.40	7.0	0.12	2.7	0.04	1.1
OTA-short-B2	0.06	11.8								
TAA-long-B	0.81	1.8	0.85	2.6	0.88	3.6	0.49	2.8	0.38	2.4
OTA-long-B	0.63	3.6	0.52	4.1	0.11	1.8				
OTA-long-B2	0.21	3.8	0.13	9.3	0.08	13.2				

and therefore, in a decreased efficiency of the radiative decay rate for OTA-short-B2 and OTA-long-B2. Furthermore, if thermal relaxation of the excited CT states due to solvent interactions with the boron acceptor is indeed possible, despite the bulkiness of the triarylboranes, this effect is certainly increased in presence of two acceptors in OTA-short-B2 and OTA-long-B2.

Since the four stronger luminescent compounds TAA-short-B, OTA-short-B, TAA-long-B, and OTA-long-B exhibit similar oscillator strengths, their radiative decay constants should also be similar in the used solvents. However, the quantum yields do differ, which might be attributed to differences in non-radiative excited state relaxation processes. In the OTA bearing D-A molecules, more atoms are present due to the more extended molecular system of OTA. Therefore, the number of available vibrational degrees of freedom is higher in OTA-short-B and OTA-long-B and allows for more efficient deactivation of the excited states.

Comparing the short to the long D-A compounds, the additional ethynyl unit only exerts a small influence on the luminescence quantum yields, compared to the stronger OTA donor and the *meta*-coupling of the two boron acceptors. This small effect is only observable in the most apolar solvents hexane, toluene, and Et₂O. Already in the weakly polar solvents THF and DCM, the effect becomes negligible.

IV.3 Summary

The aim of this comparative study was the synthesis and physicochemical investigation of six D-A compounds (Scheme IV.1) with regard to their charge transfer and solvatochromic behavior. The structural differences in the compounds allowed for the study of the influence of donor and acceptor strengths, position of D with respect to A, and the bridging length on their luminescence behavior. Consideration of all

experimental data results in some key findings.

On the basis of the cyclic voltammetry data for the donor and acceptor moieties, the trends in charge transfer energies could be predicted for all unknown compounds.

Use of OTA as a stronger electron donor compared to TAA did lead to the desired red-shift of the CT emission and a stabilization of the CT state. However, due to the increased size of the OTA-containing compounds, the ONSAGER radius was also increased. Therefore, the overall solvatochromic effect is comparable to the one in the TAA-containing compounds that exhibit a smaller dipole moment change between the ground and excited states.

Increase of the acceptor strength by attachment of a second boron mesityl acceptor influences the CT properties negatively. The two triarylboranes require attachment in *meta*-position to the amine donors which leads to a decreased electronic coupling between D and A. This in turn leads to a significant decrease in the luminescence quantum yield.

Based on these key findings, design guidelines for future amine-bridge-borane fluorophores are proposed:

First, when aiming to enhance the CT properties of such push-pull compounds the donor and acceptor strengths should be increased without a concomitant increase of the ONSAGER radius, because these effects tend to annul each other.

Second, very electron-rich arylamine donors do present themselves as perfect candidates for use in such push-pull systems, however, their size should be kept small.

Third, the acceptor strength of triarylboranes should be increased by substitution of the aryls (e.g. fluorination), rather than by attachment of several acceptors in *meta*-position.

Fourth, a high radiative decay rate of the CT state is necessary and can be achieved by strong electronic coupling between D and A. Therefore, a suitable bridging unit is necessary and *p*-phenylene and *p*-phenylene ethylene linkers show similarly positive behavior in this respect.



Photographs of the emission behavior of the strongest emitter TAA-short-B (left) and the weakest emitter OTA-short-B2 (right) in the used solvents.

V. GENERAL SUMMARY

The main aim of this thesis was the achievement of photoinduced charge accumulation in purely molecular, nanoparticle-free d^6 transition metal sensitized compounds. All investigated compounds were comprised of various combinations of an OTA donor, an AQ acceptor, and either a rhenium or ruthenium polypyridyl photosensitizer.

Despite the efforts of constant improvement of the molecular designs and the measuring parameters, no unequivocal evidence for twofold charge separation could yet be found in any of the investigated systems with the available pump-probe nanosecond setup.

The studied ruthenium dyad, triad, and pentad allowed for significantly higher excitation densities of the laser beam than their rhenium analogs and are therefore preferable for future studies.

Ru-OTA in presence of TCNB and AQ-Ru-OTA, as well as AQ-Ru-OTA-Ru-AQ in presence of diphenylthiourea displayed spectral features at high laser powers that do hint towards the presence of the second charge-separated states. Unambiguous bands could not be fully resolved with the used pump-probe nanosecond setup, but also cannot be fully attributed to noise or instrumental artifacts. Therefore, pump-pump-probe experiments using two temporally delayed excitation pulses, maybe even of different wavelengths, would certainly represent a major advantage and will be pursued in the near future. When performed with sufficiently high temporal resolution, < 10 ns, even very short-lived photoproducts might be detectable.

Employment of the strong electron donor OTA in a side project, investigating push-pull systems with boronmesityl acceptors, did not lead to the desired superior charge transfer and solvatochromic properties. However, important guidelines regarding the development of future triarylamine-triarylborane emitters could be worked out.

VI. EXPERIMENTAL PART

VI.1 Analytical Methods

General Methods

All commercially available chemicals were used without further purification. Dry DCM, Et₂O and THF were obtained from a solvent purification system of Innovative Technology. Dry toluene was bought from Sigma-Aldrich (crown cap; over molecular sieve) and used as received. The additional solvents hexane, acetone, DMF, and DMSO used for polarity dependent measurements were also bought from Sigma-Aldrich (crown cap; over molecular sieve). Thin-layer chromatography was performed on silica gel plates (60 F₂₅₄) from Merck. Silica gel (40–63 μm, Silicycle) or activated, basic aluminum oxide (Brockmann I, 50–200 μm) from Acros was used for column chromatography.

All given temperatures in the synthesis procedures are the set oil bath temperatures.

NMR Spectroscopy

¹H NMR spectra were recorded on a 250 MHz or 400 MHz Bruker Avance III, ¹³C spectra on a 500 MHz Avance III from Bruker. All shifts (δ) given below are in ppm and referenced to residual solvent peaks. Coupling constants are listed in Hz and the multiplicity is denoted as follows: singlet (s), broad singlet (bs), doublet (d), triplet (t), quartet (q), multiplet (m).

High Resolution Mass Spectrometry

The high-resolution mass spectra were measured on a Bruker maXis 4G QTOF ESI spectrometer.

Elemental Analysis

All elemental analyses were performed on a Vario Micro Cube from Elementar.

X-ray Crystallography

The crystal was measured on a Bruker Kappa Apex2 diffractometer at 123 K using graphite-monochromated Cu K α radiation.

FT-IR Spectroscopy

FT-IR spectra of the complexes in solid form were measured on a Bruker Alpha Platinum-ATR.

UV-Vis Spectroscopy

All UV-Vis spectra were recorded on a Cary 5000 UV-Vis-NIR spectrophotometer.

Cyclic Voltammetry

A VersaStat3-200 potentiostat of Princeton Applied Research was used for electrochemical experiments. The measurements were performed in dry, argon-saturated MeCN with tetrabutylammonium hexafluorophosphate (TBAPF₆) as supporting electrolyte and using a conventional three-electrode setup. A glassy carbon disc was used as the working electrode and two silver wires served as the quasi-reference and the counter electrode, respectively. All cyclovoltammograms are referenced versus the ferrocene/ferrocenium (Fc^{+ / 0}) redox couple.

Steady-state Luminescence, Lifetimes, and Quantum Yields

Steady-state luminescence spectra were obtained by a Fluorolog-322 from Horiba Jobin-Yvon.

Fluorescence lifetime measurements were done on a Hamamatsu Quantaaurus-Tau C11367-11.

Absolute photoluminescence quantum yields were measured on a Quantaaurus-QY C11347-11 from Hamamatsu.

Transient Absorption

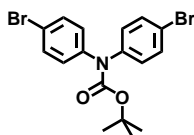
Transient absorption was measured with an LP920-KS spectrometer from Edinburgh Instruments, equipped with an R928 photomultiplier or an NIR 301/2 (InGaAs) detector (900–1700 nm, 100 ns response time), and an iCCD camera from Andor. A

frequency-tripled Quantel Brilliant b laser was used as an excitation source for measuring the Re-complexes. For the Ru-complexes, the output frequency was doubled. The duration of the laser excitation pulse was approximately 10 ns with a repetition frequency of 10 Hz. Unless otherwise stated, transient absorption spectra were obtained as time-averaged signals over a detection period of 200 ns directly after excitation.

For all optical measurements Quartz cuvettes from Starna were used.

VI.2 Syntheses of the OTA donor

OTA-pre

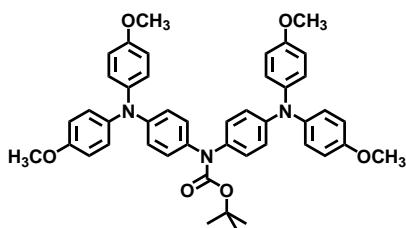


Synthesis according to literature procedure.⁹⁷

Bis(4-bromophenyl)amine (2.00 g, 6.12 mmol), 4-(*N,N*-dimethylamino)pyridine (149.5 mg, 1.22 mmol), and di-*tert*-butyl dicarbonate (2.11 mg, 9.17 mmol) were dissolved in 15 mL dry THF under N₂ atmosphere. The yellow solution was heated to reflux for 3 h. After cooling to room temperature and evaporation of the solvent the orange crude solid was filtered over a plug of SiO₂. With an eluent mixture of pentane/DCM 2:1 pure product was obtained as a white solid (2.60 g, 6.09 mmol, 100%).

¹H NMR (400 MHz, CDCl₃): 7.41–7.45 (m, 4H, AA'BB'), 7.04–7.08 (m, 4H, AA'BB'), 1.44 (s, 9H, ^tBu).

OTA-Boc



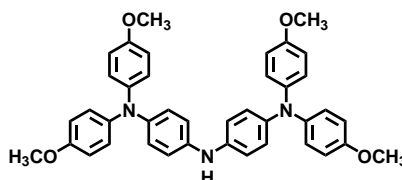
Synthesis by adapting a literature procedure.⁹⁷

OTA-pre (1.00 g, 2.34 mmol), dianisylamine (1.34 g, 5.86 mmol), NaO^tBu (4.5 g, 46.8 mmol), Pd(dba)₂ (67.2 mg, 0.12 mmol), and (HP^tBu₃)BF₄ (34.2 mg, 0.12 mmol) were dissolved in dry, de-oxygenated toluene (30 mL) under N₂ atmosphere. The mixture was stirred at 120 °C for 19 h. 100 mL H₂O was added to the cool mixture and the aqueous phase was extracted with DCM (3 x 50 mL). After drying over MgSO₄ and evaporation of the solvents the crude product was subjected to column chromatography. With DCM as eluent the pure product was obtained as a beige solid (1.42 g, 1.96 mmol, 84%).

¹H NMR (400 MHz, acetone-d₆): 7.05–7.09 (m, 4H, AA'BB'), 7.00–7.04 (m, 8H, AA'BB'),

6.87–6.91 (m, 8H, AA'BB'), 6.78–6.82 (m, 4H, AA'BB'), 3.78 (s, 12H, OCH₃), 1.41 (s, 9H, ^tBu).

OTA



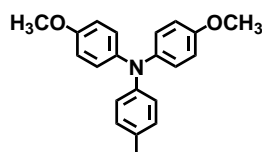
Synthesis according to literature procedure.⁹⁵

OTA–Boc (2.00 g, 2.76 mmol) was dissolved in 40 mL acetone under N₂ atmosphere. TFA (10 mL, 0.13 mol) was added dropwise and stirring at RT was continued over night. The reaction mixture was evaporated to dryness. Column chromatography on basic alumina with EtOAc as eluent yielded the product as a beige solid (1.70 g, 2.73 mmol, 99%).

¹H NMR (400 MHz, acetone-d₆ + TFA): 7.37–7.40 (m, 4H, AA'BB'), 7.14–7.18 (m, 8H, AA'BB'), 6.94–6.98 (m, 8H, AA'BB'), 6.83–6.87 (m, 4H, AA'BB'), 3.80 (s, 12H, OCH₃).

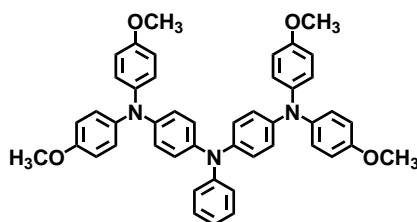
VI.3 Syntheses of General Building Blocks

TAA-ref



4-Bromotoluene (895.2 mg, 5.23 mmol), dianisylamine (1.00 g, 4.36 mmol), NaO^tBu (8.38 g, 8.72 mol), Pd(dba)₂ (125.4 mg, 0.22 mmol), and (HP^tBu₃)BF₄ (63.8 mg, 0.22 mmol) were suspended in dry toluene (50 mL), de-oxygenated and heated to reflux for 23 h. 100 mL H₂O was added to the cool reaction mixture and then extracted with DCM (3 x 50 mL). After drying over MgSO₄ the crude product was purified by column chromatography with a pentane/DCM (1:1) eluent mixture. Pure product was obtained as a brown sticky solid (1.17 g, 3.66 mmol, 84%).

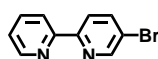
¹H NMR (400 MHz, CDCl₃): 7.07 (td, *J* = 6.6 Hz, 2.5 Hz, 6H, AA'BB'), 6.97–6.93 (m, 2H, AA'BB'), 6.89–6.82 (m, 4H, AA'BB'), 3.83 (s, 6H, OCH₃), 2.34 (s, 3H, CH₃).

OTA-ref

Synthesis based on a literature procedure.⁹⁴

OTA (200.0 mg, 0.32 mmol), bromobenzene (0.05 mL, 0.48 mmol), KO^tBu (718.1 g, 6.40 mmol), $\text{Pd}(\text{dba})_2$ (18.4 mg, 0.03 mmol), and $(\text{HP}^t\text{Bu}_3)\text{BF}_4$ (9.30 mg, 0.03 mmol) were dissolved in dry, de-oxygenated toluene (15 mL) under N_2 atmosphere. The mixture was stirred at 120 °C over night. 100 mL EtOAc was added to the cool mixture and the organic phase was washed with H_2O (3 x 50 mL). After drying over Na_2SO_4 and evaporation of the solvents the crude product was subjected to column chromatography. With EtOAc as eluent and subsequent recrystallization from MeOH, pure product was obtained as a beige solid (157.0 mg, 0.22 mmol, 70%).

^1H NMR (400 MHz, C_6D_6): 7.24 (d, $J = 7.9$ Hz, 2H, ph), 7.14–7.07 (m, 14H, AA'BB'), 7.06–7.01 (m, 4H, AA'BB' + ph), 6.81 (t, $J = 7.2$ Hz, 1H, ph), 6.74–6.68 (m, 8H, AA'BB'), 3.30 (s, 12H, OCH_3).

Br-bpy

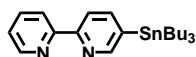
Synthesis according to literature procedure.¹¹⁸

2-pyridylzinc bromide (42.3 mL, 21.1 mmol) and $\text{Pd}(\text{PPh}_3)_4$ were mixed under N_2 atmosphere and 5-bromo-2-iodopyridine (5.00 g, 17.6 mmol) in 35 mL dry THF was added drop wise. The mixture was stirred at room temperature for 24 h. 150 mL basic EDTA-solution was added and the product was extracted with DCM (3 x 100 mL). The combined organic phases were washed with 100 mL brine and dried over MgSO_4 . After evaporation of the solvents the crude product was subjected to column chromatography (SiO_2 , pentane/ Et_2O 2:1 + 1 % NEt_3) to yield an off-white solid (3.22 g, 13.7 mmol, 78%).

^1H NMR (400 MHz, CDCl_3): 8.71–8.72 (dd, $J = 2.4$ Hz, 0.8 Hz, 1H, bpy), 8.65–8.67 (ddd, $J = 4.9$ Hz, 1.7 Hz, 0.9 Hz, 1H, bpy), 8.35–8.38 (dt, $J = 8.0$ Hz, 1.1 Hz, 1H, bpy), 8.30–8.33

(dd, $J = 8.5$ Hz, 0.8 Hz, 1H, bpy), 7.91–7.95 (dd, $J = 8.5$ Hz, 2.4 Hz, 1H, bpy), 7.78–7.84 (td, $J = 7.8$ Hz, 1.8 Hz, 1H, bpy), 7.29–7.34 (ddd, $J = 7.5$ Hz, 4.8 Hz, 1.2 Hz, 1H, bpy).

bpy–SnBu₃

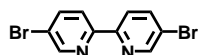


Synthesis according to literature procedure.¹¹⁹

Br–bpy (530.0 mg, 2.25 mmol) was dissolved in 15 mL Et₂O under N₂ atmosphere and cooled to -78 °C in an acetone/dry ice bath. *n*-BuLi (1.55 mL, 2.48 mmol, 1.6 M) was added drop wise and the dark red mixture was stirred for 1 h. After addition of tributyltin chloride (0.67 mL, 2.48 mmol) the reaction was stirred 1.5 h at -78 °C and over night at RT. Filtration of the solid and evaporation to dryness gave a orange oil, which was purified by column chromatography (SiO₂, pentane/EtOAc 90:10 + 1% NEt₃) to yield a yellow oil (0.5 g, 1.30 mmol, 58%).

¹H NMR (400 MHz, CDCl₃): 8.69 (t, $J = 1.3$ Hz, 1H, bpy), 8.67 (ddd, $J = 4.8$ Hz, 1.8 Hz, 0.9 Hz, 1H, bpy), 8.40–8.36 (m, 1H, bpy), 8.32 (dd, $J = 7.7$ Hz, 1.0 Hz, 1H, bpy), 7.89 (dd, $J = 7.7$ Hz, 1.6 Hz, 1H, bpy), 7.80 (td, $J = 7.7$ Hz, 1.8 Hz, 1H, bpy), 7.28 (ddd, $J = 7.6$ Hz, 4.8 Hz, 1.2 Hz, 1H, bpy), 1.61–1.51 (m, 6H, Bu₃), 1.34 (dq, $J = 14.5$ Hz, 7.3 Hz, 6H, Bu₃), 1.15–1.09 (m, 6H, Bu₃), 0.88 (t, $J = 7.3$ Hz, 9H, Bu₃).

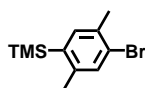
Br–bpy–Br



Synthesis by adapting a literature procedure.¹²⁰

5-bromo-2-iodopyridine (10.0 g, 35.2 mmol) was dissolved in 60 mL dry *m*-xylene and hexa-*n*-butylditin (8.90 mL, 17.61 mmol) was added to the solution. After thorough degassing of the mixture, Pd(PPh₃)₄ (814.0 mg, 0.70 mmol) was added and the reaction mixture was de-oxygenated again. The yellow suspension was heated to 180 °C for 3 d. Afterwards, the black solid was removed by hot filtration. Solvent removal and recrystallization from chloroform yielded the product as a beige solid (4.44 g, 14.1 mmol, 80%).

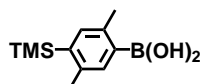
¹H NMR (400 MHz, CDCl₃): 8.70 (m, 2H, bpy), 8.27–8.30 (dd, 2H, bpy), 7.92–7.96 (dd, 2H, bpy).

TMS-xy-Br

Synthesis according to literature procedure.¹¹⁹

A solution of 2,5-dibromo-1,4-di-methylbenzene (15.0 g, 57.3 mmol) in dry THF (130 mL) was cooled to $-78\text{ }^{\circ}\text{C}$ under a N_2 atmosphere. *n*-BuLi (25.2 mL, 63.0 mmol, 2.5 M) was then added dropwise and the mixture was stirred for 2 h at $-78\text{ }^{\circ}\text{C}$. After addition of trimethylsilyl chloride (8.05 mL, 63.0 mmol) the yellow solution was stirred over night at RT. The solvents were removed in vacuo and the residue was taken up in water (50 mL) and DCM (50 mL). The aqueous phase was extracted with DCM (3 x 50 mL). The combined organic phases were washed with brine (2 x 50 mL) and dried over Na_2SO_4 . The dried crude yellow liquid was purified by filtering over a pluck of SiO_2 with pentane as eluent. This gave the product as a colorless liquid (13.8 g, 53.5 mmol, 93%).

^1H NMR (400 MHz, CDCl_3): 7.39 (s, 1H, xy), 7.32 (s, 1H, xy), 2.44 (s, 3H, CH_3), 2.41 (s, 3H, CH_3), 0.36 (s, 9H, $\text{Si}(\text{CH}_3)_3$).

TMS-xy-B(OH)₂

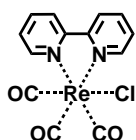
Synthesis according to literature procedure.¹²¹

TMS-xy-Br (5.20 g, 20.2 mmol) was dissolved in 90 mL dry THF under N_2 atmosphere and cooled to $-78\text{ }^{\circ}\text{C}$. *n*-BuLi (9.70 mL, 24.24 mmol, 2.5 M) was added drop wise and the mixture was stirred at room temperature for 1.5 h. After cooling to $-78\text{ }^{\circ}\text{C}$ again, trimethyl borate (2.70 mL, 24.24 mmol) was added drop wise and the reaction was stirred over night at RT. The colorless suspension was acidified with 50 mL HCl (6 N) and extracted with DCM (3 x 50 mL). The combined organic phases were dried over MgSO_4 . Evaporation of the solvents gave a yellowish solid with was purified by column chromatography (SiO_2 , pentane/ Et_2O 1:1) to yield pure white product (3.37 g, 15.2 mmol, 75%).

^1H NMR (400 MHz, CDCl_3): 7.94 (s, 1H, xy), 7.36 (s, 1H, xy), 2.76, (s, 3H, CH_3), 2.50 (s, 3H, CH_3), 0.36 (s, 9H, $\text{Si}(\text{CH}_3)_3$).

VI.4 Syntheses of ligands and metal complexes with rhenium

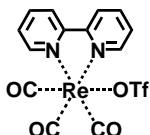
fac-Re(bpy)(CO)₃Cl



Synthesis according to literature procedure.¹⁰¹

Re(CO)₅Cl (1.00 g, 2.77 mmol) and 2,2'-bipyridine (433.0 mg, 2.77 mmol) were dissolved in 150 mL toluene and heated to reflux for 1 h. After cooling to room temperature and keeping in fridge over night the yellow solid was filtered, washed with Et₂O and dried in vacuum. The yellow product (1.24 g, 2.68 mmol, 97%) was used without further characterization.

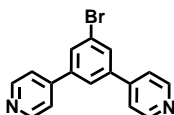
fac-Re(bpy)(CO)₃OTf



Synthesis according to literature procedure.¹⁰²

fac-Re(bpy)(CO)₃Cl (357.0 mg, 0.77 mmol) was suspended in 5 mL DCM under N₂ atmosphere and trifluoromethanesulfonic acid (0.41 mL, 4.64 mmol) was added dropwise. The clear orange mixture was stirred at RT for 1 h. Upon drop wise addition of Et₂O to the stirred reaction mixture a light yellow solid formed which was filtered, washed with Et₂O and dried in vacuum (399.0 mg, 0.69 mmol, 90%). This Re-precursor was used without further characterization.

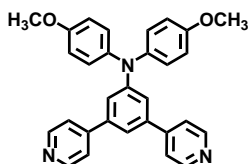
py-Br-py



1,3,5-tribromobenzene (0.50 g, 1.59 mmol), Na_2CO_3 (3.00 g, 28.3 mmol), and 4-pyridine boronic acid (586.3 mg, 4.77 mmol) were dissolved in 10 mL water and 20 mL THF under N_2 atmosphere and the suspension was de-oxygenated for 30 min. After addition of $\text{Pd}(\text{PPh}_3)_4$ (184.0 mg, 0.16 mmol) and additional degassing the mixture was heated to 90°C for 24 h. The cool solution was mixed with 50 mL water and extracted with DCM (3 x 50 mL). The combined organic phases were dried over Na_2SO_4 , the solvents were removed and subsequent column chromatography (SiO_2 , DCM + 2% NEt_3) gave a light green solid (0.18 g, 0.58 mmol, 36%).

^1H NMR (400 MHz, CDCl_3): 8.75–8.69 (m, 4H, py), 7.83 (d, $J = 1.6$ Hz, 2H), 7.77 (t, $J = 1.6$ Hz, 1H), 7.54–7.49 (m, 4H, py).

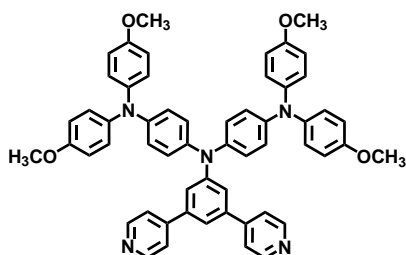
py-TAA-py



Py-Br-py (66.0 mg, 0.21 mmol), dianisylamine (58.3 mg, 0.25 mmol), NaO^tBu (404.0 mg, 4.20 mmol), $\text{Pd}(\text{dba})_2$ (6.00 mg, 0.01 mmol), and $(\text{HP}^t\text{Bu}_3)\text{BF}_4$ (3.00 mg, 0.01 mmol) were dissolved in dry, de-oxygenated toluene (5 mL) under N_2 atmosphere. The mixture was stirred at 100°C for 22.5 h. 50 mL H_2O was added to the cool mixture and the aqueous phase was extracted with DCM (3 x 50 mL). After drying over Na_2SO_4 and evaporation of the solvents the crude product was subjected to column chromatography. With DCM and 1% NEt_3 as eluent mixture the pure product was obtained as a beige solid (80.0 mg, 0.17 mmol, 83%).

^1H NMR (400 MHz, CDCl_3): 8.62 (m, 4H, py), 7.41 (m, 4H, py), 7.29 (t, $J = 1.6$ Hz, 1H), 7.20 (d, $J = 1.6$ Hz, 2H), 7.16–7.12 (m, 4H, AA'BB'), 6.90–6.86 (m, 4H, AA'BB'), 3.82 (s, 6H, OCH_3).

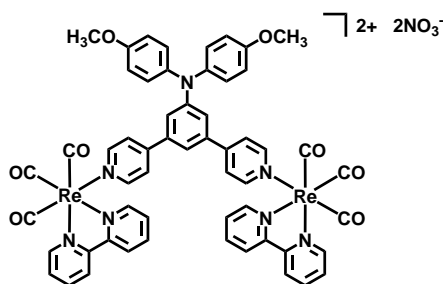
py-OTA-py



Py-Br-py (180.5 mg, 0.58 mmol) and **OTA** (0.30 g, 0.48 mmol), together with NaO^tBu (1.11 g, 11.6 mmol), $\text{Pd}(\text{dba})_2$ (13.8 mg, 0.02 mmol), and $(\text{HP}^t\text{Bu}_3)\text{BF}_4$ (6.90 mg, 0.02 mmol) were dissolved in dry, de-oxygenated toluene (25 mL) under N_2 atmosphere. The mixture was stirred at 125 °C for 19 h. 100 mL H_2O was added to the cool mixture and the aqueous phase was extracted with DCM (3 x 50 mL). After drying over MgSO_4 and evaporation of the solvents the crude product was subjected to column chromatography. With DCM and 2% NEt_3 as eluent mixture and subsequent recrystallization (hexane) the pure product was obtained as an olive-green solid (292.0 mg, 0.34 mmol, 71%).

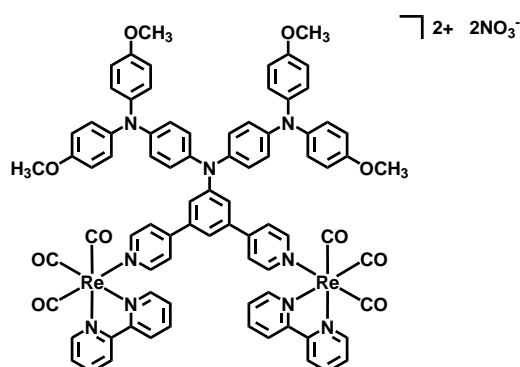
^1H NMR (400 MHz, CDCl_3): 8.66 (d, $J = 4.7$ Hz, 4H, py), 7.44 (d, $J = 6.2$ Hz, 4H, py), 7.29 (s, 3H), 7.08–7.04 (m, 8H, AA'BB'), 7.02–6.99 (m, 4H, AA'BB'), 6.91–6.87 (m, 4H, AA'BB'), 6.85–6.81 (m, 8H, AA'BB'), 3.79 (s, 12H, OCH_3).

Re₂-TAA



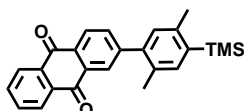
Py-TAA-py (100.0 mg, 0.22 mmol) and **Re(bpy)(CO)₃OTf** (275.4 mg, 0.48 mmol) were dissolved in 10 mL MeOH. The mixture was de-oxygenated for 45 min and heated to 85 °C over night. After evaporation to dryness the crude product was subjected to column chromatography (SiO_2 , acetone \rightarrow acetone/ H_2O /sat. KNO_3 200:9:1), the orange fraction was collected and the solvents were removed again. 50 mL H_2O was added and the product was extracted with DCM (3 x 50 mL), dried over Na_2SO_4 and the solvents were removed in vacuum. The solid was recrystallized from hexane yielding an orange solid (160.7 mg, 0.11 mmol, 50%).

^1H NMR (400 MHz, CD_3CN): 9.21 (ddd, $J = 5.5$ Hz, 1.6 Hz, 0.8 Hz, 4H, bpy), 8.37 (dt, $J = 8.3$ Hz, 1.0 Hz, 4H, bpy), 8.25 (td, $J = 7.9$ Hz, 1.5 Hz, 4H, bpy), 8.20–8.15 (m, 4H, py), 7.77 (ddd, $J = 7.6$ Hz, 5.5 Hz, 1.3 Hz, 4H, bpy), 7.37–7.32 (m, 4H, py), 7.19 (t, $J = 1.6$ Hz, 1H), 7.07–7.02 (m, 4H, AA'BB'), 6.97 (d, $J = 1.6$ Hz, 2H), 6.89–6.84 (m, 4H, AA'BB'), 3.75 (s, 6H, OCH_3). ESI-MS calculated (m/z) for $\text{C}_{56}\text{H}_{41}\text{N}_7\text{O}_8\text{Re}_2$: 656.6061; found: 656.6075. Elemental analysis calculated (%) for $\text{C}_{56}\text{H}_{41}\text{N}_9\text{O}_{14}\text{Re}_2 \cdot 2\text{H}_2\text{O}$: C 45.68, H 3.08, N 8.56; found: C 45.62, H 3.21, N 8.63.

Re₂-OTA

Py-OTA-py (100.0 mg, 0.12 mmol) and **Re(bpy)(CO)₃OTf** (148.2 mg, 0.26 mmol) were dissolved in 10 mL methanol and 3 mL chloroform. The orange solution was de-oxygenated for 25 min and heated to 85 °C for 1.5 d. After evaporation to dryness the crude product was subjected to column chromatography (SiO₂, acetone → acetone/H₂O/sat. KNO₃ 200:9:1). The obtained orange solid was dissolved in 50 mL H₂O and extracted with DCM (3 x 50 mL), dried over Na₂SO₄ and the solvents were removed in vacuum. The solid was recrystallized from hexane yielding a brown solid (83.0 mg, 0.04 mmol, 37%).

¹H NMR (400 MHz, CD₃CN): 9.23 (ddd, *J* = 5.5 Hz, 1.6 Hz, 0.7 Hz, 4H, bpy), 8.40 (dt, *J* = 8.3 Hz, 1.1 Hz, 4H, bpy), 8.27 (td, *J* = 7.9 Hz, 1.6 Hz, 4H, bpy), 8.23–8.19 (m, 4H, py), 7.80 (ddd, *J* = 7.7 Hz, 5.5 Hz, 1.3 Hz, 4H, bpy), 7.41–7.36 (m, 4H, py), 7.20 (bs, 1H), 7.12 (bs, 2H), 6.88 (td, 24H, AA'BB'), 3.78 (s, 12H, OCH₃). ESI-MS calculated (*m/z*) for C₈₂H₆₃N₉O₁₀Re₂: 853.6902; found: 853.6915. Elemental analysis calculated (%) for C₈₂H₆₃N₁₁O₁₆Re₂ · 3 H₂O: C 52.25, H 3.69, N 8.17; found: C 52.14, H 3.79, N 8.09.

AQ-xy-TMS

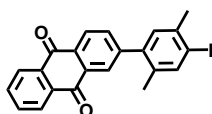
Synthesis followed a previously published protocol of ours.⁸⁸

2-bromoanthraquinone (3.32 g, 11.6 mmol), **TMS-xy-B(OH)₂** (3.08 g, 13.9 mmol), and Na₂CO₃ (3.67 g, 34.7 mmol) were dissolved in 12 mL water, 10 mL EtOH and 60 mL toluene under N₂ atmosphere and the suspension was de-oxygenated for 15 min. After addition of Pd(PPh₃)₄ (1.33 g, 1.16 mmol) and additional degassing the mixture was

refluxed for 1.5 d. The reaction solution was mixed with 100 mL H₂O and extracted with DCM (3 x 50 mL). The combined organic phases were dried over Na₂SO₄, the solvents were removed and subsequent column chromatography (SiO₂, pentane/DCM 1:1) gave a yellow solid (4.44 g, 11.6 mmol, quant.).

¹H NMR (400 MHz, CDCl₃): 8.32–8.38 (m, 3H, AQ), 8.30 (d, *J* = 1.8 Hz, 1H, AQ), 7.82 (m, 2H, AQ), 7.76–7.79 (dd, *J* = 8.0 Hz, 1.9 Hz, 1H, AQ), 7.40 (s, 1H, xy), 7.11 (s, 1H, xy), 2.49 (s, 3H, CH₃), 2.30 (s, 3H, CH₃), 0.38 (s, 9H, Si(CH₃)₃).

AQ-xy-I

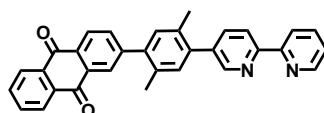


A previously published protocol was followed.⁸⁸

AQ-xy-TMS (1.97 g, 5.12 mmol) was dissolved in 10 mL DCM under N₂ atmosphere and cooled to 0 °C. A solution of ICl (563 μL, 10.8 mmol) in 40 mL MeCN was added very slowly, the yellow suspension was stirred at 0 °C for 15 min and at RT over night. After quenching with 200 mL Na₂S₂O₃-solution (5% in H₂O) and extraction with DCM (3 x 50 mL) the combined organic phases were washed with 50 mL H₂O and dried over Na₂SO₄. Evaporation to complete dryness yielded a yellow solid (2.2 g, 5.12 mmol, quant.).

¹H NMR (400 MHz, CDCl₃): 8.31–8.37 (m, 3H, AQ), 8.25 (d, *J* = 1.8 Hz, 1H, AQ), 7.80–7.85 (m, 2H, AQ), 7.79 (s, 1H, xy), 7.72–7.74 (dd, *J* = 8.0 Hz, 1.8 Hz, 1H, AQ), 7.14 (s, 1H, xy), 2.45 (s, 3H, CH₃), 2.23 (s, 3H, CH₃).

AQ-xy-bpy



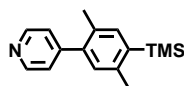
Preparation by adapting a previously published protocol.⁸⁸

AQ-xy-I (820.3 mg, 1.87 mmol) and **bpy-SnBu₃** (1.00 g, 2.25 mmol) were dissolved in 80 mL *m*-xylene under N₂ atmosphere and de-oxygenated for 30 min. After addition of Pd(PPh₃)₄ (108.0 mg, 0.09 mmol) the reaction mixture was de-oxygenated again by 3 cycles of vacuum/N₂ and heated to 150 °C for 70 h. 150 mL H₂O was added to the cool, black suspension and extracted with DCM (3 x 50 mL). The combined

organic phases were dried over MgSO_4 , the solvents were evaporated and the crude product was subjected to column chromatography (SiO_2 , DCM, then DCM+1% NEt_3). Recrystallization from pentane gave a yellow solid (640.0 mg, 1.37 mmol, 73%).

^1H NMR (400 MHz, CDCl_3): 8.73 (ddd, $J = 5.5$ Hz, 2.0 Hz, 0.9 Hz, 2H, bpy), 8.50 (dd, $J = 8.1$ Hz, 0.8 Hz, 1H, bpy), 8.46 (dt, $J = 8.0$ Hz, 1.1 Hz, 1H, bpy), 8.40 (d, $J = 8.0$ Hz, 1H, bpy), 8.38–8.32 (m, 3H, AQ), 7.89–7.80 (m, 6H, 4 AQ + 1 bpy + 1 xy), 7.34 (ddd, $J = 7.5$ Hz, 4.8 Hz, 1.8 Hz, 1H, bpy), 7.27 (s, 1H, xy), 2.36 (d, $J = 3.2$ Hz, 6H, CH_3).

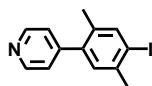
py-xy-TMS



TMS-xy-B(OH) $_2$ (1.37 g, 6.17 mmol) and 4-bromopyridine hydrochloride (1.00 g, 5.14 mmol), together with Na_2CO_3 (3.26 g, 30.8 mmol) were suspended in a mixture of H_2O /EtOH/toluene (8/6/20; v:v:v) under N_2 atmosphere and de-oxygenated for 20 min. After addition of $\text{Pd}(\text{PPh}_3)_4$ (59.4 mg, 0.05 mmol) the reaction mixture was de-oxygenated again for 10 min and heated to reflux for 1.5 d. After addition of 100 mL H_2O to the cool reaction mixture the product was extracted with DCM (3 x 50 mL), dried over MgSO_4 and the solvents were evaporated. Column chromatography on SiO_2 with an eluent mixture of pentane/DCM 2/1 + 1% NEt_3) gave the product as a light yellow solid (1.30 g, 5.09 mmol, 99%).

^1H NMR (400 MHz, CDCl_3): 8.65–8.63 (m, 2H, py), 7.37 (s, 1H, xy), 7.27–7.26 (m, 2H, py), 7.02 (s, 1H, xy), 2.46 (s, 3H, CH_3), 2.26 (s, 3H, CH_3), 0.36 (s, 9H, $\text{Si}(\text{CH}_3)_3$).

py-xy-I

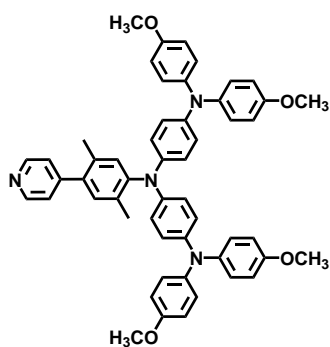


Py-xy-TMS (1.30 g, 5.09 mmol) was dissolved in 5 mL DCM under N_2 atmosphere and cooled to 0 °C. At this temperature a solution of ICl (520 μL , 10.2 mmol) in 20 mL MeCN was added dropwise and the resulting suspension was stirred at RT over night. After quenching with 200 mL sat. $\text{Na}_2\text{S}_2\text{O}_3$ -solution the product was extracted with DCM (3 x 50 mL), dried over Na_2SO_4 and the solvents were evaporated. The crude product was filtered over a plug of SiO_2 with an eluent mixture of pentane/DCM

2/1 + 1% NEt_3) and gave pure product as beige solid (1.52 g, 4.92 mmol, 97%).

^1H NMR (400 MHz, CDCl_3): 8.68–8.61 (m, 2H, py), 7.76 (s, 1H, xy), 7.25–7.18 (m, 2H), 7.06 (s, 1H, xy), 2.43 (s, 3H, CH_3), 2.19 (s, 3H, CH_3).

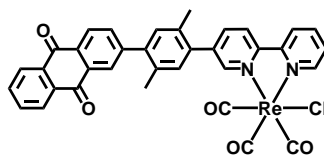
py-xy-OTA



Py-xy-I (177.2 mg, 0.57 mmol) and **OTA** (429.0 mg, 0.69 mmol), together with KO^tBu (1.28 g, 11.4 mmol), $\text{Pd}(\text{dba})_2$ (32.8 mg, 0.06 mmol), and $(\text{HP}^t\text{Bu}_3)\text{BF}_4$ (16.5 mg, 0.06 mmol) were dissolved in dry, de-oxygenated toluene (15 mL) under N_2 atmosphere. The mixture was heated to 100 °C for 2.5 d. 150 mL H_2O was added and the aqueous phase was extracted with DCM (3 x 50 mL). After drying over Na_2SO_4 and evaporation of the solvents the crude product was subjected to column chromatography. First with pure DCM, then with DCM + 1% NEt_3 as eluents the pure product was obtained as a brown solid (0.43 g, 0.53 mmol, 94%).

^1H NMR (400 MHz, CDCl_3): 8.64–8.61 (m, 2H, py), 7.29–7.26 (m, 2H, py), 7.06–6.99 (m, 10H, xy + AA'BB'), 6.87–6.77 (m, 16H, AA'BB'), 3.78 (s, 12H, OCH_3), 2.20 (s, 3H, CH_3), 2.05 (s, 3H, CH_3).

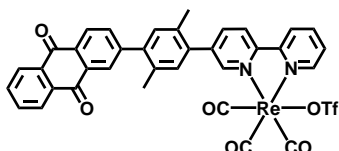
AQ-Re-Cl



AQ-xy-bpy (150.0 mg, 0.32 mmol) and $\text{Re}(\text{CO})_5\text{Cl}$ (116.3 mg, 0.32 mmol) were dissolved in 25 mL toluene and heated to reflux over night. After cooling to RT the yellow solid was filtered, washed with Et_2O and dried in vacuum (224.5 mg, 0.29 mmol, 91%).

^1H NMR (400 MHz, CDCl_3): 9.13–9.07 (m, 2H, bpy), 8.42 (d, $J = 8.0$ Hz, 1H, bpy), 8.38–8.32 (m, 3H, AQ), 8.26 (dd, $J = 9.7$ Hz, 8.0 Hz, 2H, AQ + bpy), 8.11 (ddd, $J = 8.6$ Hz, 6.9 Hz, 1.9 Hz, 2H, bpy), 7.87–7.80 (m, 3H, AQ), 7.57 (ddd, $J = 7.6$ Hz, 5.5 Hz, 1.2 Hz, 1H, bpy), 7.30 (d, $J = 6.6$ Hz, 2H, xy), 2.39 (d, $J = 11.0$ Hz, 6H, CH_3).

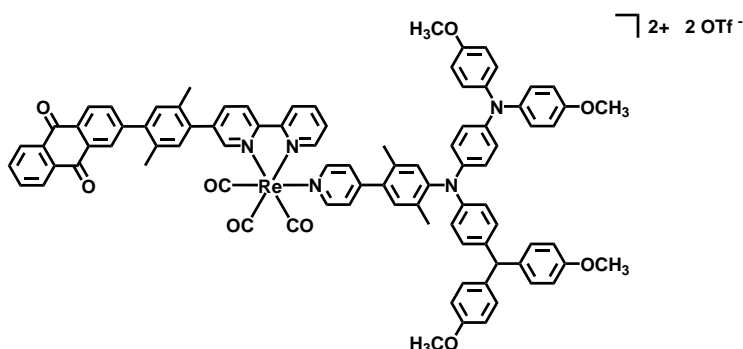
AQ-Re-OTf



AQ-Re-Cl (201.0 mg, 0.26 mmol) was suspended in 15 mL dry DCM. Trifluoromethanesulfonic acid (1.50 mL, 17 mmol) was added dropwise at RT and the solution was stirred for 2 h. Et_2O was added slowly the reaction mixture and the product precipitated as a yellow solid. After keeping in the fridge over night the solid was filtered, washed with Et_2O and dried in vacuum (190.3 mg, 0.21 mmol, 83%).

^1H NMR (400 MHz, CDCl_3): 9.16–9.10 (m, 2H, bpy), 8.42 (dd, $J = 8.0$ Hz, 2.0 Hz, 1H, bpy), 8.39–8.32 (m, 3H, AQ), 8.29 (t, $J = 7.6$ Hz, 2H, AQ + bpy), 8.24–8.15 (m, 2H, bpy), 7.8–7.79 (m, 3H, AQ), 7.66 (ddd, $J = 7.6$ Hz, 5.4 Hz, 1.3 Hz, 1H, bpy), 7.30 (d, $J = 12.6$ Hz, 2H, xy), 2.42–2.35 (m, 6H, CH_3).

AQ-Re-OTA

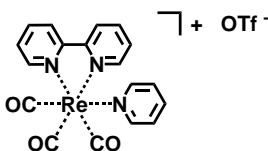


AQ-Re-OTf (80.7 mg, 0.08 mmol) and **py-xy-OTA** (74.0 mg, 0.10 mmol) were suspended in 5 mL MeOH and 5 mL CHCl_3 , de-oxygenated for 20 min and heated to reflux for 43 h. The solvents were evaporated and the residue was subjected to column chromatography with DCM + 1% MeOH, then 3% MeOH, as eluents. The obtained solid was dissolved in a minimal amount of DCM and precipitated in Et_2O

to get pure product as a dark orange solid (64.0 mg, 0.04 mmol, 47%).

^1H NMR (400 MHz, CD_3CN): 9.27–9.23 (m, 1H), 9.19 (d, $J = 1.7$ Hz, 1H), 8.44 (dd, $J = 8.2$ Hz, 4.2 Hz, 2H), 8.35–8.32 (m, 1H), 8.31–8.24 (m, 7H), 7.88 (dt, $J = 6.8$ Hz, 1.5 Hz, 3H), 7.83–7.77 (m, 1H), 7.44 (s, 1H), 7.37 (s, 1H), 7.24 (s, 2H) 6.86 (bs, 26 H), 3.73 (s, 12H), 2.35 (d, $J = 2.7$ Hz, 12H). ESI-MS calculated (m/z) for $\text{C}_{88}\text{H}_{70}\text{N}_6\text{O}_9\text{Re}$: 1541.4765; found: 1541.4774. Elemental analysis calculated (%) for $\text{C}_{89}\text{H}_{70}\text{F}_3\text{N}_6\text{O}_{12}\text{ReS}\cdot\text{Et}_2\text{O}$: C 63.29, H 4.57, N 4.76; found: C 63.01, H 4.68, N 5.11.

Re-ref

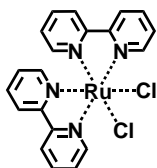


fac-**Re(bpy)(CO)₃OTf** (0.20 g, 0.35 mmol) was dissolved in 20 mL MeOH and pyridine (0.17 mL, 2.09 mmol) was added under N_2 atmosphere. The yellow reaction mixture was heated to 85 °C for 24 h. After cooling to RT the solvents were evaporated, the residue was taken up in little DCM and precipitated in hexane. This afforded the product as a yellow solid (193.5 mg, 0.30 mmol, 85%).

^1H NMR (400 MHz, CD_3CN): 9.22 (ddd, $J = 5.5$ Hz, 1.5 Hz, 0.8 Hz, 2H, bpy), 8.37 (dt, $J = 8.3$ Hz, 1.0 Hz, 2H, bpy), 8.30–8.20 (m, 4H, bpy + py), 7.85 (tt, $J = 7.7$ Hz, 1.6 Hz, 1H, py), 7.79 (ddd, $J = 7.6$ Hz, 5.5 Hz, 1.3 Hz, 2H, bpy), 7.33–7.26 (m, 2H, py).

VI.5 Syntheses of ligands and metal complexes with ruthenium

Ru-pre

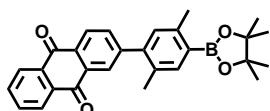


$\text{RuCl}_3\cdot 3\text{H}_2\text{O}$ (1.98 g, 9.55 mmol), 2,2'-bipyridine (3.00 g, 19.2 mmol), and lithium chloride (2.83 g, 66.9 mmol) were suspended in 17 mL dry DMF under N_2 atmosphere and

heated to reflux for 16 h. The cooled reaction mixture was concentrated, acetone was added and the product was crystallized in the fridge over night. The precipitate was filtered, washed with acetone, H₂O, and Et₂O. After drying in vacuum the product was obtained as a dark violet solid (673.0 mg, 1.39 mmol, 15%).

This Ru-precursor was used without further characterization.

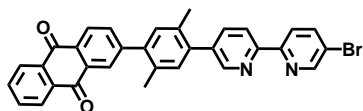
AQ-xy-B-ester



AQ-xy-I (200.0 mg, 0.46 mmol), bis-pinacolato diboron (173.8 mg, 0.68 mmol), and KOAc (198.6 mg, 2.02 mmol) were suspended in dry DMF (10 mL) and de-oxygenated for 30 min. After addition of PdCl₂(PPh₃)₂ (8.10 mg, 0.01 mmol) the mixture was heated to 100 °C for 24 h. The DMF was evaporated and the residue was taken up in 50 mL DCM and washed with H₂O repeatedly. After drying over Na₂SO₄ and evaporation of the solvents, the crude product was subjected to column chromatography. With pentane/DCM 1:1 as eluent the pure product was obtained as yellow crystals (183.0 mg, 0.42 mmol, 91%).

¹H NMR (400 MHz, CDCl₃): 8.38–8.30 (m, 3H, AQ), 8.28 (dd, *J* = 1.8 Hz, 0.5 Hz, 1H, AQ), 7.85–7.78 (m, 2H, AQ), 7.76 (dd, *J* = 8.0 Hz, 1.8 Hz, 1H, AQ), 7.72 (s, 1H, xy), 7.11 (s, 1H, xy), 2.56 (s, 3H, CH₃), 2.28 (s, 3H, CH₃), 1.38 (s, 12H, CH₃).

AQ-xy-bpy-Br

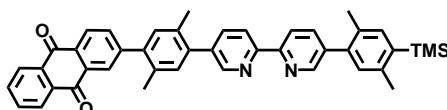


AQ-xy-B-ester (200.0 mg, 0.46 mmol), **Br-bpy-Br** (286.5 mg, 0.91 mmol), and Na₂CO₃ (146.3 mg, 1.38 mmol) were suspended in 10 mL THF and 3 mL H₂O under N₂ atmosphere and de-oxygenated for 20 min. After addition of Pd(PPh₃)₄ (35.0 mg, 0.03 mmol) the reaction mixture was de-oxygenated again for 10 min and heated to reflux over night. After cooling the reaction mixture to RT, the product was filtered and washed with MeOH. Column chromatography on SiO₂ with an eluent mixture of DCM + 1% NEt₃ yielded the product as a yellow solid (0.23 mg, 0.42 mmol, 92%).

¹H NMR (400 MHz, CDCl₃): 8.76 (dd, *J* = 3.1 Hz, 2.4 Hz, 1H, bpy), 8.71 (dd, *J* = 2.2 Hz,

0.9 Hz, 1H, bpy), 8.47 (dd, $J = 8.1$ Hz, 0.9 Hz, 1H, bpy), 8.43–8.38 (m, 2H, bpy), 8.37–8.34 (m, 3H, AQ), 7.98 (dd, $J = 8.5$ Hz, 2.4 Hz, 1H, bpy), 7.85–7.82 (m, 4H, AQ), 7.27 (s, 1H, xy), 7.25 (s, 1H, xy), 2.36 (s, 3H, CH₃), 2.35 (s, 3H, CH₃).

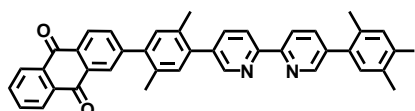
AQ-xy-bpy-xy-TMS



AQ-xy-bpy-Br (196.0 mg, 0.36 mmol), **TMS-xy-B(OH)₂** (95.8 mg, 0.43 mmol), and Na₂CO₃ (228.9 mg, 2.16 mmol) were suspended in 4 mL H₂O, 3 mL EtOH and 10 mL toluene under N₂ atmosphere and de-oxygenated for 20 min. Following the addition of Pd(PPh₃)₄ (41.6 mg, 0.04 mmol) the reaction mixture was de-oxygenated again for 15 min and heated to reflux for 2 d. After addition of 100 mL H₂O the product was extracted with DCM (3 x 50 mL), dried over Na₂SO₄ and the solvents were evaporated. Column chromatography on SiO₂ with an eluent mixture of DCM + 1% MeOH and subsequent recrystallization from pentane gave the product as a light yellow solid (0.17 mg, 0.26 mmol, 73%).

¹H NMR (400 MHz, CDCl₃): 8.74 (dd, $J = 14.3$ Hz, 2.2 Hz, 2H, bpy), 8.52 (t, $J = 8.2$ Hz, 2H, bpy), 8.40 (d, $J = 8.0$ Hz, 1H, bpy), 8.38–8.33 (m, 3H, AQ), 7.88 (dd, $J = 8.1$ Hz, 2.2 Hz, 1H, bpy), 7.85–7.80 (m, 4H, AQ), 7.41 (s, 1H, xy), 7.28 (s, 2H, xy), 7.12 (s, 1H, xy), 2.50 (s, 3H, CH₃), 2.38 (s, 3H, CH₃), 2.36 (s, 3H, CH₃), 2.33 (s, 3H, CH₃), 0.38 (s, 9H, Si(CH₃)₃).

AQ-xy-bpy-xy-I

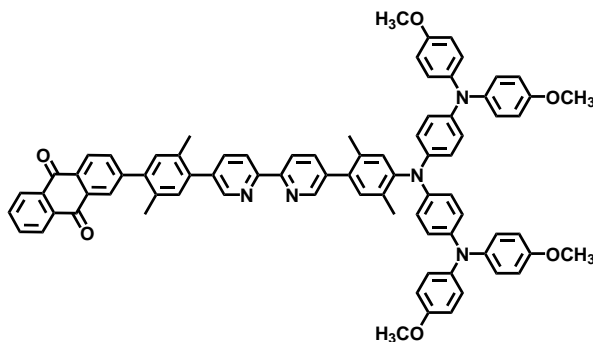


AQ-xy-bpy-xy-TMS (0.17 g, 0.26 mmol) was dissolved in 6 mL DCM under N₂ atmosphere and cooled to 0 °C. At this temperature a solution of ICl (30 μL, 0.56 mmol) in 3 mL MeCN was added dropwise and the resulting suspension was stirred at RT over night. After quenching with 200 mL 5% aqueous Na₂S₂O₃-solution the product was extracted with DCM (3 x 50 mL), dried over Na₂SO₄ and the solvents were evaporated. The crude product was passed through a pluck of SiO₂ with an eluent mixture of DCM + 1% MeOH, which gave pure product as a yellow solid (0.12 g, 0.17 mmol,

66%).

^1H NMR (400 MHz, CDCl_3): 8.77 (d, $J = 1.7$ Hz, 1H, bpy), 8.68 (d, $J = 1.7$ Hz, 1H, bpy), 8.58 (bs, 2H, bpy), 8.41 (dd, $J = 7.9$ Hz, 0.5 Hz, 1H, bpy), 8.38–8.34 (m, 3H, AQ), 7.93 (d, $J = 8.1$ Hz, 1H, bpy), 7.87–7.81 (m, 4H, AQ), 7.81 (s, 1H, xy), 7.29–7.27 (m, 2H, xy), 7.16 (s, 1H, xy), 2.47 (s, 3H, CH_3), 2.38 (s, 3H, CH_3), 2.36 (s, 3H, CH_3), 2.27 (s, 3H, CH_3).

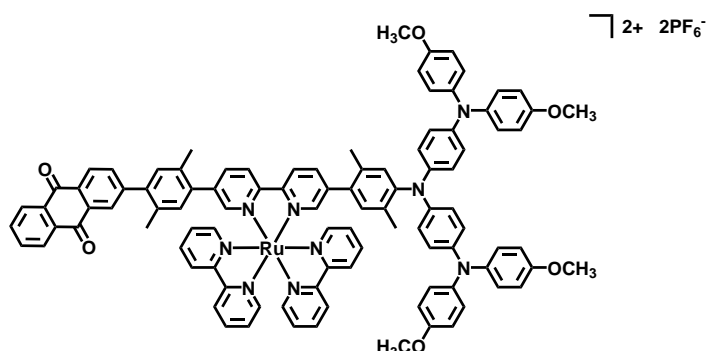
AQ–bpy–OTA



AQ–xy–bpy–xy–I (70.0 mg, 0.10 mmol) and **OTA** (68.9 mg, 0.11 mmol) were suspended in 10 mL dry, de-oxygenated toluene, together with NaO^tBu (192.2 mg, 2.00 mmol), $\text{Pd}(\text{dba})_2$ (5.80 mg, 0.01 mmol), and $(\text{HP}^t\text{Bu}_3)\text{BF}_4$ (2.90 mg, 0.01 mmol). The mixture was heated to reflux for 27 h. After evaporation of the solvent the residue was taken up in DCM (50 mL), washed with H_2O and dried over Na_2SO_4 . The crude product was subjected to column chromatography with pure DCM then DCM + 1% MeOH as eluents and subsequently recrystallized from hexane. This procedure gave the desired ligand as a brown solid (0.06 g, 0.05 mmol, 50%).

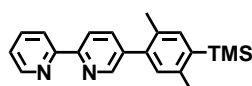
^1H NMR (400 MHz, C_6D_6): 9.01–8.95 (m, 2H, bpy), 8.95–8.90 (m, 2H, bpy), 8.50 (d, $J = 1.8$ Hz, 1H, bpy), 8.36 (d, $J = 8.0$ Hz, 1H, AQ), 8.33–8.25 (m, 2H, AQ), 7.53 (dt, $J = 8.1$ Hz, 2.2 Hz, 2H, AQ), 7.35 (dd, $J = 7.9$ Hz, 1.8 Hz, 2H, AQ), 7.27 (s, 1H, bpy), 7.21 (s, 1H, xy), 7.14–7.08 (m, 16H, AA'BB'), 6.99 (d, $J = 3.8$ Hz, 2H, xy), 6.96 (s, 1H, xy), 6.73 (d, $J = 8.7$ Hz, 8H, AA'BB'), 3.30 (s, 12H, OCH_3), 2.20 (s, 3H, CH_3), 2.08 (s, 6H, CH_3), 1.99 (s, 3H, CH_3).

AQ-Ru-OTA



AQ-bpy-OTA (60.0 mg, 0.05 mmol) and **Ru-pre** (24.4 mg, 0.05 mmol) were suspended in a de-oxygenated $\text{CHCl}_3/\text{EtOH}$ (3 mL/10 mL) solvent mixture under nitrogen atmosphere and heated to reflux for 2 d. Upon complete consumption of the starting materials, the reaction mixture was evaporated to dryness and the residue was subjected to column chromatography (SiO_2 , acetone \rightarrow acetone/ H_2O /sat. aqueous KNO_3 90:10:1). After almost complete evaporation of the acetone the desired complex was precipitated by drop wise addition of sat. aqueous KP_6 solution. Filtration and washing with H_2O and Et_2O gave a dark brown solid (64.0 mg, 0.03 mmol, 68%). ^1H NMR (400 MHz, acetone- d_6): 8.97 (dd, $J = 10.9$ Hz, 8.5 Hz, 2H, bpy), 8.85 (td, $J = 8.0$ Hz, 3.0 Hz, 4H, bpy), 8.39–8.12 (m, 15H, AQ + bpy), 8.06 (t, $J = 1.6$ Hz, 2H, bpy), 8.01–7.95 (m, 2H, bpy), 7.91 (dd, $J = 8.0$ Hz, 1.9 Hz, 1H, xy), 7.66 (ddt, $J = 7.5$ Hz, 5.7 Hz, 1.5 Hz, 2H, bpy), 7.58 (dddd, $J = 10.1$ Hz, 7.4 Hz, 5.7 Hz, 1.2 Hz, 2H, bpy), 7.24 (d, $J = 15.3$ Hz, 2H, xy), 7.13 (s, 1H, xy), 6.99 (d, $J = 8.1$ Hz, 8H, AA'BB'), 6.93–6.68 (m, 16H, AA'BB'), 3.77 (s, 12H, OCH_3), 2.29 (s, 3H, CH_3), 2.09 (s, 3H, CH_3), 2.01 (s, 3H, CH_3), 1.97 (s, 3H, CH_3). ESI-MS calculated (m/z) for $\text{C}_{100}\text{H}_{81}\text{N}_9\text{O}_6\text{Ru}$: 802.7675; found: 802.7670. Elemental analysis calculated (%) for $\text{C}_{100}\text{H}_{81}\text{F}_{12}\text{N}_9\text{O}_6\text{P}_2\text{Ru} \cdot 5.5 \text{H}_2\text{O}$: C 60.21, H 4.65, N 6.32; found: C 60.30, H 4.52, N 6.15.

bpy-xy-TMS

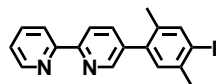


Bpy-Br (1.00 g, 4.25 mmol), **TMS-xy-B(OH) $_2$** (1.13 g, 5.10 mmol), and Na_2CO_3 (1.35 g, 12.8 mmol) were suspended in 8 mL H_2O , 20 mL EtOH and 160 mL toluene under N_2 atmosphere and de-oxygenated for 1 h. After addition of $\text{Pd}(\text{PPh}_3)_4$ (246.0 mg,

0.21 mmol) the reaction mixture was de-oxygenated again for 30 min. The mixture was heated to 90 °C for 1.5 d. 100 mL H₂O was added to the cooled reaction mixture and the aqueous phase was extracted with DCM (3 x 50 mL). After drying over Na₂SO₄ and evaporation of the solvents the crude product was subjected to column chromatography. With pentane/Et₂O (3:1) + 1% NEt₃ as eluent mixture the product was obtained as a beige solid (1.40 g, 4.21 mmol, 99%).

¹H NMR (400 MHz, CDCl₃): 8.72 (d, *J* = 4.8 Hz, 2H, bpy), 8.48 (t, *J* = 8.3 Hz, 2H, bpy), 7.83 (td, *J* = 8.1 Hz, 7.5 Hz, 2.0 Hz, 2H, bpy), 7.43 (s, 1H, xy), 7.31 (ddd, *J* = 7.4 Hz, 4.8 Hz, 1.1 Hz, 1H, bpy), 7.12 (s, 1H, xy), 2.51 (s, 3H, CH₃), 2.34 (s, 3H, CH₃), 0.40 (s, 9H, Si(CH₃)₃).

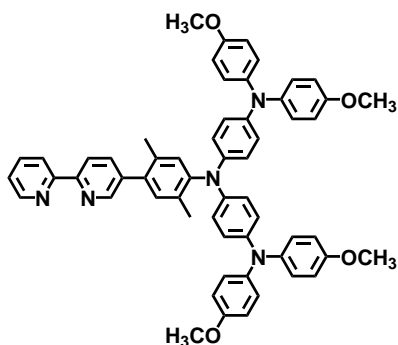
bpy-xy-I



Bpy-Br (500.0 mg, 1.50 mmol) was dissolved in 3 mL DCM under N₂ and cooled to 0 °C. ICl (0.17 mL, 3.00 mmol) in 10 mL DCM were added dropwise to the cooled reaction mixture, and it was stirred at RT over night. Excess ICl was quenched by addition of 100 mL sat. aqueous Na₂S₂O₃-solution and the aqueous phase was extracted with DCM (3 x 50 mL). After drying over Na₂SO₄ and evaporation of the solvents, the crude product was subjected to column chromatography. With pentane/Et₂O (1:1) as eluent mixture the product was obtained as a light yellow solid (0.56 g, 1.45 mmol, 97%).

¹H NMR (400 MHz, acetone-d₆): 8.70 (ddd, *J* = 4.8 Hz, 1.8 Hz, 0.9 Hz, 1H, bpy), 8.65 (dd, *J* = 2.3 Hz, 0.8 Hz, 1H, bpy), 8.56 (dd, *J* = 8.2 Hz, 0.8 Hz, 1H, bpy), 8.53 (dt, *J* = 8.0 Hz, 1.0 Hz, 1H, bpy), 7.98–7.90 (m, 2H, bpy), 7.84 (s, 1H, xy), 7.44 (ddd, *J* = 7.5 Hz, 4.8 Hz, 1.2 Hz, 1H, bpy), 7.28 (s, 1H, xy), 2.44 (s, 3H, CH₃), 2.28 (s, 3H, CH₃).

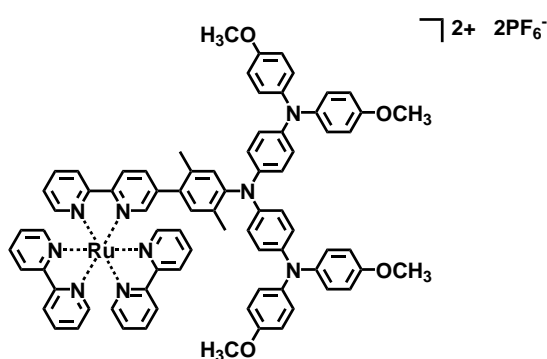
bpy-xy-OTA



Bpy-xy-I (148.6 mg, 0.38 mmol), **OTA** (200.0 mg, 0.32 mmol), NaO^tBu (615.0 mg, 6.40 mmol), $\text{Pd}(\text{dba})_2$ (9.20 mg, 0.02 mmol), and $(\text{HP}^t\text{Bu}_3)\text{BF}_4$ (4.60 mg, 0.02 mmol) were dissolved in dry, de-oxygenated toluene (15 mL) under N_2 atmosphere. The mixture was heated to 110 °C for 24 h. 150 mL H_2O was added to the cooled reaction mixture and the aqueous phase was extracted with DCM (3 x 50 mL). After drying over Na_2SO_4 and evaporation of the solvents, the crude product was subjected to column chromatography. With DCM + 1% NEt_3 the brown product fraction was eluted and recrystallization from pentane yielded a brown solid (0.28 g, 0.32 mmol, 99%).

^1H NMR (400 MHz, acetone- d_6): 8.71–8.67 (m, 2H, bpy), 8.54 (td, $J = 8.2$ Hz, 0.9 Hz, 2H, bpy), 7.97–7.91 (m, 2H, bpy), 7.42 (ddd, $J = 7.5$ Hz, 4.8 Hz, 1.2 Hz, 1H, bpy), 7.24 (s, 1H, xy), 7.12 (s, 1H, xy), 7.02–6.98 (m, 8H, AA'BB'), 6.86 (td, $J = 5.8$ Hz, 5.2 Hz, 2.9 Hz, 16H, AA'BB'), 3.77 (s, 12H, OCH_3), 2.27 (s, 3H, CH_3), 2.11 (s, 3H, CH_3).

Ru-OTA

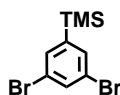


Bpy-xy-OTA (100.0 mg, 0.11 mmol) and **Ru-pre** (54.9 mg, 0.11 mmol) were suspended in 20 mL EtOH and 6 mL CHCl_3 under N_2 atmosphere and de-oxygenated for 20 min. After refluxing for 21 h, the solvents were evaporated and the residue was subjected to column chromatography. The product was eluted with a mixture of acetone/ H_2O 9:1 + 1% sat. aqueous KNO_3 , the acetone was evaporated and the product precipitated by dropwise addition of a sat. aqueous KPF_6 solution. Filtration and drying gave a dark red solid (0.11 g, 0.07 mmol, 64%).

^1H NMR (400 MHz, CD_3CN): 8.59–8.47 (m, 6H, bpy), 8.06 (dddt, $J = 8.5$ Hz, 7.0 Hz, 3.3 Hz, 1.7 Hz, 5H, bpy), 7.98 (td, $J = 8.0$ Hz, 1.4 Hz, 1H, bpy), 7.88–7.84 (m, 1H, bpy), 7.80–7.76 (m, 1H, bpy), 7.76–7.72 (m, 3H, bpy), 7.66 (d, $J = 1.7$ Hz, 1H, bpy), 7.45–7.37 (m, 4H, bpy), 7.37–7.31 (m, 1H, bpy), 7.03 (s, 1H, xy), 6.98–6.93 (m, 8H, AA'BB'), 6.93 (s, 1H, xy), 6.86–6.81 (m, 8H, AA'BB'), 6.78–6.69 (m, 8H, AA'BB'), 3.74 (s, 12H, OCH_3), 1.97 (s, 3H, CH_3), 1.85 (s, 3H, CH_3). ESI-MS calculated (m/z) for $\text{C}_{78}\text{H}_{67}\text{N}_9\text{O}_4\text{Ru}$:

647.7174; found: 647.7190. Elemental analysis calculated (%) for $C_{78}H_{67}F_{12}N_9O_4P_2Ru \cdot 2CH_3COCH_3$: C 59.29, H 4.68, N 7.41; found: C 59.24, H 4.85, N 7.63.

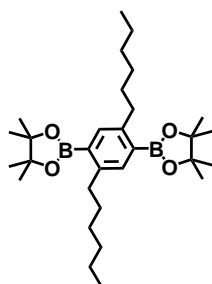
Br-TMS-Br



1,3,5-tribromobenzene (5.00 g, 15.9 mmol) was dissolved in 100 mL Et_2O under N_2 atmosphere and cooled to $-78^\circ C$. After dropwise addition of $n-BuLi$ (6.99 mL, 17.5 mmol) the suspension was stirred at $-78^\circ C$ for 3 h and $TMSCl$ was added dropwise. The reaction mixture was stirred at RT over night, quenched with 100 mL H_2O and extracted with Et_2O . The organic phase was dried over Na_2SO_4 , the solvent was evaporated and the crude product was subjected to column chromatography. With pure pentane as eluent the product was obtained as a light yellow liquid (4.34 g, 14.1 mmol, 89%).

1H NMR (400 MHz, $CDCl_3$): 7.65 (t, $J = 1.8$ Hz, 1H, ph), 7.52 (d, $J = 1.8$ Hz, 2H, ph), 0.28 (s, 9H, $Si(CH_3)_3$).

B-hex-B

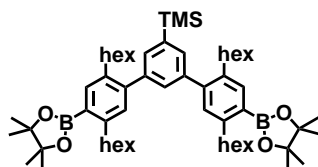


1,4-dihexyl-2,5-diiodobenzene (3.53 g, 7.09 mmol), bis-pinacolato diboron (5.40 g, 21.3 mmol), and $KOAc$ (5.57 g, 56.7 mmol) were suspended in 100 mL dry DMF and de-oxygenated for 20 min. After addition of $PdCl_2(PPh_3)_2$ (497.7 mg, 0.71 mmol) the mixture was heated to $90^\circ C$ for 2 d. The DMF was evaporated and the residue was taken up in 50 mL DCM and washed with H_2O repeatedly. After drying over Na_2SO_4 and evaporation of the solvents the crude product was subjected to column chromatography. With pure pentane, then pentane/ DCM 3:1 as eluents the pure product was obtained as a colorless crystalline solid (3.50 g, 7.02 mmol, 99%).

1H NMR (400 MHz, $CDCl_3$): 7.52 (s, 2H, hex), 2.81 (dd, $J = 9.2$ Hz, 6.8 Hz, 4H, CH_2),

1.54–1.47 (m, 4H, CH₂), 1.36 (d, $J = 10.7$ Hz, 4H, CH₂), 1.34 (s, 24H, CH₃), 1.30 (dd, $J = 6.3$ Hz, 3.5 Hz, 8H, CH₂), 0.92–0.86 (m, 6H, CH₃).

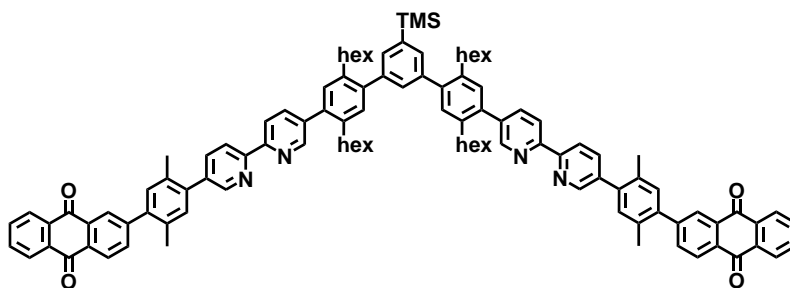
B–hex–TMS–hex–B



Br–TMS–Br (170.0 mg, 0.55 mmol), **B–hex–B** (1.10 g, 2.21 mmol), and Na₂CO₃ (604.1 mg, 5.70 mmol) were suspended in 30 mL toluene, 10 mL EtOH and 10 mL H₂O under N₂ atmosphere and the mixture was de-oxygenated for 20 min. After addition of Pd(PPh₃)₄ (109.8 mg, 0.09 mmol) the reaction mixture was heated to reflux for 3.5 d, cooled to RT, quenched with 100 mL sat. NH₄Cl solution and extracted with DCM (3 x 50 mL). The organic phase was dried over Na₂SO₄, evaporated to dryness and the residue was subjected to gravitational column chromatography. Eluting the product with pentane/DCM 10:1 then 5:1 gave a colorless oil (0.18 g, 0.20 mmol, 37%).

¹H NMR (400 MHz, CDCl₃): 7.71 (s, 2H, hex), 7.43 (d, $J = 1.7$ Hz, 2H, ph), 7.25 (t, $J = 1.7$ Hz, 1H, ph), 7.09 (s, 2H, hex), 2.92–2.84 (m, 4H, CH₂), 2.63–2.56 (m, 4H, CH₂), 1.62–1.54 (m, 4H, CH₂), 1.49 (dq, $J = 12.3$ Hz, 7.5 Hz, 4H, CH₂), 1.37 (s, 24H, CH₃), 1.36–1.29 (m, 12H, CH₂), 1.24–1.15 (m, 12H, CH₂), 0.91–0.87 (m, 6H, CH₃), 0.85–0.80 (m, 6H, CH₃), 0.30 (s, 9H, Si(CH₃)₃).

AQ–bpy–TMS–bpy–AQ

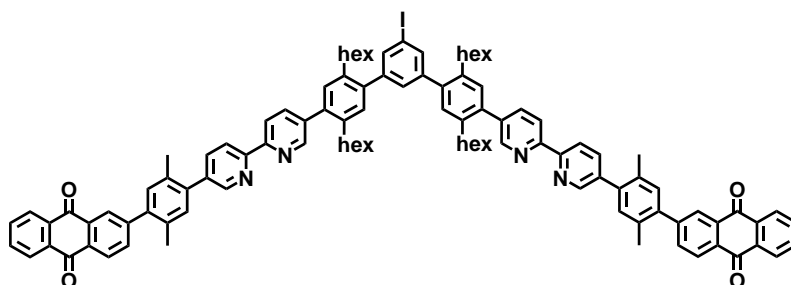


B–hex–TMS–hex–B (500.0 mg, 0.56 mmol), **AQ–xy–bpy–Br** (612.0 mg, 1.12 mmol), and Na₂CO₃ (356.2 mg, 3.36 mmol) were suspended in 20 mL H₂O, 10 mL EtOH, and 50 mL toluene under N₂ atmosphere. The suspension was de-oxygenated for 20 min. Following the addition of Pd(PPh₃)₄ (69.3 mg, 0.06 mmol) the yellow reaction mixture

was de-oxygenated again for 15 min and heated to reflux for 1.5 d. After addition of 100 mL H₂O to the cooled solution, the product was extracted with DCM (3 x 50 mL), dried over Na₂SO₄ and the solvents were evaporated. Column chromatography on SiO₂ with an eluent mixture of DCM + 1% MeOH, then DCM + 3% MeOH gave a yellow solid which was recrystallized from MeOH/hexane (v/v 1:1) (620.0 mg, 0.39 mmol, 71%).

¹H NMR (400 MHz, CDCl₃): 8.78 (s, 4H, bpy), 8.61–8.52 (m, 4H, bpy), 8.41 (d, *J* = 8.0 Hz, 2H, AQ), 8.38–8.35 (m, 6H, AQ), 7.91 (d, *J* = 8.1 Hz, 4H, bpy), 7.86–7.83 (m, 6H, AQ), 7.54 (d, *J* = 1.7 Hz, 2H, ph), 7.39 (t, *J* = 1.7 Hz, 1H, ph), 7.29 (s, 4H, xy/hex), 7.28 (s, 2H, xy/hex), 7.23 (s, 2H, xy/hex), 2.71–2.62 (m, 8H, CH₂), 2.38 (d, *J* = 7.3 Hz, 12H, CH₃), 1.58–1.52 (m, 8H, CH₂), 1.27–1.19 (m, 24H, CH₂), 0.82 (d, *J* = 5.8 Hz, 12H, CH₃), 0.35 (s, 9H, Si(CH₃)₃).

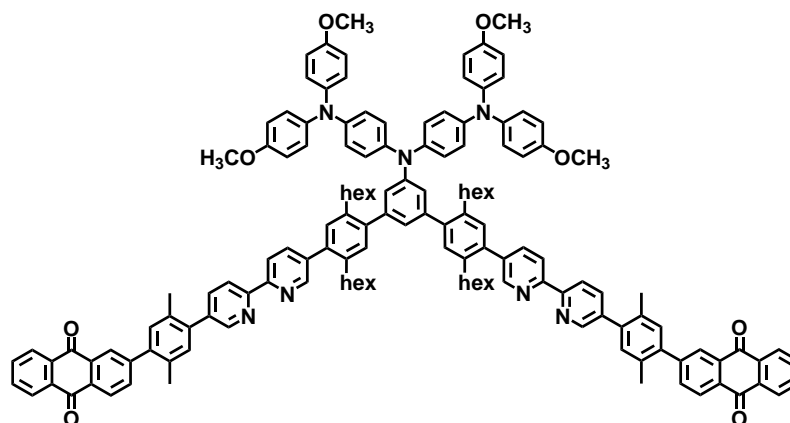
AQ–bpy–I–bpy–AQ



AQ–bpy–TMS–bpy–AQ (620.0 mg, 0.39 mmol) was dissolved in 8 mL DCM under N₂ atmosphere and cooled to 0 °C. At this temperature a solution of ICl (40.0 μL, 0.79 mmol) in 20 mL MeCN was slowly added dropwise. After stirring at 0 °C for 20 min, the ice-bath was removed and the mixture was stirred at RT over night. The reaction was quenched with sat. aqueous Na₂S₂O₃-solution (100 mL), extracted with DCM (3 x 50 mL), dried over Na₂SO₄ and the solvents were evaporated. Column chromatography on SiO₂ with an eluent mixture of DCM + 2% MeOH gave a yellow solid which was recrystallized from MeOH/hexane (v/v 1:1) (270 mg, 0.17 mmol, 43%).

¹H NMR (400 MHz, CDCl₃): 8.77 (dd, *J* = 2.3 Hz, 0.9 Hz, 2H, bpy), 8.75 (dd, *J* = 2.3 Hz, 0.9 Hz, 2H, bpy), 8.59–8.52 (m, 4H, bpy), 8.41 (d, *J* = 8.0 Hz, 2H, AQ), 8.38–8.34 (m, 6H, AQ), 7.89 (ddd, *J* = 11.1 Hz, 8.1 Hz, 2.3 Hz, 4H, bpy), 7.86–7.82 (m, 6H, AQ), 7.76 (d, *J* = 1.5 Hz, 2H, ph), 7.37 (t, *J* = 1.5 Hz, 1H, ph), 7.29 (s, 4H, xy/hex), 7.21 (d, *J* = 3.5 Hz, 4H, xy/hex), 2.65 (dt, *J* = 13.2 Hz, 7.9 Hz, 8H, CH₂), 2.38 (d, *J* = 7.2 Hz, 12H, CH₃), 1.55–1.48 (m, 8H, CH₂), 1.28–1.18 (m, 24H, CH₂), 0.87–0.78 (m, 12H, CH₃).

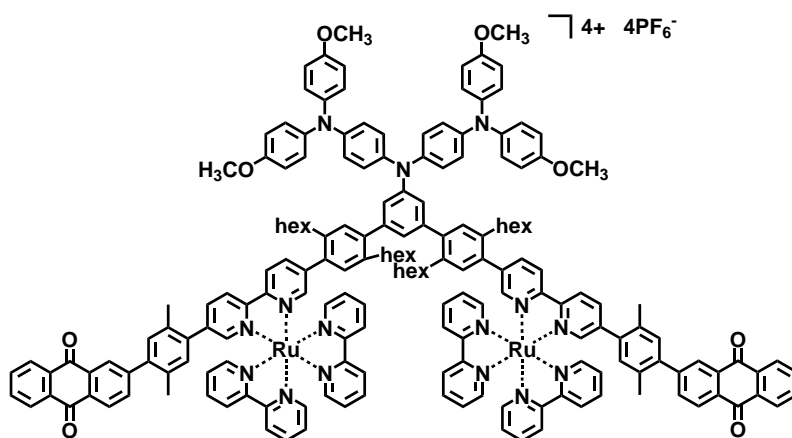
AQ–bpy–OTA–bpy–AQ



AQ–bpy–I–bpy–AQ (250.0 mg, 0.15 mmol), **OTA** (115.4 mg, 0.18 mmol), NaO^tBu (288.3 mg, 3.00 mmol), $\text{Pd}(\text{dba})_2$ (11.5 mg, 0.02 mmol), and $(\text{HP}^t\text{Bu}_3)\text{BF}_4$ (5.80 mg, 0.02 mmol) were suspended in dry, de-oxygenated toluene under N_2 atmosphere and heated to reflux for 5 d. After cooling to RT, 100 mL H_2O was added and the product was extracted with DCM (3 x 50 mL). The organic phase was dried over Na_2SO_4 , the solvents were evaporated, and the residue was subjected to column chromatography on SiO_2 . Eluting the product fraction with DCM + 2% MeOH and subsequent recrystallization from hexane gave pure product as a brown solid (200.0 mg, 0.09 mmol, 56%).

^1H NMR (400 MHz, C_6D_6): 9.07–8.99 (m, 6H, bpy), 8.92 (dd, $J = 2.2$ Hz, 0.8 Hz, 2H, bpy), 8.50 (d, $J = 1.8$ Hz, 2H, bpy), 8.36 (d, $J = 7.9$ Hz, 2H, AQ), 8.32–8.26 (m, 4H, AQ), 7.70 (dd, $J = 8.3$ Hz, 2.1 Hz, 2H, bpy), 7.60 (d, $J = 1.4$ Hz, 2H, ph), 7.54–7.50 (m, 4H, AQ), 7.37 (dd, $J = 9.2$ Hz, 2.1 Hz, 4H, AQ), 7.34 (d, $J = 1.7$ Hz, 2H, hex/xy), 7.23 (s, 2H, hex/xy), 7.15–7.06 (m, 18H, AA'BB'), 6.99 (d, $J = 5.2$ Hz, 4H, hex/xy), 6.96 (s, 1H, ph), 6.73–6.68 (m, 6H, AA'BB'), 3.31 (s, 12H, OCH_3), 2.92–2.82 (m, 4H, CH_2), 2.66–2.57 (m, 4H, CH_2), 2.09 (s, 12H, CH_3), 1.68–1.61 (m, 4H, CH_2), 1.50–1.44 (m, 4H, CH_2), 1.27–1.22 (m, 10H, CH_2), 1.16–1.05 (m, 14H, CH_2), 0.90–0.86 (m, 6H, CH_3), 0.80 (t, $J = 7.0$ Hz, 6H, CH_3). ESI-MS calculated (m/z) for $\text{C}_{146}\text{H}_{138}\text{N}_7\text{O}_8$: 705.6863; found: 705.6866. Singly protonated and triply oxidized ($m+\text{H}^+/3$).

AQ-Ru-OTA-Ru-AQ



AQ-bpy-OTA-bpy-AQ (130 mg, 0.06 mmol), **Ru-pre** (87.2 mg, 0.18 mmol), and AgNO_3 (183.5 mg, 1.08 mmol) were suspended in 5 mL CHCl_3 and 10 mL EtOH under N_2 atmosphere. The reaction mixture was de-oxygenated and heated to reflux for 3.5 d. After cooling to RT, 5 mL brine was added, the precipitated AgCl was filtered, washed with DCM, and the solvents were evaporated. The residue was subjected to column chromatography on SiO_2 . The pentad was purified by two consecutive columns with first acetone/ H_2O 9:1 + 0.5% sat. aqueous KNO_3 , then acetone/ H_2O 20:1 + 1% sat. aqueous KNO_3 . Sat. aqueous KPF_6 solution was added dropwise to an acetone/ H_2O solution of the pentad to precipitate it as the PF_6^- -salt. This gave the product as a dark red solid. (68.0 mg, 0.02 mmol, 32%).

^1H NMR (400 MHz, CD_3CN): 8.63 (dd, $J = 8.4$ Hz, 6.5 Hz, 4H), 8.55–8.50 (m, 6H), 8.48 (d, $J = 8.2$ Hz, 2H), 8.34 (d, $J = 8.1$ Hz, 2H), 8.30 (ddd, $J = 9.1$ Hz, 4.1 Hz, 2.5 Hz, 4H), 8.21 (d, $J = 1.8$ Hz, 2H), 8.18 (dd, $J = 8.4$ Hz, 1.9 Hz, 2H), 8.14–8.02 (m, 9H), 7.99–7.90 (m, 10H), 7.84 (dd, $J = 8.0$ Hz, 1.8 Hz, 2H), 7.77 (d, $J = 5.6$ Hz, 4H), 7.68 (d, $J = 1.7$ Hz, 2H), 7.63 (d, $J = 1.7$ Hz, 1H), 7.52–6.79 (m, 43H), 3.76 (s, 12H, OCH_3), 2.58–2.51 (m, 2H, CH_2), 2.28 (s, 6H, CH_3), 2.03 (s, 6H, CH_3), 1.36–1.28 (m, 4H, CH_2), 1.23–1.06 (m, 24H, CH_2), 1.02–0.89 (m, 10H, CH_2), 0.76 (td, $J = 7.0$ Hz, 3.5 Hz, 12H, CH_3). ESI-MS calculated (m/z) for $\text{C}_{186}\text{H}_{169}\text{N}_{15}\text{O}_8\text{Ru}_2$: 736.0352; found: 736.0361. Elemental analysis calculated (%) for $\text{C}_{186}\text{H}_{169}\text{F}_{24}\text{N}_{15}\text{O}_8\text{P}_4\text{Ru}_2 \cdot 2 \text{H}_2\text{O}$: C 62.75, H 4.90, N 5.90; found: C 62.72, H 5.17, N 5.92.

Sc(HMPA)₃

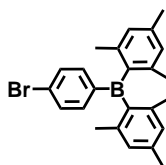
Attention! HMPA is very toxic and presumably a human carcinogen.

$\text{Sc}(\text{OTf})_3$ was dissolved in dry THF under N_2 atmosphere and 3 eq HMPA were added

dropwise. The colorless, clear solution was heated to 50 °C over night. The white precipitate was filtered, washed with THF, dried, and used without further characterization.

VI.6 Syntheses of the D-bridge-A molecules

Br-ph-B

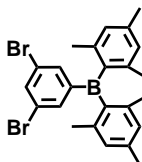


Synthesis according to literature procedure.¹⁷⁰

1,4-dibromobenzene (1.75 g, 7.42 mmol) was dissolved in 20 mL dry Et₂O under N₂ atmosphere and cooled to -78 °C. After dropwise addition of *n*-BuLi (3.40 mL, 5.44 mmol) the mixture was stirred at this temperature for 3 h. A solution of dimesitylboron fluoride (1.56 g, 5.82 mmol) in 5 mL dry Et₂O was added dropwise and the suspension was stirred at RT over night. 50 mL Et₂O was added and the organic phase was washed with 100 mL sat. NH₄Cl-solution and H₂O, respectively. After drying over Na₂SO₄, evaporation of the solvent and column chromatography with pure pentane as eluent, pure product was obtained as a white solid (2.49 g, 6.15 mmol, 80% (of applied 1,4-dibromobenzene)).

¹H NMR (400 MHz, CDCl₃): 7.48–7.50 (m, 2H, AA'BB'), 7.36–7.38 (m, 2H, AA'BB'), 6.82 (s, 4H, AA'BB'), 2.31 (s, 6H, CH₃), 1.99 (s, 12H, CH₃).

Br₂-ph-B

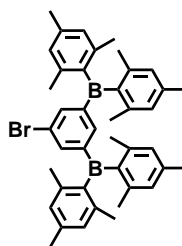


1,3,5-tribromobenzene (2.00 g, 6.35 mmol) was dissolved in 30 mL dry Et₂O under N₂ atmosphere and cooled to -78 °C. After dropwise addition of *n*-BuLi (2.54 mL, 6.35 mmol) the mixture was stirred at this temperature for 2 h. Dimesitylboron fluoride (1.70 g, 6.35 mmol) was added and the suspension was stirred at RT for 1 h.

The suspension was diluted with hexane (100 mL), washed with H₂O and dried over Na₂SO₄. Column chromatography with pure pentane gave pure product as a white solid (2.12 g, 4.38 mmol, 69%).

¹H NMR (400 MHz, CDCl₃): 7.76 (t, *J* = 1.9 Hz, 1H, ph), 7.51 (d, *J* = 1.9 Hz, 2H, ph), 6.82 (s, 4H, mesityl), 2.31 (s, 6H, CH₃), 1.97 (s, 12H, CH₃).

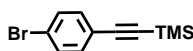
Br-ph-B2



Br₂-ph-B (2.10 g, 4.34 mmol) was treated with *n*-BuLi (1.74 mL, 4.34 mmol) and dimesitylboron fluoride (1.16 g, 4.34 mmol) in the same way as described for the preparation of Br₂-ph-B(mes)₂. After purification by column chromatography with pentane as eluent product was obtained as a white solid (2.12 g, 4.38 mmol, 69%).

¹H NMR (400 MHz, CDCl₃): 7.65 (d, *J* = 1.1 Hz, 2H, ph), 7.38 (t, *J* = 1.1 Hz, 1H, ph), 6.75 (s, 8H, mesityl), 2.28 (s, 12H, CH₃), 1.94 (s, 24H, CH₃).

Br-ph-acetylene-TMS

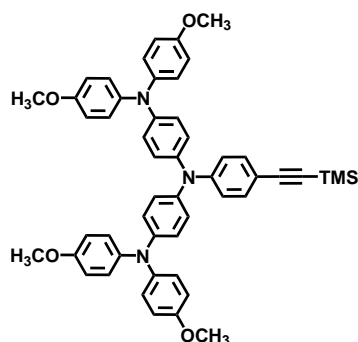


Synthesis by adaption of literature procedure.¹⁷¹

1-bromo-4-iodobenzene (2.00 g, 7.06 mmol) and trimethylsilyl acetylene (1.10 mL, 7.78 mmol) were dissolved in 30 mL dry NEt₃ under N₂ atmosphere and the mixture was thoroughly de-oxygenated. PdCl₂(PPh₃)₂ (98.2 mg, 0.14 mmol) and CuI (53.2 mg, 0.28 mmol) were added and the reaction mixture was heated to 100 °C for 30 min. After cooling to RT 100 mL sat. NH₄Cl-solution was added, the product was extracted with DCM (3 × 50 mL), the organic phases were dried over Na₂SO₄ and the solvent was evaporated. Column chromatography with pure pentane as eluent gave the pure product as a white solid (1.80 g, 7.11 mmol, quant.).

¹H NMR (400 MHz, CDCl₃): 7.41–7.45 (m, 2H, AA'BB'), 7.30–7.33 (m, 2H, AA'BB'), 0.25 (s, 9H, Si(CH₃)₃).

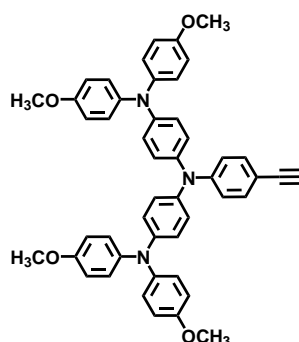
OTA-ph-acetylene-TMS



Br-ph-acetylene-TMS (150 mg, 0.59 mmol), **OTA** (307.9 mg, 0.49 mmol), NaO^tBu (941.8 mg, 9.80 mmol), $\text{Pd}(\text{dba})_2$ (28.2 mg, 0.05 mmol), and $(\text{HP}^t\text{Bu}_3)\text{BF}_4$ (14.2 mg, 0.05 mmol) were dissolved in 15 mL dry, de-oxygenated toluene under N_2 atmosphere. The mixture was stirred at 120 °C for 20 h. 100 mL brine was added to the cool mixture and the aqueous phase was extracted with DCM (3 x 50 mL). After drying over Na_2SO_4 and evaporation of the solvents the crude product was subjected to column chromatography. With DCM as eluent the pure product was obtained as a yellow oil which solidifies with time (290 mg, 0.36 mmol, 74%).

^1H NMR (400 MHz, acetone- d_6): 7.23–7.25 (m, 2H, AA'BB'), 7.0–7.06 (m, 8H, AA'BB'), 6.97–6.99 (m, 4H, AA'BB'), 6.82–6.90 (m, 14H, AA'BB'), 3.78 (s, 12H, OCH_3), 0.19 (s, 9H, $\text{Si}(\text{CH}_3)_3$).

OTA-ph-acetylene-H

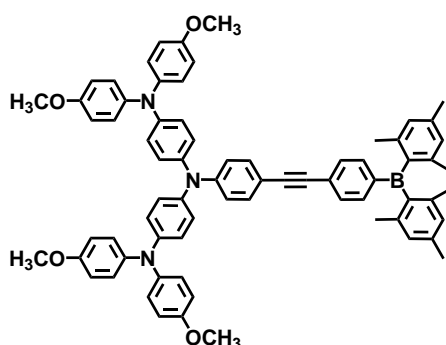


OTA-ph-acetylene-TMS (300.0 mg, 0.38 mmol) was dissolved in 10 mL dry THF under N_2 atmosphere and a TBAF-solution in THF (1.40 mL, 0.38 mmol) was added dropwise. The mixture was stirred at RT for 1.5 h. After removal of the THF, the residue was taken up in EtOAc (100 mL) and washed with H_2O repeatedly. The organic phases were dried over Na_2SO_4 and evaporated to dryness which gave pure

product as a yellow solid (250.0 mg, 0.35 mmol, 91%).

^1H NMR (400 MHz, C_6D_6): 7.38–7.36 (m, 2H, AA'BB'), 7.12–7.07 (m, 8H, AA'BB'), 7.05–6.97 (m, 10H, AA'BB'), 6.73–6.68 (m, 8H, AA'BB'), 3.29 (s, 12H, OCH_3), 2.76 (s, 1H, acetylene).

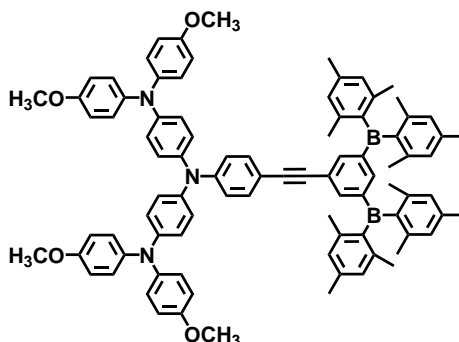
OTA-long-B



OTA-ph-acetylene-H (217.2 mg, 0.30 mmol) and **Br-ph-B** (100 mg, 0.25 mmol) were dissolved in 10 mL dry NEt_3 under N_2 atmosphere and the mixture was deoxygenated for 20 min. $\text{PdCl}_2(\text{PPh}_3)_2$ (3.51 mg, 0.005 mmol) and CuI (1.90 mg, 0.01 mmol) were added and the reaction mixture was heated to 100°C over night. After cooling to RT 100 mL sat. NH_4Cl -solution was added, the product was extracted with DCM (3 x 50 mL), the organic phases were dried over Na_2SO_4 and the solvent was evaporated. Column chromatography with an eluent mixture of pentane/DCM 1:2 yielded a bright orange oil which was crystallized as an orange solid by dropping a concentrated DCM-solution into H_2O (111.0 mg, 0.11 mmol, 42%).

^1H NMR (400 MHz, acetone- d_6): 7.50–7.52 (d, $J = 8.0$ Hz, 2H, AA'BB'), 7.44–7.46 (d, $J = 7.9$ Hz, 2H, AA'BB'), 7.33–7.37 (m, 2H, AA'BB'), 7.00–7.07 (m, 12H, AA'BB'), 6.84–6.91 (m, 18H, AA'BB' + mesityl), 3.77 (s, 12H, OCH_3), 2.28 (s, 6H, CH_3), 2.00 (s, 12H, CH_3). ^{13}C NMR (100 MHz, d_6 -acetone): 157.2, 150.2, 146.7, 146.4, 142.5, 141.9, 141.5, 140.4, 139.8, 139.1, 137.1, 133.6, 131.7, 129.3, 127.9, 127.5, 122.4, 119.8, 115.7, 114.1, 93.8, 89.3, 55.9, 23.9, 21.4. ESI-MS calculated (m/z) for $\text{C}_{72}\text{H}_{66}\text{BN}_3\text{O}_4$: 1047.5152; found: 1047.5127. Elemental analysis calculated (%) for $\text{C}_{72}\text{H}_{66}\text{BN}_3\text{O}_4$: C 82.51, H 6.35, N 4.01; found: C 82.45, H 6.65, N 3.80.

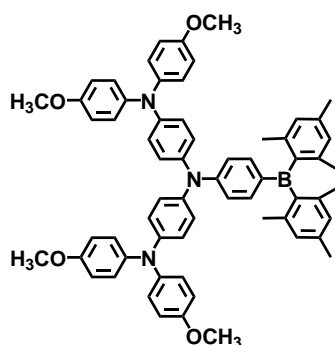
OTA-long-B2



OTA-ph-acetylene-H (180.0 mg, 0.25 mmol) and **Br-ph-B2** (194.9 mg, 0.29 mmol) were suspended in 10 mL dry NEt_3 under N_2 atmosphere and the mixture was de-oxygenated for 10 min. $\text{PdCl}_2(\text{PPh}_3)_2$ (3.50 mg, 0.005 mmol) and CuI (1.90 mg, 0.01 mmol) were added and the reaction mixture was heated to $100\text{ }^\circ\text{C}$ over night. After cooling to RT 100 mL sat. NH_4Cl -solution was added, the product was extracted with DCM (3 x 50 mL), the organic phases were dried over Na_2SO_4 and the solvent was evaporated. Column chromatography with an eluent mixture of pentane/DCM 1:2 yielded a bright yellow oil, which was crystallized as an orange solid by dropping a concentrated DCM-solution into MeOH (110.0 mg, 0.09 mmol, 34%).

^1H NMR (400 MHz, acetone- d_6): 7.66 (d, $J = 1.3$ Hz, 2H, ph), 7.54 (t, $J = 1.3$ Hz, 1H, ph), 7.25 (d, $J = 8.7$ Hz, 2H, AA'BB'), 7.07–7.01 (m, 8H, AA'BB'), 6.98 (d, $J = 8.7$ Hz, 4H, AA'BB'), 6.92–6.86 (m, 8H, AA'BB'), 6.86–6.81 (m, 6H, AA'BB'), 6.79 (s, 8H, mesityl), 3.77 (s, 12H, OCH_3), 2.24 (s, 12H, CH_3), 1.97 (s, 24H, CH_3). ^{13}C NMR (100 MHz, d_6 -acetone): 157.2, 149.9, 148.0, 146.7, 142.5, 142.2, 141.9, 141.5, 140.5, 140.2, 133.4, 129.3, 127.7, 127.4, 124.8, 122.4, 119.8, 115.8, 115.2, 114.2, 91.6, 88.9, 55.9, 23.9, 21.5. ESI-MS calculated (m/z) for $\text{C}_{90}\text{H}_{87}\text{B}_2\text{N}_3\text{O}_4$: 1295.6902; found: 1295.6878. Elemental analysis calculated (%) for $\text{C}_{90}\text{H}_{87}\text{B}_2\text{N}_3\text{O}_4 \cdot 0.5\text{H}_2\text{O}$: C 82.81, H 6.80, N 3.22; found: C 82.64, H 6.74, N 2.94.

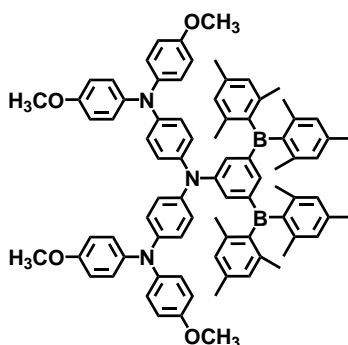
OTA-short-B



para-Br-ph-B (71.5 mg, 0.18 mmol) and OTA (100.0 mg, 0.16 mmol), together with NaO^tBu (307.6 mg, 3.20 mmol), Pd(dba)₂ (11.5 mg, 0.02 mmol), and (HP^tBu₃)BF₄ (4.60 mg, 0.02 mmol) were dissolved in 10 mL dry, de-oxygenated toluene under N₂ atmosphere. The mixture was refluxed at 125 °C for 1 h and 15 min and cooled to RT. 100 mL brine was added and the aqueous phase was extracted with DCM (3 × 50 mL). After drying over Na₂SO₄ and evaporation of the solvents the crude product was subjected to column chromatography. With pentane/DCM 1:1 then pure DCM as eluents the orange luminescent fraction was collected and recrystallized from acetone to yield a bright yellow solid (117 mg, 0.12 mmol, 77%).

¹H NMR (400 MHz, acetone-d₆): 7.31–7.25 (m, 2H, AA'BB'), 7.11–7.02 (m, 12H, AA'BB'), 6.93–6.84 (m, 12H, AA'BB'), 6.82–6.76 (m, 6H, AA'BB'), 3.78 (s, 12H, OCH₃), 2.25 (s, 6H, CH₃), 2.04 (s, 12H, CH₃; signal under acetone). ¹³C NMR (100 MHz, C₆D₆): 156.2, 152.5, 146.1, 142.4, 141.2, 140.7, 139.5, 137.6, 136.2, 128.4, 127.6, 126.5, 125.7, 121.9, 117.1, 114.9, 54.7, 23.6, 21.0. ESI-MS calculated (m/z) for C₆₄H₆₂N₃BO₄: 947.4838; found: 947.4834. Elemental analysis calculated (%) for C₆₄H₆₂N₃BO₄·0.5 H₂O: C 80.32, H 6.64, N 4.39; found: C 80.36, H 6.81, N 4.46.

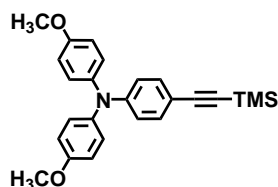
OTA-short-B2



Br-ph-B2 (117.6 mg, 0.18 mmol), **OTA** (100.0 mg, 0.16 mmol), NaO^tBu (307.6 mg, 3.20 mmol), $\text{Pd}(\text{dba})_2$ (11.5 mg, 0.02 mmol), and $(\text{HP}^t\text{Bu}_3)\text{BF}_4$ (4.60 mg, 0.02 mmol) were dissolved in 10 mL dry, de-oxygenated toluene under N_2 atmosphere. The mixture was refluxed at 125 °C for 1 h and cooled to RT. 100 mL brine was added and the aqueous phase was extracted with DCM (3 x 50 mL). After drying over Na_2SO_4 and evaporation of the solvents the crude product was subjected to column chromatography. With pentane/DCM 1:1 then pure DCM as eluents the orange fraction was collected and concentrated. Pure, orange product was obtained by dropping a concentrated DCM-solution in MeOH (120.0 mg, 0.10 mmol, 63%).

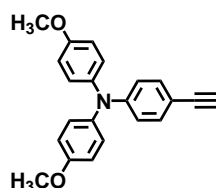
^1H NMR (400 MHz, acetone- d_6): 7.27 (d, $J = 1.1$ Hz, 2H, ph), 7.22 (t, $J = 1.1$ Hz, 1H, ph), 6.97–6.92 (m, 8H, AA'BB'), 6.90–6.84 (m, 12H, AA'BB'), 6.79–6.74 (m, 12H, AA'BB' + mesityl), 3.79 (s, 12H, OCH_3), 2.22 (s, 12H, CH_3), 1.98 (s, 24H, CH_3). ^{13}C NMR (100 MHz, d_6 -acetone): 156.8, 145.1, 142.8, 142.3, 141.4, 139.7, 138.4, 136.8, 134.2, 129.2, 127.8, 126.7, 125.7, 123.6, 120.1, 115.6, 55.9, 23.8, 21.6. ESI-MS calculated (m/z) for $\text{C}_{82}\text{H}_{83}\text{B}_2\text{N}_3\text{O}_4$: 1195.6588; found: 1195.6576. Elemental analysis calculated (%) for $\text{C}_{82}\text{H}_{83}\text{B}_2\text{N}_3\text{O}_4 \cdot 0.5\text{H}_2\text{O}$: C 81.72, H 7.02, N 3.49; found: C 81.83, H 6.95, N 3.44.

TAA-ph-acetylene-TMS



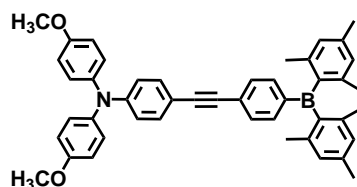
Br-ph-acetylene-TMS (1.00 g, 3.95 mmol), dianisylamine (724.5 mg, 3.16 mmol), NaO^tBu (6.30 g, 65.56 mmol), $\text{Pd}(\text{dba})_2$ (190.0 mg, 0.33 mmol), and (P^tBu_3) (0.98 mL, 0.33 mmol) were dissolved in 60 mL dry, de-oxygenated toluene under N_2 atmosphere. The mixture was stirred at 120 °C for 30 h. 100 mL brine was added to the cool mixture and the aqueous phase was extracted with DCM (3 x 50 mL). After drying over Na_2SO_4 and evaporation of the solvents the crude product was subjected to column chromatography. With pentane/DCM 1:3 as eluent mixture the pure product was obtained as a yellow solid (810.0 mg, 2.02 mmol, 64%).

^1H NMR (250 MHz, acetone- d_6): 7.27–7.19 (m, 2H, AA'BB'), 7.12–7.05 (m, 4H, AA'BB'), 6.97–6.89 (m, 4H, AA'BB'), 6.76–6.68 (m, 2H, AA'BB'), 3.80 (s, 6H, OCH_3), 0.20 (s, 9H, $\text{Si}(\text{CH}_3)_3$).

TAA-ph-acetylene-H

TAA-ph-acetylene-TMS (0.80 g, 1.99 mmol) was dissolved in 40 mL THF under N₂ atmosphere and a TBAF-solution in THF (18.0 mL, 5.40 mmol) was added dropwise. After the mixture was stirred at RT for 1 h, THF was evaporated and the residue was taken up in EtOAc and washed with H₂O (3 x 100 mL). After drying over Na₂SO₄ and evaporation of the solvent pure product was obtained as a yellow solid (0.65 g, 1.97 mmol, 99%).

¹H NMR (250 MHz, CDCl₃): 7.30–7.23 (m, 2H, AA'BB'), 7.11–7.01 (m, 4H, AA'BB'), 6.89–6.76 (m, 6H, AA'BB'), 3.80 (s, 6H, OCH₃).

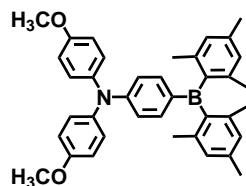
TAA-long-B

A suspension of *para*-Br-ph-B (270.0 mg, 0.67 mmol) and **TAA-ph-acetylene-H** (200.0 mg, 0.61 mmol) in 15 mL dry NEt₃ under N₂ atmosphere was de-oxygenated for 30 min. CuI (4.50 mg, 0.02 mmol) and PdCl₂(PPh₃)₂ (8.40 mg, 0.01 mmol) were added and the reaction mixture was stirred at 100 °C for 30 h. After cooling to RT 100 mL sat. NH₄Cl solution was added and the aqueous phase was extracted with DCM (3 x 50 mL). After drying over Na₂SO₄ and evaporation of the solvents the crude product was subjected to column chromatography. With pentane/EtOAc 18:1 the product fraction was eluted and then concentrated. Subsequent crystallization by dropping a concentrated DCM-solution into MeOH yielded pure product as a yellow solid (172.0 mg, 0.26 mmol, 43%).

¹H NMR (250 MHz, acetone-d₆): 7.56–7.49 (m, 2H, AA'BB'), 7.49–7.42 (m, 2H, AA'BB'), 7.39–7.32 (m, 2H, AA'BB'), 7.17–7.08 (m, 4H, AA'BB'), 6.99–6.91 (m, 4H, AA'BB'), 6.85 (s, 4H, mesityl), 6.82–6.75 (m, 2H, AA'BB'), 3.81 (s, 6H, OCH₃), 2.29 (s, 6H, CH₃), 2.00 (s, 12H, CH₃). ¹³C NMR (100 MHz, d₆-acetone): 158.9, 151.5, 147.3,

143.4, 142.5, 141.6, 140.8, 138.0, 134.5, 132.7, 130.2, 129.5, 129.4, 120.0, 116.9, 114.8, 94.7, 90.1, 56.9, 24.8, 22.4. ESI-MS calculated (m/z) for $C_{46}H_{44}BNO_2$: 653.3467; found: 653.3456. Elemental analysis calculated (%) for $C_{46}H_{44}BNO_2 \cdot 0.5H_2O$: C 83.37, H 6.84, N 2.11; found: C 83.74, H 6.83, N 2.20.

TAA-short-B



para-Br-ph-B (0.20 g, 0.51 mmol), dianisylamine (0.11 g, 0.47 mmol), NaO^tBu (0.82 g, 8.53 mmol), $Pd(dba)_2$ (23.0 mg, 0.04 mmol), and $(HP^tBu_3)BF_4$ (8.30 mg, 0.04 mmol) were dissolved in 15 mL dry, de-oxygenated toluene under N_2 atmosphere. The mixture was stirred at 120 °C for 2 h. 100 mL brine was added to the cool mixture and the aqueous phase was extracted with DCM (3 x 50 mL). After drying over Na_2SO_4 and evaporation of the solvents the crude product was subjected to column chromatography. With pentane/EtOAc 18:1 as eluent mixture the pure product was obtained as a bright yellow solid (0.24 g, 0.43 mmol, 93%).

1H NMR (250 MHz, $DMSO-d_6$): 7.21–7.10 (m, 6H, AA'BB'), 6.99–6.91 (m, 4H, AA'BB'), 6.77 (s, 4H, mesityl), 6.61 (d, $J = 8.7$ Hz, 2H, AA'BB'), 3.74 (s, 6H, OCH_3), 2.22 (s, 6H, CH_3), 1.97 (s, 12H, CH_3). ^{13}C NMR (100 MHz, $DMSO-d_6$): 156.7, 152.1, 141.4, 139.7, 138.5, 138.2, 137.2, 134.3, 128.1, 127.9, 115.3, 115.0, 55.2, 23.0, 20.7. ESI-MS calculated (m/z) for $C_{38}H_{40}BNO_2$: 553.3153; found: 553.3147. Elemental analysis calculated (%) for $C_{38}H_{40}BNO_2$: C 82.45, H 7.28, N 2.53; found: C 82.05, H 7.29, N 2.40.

VII. BIBLIOGRAPHY

- [1] Department of Economic and Social Affairs, Population Division *World Population Prospects: The 2012 Revision, Highlights and Advance Tables*. Tech. rep.; United Nations, 2013.
- [2] Lewis, N. S.; Nocera, D. G. *Proc. Natl. Acad. Sci. U S A*. **2006**, *103*, 15729.
- [3] Crabtree, G. W.; Lewis, N. S. *Physics Today* **2007**, *60*, 37.
- [4] Ciamician, G. *Science* **1912**, *36*, 385.
- [5] Balzani, V.; Moggi, L.; Manfrin, M. F.; Bolletta, F.; Gleria, M. *Science* **1975**, *189*, 852.
- [6] Swierk, J. R.; Mallouk, T. E. *Chem. Soc. Rev.* **2013**, *42*, 2357.
- [7] Foyer, C. H.; Bloom, A. J.; Queval, G.; Noctor, G. *Annu. Rev. Plant Biol.* **2009**, *60*, 455.
- [8] Das, D.; Veziroglu, T. *Int. J. Hydrogen Energ.* **2001**, *26*, 13.
- [9] Zhu, M.; Yang, C. *Chem. Soc. Rev.* **2013**, *42*, 4963.
- [10] Reineke, S.; Thomschke, M.; Lüsse, B.; Leo, K. *Rev. Mod. Phys.* **2013**, *85*, 1245.
- [11] Tachibana, Y.; Vayssieres, L.; Durrant, J. R. *Nat. Photon.* **2012**, *6*, 511.
- [12] Barber, J. *Chem. Soc. Rev.* **2009**, *38*, 185.
- [13] Kärkäs, M. D.; Johnston, E. V.; Verho, O.; Åkermark, B. *Acc. Chem. Res.* **2014**, *47*, 100.
- [14] Pace, R. J.; Stranger, R.; Petrie, S. *Dalton Trans.* **2012**, *41*, 7179.
- [15] Umena, Y.; Kawakami, K.; Shen, J.-R.; Kamiya, N. *Nature* **2011**, *473*, 55.
- [16] Barber, J. *Inorg. Chem.* **2008**, *47*, 1700.
- [17] Loll, B.; Kern, J.; Saenger, W.; Zouni, A.; Biesiadka, J. *Nature* **2005**, *438*, 1040.
- [18] Dau, H.; Haumann, M. *Coord. Chem. Rev.* **2008**, *252*, 273.
- [19] Haumann, M.; Liebisch, P.; Müller, C.; Barra, M.; Grabolle, M.; Dau, H. *Science* **2005**, *310*, 1019.

- [20] Esswein, A. J.; Nocera, D. G. *Chem. Rev.* **2007**, *107*, 4022.
- [21] Elvington, M.; Brown, J.; Arachchige, S. M.; Brewer, K. J. *J. Am. Chem. Soc.* **2007**, *129*, 10644.
- [22] Eckenhoff, W. T.; Eisenberg, R. *Dalton Trans.* **2012**, *41*, 13004.
- [23] Dau, H.; Limberg, C.; Reier, T.; Risch, M.; Roggan, S.; Strasser, P. *ChemCatChem* **2010**, *2*, 724.
- [24] Fujishima, A.; Honda, K. *Nature* **1972**, *238*, 37.
- [25] Gersten, S. W.; Samuels, G. J.; Meyer, T. J. *J. Am. Chem. Soc.* **1982**, *104*, 4029.
- [26] Gao, Y.; Duan, L.; Yu, Z.; Ding, X.; Sun, L. *Faraday Discuss.* **2014**, *176*, 225.
- [27] Brimblecombe, R.; Koo, A.; Dismukes, G. C.; Swiegers, G. F.; Spiccia, L. *J. Am. Chem. Soc.* **2010**, *132*, 2892.
- [28] Cape, J. L.; Hurst, J. K. *J. Am. Chem. Soc.* **2008**, *130*, 827.
- [29] Du, P.; Eisenberg, R. *Energy Environ. Sci.* **2012**, *5*, 6012.
- [30] Morris, A. J.; Meyer, G. J.; Fujita, E. *Acc. Chem. Res.* **2009**, *42*, 1983.
- [31] Tinnemans, A. H. A.; Koster, T. P. M.; Thewissen, D. H. M. W.; Mackor, A. *Recl. Trav. Chim. Pays-Bas* **1984**, *103*, 288.
- [32] Sato, S.; Koike, K.; Inoue, H.; Ishitani, O. *Photochem. Photobiol. Sci.* **2007**, *6*, 454.
- [33] Atkins, P. W.; de Paula, J., *Physikalische Chemie*, Fourth; Wiley-VCH: Weinheim, 2006.
- [34] Lakowicz, J. R., *Principles of Fluorescence Spectroscopy*; Kluwer Academic/Plenum Publishers: New York, 1999; Vol. 2.
- [35] Montalti, M.; Credi, A.; Prodi, L.; Gandolfi, M. T., *Handbook of Photochemistry*; CRC Press: Florida, 2006; Vol. 3.
- [36] Juris, A.; Balzani, V.; Barigelletti, F.; Campagna, S.; Belser, P.; von Zelewsky, A. *Coord. Chem. Rev.* **1988**, *84*, 85.
- [37] Karlsson, S. Single and Accumulative Electron Transfer - Prerequisites for Artificial Photosynthesis., Ph.D. Thesis, Uppsala Universitet, 2010.
- [38] Marcus, R. A. *J. Chem. Phys.* **1956**, *24*, 966.
- [39] Marcus, R. A. *J. Chem. Phys.* **1957**, *26*, 867.
- [40] Marcus, R. A. *J. Chem. Phys.* **1957**, *26*, 872.

- [41] Marcus, R. A. *Discuss. Faraday Soc.* **1960**, 29, 21.
- [42] Marcus, R. A. *J. Phys. Chem.* **1963**, 67, 853.
- [43] Marcus, R. A. *Annu. Rev. Phys. Chem.* **1964**, 15, 155.
- [44] Marcus, R.; Sutin, N. *Biochim. Biophys. Acta* **1985**, 811, 265.
- [45] Hush, N. S. *Trans. Faraday Soc.* **1961**, 57, 557.
- [46] Miller, J. R.; Calcaterra, L. T.; Closs, G. L. *J. Am. Chem. Soc.* **1984**, 106, 3047.
- [47] Closs, G. L.; Miller, J. R. *Science* **1988**, 240, 440.
- [48] Creutz, C.; Taube, H. *J. Am. Chem. Soc.* **1969**, 91, 3988.
- [49] Edwards, P.; Gray, H.; Lodge, M.; Williams, R. *Angew. Chem.* **2008**, 120, 6860.
- [50] Förster, T. *Discuss. Faraday Soc.* **1959**, 27, 7.
- [51] Dexter, D. L. *J. Chem. Phys.* **1953**, 21, 836.
- [52] Karlsson, S.; Boixel, J.; Pellegrin, Y.; Blart, E.; Becker, H.-C.; Odobel, F.; Hammarström, L. *Faraday Discuss.* **2012**, 155, 233.
- [53] Naqvi, K. R.; Staerk, H.; Gillbro, T. *Chem. Phys. Lett.* **1977**, 49, 160.
- [54] Ceroni, P.; Credi, A.; Venturi, M.; Balzani, V. *Photochem. Photobiol. Sci.* **2010**, 9, 1561.
- [55] Pellegrin, Y.; Odobel, F. *Coord. Chem. Rev.* **2011**, 255, 2578.
- [56] Manbeck, G. F.; Brewer, K. J. *Coord. Chem. Rev.* **2013**, 257, Electron Transfer in Coordination Chemistry, 1660.
- [57] Bonn, A. G.; Wenger, O. S. *Chimia* **2015**, 69, 17.
- [58] O'Neil, M. P.; Niemczyk, M. P.; Svec, W. A.; Gosztola, D.; Gaines, G. L.; Wasielewski, M. R. *Science* **1992**, 257, 63.
- [59] Imahori, H.; Hasegawa, M.; Taniguchi, S.; Aoki, M.; Okada, T.; Sakata, Y. *Chem. Lett.* **1998**, 27, 721.
- [60] Molnar, S. M.; Nallas, G.; Bridgewater, J. S.; Brewer, K. J. *J. Am. Chem. Soc.* **1994**, 116, 5206.
- [61] Elvington, M.; Brewer, K. J. *Inorg. Chem.* **2006**, 45, 5242.
- [62] Arachchige, S. M.; Brown, J.; Brewer, K. J. *J. Photochem. Photobiol., A* **2008**, 197, 13.
- [63] Zigler, D. F.; Wang, J.; Brewer, K. J. *Inorg. Chem.* **2008**, 47, 11342.

- [64] Arachchige, S. M.; Brown, J. R.; Chang, E.; Jain, A.; Zigler, D. F.; Rangan, K.; Brewer, K. J. *Inorg. Chem.* **2009**, *48*, 1989.
- [65] White, T. A.; Rangan, K.; Brewer, K. J. *J. Photo* **2010**, *209*, 203.
- [66] Konduri, R.; Ye, H.; MacDonnell, F. M.; Serroni, S.; Campagna, S.; Rajeshwar, K. *Angew. Chem. Int. Ed.* **2002**, *41*, 3185.
- [67] Konduri, R.; de Tacconi, N. R.; Rajeshwar, K.; MacDonnell, F. M. *J. Am. Chem. Soc.* **2004**, *126*, 11621.
- [68] Ghaddar, T. H.; Wishart, J. F.; Thompson, D. W.; Whitesell, J. K.; Fox, M. A. *J. Am. Chem. Soc.* **2002**, *124*, 8285.
- [69] Zhang, X.-F.; Cui, X.; Liu, Q.; Zhang, F. *ChemPhysChem* **2008**, *9*, 1514.
- [70] Zhang, X.-F.; Cui, X.; Liu, Q.; Zhang, F. *Phys. Chem. Chem. Phys.* **2009**, *11*, 3566.
- [71] Elliott, K. J.; Harriman, A.; Le Pleux, L.; Pellegrin, Y.; Blart, E.; Mayer, C. R.; Odobel, F. *Phys. Chem. Chem. Phys.* **2009**, *11*, 8767.
- [72] Matt, B.; Fize, J.; Moussa, J.; Amouri, H.; Pereira, A.; Artero, V.; Izzet, G.; Proust, A. *Energy Environ. Sci.* **2013**, *6*, 1504.
- [73] Sun, L.; Raymond, M. K.; Magnuson, A.; LeGourriérec, D.; Tamm, M.; Abrahamsson, M.; Kenéz, P. H.; Mårtensson, J.; Stenhagen, G.; Hammarström, L.; Styring, S.; Åkermark, B. *J. Inorg. Biochem.* **2000**, *78*, 15.
- [74] Huang, P.; Magnuson, A.; Lomoth, R.; Abrahamsson, M.; Tamm, M.; Sun, L.; van Rotterdam, B.; Park, J.; Hammarström, L.; Åkermark, B.; Styring, S. *J. Inorg. Biochem.* **2002**, *91*, 159.
- [75] Romain, S.; Baffert, C.; Dumas, S.; Chauvin, J.; Lepretre, J.-C.; Daveloose, D.; Deronzier, A.; Collomb, M.-N. *Dalton Trans.* **2006**, 5691.
- [76] Collomb, M.-N.; Deronzier, A. *Eur. J. Inorg. Chem.* **2009**, 2009, 2025.
- [77] Karlsson, S.; Boixel, J.; Pellegrin, Y.; Blart, E.; Becker, H.-C.; Odobel, F.; Hammarström, L. *J. Am. Chem. Soc.* **2010**, *132*, 17977.
- [78] Gray, H. B.; Maverick, A. W. *Science* **1981**, *214*, 1201.
- [79] Meyer, T. J. *Acc. Chem. Res.* **1989**, *22*, 163.
- [80] Sacksteder, L.; Zipp, A. P.; Brown, E. A.; Streich, J.; Demas, J. N.; DeGraff, B. A. *Inorg. Chem.* **1990**, *29*, 4335.
- [81] Chen, P.; Westmoreland, T. D.; Danielson, E.; Schanze, K. S.; Anthon, D.; Neveux, P. E.; Meyer, T. J. *Inorg. Chem.* **1987**, *26*, 1116.

- [82] Kalyanasundaram, K. *Coord. Chem. Rev.* **1982**, *46*, 159.
- [83] Caspar, J. V.; Meyer, T. J. *J. Am. Chem. Soc.* **1983**, *105*, 5583.
- [84] Caspar, J. V.; Meyer, T. J. *J. Phys. Chem.* **1983**, *87*, 952.
- [85] Wenger, O. S. *Coord. Chem. Rev.* **2009**, *253*, 1439.
- [86] Diaz, A. N. *J. Photochem. Photobiol., A* **1990**, *53*, 141.
- [87] Görner, H. *Photochem. Photobiol.* **2003**, *77*, 171.
- [88] Hankache, J.; Hanss, D.; Wenger, O. S. *J. Phys. Chem. A* **2012**, *116*, 3347.
- [89] Hankache, J.; Wenger, O. S. *Phys. Chem. Chem. Phys.* **2012**, *14*, 2685.
- [90] Babaei, A.; Connor, P. A.; McQuillan, A. J.; Umaphathy, S. J. *Chem. Educ.* **1997**, *74*, 1200.
- [91] Das, S.; Bhattacharya, A.; Mandal, P.; Rath, M.; Mukherjee, T. *Radiat. Phys. Chem.* **2002**, *65*, 93.
- [92] Rath, M.; Pal, H.; Mukherjee, T. *Radiat. Phys. Chem.* **1996**, *47*, 221.
- [93] Wightman, R. M.; Cockrell, J. R.; Murray, R. W.; Burnett, J. N.; Jones, S. B. *J. Am. Chem. Soc.* **1976**, *98*, 2562.
- [94] Hirao, Y.; Ito, A.; Tanaka, K. *J. Phys. Chem. A* **2007**, *111*, 2951.
- [95] Bozic-Weber, B.; Brauchli, S. Y.; Constable, E. C.; Furer, S. O.; Housecroft, C. E.; Wright, I. A. *Phys. Chem. Chem. Phys.* **2013**, *15*, 4500.
- [96] Ito, A.; Sakamaki, D.; Ichikawa, Y.; Tanaka, K. *Chem. Mater.* **2011**, *23*, 841.
- [97] Hirao, Y.; Ino, H.; Ito, A.; Tanaka, K.; Kato, T. *J. Phys. Chem. A* **2006**, *110*, 4866.
- [98] Kamino, B. A.; Morse, G. E.; Bender, T. P. *J. Phys. Chem. C* **2011**, *115*, 20716.
- [99] Ning, Z.; Tian, H. *Chem. Commun.* **2009**, 5483.
- [100] Amthor, S.; Noller, B.; Lambert, C. *Chem. Phys.* **2005**, *316*, 141.
- [101] Smieja, J. M.; Kubiak, C. P. *Inorg. Chem.* **2010**, *49*, 9283.
- [102] Sullivan, B. P.; Meyer, T. J. *J. Chem. Soc., Chem. Commun.* **1984**, 1244.
- [103] Vlček A., J. English In *Photophysics of Organometallics*, Lees, A. J., Ed.; Topics in Organometallic Chemistry, Vol. 29; Springer Berlin Heidelberg: 2010, p 115.
- [104] Pavlishchuk, V. V.; Addison, A. W. *Inorg. Chim. Acta* **2000**, *298*, 97.
- [105] Kwon, O.; Barlow, S.; Odom, S. A.; Beverina, L.; Thompson, N. J.; Zojer, E.; Brédas, J.-L.; Marder, S. R. *J. Phys. Chem. A* **2005**, *109*, 9346.

- [106] Weller, A. *Z. Phys. Chem.* **1982**, *133*, 93.
- [107] Hori, H.; Ishihara, J.; Koike, K.; Takeuchi, K.; Ibusuki, T.; Ishitani, O. *J. Photochem. Photobiol., A* **1999**, *120*, 119.
- [108] Kuss-Petermann, M.; Wolf, H.; Stalke, D.; Wenger, O. S. *J. Am. Chem. Soc.* **2012**, *134*, 12844.
- [109] Chattopadhyay, N.; Serpa, C.; Purkayastha, P.; Arnaut, L. G.; Formosinho, S. J. *Phys. Chem. Chem. Phys.* **2001**, *3*, 70.
- [110] Pawlicki, M.; Collins, H.; Denning, R.; Anderson, H. *Angew. Chem. Int. Ed.* **2009**, *48*, 3244.
- [111] Pollnau, M.; Gamelin, D. R.; Lüthi, S. R.; Güdel, H. U.; Hehlen, M. P. *Phys. Rev. B* **2000**, *61*, 3337.
- [112] Sreenath, K.; Thomas, T. G.; Gopidas, K. R. *Org. Lett.* **2011**, *13*, 1134.
- [113] Hankache, J.; Wenger, O. S. *Chem. Commun.* **2011**, *47*, 10145.
- [114] Kalyanasundaram, K. *J. Chem. Soc., Faraday Trans. 2* **1986**, *82*, 2401.
- [115] Záliš, S.; Consani, C.; Nahhas, A. E.; Cannizzo, A.; Chergui, M.; Hartl, F.; Jr., A. V. *Inorg. Chim. Acta* **2011**, *374*, 578.
- [116] Protti, S.; Fagnoni, M.; Monti, S.; Rehault, J.; Poizat, O.; Albini, A. *RSC Adv.* **2012**, *2*, 1897.
- [117] Pierri, A. E.; Pallaoro, A.; Wu, G.; Ford, P. C. *J. Am. Chem. Soc.* **2012**, *134*, 18197.
- [118] Fang, Y.-Q.; Hanan, G. S. *Synlett* **2003**, *6*, 852.
- [119] Freys, J. C.; Wenger, O. S. *Eur. J. Inorg. Chem.* **2010**, *35*, 5509.
- [120] Liu, S.-J.; Zhao, Q.; Chen, R.-F.; Deng, Y.; Fan, Q.-L.; Li, F.-Y.; Wang, L.-H.; Huang, C.-H.; Huang, W. *Chem. Eur. J.* **2006**, *12*, 4351.
- [121] So, K. H.; Kim, R.; Park, H.; Kang, I.; Thangaraju, K.; Park, Y. S.; Kim, J. J.; Kwon, S.-K.; Kim, Y.-H. *Dyes Pigm.* **2012**, *92*, 603.
- [122] Inoue, H.; Hida, M.; Nakashima, N.; Yoshihara, K. *J. Phys. Chem.* **1982**, *86*, 3184.
- [123] Lin, Z.-P.; Aue, W. A. *Spectrochim. Acta, Part A* **2000**, *56*, 111.
- [124] Katsumi, J.; Nakayama, T.; Esaka, Y.; Uno, B. *Anal. Sci.* **2012**, *28*, 257.
- [125] Raamat, E.; Kaupmees, K.; Ovsjannikov, G.; Trummal, A.; Kütt, A.; Saame, J.; Koppel, I.; Kaljurand, I.; Lipping, L.; Rodima, T.; Pihl, V.; Koppel, I. A.; Leito, I. *J. Phys. Org. Chem.* **2013**, *26*, 162.

- [126] Kütt, A.; Rodima, T.; Saame, J.; Raamat, E.; Mäemets, V.; Kaljurand, I.; Koppel, I. A.; Garlyauskayte, R. Y.; Yagupolskii, Y. L.; Yagupolskii, L. M.; Bernhardt, E.; Willner, H.; Leito, I. *J. Org. Chem.* **2011**, *76*, 391.
- [127] Howells, R. D.; Mc Cown, J. D. *Chem. Rev.* **1977**, *77*, 69.
- [128] Kantner, S. S.; Kreevoy, M. M. *J. Org. Chem.* **1977**, *42*, 865.
- [129] Kütt, A.; Leito, I.; Kaljurand, I.; Sooväli, L.; Vlasov, V. M.; Yagupolskii, L. M.; Koppel, I. A. *J. Org. Chem.* **2006**, *71*, 2829.
- [130] Sarmini, K.; Kenndler, E. *J. Biochem. Biophys. Methods* **1999**, *38*, 123.
- [131] Gupta, N.; Linschitz, H. *J. Am. Chem. Soc.* **1997**, *119*, 6384.
- [132] Hankache, J.; Niemi, M.; Lemmetyinen, H.; Wenger, O. S. *Inorg. Chem.* **2012**, *51*, 6333.
- [133] Fukuzumi, S.; Ohkubo, K.; Morimoto, Y. *Phys. Chem. Chem. Phys.* **2012**, *14*, 8472.
- [134] Fukuzumi, S.; Ohkubo, K. *Coord. Chem. Rev.* **2010**, *254*, Inorganic Reaction Mechanisms A Tribute to Ralph Pearson on the occasion of his 90th birthday, 372.
- [135] Fukuzumi, S.; Ohtsu, H.; Ohkubo, K.; Itoh, S.; Imahori, H. *Coord. Chem. Rev.* **2002**, *226*, 71.
- [136] Okamoto, K.; Imahori, H.; Fukuzumi, S. *J. Am. Chem. Soc.* **2003**, *125*, 7014.
- [137] Shannon, R. D. *Acta Crystallogr., Sect. A: Cryst. Phys., Diffr., Theor. Gen. Cryst.*, **1976**, *32*, 751.
- [138] Kawashima, T.; Ohkubo, K.; Fukuzumi, S. *Phys. Chem. Chem. Phys.* **2011**, *13*, 3344.
- [139] Donoghue, J.; Fernandez, E.; McMillan, J.; Peters, D. *J. Inorg. Nucl. Chem.* **1969**, *31*, 1431.
- [140] Greaves, M. D.; Niemz, A.; Rotello, V. M. *J. Am. Chem. Soc.* **1999**, *121*, 266.
- [141] Hatchard, C. G.; Parker, C. A. *Proc. R. Soc. Math. Phys. Eng. Sci.* **1956**, *235*, 518.
- [142] Pozdnyakov, I. P.; Kel, O. V.; Plyusnin, V. F.; Grivin, V. P.; Bazhin, N. M. *J. Phys. Chem. A* **2008**, *112*, 8316.
- [143] Vitz, E. W. *J. Chem. Educ.* **1981**, *58*, 655.
- [144] Achord, J. M.; Hussey, C. L. *Anal. Chem.* **1980**, *52*, 601.

- [145] Nissim, R.; Batchelor-McAuley, C.; Li, Q.; Compton, R. G. *J. Electroanal. Chem.* **2012**, *681*, 44.
- [146] Breslin, D. T.; Fox, M. A. *J. Org. Chem.* **1994**, *59*, 7557.
- [147] Reynolds, R.; Line, L. L.; Nelson, R. F. *J. Am. Chem. Soc.* **1974**, *96*, 1087.
- [148] Bui, T.-T.; Beouch, L.; Sallenave, X.; Goubard, F. *Tetrahedron Lett.* **2013**, *54*, 4277.
- [149] Yamamoto, M.; Tsujii, Y.; Tsuchida, A. *Chem. Phys. Lett.* **1989**, *154*, 559.
- [150] Shida, T.; Nosaka, Y.; Kato, T. *J. Phys. Chem.* **1978**, *82*, 695.
- [151] Housecroft, C. E.; Sharpe, A. G., *Anorganische Chemie*, 2nd; Pearson Education Deutschland: München, 2006.
- [152] Curcio, J. A.; Petty, C. C. *J. Opt. Soc. Am.* **1951**, *41*, 302.
- [153] Büning-Pfaue, H. *Food Chemistry* **2003**, *82*, 2nd International Workshop on Water in Foods, 107.
- [154] Hankache, J.; Niemi, M.; Lemmetyinen, H.; Wenger, O. S. *J. Phys. Chem. A* **2012**, *116*, 8159.
- [155] Gutmann, V. *Coord. Chem. Rev.* **1976**, *18*, 225.
- [156] Reichardt, C. *Chem. Rev.* **1994**, *94*, 2319.
- [157] Stahl, R.; Lambert, C.; Kaiser, C.; Wortmann, R.; Jakober, R. *Chem. Eur. J.* **2006**, *12*, 2358.
- [158] Hudson, Z. M.; Wang, S. *Acc. Chem. Res.* **2009**, *42*, 1584.
- [159] Steeger, M.; Lambert, C. *Chem. Eur. J.* **2012**, *18*, 11937.
- [160] Zhang, Z.; Edkins, R. M.; Nitsch, J.; Fucke, K.; Eichhorn, A.; Steffen, A.; Wang, Y.; Marder, T. B. *Chem. Eur. J.* **2015**, *21*, 177.
- [161] Hagfeldt, A.; Boschloo, G.; Sun, L.; Kloo, L.; Pettersson, H. *Chemical Reviews* **2010**, *110*, 6595.
- [162] Hide, F.; D'Íaz-García, M. A.; Schwartz, B. J.; Heeger, A. J. *Acc. Chem. Res.* **1997**, *30*, 430.
- [163] Kaim, W.; Schulz, A. *Angew. Chem. Int. Ed.* **1984**, *23*, 615.
- [164] Ricks, A. B.; Solomon, G. C.; Colvin, M. T.; Scott, A. M.; Chen, K.; Ratner, M. A.; Wasielewski, M. R. *J. Am. Chem. Soc.* **2010**, *132*, 15427.
- [165] Guo, Z.-H.; Jin, Z.-X.; Wang, J.-Y.; Pei, J. *Chem. Commun.* **2014**, *50*, 6088.

- [166] Lippert, E. *Z. Naturforsch. A* **1955**, *10*, 541.
- [167] Mataga, N.; Kaifu, Y.; Koizumi, M. *Bull. Chem. Soc. Jpn.* **1955**, *28*, 690.
- [168] Onsager, L. *J. Am. Chem. Soc.* **1936**, *58*, 1486.
- [169] Suppan, P. *Chem. Phys. Lett.* **1983**, *94*, 272.
- [170] Xu, X.; Ye, S.; He, B.; Chen, B.; Xiang, J.; Zhou, J.; Lu, P.; Zhao, Z.; Qiu, H. *Dyes and Pigments* **2014**, *101*, 136.
- [171] Florian, A.; Mayoral, M. J.; Stepanenko, V.; Fernández, G. *Chem. Eur. J.* **2012**, *18*, 14957.

A. ABBREVIATIONS AND SYMBOLS

ΔG_{ET}^0	free energy for electron transfer
A	acceptor
A ₁	phylloquinone
ADPs	anisotropic displacement parameters
AQ	9,10-anthraquinone
a.u.	arbitrary units
Boc	<i>tert</i> -butyloxycarbonyl
bpy	2,2'-bipyridine
CCDC	Cambridge Crystallographic Data Centre
CI	continuous irradiation
CSS1	first charge-separated state
CSS2	second charge-separated state
CT	charge transfer
CV	cyclic voltammetry/voltammogram
Cyt f	cytochrome f
D	donor
dba	dibenzylideneacetone
DCM	dichloromethane
DMAP	4-dimethylaminopyridine
DMF	dimethyl formamide
DMSO	dimethyl sulfoxide
e	elementary charge
EPR	electron paramagnetic resonance
ET	electron transfer
Et ₂ O	diethyl ether
EtOAc	ethyl acetate
EtOH	ethanol
eq	equivalent
Fc	ferrocene
FD	ferredoxin
FNR	ferredoxin-NADP ⁺ reductase

FT	Fourier transform
HFIP	hexafluoroisopropanol (1,1,1,3,3,3-hexafluoro-2- propanol)
HMPA	hexamethylphosphoramide
HRMS	high-resolution mass spectrometry
IR	infrared
MCET	metal ion-coupled electron transfer
Me	methyl
MeCN	acetonitrile
MeOH	methanol
MLCT	metal-ligand charge transfer
NADP	nicotinamide adenine dinucleotide phosphate
<i>n</i> -BuLi	<i>n</i> -butyllithium
Nd:YAG	neodymium-doped yttrium aluminium garnet
NEt ₃	triethylamine
NHE	normal hydrogen electrode
NIR	near infrared
NMR	nuclear magnetic resonance
obs	observed
OEC	oxygen evolving complex
OLED	organic light-emitting diode
OTA	oligotriarylamine
OTf	triflate
P	laser excitation power
P	photosensitizer
PC	plastocyanin
PCET	proton-coupled electron transfer
ph	phenyl
Pheo	pheophytin
PSI	photosystem I
PSII	photosystem II
PQ	plastoquinone pool
py	pyridine
Q	quencher
Q	quinone
R	distance
ref	reference
RT	room temperature

SCE	saturated calomel electrode
TAA	triarylamine
TBAPF ₆	tetrabutylammonium hexafluorophosphate
TCNB	tetracyanobenzene
TFA	trifluoroacetic acid
THF	tetrahydrofuran
TMS	trimethylsilyl
Tyr _Z	tyrosine Z
UV	ultraviolet
Vis	visible
XAS	X-ray absorption spectroscopy
xy	xylene

B. LIST OF FIGURES

I.1	Schematic structure of a system combining light-harvesting, charge separation, and fuel production. D = donor, P = photosensitizer, A = acceptor, ET = electron transfer.	3
II.1	Left: Reaction center of PSII. The surrounding protein structure was omitted for clarity. Electron transfer pathways are indicated by arrows. ¹⁴ Right: Crystal structure of the OEC with its ligand environment. ¹⁵ Reproduced with permission from ^{14,15} © Royal Society of Chemistry and Nature Publishing Group.....	6
II.2	Simplified JABLONSKI diagram.	12
II.3	Potential energy wells for exergonic electron transfer in D–A including inner and outer sphere reorganization.	14
II.4	Depiction of the normal and inverted region as proposed by MARCUS. .	16
II.5	Schematic diagram for electron-exchange triplet energy transfer according to DEXTER.	18
II.6	Schematic depiction of possible reaction pathways leading to the accumulation of charge in a DPA triad. Undesired reaction pathways are depicted with dashed arrows.	19
II.7	P–PBDCI–P	21
II.8	Trinuclear Ru–Ir–Ru (left) and Ru–Rh–Ru (right) complexes.	22
II.9	Ruthenium Photocatalysts	23
II.10	TiO ₂ –Ru–OTA.....	24
II.11	Absorption (solid trace) and emission (dashed trace) spectra of [Ru(bpy) ₃](PF ₆) ₂ on the left and [Re(bpy)(CO) ₃ (py)](OTf) on the right in MeCN at RT.	25
II.12	Latimer diagrams for the metal photosensitizers.	26
III.1	Molecular structure of the OTA donor. ADPs: 50% thermal ellipsoid probability. Carbon atoms: black; hydrogen atom: grey; nitrogen atoms: blue; oxygen atoms: red. (Symmetry operation used to generate equivalent atoms: 0.5-x, 0.5-y.)	31

III.2	IR spectra of the investigated complexes Re-ref (black), Re ₂ -TAA (blue), and Re ₂ -OTA (cyan).....	35
III.3	UV-Vis absorption spectra of the investigated complexes Re-ref (black), Re ₂ -TAA (blue), and Re ₂ -OTA (cyan).....	35
III.4	Cyclic voltammograms of Re ₂ -OTA (cyan), Re ₂ -TAA (blue), and Re-ref (black) in de-oxygenated MeCN solutions referenced to Fc ^{+ / 0}	36
III.5	Luminescence spectra of the investigated complexes (Re ₂ -TAA in blue and Re ₂ -OTA in cyan) measured on de-oxygenated 10 ⁻⁵ M MeCN solutions after excitation at 355 nm. All spectra were corrected for differences in extinction at 355 nm and normalized to the emission of Re-ref (black).	39
III.6	Steady-state luminescence spectra at of Re-ref (a), in an EtOH/MeOH 4:1) and OTA-ref (b), in MeTHF) at 77 K.	40
III.7	Luminescence decays of Re-ref (black), Re ₂ -TAA (blue), and Re ₂ -OTA (cyan) in de-oxygenated MeCN solutions (10 ⁻⁵ M) after excitation at 335 nm.	41
III.8	Top: UV-Vis absorption spectrum of a 10 ⁻⁵ M MeCN solution of Re ₂ -TAA (black) and its stepwise oxidation to Re ₂ -TAA ⁺ (blue) upon addition of increasing amounts of Cu(ClO ₄) ₂ ; bottom: transient absorption spectrum after 355 nm excitation of a 35 μM de-oxygenated MeCN solution of Re ₂ -TAA.	43
III.9	Decay of transient absorption signals at 360 nm (blue), 490 nm (cyan) and 770 nm (orange).	43
III.10	Top: stepwise chemical oxidation of a 10 ⁻⁵ M MeCN solution of Re ₂ -OTA (black) to Re ₂ -OTA ⁺ (blue) and Re ₂ -OTA ²⁺ (cyan); bottom: transient absorption spectrum of a de-oxygenated 10 ⁻⁵ M MeCN solution of Re ₂ -OTA directly after 355 nm excitation in a 50 ns time window. ...	44
III.11	Transient absorption decays of the photoproduct of Re ₂ -OTA at 420 nm and 790 nm.	45
III.12	a) Transient absorption spectrum after 355 nm excitation of a de-oxygenated 10 ⁻⁵ M MeCN solution of Re ₂ -OTA with an excess of TCNB; b) Corresponding decays at different wavelengths.	47
III.13	Intensity-dependent transient absorption spectra of a de-oxygenated 10 ⁻⁵ M MeCN solution of Re ₂ -OTA. Cyan: 3.8 mJ, blue: 1.1 mJ, and the difference spectrum in black.	48

III.14	Dependence of the signal intensity on the laser power. Left: linear dependency due to formation of $(\text{Re}^+)(\text{Re}^0)\text{-OTA}^+$ in a single-photon process. Right: non-linear behavior of intensity vs. \sqrt{P} because no two-photon process takes place.	48
III.15	Intensity-dependent transient absorption spectra obtained from the same solutions as in III.1.10. Cyan trace: 3.1 mJ, blue trace: 1.0 mJ, black: difference spectrum obtained by subtracting the blue trace from the cyan trace.	49
III.16	Emission decays of $\text{Re}_2\text{-TAA}^+$ (blue) and $\text{Re}_2\text{-OTA}^+$ (cyan) after excitation of a de-oxygenated MeCN solution at 355 nm.	50
III.17	Near infrared spectra of Re-ref (black) and the new triad AQ-Re-OTA (blue).	54
III.18	Optical absorption (left) and steady-state emission spectrum (right) of 10^{-5} M MeCN solutions of AQ-Re-OTA (blue) and Re-ref (black). The emission spectra were recorded after excitation of the de-oxygenated complexes at 355 nm.	54
III.19	Cyclic voltammogram of AQ-Re-OTA (blue) as a 1 mM solution in MeCN. The waves at -0.5 V correspond to the internal reference Me_{10}Fc . Re-ref (black) is depicted for direct comparison.	55
III.20	UV/Vis absorption spectra of 10^{-5} M MeCN solutions of pure OTA-ref (black), after addition of an excess of chloroacetic acid (blue), and triflic acid (cyan).	57
III.21	Stepwise chemical oxidation of a 10^{-5} M MeCN solution of AQ-Re-OTA with $\text{Cu}(\text{ClO}_4)_2$. Blue trace = OTA^+ , cyan trace = OTA^{2+}	58
III.22	Luminescence decays of 10^{-5} M MeCN solutions of pure AQ-Re-OTA (black), with 0.2 M benzoic acid (blue), and 0.2 M chloroacetic acid (cyan).	59
III.23	Transient absorption spectra of de-oxygenated MeCN solutions of pure AQ-Re-OTA (black), with 0.2 M benzoic acid (blue), and 0.2 M chloroacetic acid (cyan) after 355 nm excitation.	59
III.24	Transient absorption decays of photoproducts generated after excitation with a 10 ns laser pulse at 355 nm of a de-oxygenated MeCN solution of AQ-Re-OTA (a), with 0.2 M benzoic acid (b), and 0.2 M chloroacetic acid (c).	61

- III.25 Transient absorption spectra of a 10^{-5} M MeCN solution of AQ–Ru–OTA with 0.2 M chloroacetic acid at 3.4 mJ (cyan trace) and 1.1 mJ (blue trace) laser power. The blue spectrum was multiplied by a factor of 3.09 and subtracted from the cyan spectrum to give the difference spectrum in black. 61
- III.26 Synthetic route for preparation of Ru–OTA: **a)** Na_2CO_3 , $\text{Pd}(\text{PPh}_3)_4$, $\text{H}_2\text{O}/\text{EtOH}/\text{toluene}$, 90°C , over night; **b)** ICl , DCM , $0^\circ\text{C}/\text{RT}$, over night; **c)** NaO^tBu , $\text{Pd}(\text{dba})_2$, $(\text{HP}^t\text{Bu}_3)\text{BF}_4$, toluene , 110°C , 24 h; **e)** $\text{Ru}(\text{bpy})_2\text{Cl}_2$, $\text{CHCl}_3/\text{EtOH}$, reflux, 21 h. 66
- III.27 UV-Vis absorption (solid line) and steady state emission spectra (dashed line) of the triad (blue), dyad (cyan), and Ru–ref (black). 10^{-5} M MeCN solutions were used for the absorption measurements. Steady state emission was measured of de-oxygenated MeCN solutions, the spectra were corrected for differences in the absorption at 450 nm, and normalized to the Ru–ref emission. 67
- III.28 Cyclic voltammograms of Ru–ref (black), Ru–OTA (blue) and AQ–Ru–OTA (cyan) in MeCN. The waves marked by asterisks correspond to the internal references $\text{Fc}^{+/0}$ for Ru–ref and Me_{10}Fc for the triad. 68
- III.29 Energy level diagram for AQ–Ru–OTA. 69
- III.30 Normalized emission decays of Ru–ref (black), Ru–OTA (blue), and AQ–Ru–OTA (cyan). The decays were recorded on 10^{-5} M de-oxygenated MeCN solutions. 70
- III.31 Difference spectra for the chemical oxidation of OTA to OTA^+ (blue) and OTA^{2+} (cyan) obtained by addition of incremental amounts of $\text{Cu}(\text{ClO}_4)_2$ 71
- III.32 Transient absorption spectrum (left) and corresponding transient absorption kinetics (right) of the Ru–OTA dyad in a de-oxygenated 10^{-5} M MeCN solution. 71
- III.33 Left: Power-dependent transient absorption spectra of Ru–OTA in presence of an excess of TCNB after excitation at 532 nm. Blue: 10 mJ; cyan: 75 mJ. Right: Decays of the transient absorption signals at 378 (blue), 459 (cyan), and 795 nm (orange). All spectra were recorded on de-oxygenated MeCN solutions. 73
- III.34 Top: Difference Spectra of OTA^+ (grey trace) and OTA^{2+} (black trace) obtained by chemical oxidation with $\text{Cu}(\text{ClO}_4)_2$. Bottom: Difference spectrum of the high- and low-energy spectra as shown in Figure III.33 after normalization. 74

III.35	Left: Transient absorption spectra after excitation of a 10^{-5} M MeCN solution of AQ–Ru–OTA at 532 nm. High and low-energy spectra are shown with cyan (58 mJ) and blue (2.1 mJ) traces. Difference spectrum after normalization at the isosbestic points and subtraction of the blue from the cyan spectrum (orange trace). Right: Transient absorption decays of the signals at 415, 565, and 685 nm.	75
III.36	Transient absorption spectra of de-oxygenated $2.5 \cdot 10^{-5}$ M MeCN solutions of AQ–Ru–OTA with 400 eq of Sc^{3+} , Eu^{3+} , Mg^{2+} , Ca^{2+} , and Ba^{2+} . For better visualization the red and green spectra were multiplied by a factor of 5. The spectrum of the pure triad is shown as reference (black).	78
III.37	Decays of the transient photoproduct in presence of various metal ions. a) Ba^{2+} , b) Ca^{2+} , c) Mg^{2+} , d) Eu^{3+} , and e) Sc^{3+}	80
III.38	Emission decays of AQ–Ru–OTA with increasing Sc^{3+} concentrations. Right: Plot of k_{ET} vs $c(\text{Sc}^{3+})$	80
III.39	Left: Transient absorption spectra after excitation of AQ–Ru–OTA at 532 nm in de-oxygenated MeCN with increasing amounts of Sc^{3+} (0.5–400 eq). Right: Ground state absorption spectra of the sample solutions. The color code is the same as on the left and the spectrum in pure MeCN is depicted in black for comparison.	81
III.40	Kinetic absorption decays of the band at 420 nm (Figure III.39) in presence of various Sc^{3+} concentrations in de-oxygenated MeCN solution. .	82
III.41	Left: Transient absorption spectra at high (80 mJ, cyan) and low (10 mJ, blue) pulse energies after excitation of de-oxygenated MeCN solutions at 532 nm. Difference spectrum after normalization at 478 and 1285 nm and subtraction of the low from the high energy spectrum. Right: Kinetic absorption decays of the photoproduct at different wavelengths.	83
III.42	Ground-state absorption spectra of AQ–Ru–OTA in pure MeCN (black trace) and in presence of 1000 eq of diphenylthiourea (grey trace). .	85
III.43	Transient absorption spectra of AQ–Ru–OTA in presence of 1000 eq diphenylthiourea after excitation at 532 nm. Top: high energy spectrum = cyan (56–66 mJ), low energy spectrum = blue (11–12 mJ). Bottom: Difference spectrum obtained by subtraction of the low from the high energy spectrum after normalization to the isosbestic points at 478 and 1285 nm.	86

- III.44 Absorption decays of the bands at 418, 538, 680, and 780 nm recorded after excitation of the de-oxygenated, diphenylthiourea containing MeCN solution with a 532 nm laser pulse (56 mJ). 87
- III.45 Left: Absorption spectra of $[\text{Fe}(\text{phen})_3]^{2+}$ with increasing concentrations. Right: Calibration points and fit for the determination of the molar extinction coefficient. 91
- III.46 Left: Absorption spectra recorded after increasing irradiation times. Right: Amount of Fe^{2+} (mol) vs the irradiation period. 92
- III.47 UV-Vis absorption spectra after five successive measurements. **a)** Ru-OTA + O_2 ; **b)** Ru-OTA + N_2 ; **c)** AQ-Ru-OTA + O_2 ; **d)** AQ-Ru-OTA + N_2 . Complex concentrations were 10^{-5} M with 0.02 M $\text{Sc}(\text{OTf})_3$ 95
- III.48 UV-Vis absorption spectra of aerated MeCN solutions of **a)** Ru-OTA and **b)** AQ-Ru-OTA after 15 min in the dark (grey traces) and five successive measurements (black traces). Complex concentrations were 10^{-5} M with 0.02 M $\text{Sc}(\text{OTf})_3$ 95
- III.49 Changes in absorption upon continuous irradiation of aerated solutions of **a)** Ru-OTA (blue trace: 10 min; cyan trace: 3 h) and **b)** AQ-Ru-OTA (cyan trace: 30 min) in MeCN. $\lambda_{exc} = 450$ nm. 96
- III.50 Top: Normalized spectra of Ru-OTA (blue) and AQ-Ru-OTA (cyan) in aerated MeCN solutions. Chemically generated OTA^{2+} spectrum in black. Bottom: Difference spectra of the dyad (blue) and triad (cyan) after subtraction of the OTA^{2+} spectral signatures. 98
- III.51 Continuous irradiation of aerated MeCN solutions of Ru-OTA in presence of an excess of Sc^{3+} . Excitation occurred at a) 430 nm and b) 500 nm. 100
- III.52 Continuous irradiation of aerated MeCN solutions of Ru-OTA (a) and AQ-Ru-OTA (b) at 450 nm in absence of Sc^{3+} . Cyan traces: after 3 h. . . . 101
- III.53 Difference spectra recorded on aerated MeCN solutions kept in the dark. **a)** Ru-OTA + Sc^{3+} (blue trace = 10 min, cyan trace = 3 h), **b)** AQ-Ru-OTA + Sc^{3+} (cyan trace = 30 min), **c)** Ru-OTA without Sc^{3+} (cyan trace = 3 h), and **d)** AQ-Ru-OTA without Sc^{3+} (cyan trace = 3 h). . . 102
- III.54 Difference spectra after continuous irradiation of de-oxygenated MeCN solutions of Ru-OTA (a)) and AQ-Ru-OTA (b)) in presence of 0.02 M Sc^{3+} at 450 nm. **a)** blue trace = 9 h. **b)** blue trace = 2 h, cyan trace = 9 h. 103

III.55	Top: Difference spectra after 9 h of irradiation (black), of 47% OTA ⁺ (blue), and 23% OTA ²⁺ (cyan). Bottom: Difference spectrum after subtraction of the oxidized OTA contributions.	104
III.56	Difference spectra after continuous irradiation of de-oxygenated MeCN solutions of Ru-OTA (a) and AQ-Ru-OTA (b) in absence of Sc ³⁺ at 450 nm.	105
III.57	Difference spectra recorded on de-oxygenated MeCN solutions kept in the dark for the duration of 9 h. a) Ru-OTA + Sc ³⁺ , b) AQ-Ru-OTA + Sc ³⁺ , c) Ru-OTA without Sc ³⁺ , and d) AQ-Ru-OTA without Sc ³⁺ . The cyan traces correspond to the spectra recorded after 9 h in the dark.	106
III.58	Absorption spectra of AQ-Ru-OTA in pure MeCN (black trace) and of the de-oxygenated, irradiated solution after addition of NEt ₃	107
III.59	Cyclic voltammograms of Ru-ref (black trace) and AQ-Ru-OTA-Ru-AQ (blue trace) in Ar-purged MeCN solutions. The internal references Fc ^{+ / 0} for Ru-ref and Me ₁₀ Fc for the pentad are marked by asterisks. ...	110
III.60	Absorption (solid trace) and steady-state emission (dashed trace) spectra of AQ-Ru-OTA-Ru-AQ in blue. The spectra of Ru-ref are shown for comparison (black traces). Complexes were measured in de-oxygenated 10 ⁻⁵ M MeCN solutions. Emission spectra were corrected for differences in absorption at 450 nm and normalized to the emission of Ru-ref.	112
III.61	Absorption spectra recorded on de-oxygenated, 10 ⁻⁵ M solutions of AQ-Ru-OTA-Ru-AQ in various solvents. MeCN = black, MeCH/H ₂ O = blue, and HFIP = cyan.	113
III.62	Emission decays of AQ-Ru-OTA-Ru-AQ in de-oxygenated MeCN (black), MeCN/H ₂ O (blue), and HFIP (cyan). Excitation occurred at 532 nm and detection at 610 nm.	114
III.63	Top: Spectral characteristics of OTA ⁺ (blue) and OTA ²⁺ (cyan) after chemical oxidation in MeCN. Bottom: Transient absorption spectra of AQ-Ru-OTA-Ru-AQ in MeCN (black), MeCN/H ₂ O (blue), and HFIP (cyan). All spectra were measured of 10 ⁻⁵ M de-oxygenated solutions. .	114
III.64	Transient absorption decays of the photoproducts in MeCN (a), MeCN/H ₂ O (b), and HFIP (c).	116
III.65	a) MeCN, b) MeCN/H ₂ O, and c) HFIP. Top: Intensity-dependent transient absorption spectra (cyan = high energy; blue = low energy). Bottom: Corresponding difference spectra.	118

- III.66 Ground state absorption spectra of 10^{-5} M MeCN solutions of the pure pentad (black trace) and with 2000 eq diphenylthiourea (grey trace). . . . 119
- III.67 Top: Transient absorption spectra of AQ–Ru–OTA–Ru–AQ in presence of an excess of diphenylthiourea at low (10 mJ; blue trace) and high energies (60 mJ; cyan trace). Bottom: Difference absorption spectrum by subtraction of the blue from the cyan trace. The spectra were normalized to the isosbestic points (478 nm and 1285 nm) prior to subtraction. All measurements were performed in de-oxygenated MeCN solutions. 120
- III.68 Stepwise chemical oxidation of AQ–Ru–OTA–Ru–AQ by addition of incremental amounts of $\text{Cu}(\text{ClO}_4)_2$. Blue trace: OTA^+ ; cyan trace: OTA^{2+} . The arrows mark the isosbestic points used for normalization of the transient absorption spectra. 121
- III.69 Kinetic absorption decays of the transient absorption bands at 413, 540, and 740 nm after excitation with a laser pulse of 60 mJ in presence of an excess of diphenylthiourea. 121
- IV.1 Cyclic voltammograms of the six fluorophores in dry, Ar-purged THF in presence of 0.1 M TBAPF₆. Left: **a)** TAA-short-B, **b)** OTA-short-B, and **c)** OTA-short-B2. Right: **d)** TAA-long-B, **e)** OTA-long-B, and **f)** OTA-long-B2. Potential sweep rates are 0.1 V/s. 129
- IV.2 Absorption (solid traces) and emission spectra (dashed traces) of TAA-short-B (black, $\lambda_{exc} = 370$ nm), OTA-short-B (blue, $\lambda_{exc} = 330$ nm), and OTA-short-B2 (cyan, $\lambda_{exc} = 345$ nm). All spectra were recorded on 10^{-5} M hexane solutions under ambient conditions and the emission spectra were normalized. λ_{exc} is the respective excitation wavelength. 131
- IV.3 Absorption (solid traces) and emission spectra (dashed traces) of TAA-long-B (black, $\lambda_{exc} = 390$ nm), OTA-long-B (blue, $\lambda_{exc} = 345$ nm), and OTA-long-B2 (cyan, $\lambda_{exc} = 345$ nm). All spectra were recorded on 10^{-5} M hexane solutions under ambient conditions and the emission spectra were normalized. λ_{exc} is the respective excitation wavelength. . . . 132
- IV.4 Absorption spectra of **a)** TAA-short-B, **b)** OTA-short-B, **c)** OTA-short-B2, **d)** TAA-long-B, **e)** OTA-long-B, and **e)** OTA-long-B2 recorded on 10^{-5} M solutions in hexane (black), toluene (blue), Et₂O (cyan), THF (red), and DCM (orange). 133

IV.5	Emission spectra of a) TAA–short–B, b) OTA–short–B, c) OTA–short–B2, d) TAA–long–B, e) OTA–long–B, and e) OTA–long–B2 recorded on 10^{-5} M solutions in hexane (black), toluene (blue), Et ₂ O (cyan), THF (red), and DCM (orange).	134
IV.6	LIPPERT-MATAGA plots of the STOKES shift vs. the orientation polarizability Δf . a) TAA–short–B, b) OTA–short–B.	135
IV.7	LIPPERT-MATAGA plot of the STOKES shift vs. the orientation polarizability Δf for TAA–long–B.	136
IV.8	Illustration of increased ONSAGER radii in TAA–short–B (left) and OTA–short–B (right).	136

C. LIST OF TABLES

III.1	Redox potentials in MeCN. All values are given in V vs. $\text{Fc}^{+/0}$	37
III.2	Luminescence origin and triplet energies.	40
III.3	Redox potentials in Ar-purged MeCN solutions. All values are given in V vs. $\text{Fc}^{+/0}$	69
III.4	Used metal ions and their radii. ¹³⁷	77
III.5	Sample preparation for the calibration curve.	90
III.6	Extinction coefficients in $\text{M}^{-1}\text{cm}^{-1}$ for OTA^+ and OTA^{2+} species. Per- centages are given in parentheses.	97
III.7	GUTMANN acceptor numbers (AN) ¹⁵⁵ and dielectric constants (ϵ) ¹⁵⁶ of the solvents used. H_2O represents the MeCN/ H_2O mixture.	117
IV.1	Synthesized D–A compounds with overall yields and colors.	128
IV.2	Redox potentials in THF given in V vs. $\text{Fc}^{+/0}$	130
IV.3	Solvents and their polarity in terms of REICHHARDT parameters E_{T}^{N} . ¹⁵⁶ .	132
IV.4	Luminescence quantum yields (ϕ) and lifetimes (τ in ns) of the fluo- rophores in the different solvents. Measured in aerated solvents under ambient conditions.	138

D. CURRICULUM VITAE

Personal Details

Name Annabell G. Bonn
Date of Birth June 3rd, 1986
Birthplace Miltenberg, Bavaria, Germany

Education

2012 - 2015 University of Basel (CH)
PhD thesis: *“Towards Photoinduced Charge Accumulation in Purely Molecular d^6 Metal Complexes with Oligo-Triarylamine Donors”*
Supervisor: Prof. Dr. Oliver S. Wenger

2011 - 2012 Georg-August University Göttingen (D)
Started PhD thesis under supervision of Prof. Dr. Oliver S. Wenger

2011 Fraunhofer Institut für Silicatforschung, Würzburg (D)
Diploma thesis: *“Modification of polymeric precursors for the preparation of SiC-filaments with a diameter of 100 μm for application in MMC's”*
Supervisors: Dr. Andreas Nöth, Dr. Jürgen Clade

2005 - 2011 Julius-Maximilians University Würzburg (D)
Chemistry Studies; Degree: diploma

1996 - 2005 Karl-Ernst Academic High School Amorbach (D)
A-level: Chemistry, Mathematics, English, History

Publications

Journal Articles

First Reuter, L. G.; Bonn, A. G.; Stückl, A. C.; He, B.; Pati, P. B.; Zade, S.; Wenger, O. S.

“Charge Delocalization in a Homologous Series of α,α' -Bis(di-anisylamino)-Substituted Thiophene Monocations”

J. Phys. Chem. A **2012**, 116, 7345.

Second Bonn, A. G.; Neuburger, M.; Wenger, O. S.

“Photoinduced Electron Transfer in Rhenium(I) – Oligotriarylamine Molecules”

Inorg. Chem. **2014**, 53, 11075.

Third Bonn, A. G.; Wenger, O. S.

“Photoinduced Charge Accumulation in Molecular Systems”

Chimia **2015**, 69, 17.

Fourth Bonn, A. G.; Wenger, O. S.

“Charge Transfer Emission in Oligotriarylamine–Triarylborane Compounds”

J. Org. Chem. **2015**, 80, 4097.

Posters

First XXIV IUPAC Symposium on Photochemistry

“Mixed-Valence Phenomena in Amino-Decorated Thiophene Cations”

07/2012 in Coimbra, Portugal

Second SCS Fall Meeting

“Towards Accumulative Electron Transfer in a Molecular System”

09/2013 in Lausanne, Switzerland

Talks

First PhD Community (PCC), University of Basel

“Electron Transfer in the Wenger Group”

02/2013

Second National Centres of Competence in Research (NCCR),

Molecular Systems Engineering, Lunch Meeting

“Working towards charge accumulation in d^6 transition metal complexes”

02/2015